Receiver Design for Nonlinearly Distorted OFDM Signals: Applications in Radio-over-Fiber Systems

Thesis Submitted in Candidature for the Degree of
Doctor of Philosophy

November 2011

João Manuel Barbosa de Oliveira

Departamento de Engenharia Eletrotécnica e de Computadores
Faculdade de Engenharia da Universidade do Porto

Thesis Identification

Title:	Receiver Design for Nonlinearly Distorted OFDM Signals: Applications in Radio-over-Fiber Systems
Keywords:	OFDM, Channel estimation, Multipath channel, Nonlinear channel, Radio-over-fiber, CFO, Optimum receiver, ML, MMSE receiver, LMS
Start:	January 2006
Candidate information:	
Name:	João Manuel Barbosa de Oliveira
e-Mail:	dee05002@fe.up.pt
Curriculum Vitae:	http://www.fe.up.pt/∼dee05002/cv.pdf
Supervisor information:	
Name:	Henrique Manuel de Castro Faria Salgado
e-Mail:	hsalgado@fe.up.pt
Curriculum Vitae:	http://www.fe.up.pt/∼hsalgado/
Co-supervisor information:	
Name:	Miguel Raul Dias Rodrigues
e-Mail:	mrodrigues@dcc.fc.up.pt
Curriculum Vitae:	http://www.dcc.fc.up.pt/∼mrodrigues/
Educational Establishment:	Faculdade de Engenharia da Universidade do Porto
Research Institution:	INESC Porto

Statement of Originality

The work presented in this thesis was carried out by the candidate. It has not been presented previously for any degree, nor is it at present under consideration by any other degree awarding body.

Candidate:

(João Manuel Barbosa de Oliveira)

Supervisors:

(Henrique Manuel de Castro Faria Salgado)

(Miguel Raul Dias Rodrigues)

Statement of Availability

I hereby give consent for my thesis, if accepted, to be available for photocopying and for interlibrary loan, and for the title and summary to be made available to outside organizations.

Candidate:

_____

(João Manuel Barbosa de Oliveira)

"When you want something, all the universe conspires in helping you to achieve it."

–Paulo Coelho

Acknowledgements

First of all, I am sincerely indebted to my supervisors, Professor Henrique Salgado and Professor Miguel Rodrigues, for their continuous support and guidance, valuable advices and hours of thoughtful discussions throughout the course of work.

I would like to thank Instituto de Engenharia de Sistemas e Computadores do Porto (INESC Porto) for providing me the facilities necessary to my research work.

I am also grateful to Professor Izzat Darwazeh at University College London for providing me the opportunity to work in his research group.

I would like to acknowledge Fundação para a Ciência e a Tecnologia for providing me with financial support.

I thank all my friends and colleagues at INESC Porto specially Pedro Mota, Luís Pessoa, Mário Pereira and Qi Luo for their friendship as well as for all the fruitful discussions that we have had.

I thank my family, in particular my parents, Domingas and Manuel, and my sister, Ana, for their continuous support, help and encouragement. I also extend my thanks to my parents-in-law, sisters-in-law and brother-in-law for all their interest and support.

Last, but not the least, I am deeply grateful to my wife, Joana, for her tireless support, encouragement and comprehension throughout this work. Her unbounded patience and love have been so comforting. Thank you for being a source of hope and inspiration.

Abstract

This thesis is concerned with the study and development of receiver structures based on post-compensation techniques in order to mitigate the effects of both nonlinear and linear dispersive phenomena associated with communications channels and devices as well as the result of their interaction in the transmission of OFDM signals. Although the work presented here can be applied to any OFDM memoryless nonlinear transmission system, it focus on intensity modulated/direct detection radio-over-fiber uplink systems.

The impact of bandpass nonlinear channels exhibiting both AM/AM and AM/PM distortion in the transmission of OFDM signals is addressed. The optimum receiver and an associated iterative receiver that compensates for nonlinear distortion and AWGN are presented. Subsequently, a simpler linear receiver structure based on the minimization of the mean-squared error for nonlinearly distorted OFDM signals in the presence of AWGN is proposed and its structure is analytically derived. An extensive performance study of the referred techniques is conducted considering different system transmission and signal parameters such as constellation schemes, number of subcarriers, output back-offs and AWGN power spectral density levels. Moreover, a study of the impact on the signal transmission of two impairments namely an additional AWGN source before the nonlinear channel, as in RF uplink systems, and a carrier frequency offset at the receiver is also performed. Also, the robustness of the iterative receiver to these impairments is assessed.

In typical RF uplink systems, signals are first distorted by a wireless channel and then by a nonlinear element such as an high-power amplifier or an electro-optic converter. The impact of both multipath and bandpass nonlinear channels on the performance of OFDM signals transmission is addressed. Moreover, both channel estimation operation and signal equalization are also a subject of study. A new channel frequency response estimator structure based on the minimization of the mean-squared error is proposed for both Rayleigh and Rician distributed fading channels. Additionally, an extension to the estimator which includes compensation of carrier frequency offset is also presented. An extensive performance assessment of this estimator as well as of the perfect estimator and the simpler zero-forcing based estimator is conducted for different system transmission and signal parameters. Results for both conventional one-tap equalizer and an iterative maximum likelihood based receiver fed with channel estimates are also presented.

Finally, the techniques developed are applied to assess and improve the performance of intensity modulated/direct detection radio-over-fiber uplink systems. As impairments, we consider that the OFDM signal suffers from fading, antenna noise, nonlinearities from a Mach-Zehnder modulator, carrier frequency offset and noise from the photodiode. Several simulation results are presented and discussed for the transmission of two OFDM signals based on IEEE802.11g/n and ECMA-368 standards and the performances of the techniques are discussed.

Sumário

Esta tese está relacionada com o estudo e desenvolvimento de estruturas de recetores basedos em técnicas de pós-compensação a fim de combater os efeitos de fenómenos não-lineares e lineares dispersivos associados a canais de comunicação e dispositivos, bem como o resultado da sua interação na transmissão de sinais OFDM. Embora este trabalho possa ser aplicado a quaisquer transmissões de sinais OFDM sobre sistemas não-lineares sem memória, o mesmo foi elaborado tendo em vista ligações ascendentes de sistemas rádio-sobre-fibra baseados em modulação em intensidade e deteção direta.

O impacto na transmissão de sinais OFDM de canais não-lineares passa-banda exibindo distorções AM/AM e AM/PM é abordado. O recetor ótimo e um recetor iterativo que compensam a distorção não-linear e ruído AWGN são apresentados. Posteriormente, uma estrutura simples de um recetor linear baseado na minimização do erro quadrático médio para sinais OFDM distorcidos por uma não-linearidade na presença de ruído AWGN é proposta e a sua estrutura é analiticamente derivada. Um estudo exaustivo do desempenho destes recetores é efetuado, considerando diferentes parâmetros de sinal e do sistema de transmissão, tais como constelação, número de sub-portadoras, *back-off* de saída e níveis de densidade de potência do ruído AWGN. É também efetuado o estudo do impacto na transmissão de duas novas penalidades, nomeadamente o de uma fonte extra de ruído AWGN antes do canal não-linear, como acontence no sentido ascendente de sistemas RF, e o de desvios na frequência da portadora RF no recetor. Adicionalmente, é também analisada a robustez do recetor iterativo a estas penalidades.

Tipicamente, em sistemas RF ascendentes, os sinals são distorcidos por um canal sem-fios e posteriomente por um dispositivo não-linear, como um amplificador de alta potência ou um conversor eletro-ótico. O impacto de canais multi-percurso e não-lineares no desempenho da transmissão de sinais OFDM é abordado. Adicionalmente, as operações de estimação do canal e equalização de sinal são abordadas. Um estimador de canal baseado na minimização do erro quadrático médio é proposto para canais multi-percurso com distribuição de Rayleigh e Rician, assim como uma extensão que lhe permite compensar desvios na frequência. Um estudo do desempenho deste estimador bem como do estimador perfeito e de um simples baseado em *zero-forcing* para diferentes parâmetros do sinal e do sistema de transmissão é efetuado. Adicionalmente, são apresentados resultados tanto para o equalizador *one-tap* bem como para um recetor iterativo baseado em máxima verossimilhança com conhecimento da estimação do canal.

Por fim, as técnicas desenvolvidas são aplicadas para avaliar e melhorar o desempenho de ligações ascendentes de sistemas rádio-sobre-fibra. Como penalidades, é considerado que o sinal sofre desvanecimento, ruído de antena, não-linearidades de um modulador Mach-Zehnder, desvios na frequência e ruído do fotodíodo. Diversos resultados de simulação são apresentados e discutidos para a transmissão de sinais OFDM baseados nos *standards* IEEE802.11g/n e ECMA-368 e os desempenhos das várias técnicas são discutidos.

Contents

1 Introduction **1**

1.1 Thesis organization 3

1.2 Contributions 5

2 OFDM basics **11**

2.1 Introduction 11

2.2 Design of OFDM signals 13

2.2.1 Continuous-time implementation 14

2.2.2 Discrete-time implementation 17

2.2.3 Cyclic prefix 20

2.2.4 Spectral shaping and band limiting 22

2.2.5 Digital/Analog conversion 25

2.3 OFDM Drawbacks 27

2.3.1 Sensitivity to nonlinear distortion 28

2.3.2 Impact of synchronization errors 30

2.3.2.1 Carrier frequency offset 31

2.3.2.2 Symbol timing errors 35

2.4 Summary 37

3 Optimum OFDM receiver for memoryless nonlinear systems **39**

3.1 Introduction 39

3.2 Memoryless bandpass nonlinear systems 39

3.2.1 Analytical approach 40

3.2.2 Power series approach 42

3.3 Optimum receiver structure derivation 45
3.3.1 Sufficient statistics extractor 49
3.3.2 Maximum likelihood sequence estimation 50
3.3.3 Iterative ML detection algorithm 55
3.4 Summary 58

4 The MMSE OFDM receiver for memoryless nonlinear channels 59
4.1 Introduction 59
4.2 Minimum mean-squared error cost function 60
4.3 MMSE receiver structure derivation 60
4.3.1 Analytical computation of the matrix $\mathbf{M}_\alpha$ 69
4.4 Performance evaluation 76
4.4.1 Adaptive algorithms for the MMSE receiver 80
4.4.1.1 Least mean square algorithm 82
4.5 Summary 85

5 Receivers performance assessment 87
5.1 Introduction 87
5.2 Intermodulation distortion analysis 88
5.3 ML receiver performance assessment 105
5.3.1 Impact of the output back-off 106
5.3.2 Impact of the AWGN PSD 109
5.3.3 Optimum nonlinear operation point 112
5.3.4 Influence of the number of subcarriers used 118
5.3.5 Performance impact of both size of search region and number of iterations used 121
5.4 MMSE receiver performance assessment 128
5.5 Analysis of the impact of an AWGN source before the bandpass nonlinearity 134
5.6 Effect of carrier frequency and phase offsets 144
5.7 Summary 150

6 Channel estimation in an uplink system configuration 153

6.1 Introduction 153
6.2 Multipath channel modeling 155
6.3 Equalization of faded OFDM signals in a nonlinear system 158
6.4 OFDM channel estimation 162
6.4.1 Zero-forcing estimator 163
6.4.2 A novel MMSE channel estimator 164
6.4.2.1 Rayleigh fading channel case 169
6.4.2.2 Rician fading channel case 171
6.4.3 Extension of MMSE channel estimator for OFDM signals with carrier frequency and phase offsets 173
6.5 Performance evaluation 175
6.5.1 Rayleigh fading channel 180
6.5.2 Rician fading channel 189
6.5.3 Joint multipath channel and carrier frequency and phase offsets estimations 192
6.6 Considerations on the MMSE channel estimator structure, complexity and performance 194
6.7 Summary 195

7 Radio-over-fiber system case study 197

7.1 Introduction 197
7.2 Broadband wireless standards evolution 199
7.2.1 The 60 GHz frequency spectrum region 199
7.3 The radio-over-fiber concept 201
7.3.1 The optical medium: single-mode fiber versus multi-mode fiber . . 203
7.3.2 Techniques for RF signal generation and transportation 205
7.3.2.1 Basic direct intensity modulation 205
7.3.2.2 Electro-absorption transceiver 208
7.3.3 Chromatic dispersion induced effects 209
7.4 IM/DD externally modulated RoF uplink system 211
7.4.1 The Mach-Zehnder modulator lowpass equivalent response 213

7.4.2 The PIN photodiode response 217
7.5 Simulation results 218
7.5.1 IEEE802.11g/n over fiber 219
7.5.1.1 Non-fading channel 222
7.5.1.2 Rician fading channel 227
7.5.2 MB-OFDM ECMA-368 over fiber 231
7.5.2.1 Non-fading channel 234
7.5.2.2 Rician fading channel 237
7.6 Summary 241

8 Concluding remarks 243
8.1 Recommendation for future work 247

A Signal statistical properties & representation 251
A.1 Stationary stochastic processes 251
A.2 Representation of signals and systems 253
A.2.1 Equivalent lowpass representation of bandpass signals 254
A.2.2 Equivalent lowpass stationary stochastic processes representation . 259
A.2.2.1 Narrowband white noise representation 260

B PLCP preamble channel estimation sequences 261

Bibliography 263

List of Figures

1.1 Uplink radio-over-fiber system model. 3

2.1 Scheme of continuous-time model for baseband OFDM transmitter and receiver. 14

2.2 Representation of three subcarriers that constitutes a baseband OFDM symbol for subcarrier frequency spacing of $1/T$. 16

2.3 Scheme of discrete-time models for OFDM transmitter and receiver and their main elements. 18

2.4 Addition of the cyclic prefix to an OFDM symbol. 21

2.5 Example of a spectrum mask for an OFDM signal (ECMA-368 std. [1]). . 23

2.6 Power density spectra of OFDM signals with 32 and 1024 subcarriers. . . 24

2.7 Windowing process applied to an OFDM signal. 25

2.8 OFDM symbol boundary smoothness using a raised cosine window with different roll-off factors. 25

2.9 PSD of OFDM signals with 32 and 1024 subcarriers and with $BW_{3dB} = 528\,\text{MHz}$ centered at a given frequency $f_c \gg BW_{3dB}/2$ after applying raised cosine windows with different roll-off factors, β. 26

2.10 Non oversampled OFDM spectrum. 27

2.11 Oversampled OFDM spectrum. 28

2.12 Spectrum of the response of a third-order nonlinearity to a three subcarriers OFDM signal. 29

2.13 Total number of third-order IMPs that fall in a specific subchannel for OFDM signals. 30

2.14 Number of third-order IMPs that fall in subchannel at the center, edge and its overall for OFDM signals. 31

2.15 Frequency offset illustration. 32

2.16 Constellations of four consecutive (a) OFDM/QPSK and (b) OFDM/16-QAM symbols affected by a frequency offset of $\delta f = \Delta f/30$ and a phase offset of $\phi = 0$. 34

2.17 ICI term contribution power relative to its maximum as a function of subcarrier index for normalized frequency offsets of 0, 1/30 and 1/10. . . 35

2.18 Constellations of (a) OFDM/QPSK and (b) OFDM/16-QAM signals with 128 subcarriers affected by a symbol timing error of $\delta t = T_{CP}/500$. 36

3.1 Block diagram representation of the bandpass nonlinear channel model. . 41

3.2 Equivalent baseband OFDM communications system model. 45

3.3 Equivalent lowpass representation of the OFDM optimum receiver structure. 53

3.4 Block diagram of the iterative ML algorithm. 56

4.1 Structure of the linear MMSE OFDM receiver. 61

4.2 Equivalent baseband OFDM communications system model. 64

4.3 Alternative structure of the MMSE OFDM receiver. 68

4.4 Covariance matrix of the vector $\mathbf{Y}_k$ for OFDM/BPSK signals with 16 subcarriers and an OBO value of 2 dB. 73

4.5 Expectation values $\mathrm{E}\left[Y_{k,i}Y_{k,m}^*\right]$, with $i = -15, \cdots, 30$ and parameterized in m, for OFDM/BPSK signals with 16 subcarriers and an OBO value of 2 dB. 73

4.6 Cross-covariance matrix of the vectors $\mathbf{Y}_k$ and $\mathbf{S}_k$ for OFDM/BPSK signals with 16 subcarriers and an OBO value of 2 dB. 75

4.7 Expectation values $\mathrm{E}\left[S_{k,n}Y_{k,m}^*\right]$, with $m = -15, \cdots, 30$ and parameterized in n, for OFDM/BPSK signals with 16 subcarriers and an OBO value of 2 dB. 75

4.8 Matrix of coefficients α for OFDM/BPSK signals with 16 subcarriers, an OBO value of 2 dB and considering AWGN PSD $N_0 = 6.3 \times 10^{-9}$ W/Hz. . 76

4.9 Analytical and simulated mean-squared errors as function of OBO for OFDM/BPSK signals with 16 subcarriers and for two AWGN PSD levels. 78

4.10 Analytical and simulated mean-squared errors as function of the SNR per bit for OFDM/M-PSK and OFDM/16QAM signals with 16 subcarriers for an OBO value of 2.5 dB. 78

4.11 Analytical mean-squared errors as a function of the size of constellation, M, for OFDM/M-PSK signals with 16 subcarriers, a SNR per bit of 10 dB and for two OBO values. 79

4.12 Analytical and simulated mean-squared errors as a function of the number of subcarriers for OFDM/BPSK signals for different OBO values and a SNR per bit of 20 dB. 79

4.13 MMSE OFDM receiver with adaptive structure for estimation and adjustment of the matrix of coefficients $\mathbf{M}_\alpha$. 81

4.14 Estimation squared error as a function of the number of iterations for OFDM/BPSK signals with 16 subcarriers and for an OBO value of 3 dB. The dashed line represents the analytical minimum mean-squared error. . 84

5.1 Output back-off as a function of the input back-off for a third-order nonlinearity with $c_1 = 1$, $c_2 = 0$ and $c_3 = -0.20$, OFDM/BPSK signals and considering different number of subcarriers. 88

5.2 Equivalent baseband model used to study the impact of nonlinearities in OFDM signals transmissions. 89

5.3 Power spectrum density comparison for different OBO values and considering OFDM/QPSK signals with 16 subcarriers. 94

5.4 Power spectrum density comparison for different OBO values and considering OFDM/QPSK signals with 64 subcarriers. 94

5.5 (a) Received constellation and (b) received averaged constellation for different OBO values considering OFDM/QPSK signals with 64 subcarriers. 96

5.6 (a) Received constellation and (b) received averaged constellation for different OBO values considering OFDM/16-QAM signals with 64 subcarriers. 96

5.7 Deterministic compression gain term affected by desensitization terms in a (a) constellation representation and (b) received constellation point conditioned to a transmitted symbol $S^i_{k,n}$ (right), for OFDM/QPSK signals with an OBO value of 3 dB and different number of subcarriers. 97

5.8 Deterministic compression gain term affected by desensitization terms in a (a) constellation representation and (b) received constellation point conditioned to a transmitted symbol $S^i_{k,n}$ (right), for OFDM/16-QAM signals with an OBO value of 3 dB and different number of subcarriers. . 97

5.9 Simulation and analytical results of the (a) normalized amplitude and (b) phase of the averaged received complex symbol conditioned and relative to a specific transmitted symbol $S^i_{k,n}$ as a function of the subcarrier index for different OBO values and OFDM/16-QAM signals with 64 subcarriers. 98

5.10 Simulation and analytical results of the (a) relative amplitude and (b) phase of the averaged received complex symbol conveyed in subchannel $N/2$ as a function of the constellation point index for different OBO values and OFDM/16-QAM signals with 64 subcarriers. 99

5.11 Simulation and analytical results of the (a) relative amplitude and (b) phase of the averaged received complex symbol conveyed in subchannel $N/2$ as a function of the number of the number of subcarriers for different OBO values considering OFDM/16-QAM signals. 100

5.12 Amplitude and phase of the CAGC coefficient as a function of the output back-off for OFDM/16-QAM signals with 8, 16, 32, 64 and 128 subcarriers. 101

5.13 Normalized variance of the in-phase component of the IMD term in both subchannels at the center and edge as a function of the number of subcarriers for OFDM/16QAM and OFDM/QPSK signals and considering different OBO values. 102

5.14 Normalized variance of the in-phase component of the IMD term in the subchannel at the center as a function of the size of constellation, M, for OFDM/M-PSK signals and considering different OBO values. 103

5.15 Normalized variance of the IMD term in the subchannel at the center as a function of the constellation point index, i, for OFDM/16-QAM signals and considering different OBO values and number of subcarriers used. . . 104

5.16 Normalized variance of the IMD term in the subchannel at the center as a function of the constellation point index, i, for OFDM/QPSK signals and considering different OBO values and number of subcarriers used. . . 104

5.17 Bit error rate versus subcarrier index for OFDM/BPSK signals with 64 subcarriers, an SNR per bit of 10 dB and different OBO values. Results for both conventional receiver and iterative ML algorithm are presented. . 106

5.18 Bit error rate vs output back-off for OFDM/BPSK signals with 16 and 64 subcarriers and AWGN PSDs of 8×10^{-10} W/Hz and 2×10^{-10} W/Hz, respectively. Results for conventional, iterative ML and optimum ML receivers are presented. 107

5.19 Bit error rate vs output back-off for OFDM/BPSK signals with 16 and 64 subcarriers and AWGN PSDs of 4×10^{-10} W/Hz and 1×10^{-10} W/Hz, respectively. Results for conventional, iterative ML and optimum ML receivers are presented. 108

5.20 Bit error rate vs output back-off for OFDM/16-QAM signals with 16 and 64 subcarriers and AWGN PSDs of 8×10^{-10} W/Hz and 2×10^{-10} W/Hz, respectively. Results for conventional and iterative ML receivers are presented. 109

5.21 Bit error rate vs output back-off for OFDM/16-QAM signals with 16 and 64 subcarriers and AWGN PSDs of 4×10^{-10} W/Hz and 1×10^{-10} W/Hz, respectively. Results for conventional and iterative ML receivers are presented. 110

5.22 Bit error rate versus E_b/N_0 for OFDM/BPSK and OFDM/QPSK signals with 16 subcarriers, considering different back-offs and number of iterations for the iterative ML algorithm. 111

5.23 Bit error rate versus E_b/N_0 for OFDM/8-PSK signals with 16 subcarriers, considering different back-offs and number of iterations for the iterative ML algorithm. 111

5.24 Bit error rate versus E_b/N_0 for OFDM/16-PSK and OFDM/16-QAM signals with 16 subcarriers and considering different back-offs and number of iterations for the iterative ML algorithm. 112

5.25 Total degradation versus output back-off for both OFDM/BPSK and OFDM/QPSK signals with 16 subcarriers when considering both conventional receiver and iterative ML algorithm. Results for a bit error rate target of 10^{-3}. 114

5.26 Total degradation versus output back-off for both OFDM/8-PSK and OFDM/16-PSK signals with 16 subcarriers when considering both conventional receiver and iterative ML algorithm. Results for a bit error rate target of 10^{-3}. 114

5.27 Total degradation versus output back-off for both OFDM/BPSK and OFDM/QPSK signals with 64 subcarriers when considering both conventional receiver and iterative ML algorithm. Results for a bit error rate target of 10^{-3}. 115

5.28 Total degradation versus output back-off for both OFDM/8-PSK and OFDM/16-PSK signals with 64 subcarriers when considering both conventional receiver and iterative ML algorithm. Results for a bit error rate target of 10^{-3}. 115

5.29 Minimum (and optimum) total degradation versus size of constellation for OFDM/M-PSK signals with 16 and 64 subcarriers when considering both conventional receiver and iterative ML algorithm. Results for a bit error rate target of 10^{-3}. 116

5.30 Minimum (and optimum) output back-off versus size of constellation for OFDM/M-PSK signals with 16 and 64 subcarriers when considering both conventional receiver and iterative ML algorithm. Results for a bit error rate target of 10^{-3}. 117

5.31 Bit error rate as a function of the number of subcarriers for an OFDM/BPSK signal with $E_b/N_0 = 5\,\mathrm{dB}$ and various OBO values. 120

5.32 Bit error rate as a function of the number of subcarriers for an OFDM/BPSK signal with $E_b/N_0 = 10\,\mathrm{dB}$ and various OBO values. 120

5.33 Bit error rate as a function of the number of subcarriers for an OFDM/16-PSK signal with $E_b/N_0 = 15\,\text{dB}$ and various OBO values. 122

5.34 Bit error rate as a function of the number of subcarriers for an OFDM/16-PSK signal with $E_b/N_0 = 25\,\text{dB}$ and various OBO values. 122

5.35 Bit error rate versus size of the search region for the iterative ML algorithm considering OFDM/BPSK signals with 16 subcarriers and different OBO and AWGN PSD values. 123

5.36 Bit error rate vs. number of iterations of the iterative ML algorithm for an OFDM/BPSK signal with 16 subcarriers, OBO = 3.3 dB and considering different AWGN PSD values. 126

5.37 Bit error rate vs. number of iterations of the iterative ML algorithm for an OFDM/BPSK signal with 16 subcarriers, OBO = 2.5 dB and considering different AWGN PSD values. 126

5.38 Bit error rate vs. number of iterations of the iterative ML algorithm for an OFDM/BPSK signal with 64 subcarriers, OBO = 3.3 dB and considering different AWGN PSD values. 127

5.39 Bit error rate vs. number of iterations of the iterative ML algorithm for an OFDM/BPSK signal with 64 subcarriers, OBO = 2.5 dB and considering different AWGN PSD values. 127

5.40 Bit error rate versus number of subcarriers used for OFDM/BPSK signals with an OBO value of 3.3 dB and SNR per bit of 10 dB. Results considering several OFDM receivers are presented. 130

5.41 Bit error rate versus number of subcarriers used for OFDM/BPSK signals with an OBO value of 2.5 dB and SNR per bit of 10 dB. Results considering several OFDM receivers are presented. 130

5.42 Semi-analytic bit error rate versus OBO value for OFDM/BPSK signals with 8 and 16 subcarriers and different AWGN PDS levels. Both OFDM signals have the same SNR per bit at each OBO value. 132

5.43 Bit error rate versus SNR per bit for an OFDM/BPSK with 8 subcarriers and for two OBO values. Results considering several OFDM receivers are presented. 133

5.44 Bit error rate versus SNR per bit for an OFDM/BPSK with 16 subcarriers and for two OBO values. Results considering several OFDM receivers are presented. 133

5.45 Equivalent baseband OFDM communication system model with the presence of antenna noise. 134

5.46 CDF of $N'_{k,n}$ for OFDM/BPSK signals with an SNR per bit of 5 dB and an OBO value of 2.5 dB. Results for different number of subcarriers are presented. 139

5.47 CDF of $N'_{k,n}$ for OFDM/BPSK signals with an SNR per bit of 5 dB and an OBO value of 1.4 dB. Results for different number of subcarriers are presented. 139

5.48 CDF of $N'_{k,n}$ for OFDM/16-PSK signals with an SNR per bit of 5 dB and an OBO value of 1.4 dB. Results for different number of subcarriers are presented. 141

5.49 Kurtosis and skewness coefficient values of RV $N'_{k,n}$ for OFDM/BPSK and OFDM/16-PSK signals as a function of the number of subcarriers used for an OBO value of 1.4 dB and an SNR per bit of 5 dB. 142

5.50 Bit error rate performance vs. output back-off for OFDM/BPSK signals with 16 and 64 subcarriers considering conventional, iterative ML algorithm and (non-optimum) ML receivers. Antenna noise relation is considered to be $N_0^{AN}|_{N=16} = 4N_0^{AN}|_{N=64}$ to ensure the same SNR per bit immediately before the nonlinear channel. 143

5.51 Received constellation when considering OFDM/QPSK signals with 64 subcarriers, a linear channel transmission and different frequency offset scenarios. 147

5.52 Received constellation when considering OFDM/QPSK signals with 64 subcarriers, an output back-off of 3 dB and different frequency offset scenarios. 147

5.53 In-phase variance component of the received OFDM/QPSK signal as a function of carrier frequency offset. OFDM signal is considered to have 64 subcarriers and different OBO values. 148

5.54 Bit error rate as a function of carrier frequency offset for OFDM/QPSK signals with 64 subcarriers, an OBO value of 3 dB and different SNR per bit values. 149

5.55 Total degradation versus output back-off for OFDM/QPSK signals with 64 subcarriers considering both the conventional receiver and iterative ML algorithm and different CFO values for a target BER of 10^{-3}. 150

6.1 Illustration of multipath propagation in both LOS and NLOS transmissions. 154

6.2 Illustrative example of Rayleigh distributed channel frequency responses. . 159

6.3 Illustrative representation of OFDM subcarrier flat fading frequency responses of a multipath channel. 159

6.4 Equivalent baseband OFDM wireless communication model. 161

6.5 Representation of (a) block-type and (b) comb-type pilot subcarrier arrangements. 163

6.6 Structure of the channel frequency response MMSE estimator. 165

6.7 Alternative structure of the channel frequency response MMSE estimator. 168

6.8 Normalized values for the real part of the matrix $\mathrm{E}\left[Y_{k,i}Y_{k,m}^{*}|\mathbf{S}'\right]$ considering a 6 taps multipath channel followed by a linear channel (OBO = $+\infty$) for $N = 16$. 172

6.9 Normalized values for the real part of the matrix $\mathrm{E}\left[Y_{k,i}Y_{k,m}^{*}|\mathbf{S}'\right]$ considering a 6 taps multipath channel followed by a nonlinear channel for an OBO value of 7.7 dB and $N = 16$. 172

6.10 Analytical and simulated mean-squared errors as function of E_b/N_0 for OFDM signals with 16 subcarriers and OBO values of 4.10 dB, 7.68 dB and 10.45 dB. Results presented are for 6 taps channels. 178

6.11 Mean-squared error as a function of the output back-off for OFDM signals with 16 subcarriers for E_b/N_0 values of 30 dB and 40 dB and considering channels with 3, 6 and 10 taps. 178

6.12 Mean-squared error as function of the number of subcarriers for OFDM signals with OBO values of 4.10 dB, 7.68 dB and 10.45 dB and E_b/N_0 values of 30 dB and 40 dB. Results presented are for 6 taps channels. . . . 179

6.13 Bit error rate as a function of E_b/N_0 for faded OFDM/BPSK signals with 16 subcarriers, OBOs of 4.1 dB, 7.7 dB and 10.4 dB considering ZF, MMSE and perfect channel estimations and a one-tap equalizer. Results given are for 6 taps channels. 181

6.14 Bit error rate vs OBO for faded OFDM/{2,4,8,16}-PSK/16-QAM signals with 64 subcarriers and considering ZF, MMSE and ideal channel estimations and a one-tap equalizer. Results given are for 6 taps channels and AWGN PSDs of $N_0/K = 2.5 \times 10^{-13}$ W/Hz, where $K = \log_2(M)$. 182

6.15 Bit error rate vs number of subcarrier used for faded OFDM/BPSK signals for OBO values of 7.7 dB and 10.4 dB and for an E_b/N_0 value of 40 dB considering ZF, MMSE and ideal channel estimations and a one-tap equalizer. Results for 6 taps channels. 183

6.16 Bit error rate vs the number of channel taps for faded OFDM/BPSK signals with 16 subcarriers, OBOs of 7.7 dB and 10.4 dB and E_b/N_0 values of 30 dB and 40 dB considering ZF, MMSE and ideal channel estimations and a one-tap equalizer. 184

6.17 Bit error rate vs the number of channel taps for faded OFDM/BPSK signals with 64 subcarriers, OBOs of 7.7 dB and 10.4 dB and E_b/N_0 values of 30 dB and 40 dB considering ZF, MMSE and ideal channel estimations and a one-tap equalizer. 184

6.18 Bit error rate vs OBO for faded OFDM/BPSK signals with 16 subcarriers and an AWGN PSD of 1×10^{-12} W/Hz considering ZF, MMSE and ideal channel estimations, both one-tap equalizer and it. ML algorithm and various taps channels. 186

6.19 Bit error rate vs OBO for faded OFDM/BPSK signals with 64 subcarriers and an AWGN PSD of 2.5×10^{-13} W/Hz considering ZF, MMSE and ideal channel estimations, both one-tap equalizer and it. ML algorithm and various taps channels. 186

6.20 Total degradation vs OBO for faded OFDM/BPSK signals with 16 and 64 subcarriers considering ZF, MMSE and ideal channel estimations and both one-tap equalizer and iterative ML algorithm for a BER = 10^{-3}. Results for 6 taps channels. 188

6.21 Comparison of required E_b/N_0 to achieve BER = 10^{-3} as a function of OBO for faded OFDM/B-QPSK signals with 64 subcarriers considering ZF, MMSE and ideal channel estimations and both one-tap equalizer and it. ML algorithm. Results for 6 taps channels. 189

6.22 Bit error rate vs Rician K-factor for faded OFDM/BPSK signals with 64 subcarriers and an OBO of 3.4 dB for two E_b/N_0 levels of 10 dB and 20 dB. Results for 6 taps channels considering ZF, MMSE and ideal channel estimations and both one-tap equalizer and iterative ML algorithm. . . . 191

6.23 Comparison of required E_b/N_0 to achieve a bit error probability of 10^{-3} as a function of Rician K-factor for faded OFDM/BPSK signals with 64 subcarriers considering ZF, MMSE and ideal channel estimations and both one-tap equalizer and iterative ML algorithm. 192

6.24 Bit error rate vs normalized CFO for faded OFDM/BPSK signals with 16 and 64 subcarriers and an OBO of 10.4 dB for two E_b/N_0 levels of 30 dB and 40 dB. Results for Rayleigh distributed channels considering ZF, MMSE and ideal channel estimations followed by a one-tap equalizer. 193

6.25 Total degradation vs OBO for faded OFDM/BPSK signals with 64 subcarriers affected by CFO considering ZF, MMSE and ideal channel estimations and both one-tap equalizer and iterative ML algorithm for a BER = 10^{-3}. Results for 6 taps channels. 194

7.1 Data rates and range requirements for wireless standards and applications. 199

7.2 In-building radio-over-fiber concept. 201

7.3 Generic architecture of an RF-over-fiber system. 202

7.4 Generation of optical intensity modulated signal using (a) a LASER and (b) an external modulator. 206

7.5 Schematic of the relationship between output optical power and RF signal amplitude for (a) a LASER and (b) an external Mach-Zehnder modulator (MZM). 206

7.6 Representation of an intensity modulation direct detection (IM/DD) RoF link. 207

7.7 Representation of a base station based on a single R-EAM. 209

7.8 RF power degradation due to chromatic dispersion as a function of (a) optical fiber length and (b) RF frequency. Results for a fiber dispersion parameter $D = 17\,\mathrm{ps/nm/km}$ and an optical wavelength $\lambda_0 = 1550\,\mathrm{nm}$. . . 210

7.9 Optical single sideband (SSB) generation using (a) a fiber Bragg grating (FBG) and (b) a dual-arm MZM with a 90 degree phase shifter. 211

7.10 Schematic representation of the considered case study: uplink radio-over-fiber system based on external modulation of a LASER. 212

7.11 A Mach-Zehnder Modulator layout representation. 214

7.12 Receiver noise spectral density as a function of the mean incident optical power. Results for $\mathcal{R} = 1\,\mathrm{A/W}$. 219

7.13 IEEE802.11g/n 2.4 GHz spectrum division for non-overlapping channels. . 220

7.14 Mapping of the different types of subcarriers to logical frequencies. 221

7.15 IEEE802.11g PLCP packet data unit structure. 222

7.16 Total degradation as a function of the modulation index considering both the conventional receiver and ML algorithm with 1 and 5 iterations for a target bit error rate of 10^{-3} and for normalized CFO values of 0% and 5%. 224

7.17 Bit error rate as a function of the modulation index considering both the conventional receiver and ML algorithm with 1 and 5 iterations. Results for two SNR levels at the BS antenna, $\mathrm{SNR_{AN}} = +\infty$ and $\mathrm{SNR_{AN}} = 20\,\mathrm{dB}$. 226

7.18 Bit error rate as a function of the number of iterations of the ML algorithm for two Hamming distances and considering two modulation index values $m_i = 0.40$ and $m_i = 0.50$. 226

7.19 Power delay profile of a 6 tap channel. 228

7.20 Total degradation as a function of the modulation index considering the ZF, MMSE and perfect channel estimations and both the one-tap equalizer and the 5 iterations ML algorithm for a target bit error rate of 10^{-3}. Results are plotted for normalized CFO values of 0% and 5%. 229

7.21 Bit error rate as a function of the modulation index considering the ZF, MMSE and perfect channel estimations and both the one-tap equalizer and the 5 iterations ML algorithm. Results for two SNR levels at the BS antenna, $\mathrm{SNR_{AN}} = +\infty$ and $\mathrm{SNR_{AN}} = 20\,\mathrm{dB}$. 230

7.22 ECMA-368 spectrum division. 232

7.23 Example of a TF coding using the first three bands. 232

7.24 Mapping of the different types of subcarriers to logical frequencies. 234

7.25 ECMA-368 PLCP packet data unit structure. 235

7.26 Total degradation as a function of the modulation index considering both the conventional receiver and ML algorithm with 1 and 5 iterations for a target bit error rate of 10^{-3}. Results are plotted for normalized CFO values of 0% and 10%. 236

7.27 Bit error rate as a function of the modulation index considering both the conventional receiver and ML algorithm with 1 and 5 iterations. Results for two SNR levels at the BS antenna, $\mathrm{SNR_{AN}} = +\infty$ and $\mathrm{SNR_{AN}} = 15\,\mathrm{dB}$. 236

7.28 Bit error rate as a function of the number of iterations of the ML algorithm for a Hamming distance of one and considering two modulation index values $m_i = 0.50$ and $m_i = 0.60$. 238

7.29 Total degradation as a function of the modulation index considering the ZF, MMSE and perfect channel estimations and both the one-tap equalizer and the 5 iterations ML algorithm for a target bit error rate of 10^{-3}. Results for normalized CFO values of 0% and 10%. 239

7.30 Bit error rate as a function of the modulation index considering the ZF, MMSE and perfect channel estimations and both the one-tap equalizer and the 5 iterations ML algorithm. Results for two SNR levels at the BS antenna, $\mathrm{SNR_{AN}} = +\infty$ and $\mathrm{SNR_{AN}} = 15\,\mathrm{dB}$. 240

A.1 Amplitude spectrum representation of a real bandpass signal and its equivalent lowpass. 256

List of Tables

5.1 Minimum degradation improvements for the five iterations ML algorithm. 118

7.1 IEEE802.11g/n simulation related parameters 221

7.2 MB-OFDM UWB TFCs for Band Group #1 233

7.3 ECMA-368 simulation related parameters 234

B.1 IEEE802.11g/n PCLP preamble frequency-domain channel estimation sequence 261

B.2 ECMA-368 PLCP preamble frequency-domain channel estimation sequence 262

List of Abbreviations

ADC	Analog to Digital Converter
ADSL	Asymmetric Digital Subscriber Line
AGC	Automatic Gain Control
AM	Amplitude Modulation
AN	Antenna Noise
AWG	Arrayed Waveguide Grating
AWGN	Additive White Gaussian Noise
BB	Base-Band
BER	Bit Error Rate
BO	Back-Off
BPF	Band-Pass Filter
BPSK	Binary Phase-Shift Keying
BS	Base Station
CAGC	Complex Automatic Gain Control
CATV	Cable TV
CDF	Cumulative Density Function
CF	Carrier Frequency
CFO	Carrier Frequency Offset
CLT	Central Limit Theorem
CNR	Carrier-to-Noise Ratio
COTS	Commercial Off-The-Shelf
CP	Cyclic Prefix
CS	Central Station
CW	Continuous Wave

DAB	Digital Audio Broadcasting
DAC	Digital to Analog Converter
DCM	Dual Carrier Modulation
DC	Direct Current
DD	Direct Detection
DFB	Distributed Feedback LASER
DFT	Discrete Fourier Transform
DIY	Do It Yourself
DSB	Double-Side Band
DSL	Digital Subscriber Line
DSP	Digital Signal Processor
DVB	Digital Video Broadcasting
E/O	Electrical-to-Optical Conversion
EAM	Electro-Absorption Modulator
EAT	Electro-Absorption Transceiver
ECMA	European Computer Manufacturers Association
erfc	Complementary Error Function
FBG	Fiber Bragg Grating
FDM	Frequency Division Multiplexing
FDS	Frequency Domain Spreading
FCC	Federal Communications Commission
FEC	Forward Error Correction
FFT	Fast Fourier Transform
FM	Frequency Modulation
FPGA	Field-Programmable Gate Array
FSPL	Free-Space Path Loss
FT	Fourier Transform
FWA	Fixed Wireless Access
GI	Guard Interval
GSM	Global System for Mobile Communications
HD	High Definition

HDSL	High bit-rate Digital Subscriber Line
HPA	High Power Amplifier
HSDPA	High-Speed Downlink Packet Access
HSUPA	High-Speed Uplink Packet Access
IBO	Input Back-Off
ICI	Inter-Carrier Interference
IDFT	Inverse Discrete Fourier Transform
IEEE	Institute of Electrical and Electronics Engineers
IF	Intermediate Frequency
IFFT	Inverse Fast Fourier Transform
IFT	Inverse Fourier Transform
iid	Independent and Identically Distributed
IM	Intensity Modulation
IMD	Inter-Modulation Distortion
IMP	Inter-Modulation Product
IR	Impulse Response
ISI	Inter-Symbol Interference
ITU	International Telecommunication Unit
LAN	Local Area Network
LASER	Light Amplification by Stimulated Emission of Radiation
LHS	Left-Hand Side
LMS	Least Mean Square
LO	Local Oscillator
LOS	Line-of-Sight
LPF	Lowpass Filter
LTE	Long-Term Evolution
MAC	Media Access Control
MAN	Metropolitan Area Network
MAP	Maximum a Posteriori
MB-OFDM	Multi-Band Orthogonal Frequency Division Multiplexing
MBWA	Mobile Broadband Wireless Access

MCM	Multi-Carrier Modulation
MIMO	Multiple-Input Multiple-Output
ML	Maximum Likelihood
MLSE	Maximum Likelihood Sequence Estimator
MMF	Multi-Mode Fiber
MMSE	Minimum Mean Squared Error
MSE	Mean Squared Error
MZM	Mach-Zehnder Modulator
NL-MMSE	Nonlinear Minimum Mean Squared Error
NLMS	Normalized Least Mean Square
NLOS	Non-Line-of-Sight
O/E	Optical-to-Electrical Conversion
OADM	Optical Add/Drop Multiplexer
OBO	Output Back-Off
OFDM	Orthogonal Frequency Division Multiplexing
OFM	Optical Frequency Multiplication
OIL	Optical Injection Locking
OPLL	Optical Phase Locked Loops
OXC	Optical Cross Connect
P/S	Parallel to Serial Conversion
PAN	Personal Area Network
PAPR	Peak-to-Average Power Ratio
PD	Photodiode
PDF	Probability Density Function
PDP	Power Delay Profile
PF-GIPOF	Perfluorinated Graded-Index Polymer Optical Fiber
PHY	Physical Layer
PLCP	Packet Layer Convergence Protocol
PM	Phase Modulation
PSK	Phase-Shift Keying
POF	Polymer Optical Fiber

PON	Passive Optical Network
PPDU	PLCP Packet Data Unit
PSD	Power Spectral Density
PSDU	PLCP Service Data Unit
QAM	Quadrature Amplitude Modulation
QPSK	Quadrature Phase-Shift Keying
R-EAM	Reflective Electro-Absorption Modulator
RF	Radio Frequency
RHS	Right-Hand Side
RIN	Relative Intensity Noise
RLS	Recursive Least Square
RMS	Root Mean Square
RN	Receiver Noise
RoF	Radio-over-Fiber
RV	Random Variable
S/P	Serial to Parallel Conversion
SCM	Sub-Carrier Multiplexing
SD	Standard Definition
SFDR	Spurious Free Dynamic Range
SMF	Single-Mode Fiber
SNR	Signal-to-Noise Ratio
SSA	Solid-State Amplifier
SSB	Single-Side Band
TD	Total Degradation
TDS	Time Domain Spreading
TDL	Tapped Delay Line
TDM	Time Division Multiplexing
TF	Transfer Function
TFC	Time-Frequency Code
TWT	Traveling-Wave Tube
UBB-HAN	Ultra Broad-Band Home Area Network

UWB	Ultra Wide-Band
VCSEL	Vertical Cavity Surface Emitting LASER
VHDSL	Very High bit-rate Digital Subscriber Line
WC	Wireless Channel
WCDMA	Wide-Band Code Division Multiple Access
WDM	Wavelength Division Multiplexing
WiMAX	Worldwide Interoperability for Microwave Access
WLAN	Wireless Local Area Network
WMAN	Wireless Metropolitan Area Network
WPAN	Wireless Personal Area Network
WSSUS	Wide-Sense Stationary Uncorrelated Scattering
ZF	Zero-Forcing

List of Symbols

$(\cdot)^H$	Conjugate transpose operator
$(\cdot)^T$	Transpose operator
$(\cdot)^*$	Complex conjugate operator
$\|\cdot\|$	Norm of vector
$\|\cdot\|$	Absolute value of a vector or random variable
$\angle\cdot$	Angle of a vector or random variable
a	Distance between electrodes plates of the MZM
a_i	Fourier coefficient
$A_{[P_{out,max}]}$	Input amplitude that originates the maximum output power
$A_x(t)$	Baseband modulated envelope of signal $x(t)$
b_i	Fourier coefficient
B	Channel bandwidth
c	Speed of light
c_i	Power series coefficient
$\tilde{c}_i$	Lowpass equivalent power series coefficient
C	Complex automatic gain control coefficient applied to an arbitrary subchannel
C_n	Complex automatic gain control coefficient applied to subchannel n
D	Optical fiber dispersion parameter
$D(A,B)$	Euclidean distance between vectors A and B
$D^{HAM}(A,B)$	Hamming distance between vectors A and B
$D^i_{k,n}$	Deterministic term of the received complex symbol in subchannel n and time slot k conditioned to a

	transmitted complex symbol $S_{k,n}^{i}$
e_θ	Error of the estimator $\hat{\theta}$
$e_{k,n}$	Error of the MMSE estimator associated with subcarrier n in time slot k
$\mathbf{e}_k$	Error vector of the MMSE estimator in time slot k
E	Electric field change applied to the MZM
$\mathrm{E}[\cdot]$	Expected value operator
$E_{in}(t)$	Electric field applied at the input of the MZM
E_b	Energy per bit
$E_{out}(t)$	Electric field at the output of the MZM
f_0	Frequency of the first subcarrier of the OFDM signal
f_c	Center frequency of the bandpass signal
$f_{d,max}$	Maximum Doppler shift
f_{RF}	RF frequency
$f(\cdot)$	Input-output characteristic of the nonlinear channel
$F[\cdot]$	AM/AM input-output characteristic of the nonlinear channel
$F_X(x)$	Cumulative distribution function
$g_n(t)$	Orthonormal time-limited base functions
$\tilde{G}[\cdot]$	Lowpass equivalent input-output characteristic of the nonlinear channel
h	Hamming distance
$\tilde{h}_l$	Tap complex gain/attenuation factor
$\tilde{h}(\tau, t)$	Lowpass equivalent representation of the impulse response of time-variant channels
$\tilde{h}_p(t)$	Path complex gain/attenuation factor
$H_{k,n}$	Frequency response of the multipath channel in subchannel n and time slot k
$\tilde{H}(f, t)$	Lowpass equivalent representation of the frequency response of time-variant channels
$\hat{H}_{k,n}$	Estimate of $H_{k,n}$
$\hat{H}_{k,n}^{ZF}$	ZF estimate of $H_{k,n}$

$\hat{\mathbf{H}}$	Estimate vector of the multipath channel frequency response
i	Arbitrary discrete index
$i(t)$	Time-varying component of the photocurrent
I_0	DC component of the photocurrent
$I_0(\cdot)$	Modified Bessel function of the first kind with order zero
$I(t)$	Photocurrent
I_{RIN}^2	RIN PSD referred at the photodiode output
I_{SN}^2	Shot noise PSD referred at the photodiode output
I_{TN}^2	Thermal noise PSD referred at the photodiode output
$\Im\{\cdot\}$	Imaginary part of a complex-valued signal or random variable
j	$\sqrt{-1}$, arbitrary discrete index
k	Time slot, arbitrary discrete index
k_B	Boltzman constant
K	Rician factor
l	Arbitrary discrete index
$l\left(A\middle\vert B\right)$	Log-likelihood function
L	Maximum order of the nonlinearity, optical fiber length, dielectric material length of the MZM
$L\left(A\middle\vert B\right)$	Likelihood function
L_{null}	Optical fiber length at which the RF power is null
L_{OF}	Optical fiber attenuation value
L_{WC}	Wireless channel attenuation value
m	Arbitrary discrete index
m_i	MZM modulation index
M	Constellation size of the digital modulation scheme
M_l	Number of taps considered for the TDL model
M_p	Total number of paths
$\mathbf{M}_\alpha$	Matrix of coefficients $\alpha_{i,n}$
$\mathbf{M}_\alpha[i]$	Matrix of coefficients $\alpha_{i,n}$ at iteration i
$\mathbf{M}_\beta$	Matrix of coefficients $\beta_{i,n}$
$\hat{\mathbf{M}}_\alpha^{LMS}[i]$	LMS estimate of matrix $\mathbf{M}_\alpha[i]$

$\hat{\mathbf{M}}_{\alpha}^{NLMS}[i]$	NLMS estimate of matrix $\mathbf{M}_{\alpha}[i]$
n	Subcarrier index
$n(t)$	Zero-mean additive white Gaussian noise process
$\tilde{n}(t)$	Complex envelope of the signal $n(t)$
$n'(t)$	Additional noise term due to antenna noise
$\tilde{n}'(t)$	Complex envelope of the signal $n'(t)$
$\tilde{n}_p(t)$	Complex envelope of the noise term that is projected onto the set of $L(N-1)+1$ basis functions
$\tilde{n}_{AN}(t)$	Complex envelope of the antenna noise
$\tilde{n}_{RN}(t)$	Complex envelope of the receiver noise
N	Number of subcarriers
N_0	Power spectrum density of the additive white Gaussian noise
N_0^{AN}	Power spectral density of the antenna noise
N_0^{RN}	Power spectral density of the receiver noise
N_D	Number of data subcarriers
N_{DFT}	Size of the DFT
N_{FFT}	Size of the FFT
N_G	Number of guard subcarriers
$N_{k,n}$	Sample value of the additive white Gaussian noise process in subchannel n and time slot k
$N'_{k,n}$	Sample value of $n'(t)$ in subchannel n and time slot k
N_P	Number of defined pilot subcarriers
N_T	Number of total subcarriers used
$O(\cdot)$	Complexity cost order
$p\left(A\right)$	Probability density function of a random variable A
$p\left(A\middle\vert B\right)$	Conditional probability density function of a random variable A given B
$p_{out}(t)$	Time-varying component of $P_{out}(t)$
$\tilde{p}_{out,\omega}(t)$	Complex envelope of $p_{out}(t)$ after zonal filter
$P_{0,MZM}$	Steady-state component of $P_{out}(t)$
$P_{0,PD}$	Steady-state component of $P_{in,PD}(t)$

P_{AN}	Equivalent base station antenna noise power
$P\left(A\right)$	Probability of a random variable A
$P\left(A\middle\vert B\right)$	Conditional probability of a random variable A given B
$P\left(c\middle\vert B\right)$	Conditional probability of a correct decision of a random variable given B
$P(e)$	Probability of error of a random variable
$P\left(e\middle\vert B\right)$	Conditional probability of a decision error of a random variable given B
P_{CW}	Optical power of the CW LASER at the input of the MZM
$P_{in,0}$	Average input signal power
$P_{in,PD}(t)$	Photodiode incident optical power
$P_{in,max}$	Input power corresponding to the maximum output power
$P_{out}(t)$	Intensity response of the MZM
$P_{out,0}$	Average output signal power
$P_{out,max}$	Maximum output power
P_{RF}	Total RF power
q	Electron charge
r	Pockels coefficient
$r_{k,q}$	Received sampled equivalent baseband OFDM signal
$r(t)$	Bandpass received signal
$\tilde{r}(t)$	Complex envelope of the signal $r(t)$
$\tilde{r}_1(t)$	Complex envelope of the part of $\tilde{r}(t)$ that is extracted by the set of $L(N-1)+1$ basis functions
$\tilde{r}_2(t)$	Complex envelope of the signal that can be viewed as the remainder term of the noise process that is not extracted by the set of $L(N-1)+1$ basis functions
$\tilde{r}'(t)$	Complex envelope of the received signal affected by carrier frequency and phase offsets
$\dot{\tilde{r}}(t)$	Complex envelope of the received OFDM signal affected by fading, nonlinearities, AWGN and carrier frequency and phase offsets
R_b	Overall bitrate

$R_{k,n}$	Complex symbol conveyed in subchannel n and time slot k
$R'_{k,n}$	Complex symbol conveyed in subchannel n and time slot k affected by carrier frequency and phase offsets
$R^i_{k,n}$	Complex symbol conveyed in subchannel n and time slot k conditioned to a transmitted complex symbol $S^i_{k,n}$
R_{load}	Photodiode load resistance
$\mathbf{R}_k$	Received symbol vector in time slot k
$\mathcal{R}$	Photodiode responsivity
$\Re\{\cdot\}$	Real part of a complex-valued signal or random variable
$s_{k,q}$	Transmitted sampled equivalent baseband OFDM signal
$s(t)$	Bandpass transmitted OFDM signal
$\tilde{s}(t)$	Complex envelope of the signal $s(t)$
$\tilde{s}_k(t)$	Complex envelope of the transmitted OFDM symbol in time slot k
$S_{k,n}$	Complex symbol transmitted by subcarrier n in time slot k
$\mathbf{S}_k$	Transmit symbol vector in time slot k
$\mathbf{S}'$	Known vector of transmitted complex symbols for MMSE channel estimation
$\mathbf{S}^{(i)}_{\{l\}}$	One element of the set of possible estimates of vector $\mathbf{S}$ at iteration l
$\hat{\mathbf{S}}$	Estimate of vector $\mathbf{S}$
$\hat{\mathbf{S}}_{\{l\}}$	Estimate of vector $\mathbf{S}$ at iteration l
$\mathrm{SNR}_{\mathrm{AN}}$	SNR at the base station antenna
SNR_{loss}	SNR loss of a cyclic extended OFDM signal
t_0	Constant time delay
t_k	Sampling instant
T	OFDM symbol duration, temperature
T_a	Base station antenna temperature
T_c	Time coherence of the channel
T_{CP}	Cyclic prefix duration
T_{FFT}	FFT period
T_{GI}	Guard interval duration

T_{SYM}	Total symbol duration
T_W	Window duration
$u_n(t)$	Impulse response of the nth linear filter
$U^i_{k,n}$	Useful received complex symbol in subchannel n and time slot k affected by a phase shift and attenuation due to CFO and conditioned to a transmitted complex symbol $S^i_{k,n}$
$U'^i_{k,n}$	Useful received complex symbol in subchannel n and time slot k affected by nonlinear channel, phase shift and attenuation due to CFO and conditioned to a transmitted complex symbol $S^i_{k,n}$
$v(t)$	AC component of the voltage signal applied to the MZM
V	Voltage change applied to the MZM
V_b	DC bias voltage applied to the MZM
$V_1(t)$	Voltage signal applied in arm one of the MZM
$V_2(t)$	Voltage signal applied in arm two of the MZM
V_π	Voltage required to induce a π phase shift in the optical signal
$W_{k,n}$	Additional noise term due to ICI in subchannel n and time slot k
$W^i_{k,n}$	Additional noise term due to IMD in subchannel n and time slot k conditioned to a transmitted complex symbol $S^i_{k,n}$
$W'^i_{k,n}$	Additional noise term due to IMD and ICI due to CFO in subchannel n and time slot k conditioned to a transmitted complex symbol $S^i_{k,n}$
$\overline{W}^i_n$	Mean value of $W^i_{k,n}$
$x(t)$	Input bandpass signal
$\tilde{x}(t)$	Complex envelope of the signal $x(t)$
$y(t)$	Nonlinearly distorted OFDM signal, output of the memoryless nonlinear channel
$\tilde{y}(t)$	Complex envelope of the signal $y(t)$
$Y_{k,n}$	Nonlinearly distorted complex received symbol conveyed in subchannel n and time slot k
$\dot{Y}_{k,n}$	Faded and nonlinearly distorted complex received symbol conveyed in subchannel n and time slot k affected by carrier frequency

	and phase offsets
$\mathbf{Y}_k$	Vector of nonlinearly distorted complex received symbols in time slot k
$\dot{\mathbf{Y}}_k$	Vector of nonlinearly distorted complex received symbols in time slot k affected by carrier frequency and phase offsets
$\mathbf{Y}\left(\mathbf{S}^{(i)}\right)$	Vector of nonlinearly distorted complex received symbols for the transmitted sequence $\mathbf{S}^{(i)}$
Z_{WC}	Wireless channel length
${}^{zm}W^{i}_{k,n}$	Zero-mean IMD term in subchannel n and time slot k, nonlinear noise term in subchannel n and time slot k
α	Attenuation factor due to CFO considering the transmission over a linear channel
$\alpha_{i,n}$	Coefficient of the MMSE receiver structure
α_m	Angle between direction of motion and received signal
α_{n_l}	Attenuation factor due to CFO considering the transmission over a nonlinear channel
α_{x,n_l}	Attenuation factor due to CFO when considering both multipath and nonlinear channels
β	Roll-off factor of the raised cosine window
β_2	Kurtosis coefficient
$\beta_{i,n}$	Coefficient of the MMSE channel estimator structure
γ_1	Skewness coefficient
γ_k	Time-varying phase shift factor in time slot k due to CFO considering the transmission over a linear channel
γ_{k,n_l}	Time-varying phase shift factor in time slot k due to CFO considering the transmission over a nonlinear channel
γ_{k,x,n_l}	Time-varying phase shift factor due to CFO when considering both multipath and nonlinear channels
Δ	Gradient operator
$\delta(\cdot)$	Kronecker delta product
δf	Carrier frequency offset

δt	Symbol timing error
$\delta f/\Delta f$	Normalized carrier frequency offset
$\delta\phi$	Phase shift
$\delta\phi_1(t)$	Phase change in arm one of the MZM
$\delta\phi_2(t)$	Phase change in arm two of the MZM
Δf	Frequency separation between consecutive subcarriers
Δn	Refractive index change
θ	Arbitrary parameter
$\theta_x(t)$	Phase of signal $x(t)$
$\hat{\theta}$	Estimate of θ
λ_0	Optical wavelength
μ_i	ith central moment of a distribution
μ_{LMS}	Step size of the LMS algorithm
μ_{NLMS}	Step size of the NLMS algorithm
$\hat{\mu}_i$	Estimate of the ith central moment of a distribution
$\hat{\mu}'_i$	Estimate of the ith central moment of a distribution around the origin
ν	Relative velocity
ξ	Total mean-squared error
ξ_n	Mean-squared error associated with subcarrier n
ξ_n^{conv}	Mean-squared error associated with subcarrier n considering a conventional receiver
ξ_n^{min}	Minimum mean-squared error associated with subcarrier n
${\sigma_n^i}^2$	Variance of the nonlinear noise in subchannel n given that $S_{k,n}^i$ was transmitted
σ_S^2	Mean square of the transmitted symbols
σ_v	Standard deviation of the voltage signal applied to the MZM
Σ_A	Covariance of random vector A
Σ_{AB}	Cross-covariance of random vectors A and B
τ_{rms}	RMS delay spread
ϕ	Constant phase offset

$\Phi[\cdot]$	AM/PM input-output characteristic of the nonlinear channel
$\Omega(\tau)$	Power delay profile

Chapter 1

Introduction

Orthogonal frequency division multipexing (OFDM) has its roots back in the 1960s but it was not until the late 1990s that OFDM emerged as the key modulation for high data rate in both wired and wireless standards. It is indeed one of the most widespread modulations in current wireless standards [1–12]. Moreover, it is also being proposed for future wireless standards, in particular for the 60 GHz frequency region standards where multi-Gigabit signals can be accommodated [13]. Its high robustness to inter-symbol interference from dispersive channels and its unique orthogonal frequency scheme capable of transporting dozens to thousands of subchannels simultaneously with a very high spectral efficiency have led OFDM to be considered one of the best modulation formats for wireless standards.

In the past few years, we have witnessed a continuously growing demand for bandwidth. Broadband connections that were almost exclusive to large buildings and crowded spaces are now commonly seen in residential homes. In fact, we are moving on to an era of communication "anytime, anywhere, and with anything" and experiencing an exponential increase of personal wireless devices with powerful digital signal processors (DSP) capable to communicating at rates of dozens of Megabit per second and beyond. As a consequence, this high demand for bandwidth brings new challenges for network and system integrators engineers. Moreover, 60 GHz wireless standards force the use of picocellular architectures due to high propagation losses associated with that frequency region and, consequently, to an increase of the number of base stations (BS). To respond to the continuous increase of the throughput of each BS, and also to the high

costs inherent to a large number of high speed electronic transceivers at each BS, an attractive solution is to use an optical fiber backbone to connect all BSs to the central station (CS). The radio-over-fiber (RoF) concept merges both wireless and optical worlds and has been studied over the years as a promising communication paradigm for broadband services [14–28]. Its advantages include low loss, huge available bandwidth, centralization of complex and expensive devices at the CS and very simple BS structures at minimum costs. Moreover, in a (ideal) RoF network, several wireless signals and standards can be transported and distributed to the BS antennas through the same medium in a transparent way.

However, channel links are not perfect and the optical channel is no different. They may suffer from optical fiber dispersion and nonlinear (Kerr) effects, noise from LASERs and optical-to-electrical converters (O/E) such as photodiodes and nonlinear effects from the electrical-to-optical converters (E/O), among others. In fact, and mainly with respect to the transmission of OFDM signals, the nonlinear distortion from the E/O converter can severely affect the RF signal.

The impact of a nonlinear channel on the transmission of OFDM signals has been a subject of extensive research [29–34]. Furthermore, techniques that use pre-distortion techniques to minimize the nonlinear distortion based on clipping, peak-to-average power ratio (PAPR) reduction, tone reservation and injection and coding schemes have been also proposed [35–44]. Yet, in radio-over-fiber transmission systems, RF signals are also distorted by the fading phenomena from multipath channels. Moreover, in typical uplink RoF systems (see Figure 1.1), no signal processing and/or compensation is performed at the BS. In fact, the impact of nonlinear channels on faded OFDM signals and the resultant interaction of both distortions, which typically occurs in the uplink scenario, as well as post-compensation based techniques suitable for those systems are still not well exploited in the literature. Channel estimation and equalization techniques that take the faded and then nonlinearly distorted OFDM signal and processes it to optimally estimate both the frequency response of the multipath channel and the transmitted complex symbols are also required.

The main goal of this thesis is the development of OFDM post-compensation techniques to overcome the impairments from multipath and nonlinearities from the E/O

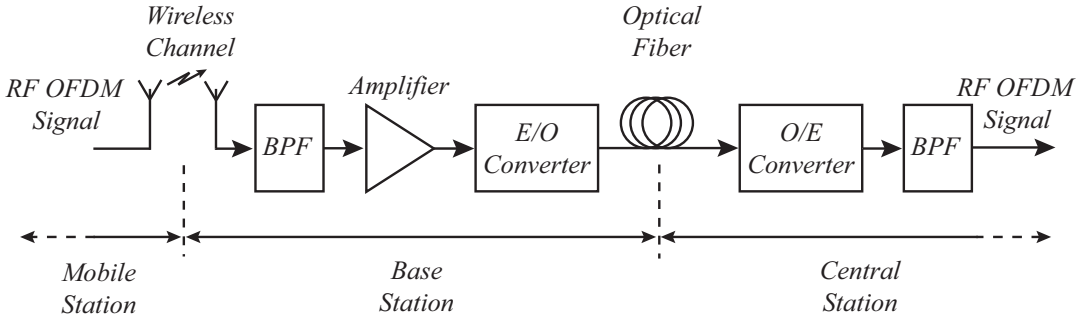

FIGURE 1.1: Uplink radio-over-fiber system model.

converter in radio-over-fiber uplink systems. The impact of those impairments in the system performance as well as the impact of additional impairments namely carrier frequency offset and antenna noise are also investigated.

1.1 Thesis organization

This thesis consists of this introduction followed by six main chapters, the concluding remarks and two appendices.

In chapter 2, an overview of the orthogonal frequency division multiplexing (OFDM) is presented. Here we address and describe the main system blocks of an OFDM implementation, namely blocks responsible for the following operations: cyclic prefix, windowing, pilot insertion, ADC/DAC operations, time/frequency synchronization and channel estimation. Moreover, both nonlinear distortion and time/frequency synchronization errors are also discussed.

In chapter 3, we start by introducing memoryless bandpass nonlinear systems and how to model them using a lowpass equivalent representation through a power series approach. The power series model of a bandpass nonlinearity will be the basis of the models and calculations in the rest of the thesis. Subsequently, we derive the optimum receiver structure in terms of error probability for nonlinearly distorted OFDM signals in AWGN which includes a sufficient statistics extractor and a maximum likelihood sequence estimator (MLSE) algorithm. An algorithm that iteratively searches for the transmitted vector that maximizes the likelihood in the neighborhood of a first estimate given by a conventional receiver is also addressed. Moreover, a modification of

the algorithm that permits to choose the size of the search region in each iteration is proposed.

In chapter 4, we propose a structure for a receiver that minimizes a specific metric, namely the mean squared error (MSE) between the transmit vector and its estimate for nonlinearly distorted OFDM signals corrupted by AWGN. The structure for the receiver is derived and its solution is also analytically derived and computed for OFDM signals conveying symbols from M-PSK and 16-QAM constellation schemes. Its performance in terms of MSE is analytically evaluated and compared with simulation results. Additionally, a least mean squares (LMS) based adaptive algorithm to iteratively estimate and adjust the filter coefficients is also proposed.

In chapter 5, we start by introducing and describing the characteristics of the nonlinear channel used throughout the chapter as well as some important concepts. Then, an analytical and simulation analysis of the impact of the nonlinear channel on the received symbols constellation is performed considering the transmission of OFDM signals conveying symbols from M-PSK and 16-QAM constellation schemes. In particular we analyze the role of the inter-modulation distortion (IMD) terms and both compression and desensitization terms in the degradation of the received constellation. Subsequently, an extensive performance assessment of the conventional, the ML, the iterative ML, the MMSE and the proposed joint MMSE/iterative ML receivers is performed and their results are compared and discussed. Then, an analysis of the degradation induced by both an AWGN noise source before the nonlinear channel, as occurs in uplink systems, and a frequency offset between receiver and transmitter is also addressed. The robustness of the iterative ML algorithm to these impairments is also a subject of discussion.

In chapter 6, we propose a channel estimation structure for faded OFDM signals also affected by nonlinear distortion and corrupted by AWGN. The system is intended to describe an uplink RoF transmission system. We start by introducing multipath channels and their commonly used models. Subsequently, a new MMSE channel frequency response estimator is analytically derived and its performance in terms of MSE is analytically evaluated and compared with simulation results. Also, its performance in terms of bit error rate is compared with both perfect and conventional zero-forcing (ZF) based estimators. Additionally, the estimator is extended in order to account for both

carrier frequency and phase offsets between transmitter and receiver. Moreover, a study of the optimality of the iterative ML algorithm acting as an equalizer is also performed. Several simulation results are presented and discussed.

In chapter 7, we present a case study application for the techniques detailed in this thesis for an intensity modulation/direct detection (IM/DD) RoF uplink system. We start by giving an overview on current and future wireless standards and their evolution. Then, we introduce the radio-over-fiber concept, its main characteristics, technologies, architectures and impairments. In our case study, we concentrate on the nonlinear distortion effect from the electro-optic converter, namely the Mach-Zehnder modulator. Subsequently, our case study is presented and mathematically defined and several simulation results are also presented and discussed for the transmission of two OFDM signals based on IEEE802.11g/n and ECMA-368 standards.

Finally, chapter 8 presents some concluding remarks. Further research work on this field is also identified.

Additionally, two appendices are included. Appendix A introduces some signal statistical properties and representation used in the thesis and Appendix B lists the frequency-domain channel estimation sequences defined in the IEEE802.11g/n and ECMA-368 standards.

1.2 Contributions

The main goal of this research work is to study and develop post-compensation receiver structures in order to mitigate the effects of both nonlinear and multipath channels and their interaction. The impact of those impairments in the transmission of OFDM signals is also studied. Additionally, the work focuses on IM/DD radio-over-fiber uplink systems. Nevertheless, it can be applied to any OFDM memoryless nonlinear transmission system. For this, new post-compensation techniques were analytically derived and computed. All simulation procedures and analytical computations were first implemented in Matlab and then optimized and implemented in C++. Furthermore, all Matlab/C++ scripts and functions used are original, entirely designed and developed from scratch.

The main contributions from this research work can be summarized as follows:

- Extension of the iterative ML algorithm to include a custom search region size based on an Hamming distance of one up to 2^{KN}, where K is the number of bits per symbol and N is the number of subcarriers. An extensive analysis in terms of bit error rate performance was conducted for the iterative ML algorithm. The impact of both size of search region and number of iterations used was addressed as well as a study of the performance of the algorithm when considering different number of subcarriers and constellation schemes. Results for total degradation of the nonlinear system were evaluated and optimum operation points in terms of output back-off values were also obtained.

- The optimality of both the ML receiver and the iterative ML algorithm and their robustness in an uplink scenario were tested, i.e., where an additional AWGN noise source before the nonlinearity is also considered. A detailed analysis in terms of cumulative density function (CDF) and kurtosis/skewness coefficients of the additional noisy term was performed. It was found that this additional term approaches well a Gaussian distribution under certain conditions.

- The impact of a carrier frequency offset (CFO) on the optimality of the iterative ML algorithm was studied. Results have shown that despite the additional noise term given by the CFO, the algorithm is still able to process the nonlinear noise and still outperform the conventional receiver.

- Development of an MMSE receiver structure for nonlinearly distorted OFDM signals in the presence of AWGN. The structure was analytically derived and it was found that it can also be seen as a conventional receiver capable of extracting a set of sufficient statistics followed by a linear transformation. The expressions that give the optimum linear transformation were also analytically derived and computed for M-PSK and 16-QAM modulations. Yet, they can be extended to generic M-QAM schemes. Alternatively, an iterative algorithm based on least mean-squares (LMS) was also proposed to search for the optimum coefficient values and to be able to track channel fluctuations.

- An investigation of the performance of the proposed MMSE receiver structure, both analytically and by means of simulation, in terms of mean squared error and,

by means of simulation, in terms of bit error rate was conducted. It was found that the MMSE is suitable for OFDM/BPSK signals with a relatively low number of subcarriers. Additionally, under these circumstances it even outperforms the iterative ML algorithm. Yet, for higher constellation sizes and/or signals with more than 24 subcarriers it was found to be inadequate.

- A joint MMSE/iterative ML algorithm for nonlinearly distorted OFDM signals in the presence of AWGN is proposed and its performance investigated. While the MMSE is best for a low number of subcarriers, the iterative ML algorithm has the opposite behavior. By combining both, it was found that its performance surpasses the best individual algorithm performances.

- Development of an MMSE channel estimator structure capable of processing faded OFDM signals that subsequently suffer from nonlinear distortion and are corrupted by AWGN. This estimator, designed specifically for uplink transmission scenarios, takes into account the potentially significant correlation between complex symbols conveyed by different subcarriers due to both multipath and nonlinear distortion. The structure is also found to be given by a sufficient statistics extractor followed by a linear transformation. We have analytically derived expressions for the optimum linear transformation for both Rayleigh and Rician distributed fading channels. Moreover, an extension of the structure to include compensation of carrier frequency and phase offsets is also presented.

- Investigation of the performance of the proposed MMSE channel estimator for several M-PSK and 16-QAM modulations as well as for different number of subcarriers and output back-offs. Moreover, the iterative ML algorithm is used to estimate the transmitted complex symbols, along with the conventional one-tap equalizer.

- Verification of the research work developed in a specific application: IM/DD externally modulated RoF uplink system. The applicability of the previously referred techniques is a subject of study. We consider the transmission of two OFDM signals based on the IEEE802.11g/n and UWB ECMA-368 standards.

- Development of "software tools" implemented in Matlab and then optimized in C++ for the computation of all analytical expressions and Monte Carlo simulations performed.

The contributions of this research work have led to the following publications:

- J.M.B. Oliveira, L.M. Pessoa, H.M. Salgado, I. Darwazeh, "Signal processing techniques for transmission impairments compensation in optical systems", Proceedings of 12th International Conference on Transparent Optical Networks (ICTON) 2010, Munich, Germany, June 2010.
- J.M.B. Oliveira, M.R.D. Rodrigues and H.M. Salgado, "MMSE receivers for non-linearly distorted OFDM signals", Proceedings of 7th Conference on Telecommunications (Conftele) 2009, Santa Maria da Feira, Portugal, May 2009.
- J.M.B. Oliveira, M.R.D. Rodrigues and H.M. Salgado, "Optimum receivers for non-linearly distorted OFDM signals in wireless-over-fiber applications: Impact of antenna noise," Proceedings of the IEEE International Conference on Ultra-Wideband (ICUWB) 2008, Hannover, Germany, September 2008.
- J.M.B. Oliveira, M.R.D. Rodrigues and H.M. Salgado, "Optimum receivers for non-linear distortion compensation of OFDM signals in fiber supported wireless applications", Proceedings of the 2007 IEEE International Topical Meeting on Microwave Photonics (MWP) 2007, Victoria, B.C., Canada, October 2007.
- J.M.B. Oliveira, M.R.D. Rodrigues and H.M. Salgado, "Non-Linear distortion compensation of OFDM signals in radio-over-fiber systems", Proceedings of the V Symposium on Enabling Optical Networks and Sensors (SEON) 2007, Aveiro, Portugal, June 2007.
- J.M.B. Oliveira, H.M. Salgado and M.R.D. Rodrigues, "Large signal analysis of Mach-Zehnder modulator intensity response in a linear dispersive fiber", Proceedings of the London Communications Symposium (LCS) 2006, London, United Kingdom, September 2006.

Additionally, Oliveira has also been actively involved in European Union projects UROOF – "Photonics Components for Ultra-Wideband Radio over Optical Fibre" and,

recently, DAPhNE – "Developing Aircraft Photonic Networks". Within the framework of these projects, extensive experimental evaluation of the performance of OFDM signals over fiber links have been conducted which constitutes the basis and supports future work on the topic of this thesis, namely, receiver design for nonlinearly distorted OFDM signals. This is discussed in chapter 8 in the section concerning future work. As a result of this involvement, Oliveira is both author and co-author in the following published papers in conferences, journals and book chapters, concerning the transmission of OFDM signals in IM/DD radio-over-fiber systems based on both low-cost commercial off-the-shelf (COTS) components and colorless and passive BS transceivers:

Book chapters:

- J. Oliveira, L. Pessoa, D. Coelho, H. Salgado, and J. Castro, "Performance assessment of UWB-over-fiber and applications", Ultra Wideband, Accepted for publication on InTech, 2012.

Journals:

- L. Pessoa, J. Oliveira, D. Coelho, J. Castro, and H. Salgado, "Experimental evaluation of a R-EAM and noise impact analysis for UWB and Wi-Fi transmission in RoF networks", Accepted for publication on Annals of Telecommunications, 2012.
- S. Silva, L. Pessoa, J. Oliveira, D. Coelho, J. Castro, and H. Salgado, "Performance evaluation of zero-biased VCSEL for high speed data transmission", Journal of Instrumentation, vol. 5, p. C11012, 2010.

Conferences:

- D. Coelho, J. Oliveira, L. Pessoa, J. Castro, and H. Salgado, "Experimental and Theoretical Performance Assessment of WiFi-over-Fiber Using Low Cost Directly Modulated VCSELs", Accepted for the $14th$ International Conference on Transparent Optical Networks (ICTON) 2012, Coventry, United Kingdom, July 2012.
- D. Coelho, J. Oliveira, L. Pessoa, H. Salgado and J. Castro, "Performance analysis of WDM-PON architecture for wireless services distribution in aircraft networks",

in Conference on Electronics, Telecommunications and Computers (CETC) 2011, Lisbon, Portugal, November 2011.

- L. Pessoa, D. Coelho, J. Oliveira, J. Castro, and H. Salgado, "Assessment of noise impact on UWB signals in R-EAM based optical links", in IEEE Avionics, Fiber-Optics and Photonics Technology Conference (AVFOP) 2011, San Diego, USA, October 2011.

- L. Pessoa, D. Coelho, J. Oliveira, J. Castro, and H. Salgado, "Wireless services distribution over GPON for avionics", in 37th European Conference and Exhibition on Optical Communication (ECOC) 2011, Geneva, Switzerland, September 2011.

- L. Pessoa, D. Coelho, J. Oliveira, J. Castro, and H. Salgado, "Experimental evaluation of R-EAM performance in RoF Networks, in Proceedings of the International Symposium on Green Radio over Fibre & All optical Technologies for Wireless Access Networks (GROWAN) 2011, Brest, France, June 2011.

- J. Oliveira, S. Silva, L. Pessoa, D. Coelho, H. Salgado, and J. Castro, "UWB radio over perfluorinated GI-POF for low-cost in-building networks", Proceedings of the 2010 IEEE International Topical Meeting on Microwave Photonics (MWP) 2010, Montreal, Canada, October 2010.

- J. Oliveira, S. Silva, L. Pessoa, D. Coelho, H. Salgado, and J. Castro, "Performance evaluation of MB-OFDM UWB over GI-POF", Proceedings of the $15th$ European Conference on Networks and Optical Communications (NOC) 2010, Faro, Portugal, June 2010.

Chapter 2

OFDM basics

2.1 Introduction

This chapter introduces the basics of an OFDM system and its major system blocks. The OFDM concept is based on dividing the available spectrum by a number of narrowband and low rate orthogonal subcarriers, making it a particular case of a multi-carrier modulation (MCM) scheme like conventional frequency division multiplexing (FDM). This allows the information to be separated in lower rate sub-streams and to be transmitted in different subcarriers.

Because of its orthogonal multi-carrier scheme, OFDM has many advantages for wireless applications, such as good performance in multipath and fading environments. By using a large number of parallel low rate subcarriers, the symbol period per subcarrier is considerable high and consequently the bandwidth of the modulated subcarrier becomes narrower than the coherence bandwidth of the time dispersive channel [45]. Therefore, each subcarrier experiences flat fading in multipath channels, rather than frequency selective fading, avoiding inter-symbol interference (ISI) problems and hence greatly simplifying receiver and equalizer structures.

The orthogonal characteristic of the subcarriers is achieved by selecting a group of frequencies that are orthogonal, from a mathematical point of view. This property allows the spectrum of each subcarrier to overlap the others without interfering with them, providing a high spectral efficiency. In fact, orthogonality ensures a complete elimination of crosstalk between subcarriers and a substantial simplification of the transmitter

and receiver (compared to the conventional FDM), avoiding the need of a separate filter for each subcarrier to recover information from the sub-streams. To avoid ISI between consecutive OFDM symbols in a time dispersive channel and still guarantee orthogonality between subcarriers, a guard interval (GI) in the form of a cyclic prefix (CP) must be appended at the beginning of the OFDM symbol.

The concept of MCM systems can be traced back to the early 1950s when Collins Radio Co. [46] developed the military "Kineplex" system, which consisted in a multi-tone transmission system over a high frequency radio channel subject to severe multipath fading. The first OFDM systems were presented in 1966 and 1967 by Chang [47] and Saltzberg [48], respectively. In 1971 a major contribution for the OFDM complexity problem was presented by Weinstein and Ebert [49] by introducing the discrete-time OFDM using fast Fourier transform (FFT) techniques for the modulation and demodulation processes. Moreover, the use of highly efficient inverse DFT (IDFT) and DFT implementations, such as fast Fourier transform (FFT) algorithms [50], instead of continuous-time modulation and demodulation procedures, respectively, have made OFDM both practical and attractive to use. This contribution, in combination with the fact that at this time digital signal processing (DSP) techniques were also in development in modems, helped making OFDM a more practical modulation scheme to use.

In the 1990s/2000s OFDM was studied and adopted for wired DSLs standards, such as asymmetric digital subscriber line (ADSL) [51, 52], ADSL2/2+ [53, 54], high bitrate digital subscriber line (HDSL) [55–57], very high bitrate digital subscriber line (VHDSL) [58, 59] and VHDSL2 [60], which by 2009 is the most advanced DSL standard, permitting data rates up to 200 Mb/s on twisted copper wire pairs.

Due to its high performance and robustness in multipath fading channels, OFDM has been highly exploited for broadband wireless applications. In fact, OFDM has been leading the RF modulation techniques and is being adopted in and proposed to almost every major communications standards such as digital video broadcasting (DVB) [2], digital audio broadcasting (DAB) [3], IEEE 802.11a/g/n wireless local area networks (WLAN) [4–6], WiMAX IEEE 802.16/e wireless metropolitan area networks (WMAN) [7, 8], IEEE 802.20 mobile broadband wireless access (MBWA) [9] and WiMedia ultra

wide-band (UWB) wireless personal area networks (WPAN) [1], based on the multi-band (MB-)OFDM proposal of the former IEEE 802.15 task group 3a [61, 62]. Recently, OFDM is also being studied for the upcoming $4th$ generation (4G) mobile communication systems, namely the long-term evolution (LTE) [10–12].

For the past few years, OFDM also gained a huge attention by the optical communication community for long-haul transmissions using coherent and direct detection [63–65]. Recent experimental results using OFDM for very high transmission rates are also supporting this modulation as the standard for the future 100 Gb/s Ethernet [65–67].

In this chapter we start by describing the continuous and discrete time implementations of the OFDM in sections 2.2.1 and 2.2.2. Then, the main elements of an OFDM communication system, namely pilot insertion, cyclic prefix, windowing, ADC/DAC operations, time/frequency synchronization and channel estimation are outlined in sections 2.2.3 through 2.2.5. Finally, in section 2.3 it is discussed two of the major drawbacks of OFDM systems, specifically nonlinear distortion (section 2.3.1) and time/frequency synchronization errors (section 2.3.2).

2.2 Design of OFDM signals

From a mathematical point of view, a set of signals are said to be orthogonal if all inner products between them are equal to zero. In a multiplexing communications system, orthogonality ensures no crosstalk between subchannels and consequently a demodulation of the sub-streams without inter-carrier interference (ICI). In fact, several communication schemes that use techniques such as time-division multiplexing (TDM) and conventional FDM are orthogonal by nature. In TDM signals, each subchannel is transmitted in a specific time slot, while in a conventional FDM system adjacent subchannels are spaced out in frequency by guard bands to relax the requirements of the receiver's bandpass filters roll offs. In other words, orthogonality between two signals is always achieved if they do not overlap either in time or in frequency domain. Nevertheless, a signal can not be strictly band limited and time limited [68].

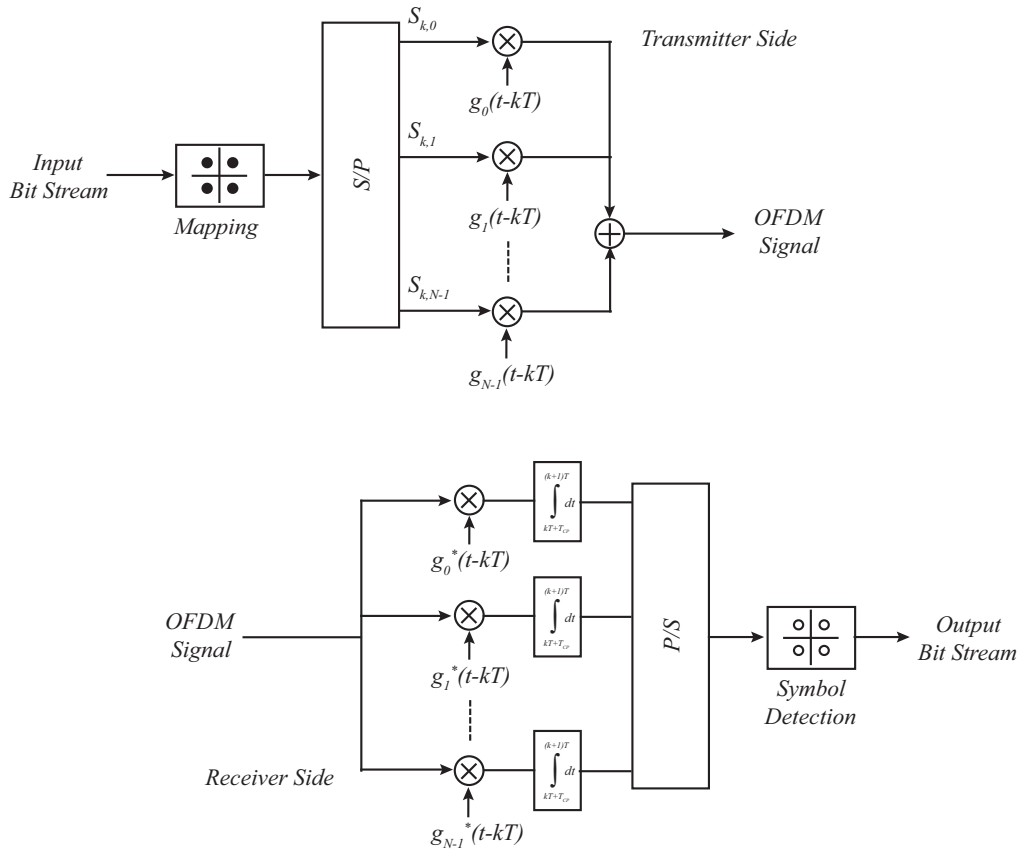

FIGURE 2.1: Scheme of continuous-time model for baseband OFDM transmitter and receiver.

2.2.1 Continuous-time implementation

An OFDM signal is based on time-limited pulses that are orthogonal in the frequency domain. It can be viewed as N orthogonal subcarriers modulated by N parallel sub-streams conveying data symbols. In a mathematical approach, it is equivalent to express an OFDM signal as a sum of orthogonal time-limited subcarriers, $g_n(t)$, that are shifted in time and frequency and then multiplied by data symbols. A continuous-time model for OFDM systems is represented in Figure 2.1.

Let us begin by expressing the OFDM signal in terms of its complex envelope (or its equivalent baseband) as (see Appendix A)

$$s(t) = \Re\left\{\tilde{s}(t)e^{j2\pi f_0 t}\right\} \tag{2.1}$$

where $\tilde{s}(t)$ and f_0 are the complex envelope and the frequency of the first subcarrier of the bandpass signal $s(t)$. The equivalent baseband OFDM signal transmitted in consecutive

symbol intervals can be written as

$$\tilde{s}(t) = \sum_{k=-\infty}^{\infty} \tilde{s}_k(t) = \sum_{k=-\infty}^{\infty} \sum_{n=0}^{N-1} S_{k,n} g_n(t - kT) \tag{2.2}$$

where the equivalent baseband of the OFDM signal in time slot k is given by

$$\tilde{s}_k(t) = \sum_{n=0}^{N-1} S_{k,n} g_n(t - kT) \tag{2.3}$$

and where T and $S_{k,n}$ are the OFDM symbol duration and the complex symbol transmitted by subcarrier n in time slot k, respectively. From a geometric point of view, we can say that each signal $g_n(t)$ is a transmit pulse, the set of pulses $g_n(t), n = 0, \cdots, N-1$, constitutes the transmit base and $\mathbf{S}_k = [S_{k,0}, \cdots, S_{k,N-1}]^T$ is the transmit symbol vector in time slot k. Note that (2.3) can be used to represent any real-valued energy signal and not just OFDM signals. For our specific case of OFDM signals, a particular orthogonal base composed of orthogonal functions must be used.

The transmit base used in OFDM are given by time-limited complex exponentials. Hence, each baseband subcarrier, $g_n(t)$, is given by

$$g_n(t) = \begin{cases} \frac{1}{\sqrt{T}} e^{j2\pi n \Delta f t}, & 0 < t < T \\ 0, & \text{otherwise} \end{cases} \tag{2.4}$$

where Δf is the frequency separation between consecutive subcarriers, which is chosen to be an integer multiple of the inverse of the OFDM symbol duration, T, i.e., $\Delta f = p/T$. Note that the complex exponentials in (2.4) satisfy the orthonormal requirement of OFDM signals given by the following condition [68]

$$\begin{aligned} \langle g_n(t - kT), g_i(t - kT) \rangle &\triangleq \int_{-\infty}^{\infty} g_n(t - kT) g_i^*(t - kT) dt \\ &= \frac{1}{T} \int_{kT}^{(k+1)T} e^{j\frac{2\pi p(n-i)}{T} t} dt \\ &= \left[\frac{e^{j2\pi p(n-i)} - 1}{j2\pi p(n-i)} \right] \\ &= \delta(n - i), \quad n, i = 0, \cdots, N-1 \text{ and } p \in \mathbb{N} \end{aligned} \tag{2.5}$$

where $\delta(\cdot)$ represents the Kronecker delta product.

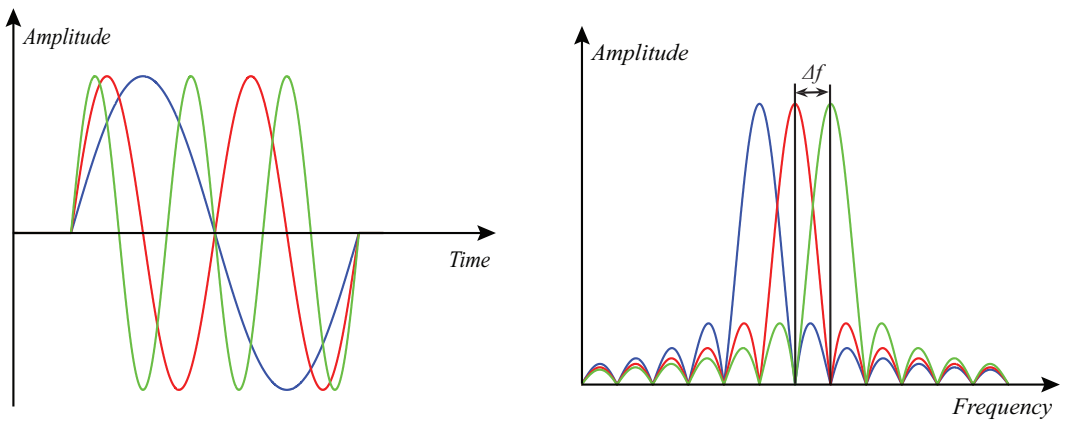

(a) Time-domain representation (b) Frequency-domain representation

FIGURE 2.2: Representation of three subcarriers that constitutes a baseband OFDM symbol for subcarrier frequency spacing of $1/T$.

In other words, all subcarriers have an integer number of periods per OFDM symbol, resulting in orthogonality [68, 69]. Figure 2.2(a) depicts an illustrative example of the orthogonal components for a baseband OFDM symbol with three subcarriers.

The choice of the subcarrier frequency spacing, Δf, can be more easily understood in the frequency domain. As a result of the rectangular window shape, with duration T (see (2.4)), each subcarrier spectrum has a *cardinal sine* shape with the peak of its main lobe at the center frequency and side lobes with nulls periodically spaced by the inverse of OFDM signal period. In order to respect the orthogonality requirement of the subcarriers, the frequency spacing between adjacent subcarriers must be an integer multiple of the inverse of the OFDM symbol duration T, i.e., $\Delta f = p/T$. By setting the multiplier factor p to be equal to 1, the subcarrier spacing equals the distance between the main lobe peak and the nearest null, as it is shown in Figure 2.2(b). Despite the evident overlap between subcarriers' spectra, it can be seen that the peak of each subcarrier corresponds to the nulls of all other subcarriers. This ensures orthogonality between subcarriers and immunity to ICI. Although higher values for p could also be used, the minimum subcarrier frequency spacing provides highest spectral efficiency.

At the receiver, and considering an ideal transmission channel, the complex symbols conveyed in subchannel n and time slot k can be completely recovered by projecting the

received signal onto the base $g_n(t)$, i.e.,

$$\begin{aligned} R_{k,n} = \langle \tilde{s}(t), g_n(t-kT) \rangle &\triangleq \int_{-\infty}^{\infty} \tilde{s}(t) g_n^*(t-kT) dt \\ &= \frac{1}{\sqrt{T}} \int_{kT}^{(k+1)T} \tilde{s}(t) e^{-j\frac{2\pi n}{T}t} dt \\ &= S_{k,n} \end{aligned} \tag{2.6}$$

In other words, the received complex symbols are given by the definition of *inner product*. From (2.6) we can see that the optimum detector for each subcarrier is given by a matched filter to it. Thus, the optimum detector for an OFDM signal can be viewed as a set of N correlators given by the complex conjugate functions of the base functions $g_n(t), n = 0, \cdots, N-1$, as it is depicted in Figure 2.1.

Alternatively to the set of correlators, we may also use a corresponding set of *matched filters* to build the detector. Consider again (2.6), from which we can completely recover the transmitted symbols (considering an ideal channel transmission), we can rewrite it as

$$\begin{aligned} R_{k,n} &= \int_{-\infty}^{\infty} \tilde{s}(t) g_n^*(t-kT) dt \\ &= \left[\int_{kT}^{(k+1)T} \tilde{s}(\tau) g_n^*(\tau - t + kT) d\tau \right]_{t=kT} \\ &= [\tilde{s}(t) * g_n^*(-t+kT)]_{t=kT} \end{aligned} \tag{2.7}$$

Accordingly, we can see that the optimum detector can also be implemented using a set of N matched filters. Note that (2.7) is only equivalent to (2.6) when the sampling time is $t = kT$.

2.2.2 Discrete-time implementation

OFDM transmitters and receivers can be implemented using continuous-time or discrete-time based systems. The first OFDM transceivers were based on continuous-time systems. However, for high data rates and a large number of subcarriers, continuous-time based OFDM systems are practically prohibitive due to the extreme complexity associated with the implementation of large banks of phase lock oscillators in the analog domain. On the other hand, discrete-time implementation can be efficiently implemented

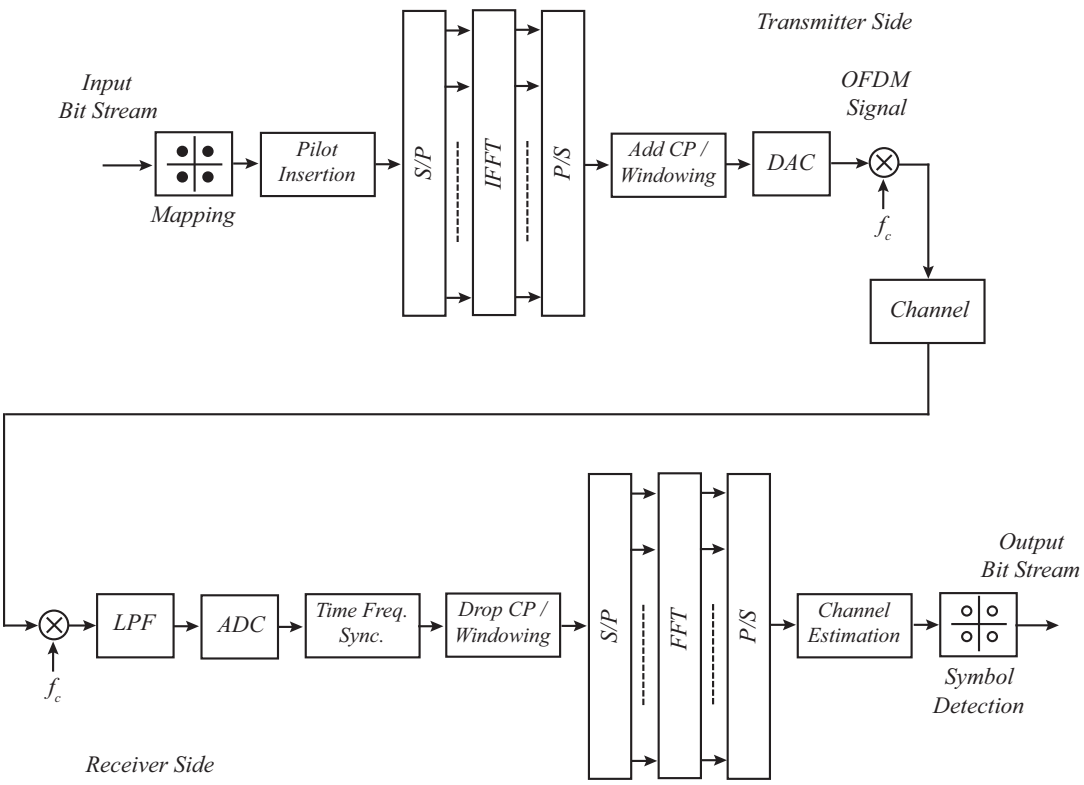

FIGURE 2.3: Scheme of discrete-time models for OFDM transmitter and receiver and their main elements.

using an inverse discrete Fourier transform (IDFT) and a discrete Fourier transform (DFT) at the transmitter and the receiver, respectively [45]. In Figure 2.3 it is depicted the discrete-time implementation based on efficient FFT algorithms of an OFDM signal communication scheme and its main system blocks that include pilot insertion, cyclic prefix insertion, windowing synchronization and channel estimation operations. These elements will be addressed in the following sections and chapters.

As seen from Figure 2.2(b), the bandwidth of the OFDM signal is not perfectly band limited. Yet, for a high number of subcarriers, the bandwidth of the OFDM signal will in fact tend to N/T. By sampling the OFDM signal at the Nyquist rate of N/T and using an ideal filter design at the analog-to-digital converter (ADC) and digital-to-analog converter (DAC), it is possible to reconstruct the continuous-time signal $\tilde{s}(t)$. From (2.2) and (2.4), the kth sampled equivalent baseband OFDM signal can be given by

$$\tilde{s}(kT + qT/N) = \frac{1}{\sqrt{T}} \sum_{n=0}^{N-1} S_{k,n} e^{j\frac{2\pi n}{T}\left(q\frac{T}{N}\right)} = \frac{1}{\sqrt{T}} \sum_{n=0}^{N-1} S_{k,n} e^{j\frac{2\pi n}{N}q} = \frac{N}{\sqrt{T}} s_{k,q}, \tag{2.8}$$

for $q = 0, \cdots, N-1$ and where $s_{k,q}$ is the IDFT of size N of the complex symbols to be conveyed in each subchannel and is defined as

$$s_{k,q} = \frac{1}{N} \sum_{n=0}^{N-1} S_{k,n} e^{j\frac{2\pi}{N}nq}, \quad q = 0, \cdots, N-1 \tag{2.9}$$

From (2.8) it follows that a sampled baseband OFDM symbol can be generated by taking the IDFT of the sequence of complex symbols $[S_{k,0}, \cdots, S_{k,N-1}]$, affected by the multiplicative factor $N/\sqrt{T}$.

The continuous baseband signal after DAC and ADC operations is given by

$$\tilde{r}(t) = \frac{N}{\sqrt{T}} \sum_{k=-\infty}^{\infty} \sum_{q=0}^{N-1} s_{k,q} \delta(t - kT - qT/N) * h_{DAC}(t) * h_{ADC}(t) \tag{2.10}$$

where $h_{DAC}(t)$ and $h_{ADC}(t)$ are the impulse responses of the DAC and ADC filters, respectively. Considering an ideal channel transmission and ADC and DAC impulse responses given by $h_{DAC} = \text{sinc}(tN/T)$ and $h_{ADC} = 1/\sqrt{T}\text{sinc}(tN/T)$, the received signal after ADC/DAC is given by

$$\tilde{r}(t) = \sum_{k=-\infty}^{\infty} \sum_{q=0}^{N-1} s_{k,q} \delta(t - kT - qT/N) * \text{sinc}(t - kT - qT/N) \tag{2.11}$$

and the kth received signal at a rate N/T reduces to

$$r_{k,q} = s_{k,q} \tag{2.12}$$

Consequently, the received complex symbols conveyed by subchannel n on time slot k are given by the taking the DFT of (2.12), i.e.,

$$\begin{aligned} R_{n,k} &= \text{DFT}\{r_{k,q}\} \\ &= \sum_{q=0}^{N-1} \left[\frac{1}{N} \sum_{n'=0}^{N-1} S_{k,n'} e^{j\frac{2\pi}{N}n'q} \right] e^{-j\frac{2\pi}{N}nq} \\ &= S_{k,n'} \delta(n - n') \end{aligned} \tag{2.13}$$

Therefore, the complex symbols conveyed in each subchannel can be recovered by

sampling the equivalent baseband continuous OFDM signal at a rate of N/T and using IDFT/DFT operations, or equivalent but more efficient Fourier algorithms like IFFT/FFT, instead of a continuous-time modulator/demodulator.

Summarizing, at the transmitter side the complex symbols are grouped in sequences of length N at the serial-to-parallel (S/P) converter. The time-domain samples of the signal are generated by the IFFT, converted from parallel to serial (P/S) and then processed by the digital-to-analog converter (DAC) before being up-converted. Analogously, but in a reverse order, at the receiver's side the passband OFDM signal is down-converted and digitized by the analog-to-digital converter (ADC). After the serial-to-parallel conversion, the complex symbols are recovered by taking the FFT of the sequence of length N of samples of the baseband OFDM signal.

2.2.3 Cyclic prefix

So far, it has always been considered that the channel between transmitter and receiver is ideal. Yet, when an OFDM signal travels through a multipath channel, its dispersive behavior is responsible for the loss of orthogonality between subcarriers, which in turn causes ICI. In a multipath channel the signal is scattered, diffracted and reflected in several objects before reaching the antenna. As a result, multiple delayed versions of the transmitted signal caused by different paths lengths are received. Since every delayed received component is a poorly synchronized signal, their set of base pulses are no longer orthogonal [68]. Moreover, due to the spread of symbols, dispersive channels can also cause ISI between successive OFDM symbols. In chapter 6 the transmission of OFDM signals over multipath channels will be addressed and discussed in more detail.

In order to avoid ISI between adjacent OFDM symbols, a silent guard interval can be added at the beginning of each OFDM symbol. Unfortunately, a silent guard interval only avoids ISI between successive OFDM symbols and, thus, ICI is still an issue. In 1980, Peled and Ruiz [70] solved this problem by introducing a cyclic prefix to each OFDM symbol. This special case of guard interval guarantees preservation of orthogonality between subcarriers and prevents ISI between successive OFDM symbols. The cyclic extension is illustrated in Figure 2.4. Each OFDM symbol is cyclically extended and a prefix is appended to it. This operation consists in copying the last part

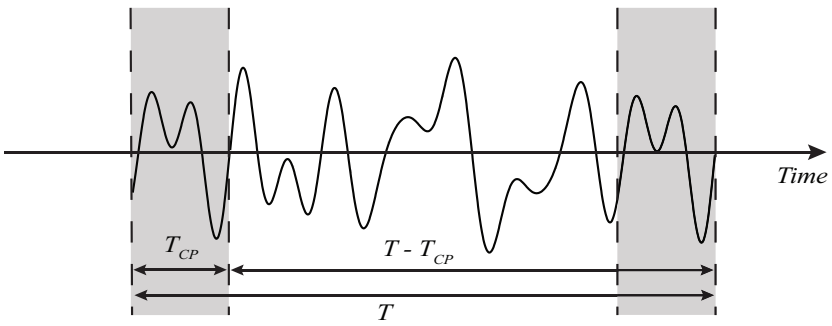

FIGURE 2.4: Addition of the cyclic prefix to an OFDM symbol.

of the OFDM symbol and adding it to its beginning as a preamble. At the receiver, the cyclically extended OFDM signal becomes periodic, which turns the effect of the time-dispersive channel to a cyclic convolution, implying orthogonality when the cyclic prefix is longer than the dispersive channel impulse response. As a result, the effect of the channel becomes multiplicative, i.e., the received constellation is given by a simple pointwise multiplication of the transmitted data and the transfer function of the channel. Therefore, each received subcarrier is affected by a complex gain (amplitude gain and phase rotation), implying a simple one-tap equalization procedure at the receiver.

From a mathematical point of view, the equivalent baseband OFDM signal is given by

$$\tilde{s}_k(t) = \frac{1}{\sqrt{T - T_{CP}}} \sum_{n=0}^{N-1} S_{k,n} e^{j\frac{2\pi n(t-kT-T_{CP})}{T-T_{CP}}}, \quad kT < t < (k+1)T \tag{2.14}$$

where T_{CP} is the duration of the cyclic prefix and T is now the OFDM total symbol period, i.e., it is the duration of the useful part of the OFDM signal plus the duration of the cyclic prefix.

It is important to state that the insertion of a guard interval has its own drawbacks. When increasing the length of the cyclic prefix, the total energy transmitted increases as well, while the energy of the useful part of the OFDM signal stays unchanged. This can be viewed as a loss of effective transmit power, i.e., a signal-to-noise ratio (SNR) loss because of the discarded cyclic prefix at the receiver. The SNR loss of a cyclically extended OFDM signal is given by

$$\begin{aligned} \mathrm{SNR}_{loss} &= -10\log_{10}\left(1 - \frac{T_{CP}}{T}\right) \\ &= -10\log_{10}\left(\frac{T - T_{CP}}{T}\right) \end{aligned} \tag{2.15}$$

where T_{CP}/T is the relative length of the cyclic prefix. Usually the cyclic prefix has a length no more than a quarter of the symbol period, which represents an SNR loss of 1.2 dB.

The insertion of a cyclic prefix leads also to a reduction of the bitrate by the same amount as the SNR, i.e., for a given bit rate per subchannel before the insertion of the cyclic prefix, R_b, the overall bitrate of the OFDM system comes affected by the relative length of the cyclic prefix and is now equal to $R_b(1 - T_{CP}/T)$.

Ideally, the duration of the cyclic prefix should be larger than the maximum excess delay of the multipath channel, otherwise elimination of ISI between successive symbols is not guaranteed. Nevertheless, in the real world, multipath channels have impulse responses that decay exponentially with time and can have a relatively high excess delay, leading to impractical cyclic prefix lengths and high SNR losses. Therefore, a truncated version of the channel impulse response must be used, resulting in a ISI penalty.

Besides providing protection against ICI and ISI, the introduction of a cyclic prefix can also provide robustness against symbol timing errors. Due to the cyclic nature of the OFDM symbol, a shift on the observation window will only introduce a phase offset in all subcarriers. This phase rotation is proportional to the subcarrier index (or frequency) and symbol timing and can be fully compensated by the equalizer at the receiver. A more detailed description of symbol timing errors and its impact is performed later in section 2.3.2.2.

2.2.4 Spectral shaping and band limiting

As previously referred in section 2.2.1, rectangular pulse shapes of the OFDM symbols translate into a cardinal sine shape of the amplitude in the frequency domain, which can lead to a large signal bandwidth caused by its side lobes.

In practical systems, it is mandatory that the signal does not exceed a certain spectral mask that is typically defined in protocol standards. The spectrum mask specifies the maximum levels for the transmitted signal power out of band. Figure 2.5 depicts as an example the spectrum mask of the ECMA-368 standard [1].

The number of subcarriers do have an influence on the decrease of the side lobes. By fixing the 3 dB bandwidth of the OFDM signal and increasing the number of subcarriers,

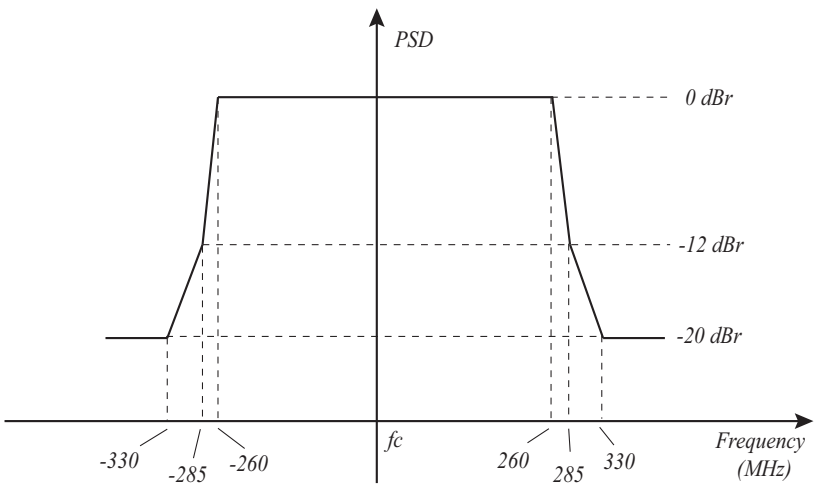

FIGURE 2.5: Example of a spectrum mask for an OFDM signal (ECMA-368 std. [1]).

it can be seen from Figure 2.6 that the spectrum of each subcarrier becomes narrower. As a consequence, the overall side lobes also exhibit a fast decay. Nevertheless, it may not be as steeper as it should be in order to comply with the majority of the standards.

The reduction of the level of the side lobes can be implemented using digital filtering or a technique known as *windowing*. By using digital filtering it is important to choose a filter design type, usually Butterworth filters, that present a flat amplitude response and a phase as linear as possible over the main lobe of the OFDM signal. This procedure results in a loss of guard interval length and, consequently, its robustness to time-dispersive channels can be impaired. Despite its performance, digital filtering can be a quite complex operation since high signal bandwidths and restrictive mask requirements may require very high order filters. To overcome this, a very simple technique named windowing is commonly used for side lobes reduction.

By applying a window to an OFDM symbol, the rectangular pulse shape of the OFDM symbol is smoothed at its boundaries. The implementation of this technique is represented in Figure 2.7. First, the OFDM symbol is cyclically extended by T_W and a postfix is appended. Then, a window is applied to the boundaries. Note that the OFDM signal maintains its original form in the interval $kT - T_{CP} + T_W < t < (k+1)T - T_{CP}$. This represents a reduction of T_W in the guard interval length, which can affect its robustness to a time-dispersive multipath channel. At the receiver, the guard interval is discarded and the orthogonality of the subcarriers is restored by simply setting the start time of the OFDM demodulation to kT [45, 68] (see Figure 2.7).

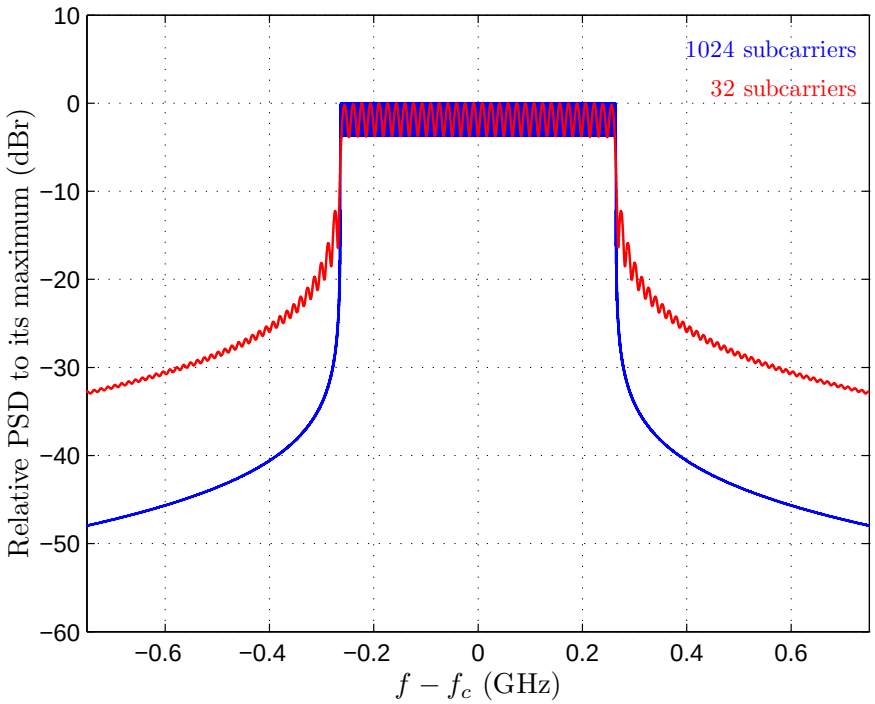

FIGURE 2.6: Power density spectra of OFDM signals with 32 and 1024 subcarriers.

A very common window used in OFDM is the raised cosine window. By applying a window of the form $\cos^2(\phi)$ to the signal boundaries in intervals $kT - T_{CP} < t < kT - T_{CP} + T_W$ and $(k+1)T - T_{CP} < t < (k+1)T - T_{CP} + T_W$, the spectrum will present side-lobes that decay faster. For illustrative purposes, this operation and its effect on the signal boundaries is depicted in Figure 2.8 for different roll-off factors.

In Figure 2.9 it is represented the power spectra density of OFDM signals with 32 and 1024 subcarriers with their pulse shape smoothed by raised cosine windows using different roll-off factors, $\beta = T_W/T$. It can be seen that the side lobes decay rapidly with the increase of the roll-off factor, hence, increasing the spectral efficiency. Even for small roll-off factors, the reduction of the side lobes of the OFDM spectrum is notorious and can be sufficient to fulfill the requirements. Despite the resultant reduction of the cyclic prefix due to windowing, its benefits are usually greater than its drawbacks.

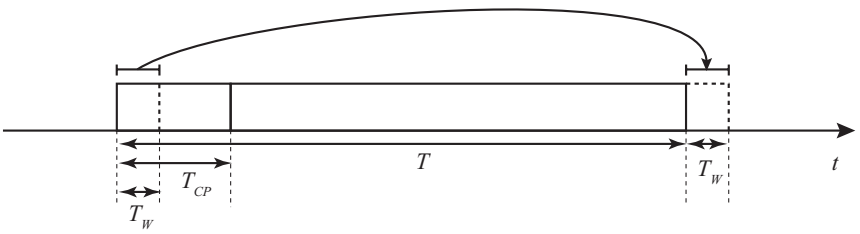

(a) Postfix cyclic extension of the OFDM signal.

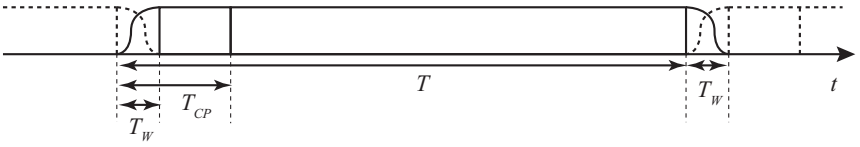

(b) Smoothing window for the OFDM signal.

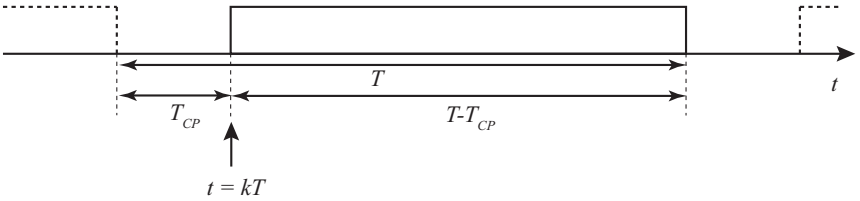

(c) Removal of cyclic prefixes at the receiver side.

FIGURE 2.7: Windowing process applied to an OFDM signal.

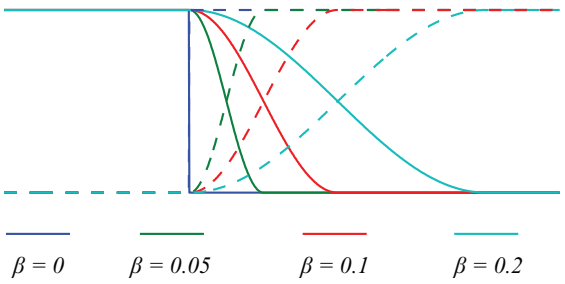

FIGURE 2.8: OFDM symbol boundary smoothness using a raised cosine window with different roll-off factors.

2.2.5 Digital/Analog conversion

From Figure 2.3 it can be seen that the OFDM modulator structure is only responsible for the generation of a digitized baseband signal. Thus, both digital-to-analog and frequency up-conversion operations must be performed before launching the signal through

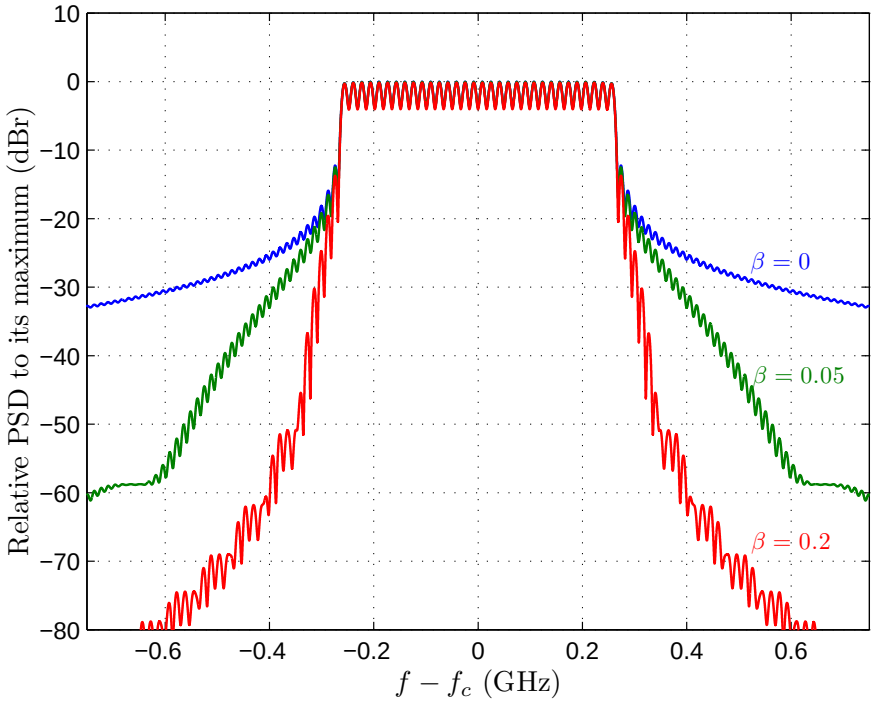

(a) $N = 32$, $T = 75.758\,\text{ps}$ and $T_{CP} = 15.152\,\text{ps}$.

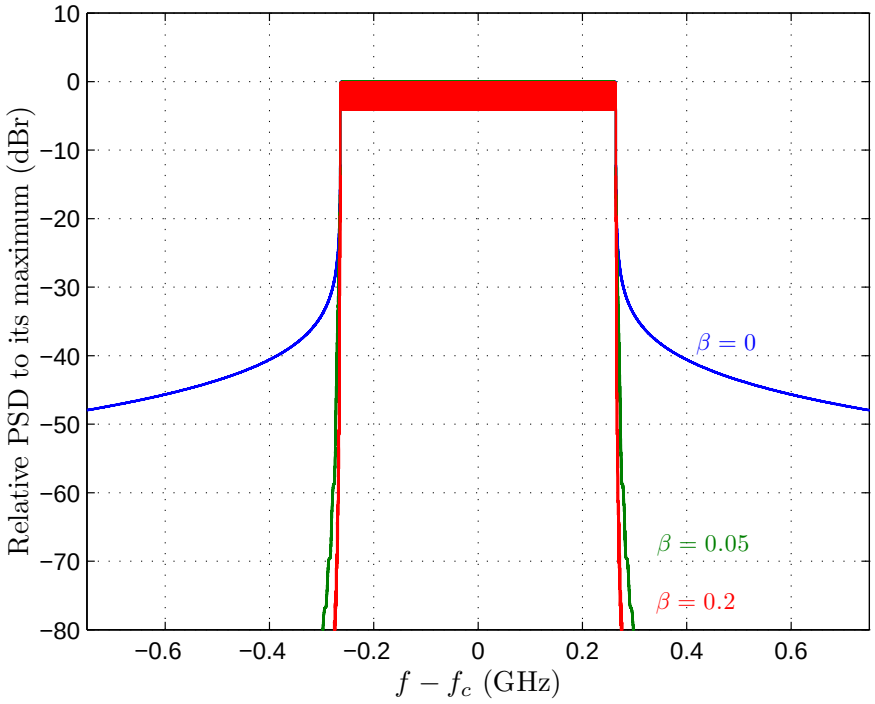

(b) $N = 1024$, $T = 2.424\,\text{ns}$ and $T_{CP} = 0.484\,\text{ns}$

FIGURE 2.9: PSD of OFDM signals with 32 and 1024 subcarriers and with $BW_{3dB} = 528\,\text{MHz}$ centered at a given frequency $f_c \gg BW_{3dB}/2$ after applying raised cosine windows with different roll-off factors, β.

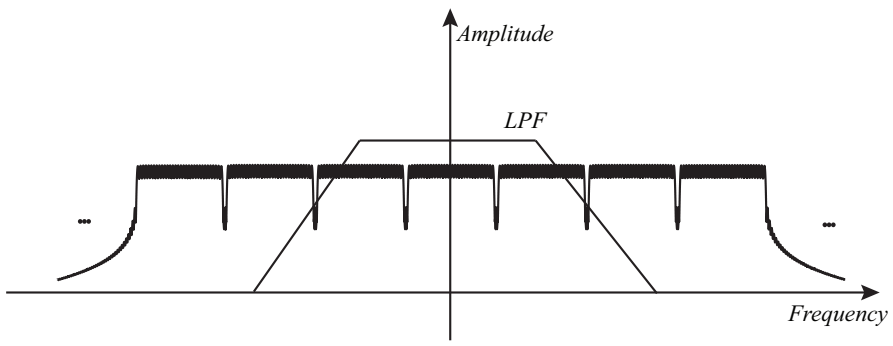

FIGURE 2.10: Non oversampled OFDM spectrum.

the channel. The digital-to-analog conversion (DAC) operation can be performed by applying a lowpass filter (LPF) with a cut-off frequency higher than the Nyquist frequency of the baseband signal in order to eliminate the signal components at frequencies beyond Nyquist frequency [68]. Figure 2.10 shows the periodic spectrum of a discrete OFDM signal. The LPF response must be flat over the signal, i.e. for $|f| < N/(2T)$, and decay rapidly enough to suppress the images [69, 71]. As it can be seen from Figure 2.10, it is not possible to design a LPF that meets the specifications. In order to overcome the analog LPF design issues, it is common to perform an oversample of the discrete OFDM signal. This oversampling operation is based on *zero-padding* and it is implemented using an IFFT with a number of points higher than the number of useful subcarriers. Figure 2.11 represents the same OFDM signal as in Figure 2.10 but with an oversampling factor given by N_{FFT}/N, where N_{FFT} is the length of the IFFT/FFT, and the response of a LPF with a cut-off frequency higher than the Nyquist frequency. By choosing a sufficiently high N_{FFT} it is possible to relax the requirements of the analog filter specifications.

Due to DC offset often originated by DACs and ADCs and, consequently, high distortion near DC, it is common to avoid data carriage at the DC subcarrier [45].

2.3 OFDM Drawbacks

OFDM modulated signals are known to present good performances in the presence of time-dispersive channels and to require relatively simple equalization processes, in contrast to single-carrier modulation schemes. However, due to its multi-carrier nature

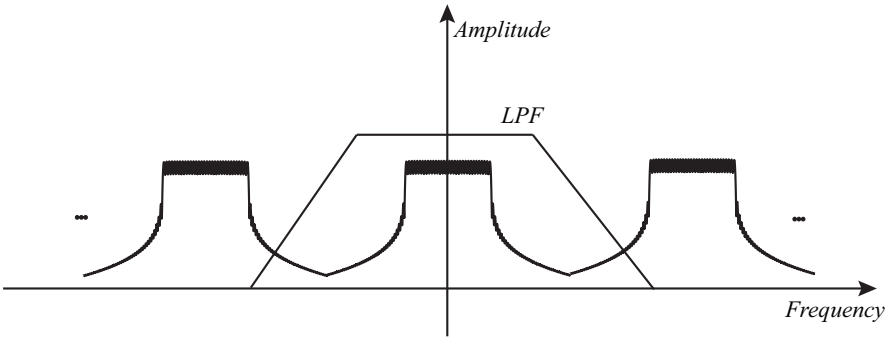

FIGURE 2.11: Oversampled OFDM spectrum.

it also exhibits a high peak-to-average ratio (PAPR) and a high sensitivity to nonlinear distortion. Another major drawback in OFDM signals is its high vulnerability to synchronization errors, specially frequency offset and time offset errors.

The impact of nonlinear distortion and synchronization errors in OFDM signals are discussed in sections 2.3.1 and 2.3.2, respectively.

2.3.1 Sensitivity to nonlinear distortion

One of the main disadvantages in using multi-carrier modulation schemes, and OFDM in particular, is its high PAPR. In a transmission system there may be several elements that do not have linear input-output characteristics, hence, nonlinear distortion is expected. Usually, most of the nonlinear distortion in a system comes from the transmitter's side, more specifically, from high power amplifiers that are required in RF communications. As a result, when a multi-carrier signal passes through a nonlinear element, several inter-modulation products (IMP) and harmonics from the beat between subcarriers will arise and fall inside and outside the signal's band. The new in-band components causes a degradation in the transmission which results in a BER penalty, whereas the out-of-band components causes spectral spreading and interference to nearby channels.

Let us consider an OFDM signal transmission with three subcarriers at frequencies f_1, f_2 and f_3 with an uniform frequency spacing, i.e., $f_{i+1} - f_i = \Delta f, \forall i$. In Figure 2.12 it is depicted some of the inter-modulation products (IMPs) combinations and harmonics that are generated given a channel exhibiting a nonlinear behavior up to the third-order, i.e., $f(x) = a + bx + cx^2 + dx^3$. Several IMPs of the type $f_i + f_j - f_k$ and $2f_i - f_j$ will fall within the transmission band and interfere with original subchannels, causing a severe degradation in the error rate. Fortunately, second and third order IMPs of types $f_i \pm f_j$

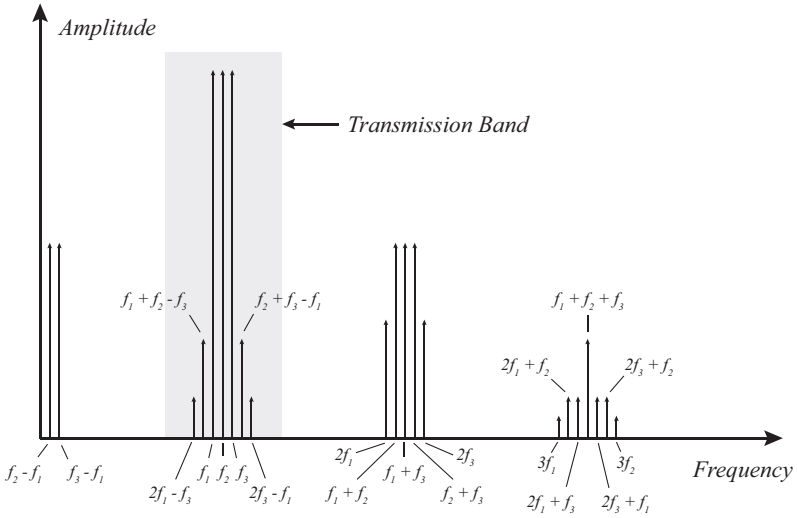

FIGURE 2.12: Spectrum of the response of a third-order nonlinearity to a three subcarriers OFDM signal.

and $f_i+f_j+f_k$, respectively, and harmonics, $2f_i$ and $3f_i$, are easily filtered since they lie outside the transmission band, with the exception for signals with bandwidths greater than an octave.

In the group of third-order IMPs of type $f_i + f_j - f_k$ there are two particular combinations: first, the combination for $i = j = k$ that generates an IMP term called *compression* of the linear term at f_i; and second, the combination for $i \neq j$ and $j = k$ that generates another IMP usually called *desensitization* at f_i caused by subchannel at f_j [72]. In a memoryless nonlinearity, both terms can be viewed as gain/attenuation factors.

Figure 2.13 shows the total number of third-order IMPs of types $f_i + f_j - f_k$ and $2f_i - f_j, \forall i \neq j \neq k$ that fall in a specific subchannel n of an OFDM signal with different numbers of subcarriers. Additionally, Figure 2.14 shows the number of IMPs that fall in the subchannel at the center and at the edge as well as the total number of IMPs that are generated for a given number of subcarriers. Note that this result only indicates the number of different IMPs types and not its weight in the overall nonlinear distortion. A very interesting and important result given by Figures 2.13 and 2.14 is that the number of IMPs that fall in subchannels at the center is higher than the ones that fall in subchannels on the edge. Consequently, it is expected that subchannels at the center of the OFDM signal will suffer from a higher degradation than the ones at the edge. The resultant distortion from the IMD term is often denoted as *nonlinear noise*.

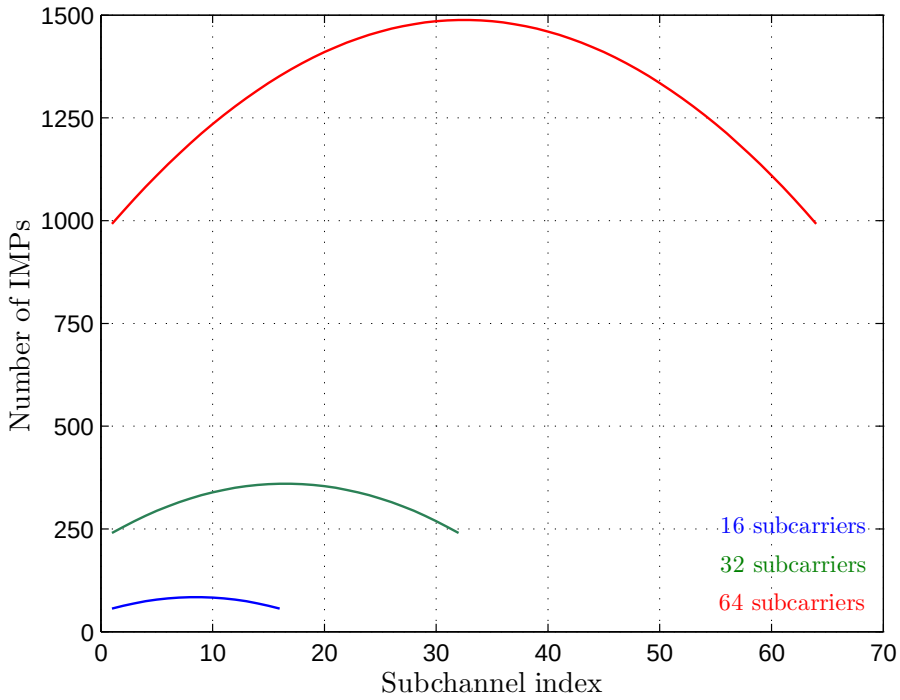

FIGURE 2.13: Total number of third-order IMPs that fall in a specific subchannel for OFDM signals.

In order to mitigate the effect of nonlinear elements in the OFDM signal transmission, several techniques based on PAPR reduction have been proposed [35, 36, 44]. The most common techniques include clipping [37, 38], tone reservation and injection [39], selected mapping (SLM) [40, 41] and coding schemes [42].

2.3.2 Impact of synchronization errors

Demodulation and detection of OFDM is not an easy task. As a main drawback in multi-carrier systems, synchronization errors can induce extreme degradation to its performance. Time, frequency and phase offsets can occur due to oscillator impairments and sample clock differences between transmitter and receiver [45, 68, 69].

Several frequency offset and time offset synchronization and compensation schemes have been proposed in literature [73–79]. These techniques can be divided in two groups: data-aided and non data-aided (or blind) synchronization schemes. When considering high data rate transmissions, the time used for synchronization is crucial and must be as short as possible. Therefore, data-aided synchronization techniques that use special training sequences and pilot subcarriers are frequently applied. The non-data aided, or

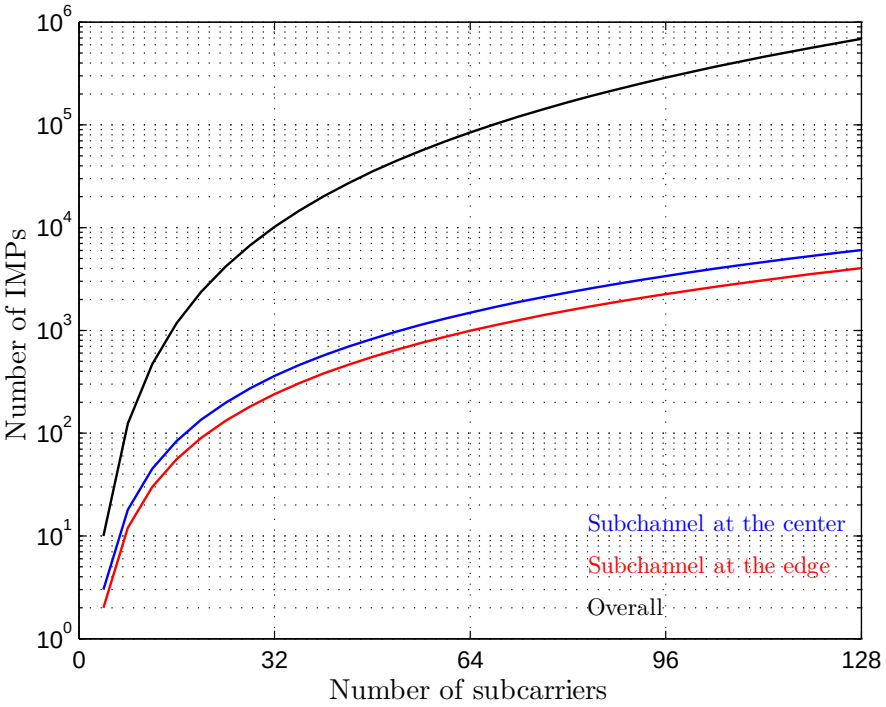

FIGURE 2.14: Number of third-order IMPs that fall in subchannel at the center, edge and its overall for OFDM signals.

blind synchronization schemes do not require the transmission of a known sequence. The most common blind schemes exploit signal redundancy present in the cyclic prefix of the OFDM signal and the cyclostationarity introduced by the pulse shaping operation.

Carrier frequency offset and symbol timing errors are described in more detail in the following sections.

2.3.2.1 Carrier frequency offset

In OFDM systems the subcarrier frequency spacing, Δf, is typically much smaller than the total bandwidth and as a result, the tolerable frequency offset becomes a very small fraction of the total bandwidth, making it hard to frequency synchronize. Frequency offsets can have its origin in differences in oscillators in transmitter and receiver, phase-noise introduced by nonlinear channels or Doppler shifts. When a frequency offset is present, orthogonality between subcarriers is lost, resulting in ICI [45, 75].

In Figure 2.15 we depict a frequency offset example between subcarriers' frequency of the transmitted and received signal. If a frequency offset is present at the demodulation process, it can be viewed as a shift in the receiver's oscillator sampling operation in the

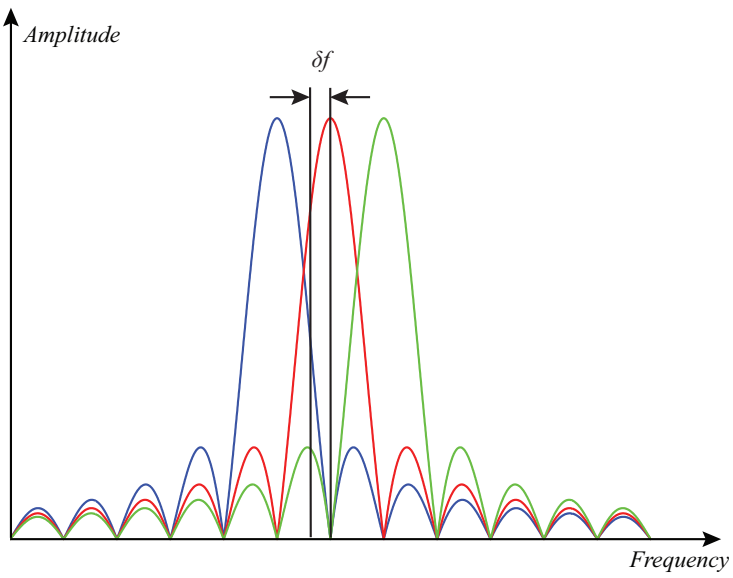

FIGURE 2.15: Frequency offset illustration.

frequency domain. Thus, instead of performing a frequency sampling at each cardinal sine function's peak, where all other cardinal sine functions equal zero, a non-optimum sampling frequency is performed. Here, two undesirable and destructive effects take place. First, the reduction of the subchannel amplitude and second the destructive ICI effect from the interference of others subcarriers due to their loss of orthogonality [31, 80].

A carrier frequency and phase offsets can be mathematically modeled as a frequency shift, δf, and a constant phase offset, ϕ. Therefore, the equivalent lowpass of the received signal can be written as [45, 75].

$$\tilde{r}'(t) = \tilde{r}(t)e^{j(2\pi\delta f t+\phi)} \tag{2.16}$$

Using (2.6), the received complex modulated symbol in time slot k and subcarrier n in the presence of a frequency and phase offset is given by

$$\begin{aligned} R_{k,n} &= \int_{kT}^{(k+1)T-T_{CP}} \tilde{r}'(t)g_n^*(t-kT)dt \\ &= \sum_{n'=0}^{N-1} S_{k,n'} \int_{kT}^{(k+1)T-T_{CP}} \left[e^{j(2\pi\delta f t+\phi)} g_{n'}(t-kT)g_n^*(t-kT)\right] dt \\ &= \sum_{n'=0}^{N-1} S_{k,n'} \mathrm{sinc}\left[(n'-n)+\delta f(T-T_{CP})\right] e^{j[\pi\delta f((2k+1)T+T_{CP})+\pi(n'-n)+\phi]} \end{aligned} \tag{2.17}$$

where $\text{sinc}(\cdot)$ denotes the cardinal sine function defined as $\text{sinc}(x) = \frac{\sin(\pi x)}{\pi x}$.

Due to the frequency and phase offsets, the orthogonality between subcarriers is corrupted. In fact, the integral in (2.17) is not equal to one for $n = n'$ and zero for $n \neq n'$ as it happens in the ideal case previously described in section 2.2.1. Moreover, the result of the effect of frequency and phase offsets is easier to view by splitting (2.17) in two terms. The first term is given for $n = n'$ and represents a time-varying phase rotation of the complex modulated symbol affected by an attenuation factor. The second term is for $n \neq n'$ and accounts the ICI between subcarriers. Frequency offsets, δf, are usually very small in comparison to the subcarrier frequency spacing, Δf. When $\delta f \ll \Delta f$, the term for $n = n'$ is dominant and all other terms contribute with an additive distortion to the complex modulated symbol. The complex symbol conveyed in subchannel n in time slot k can then be written as

$$R_{k,n} = \alpha e^{j\gamma_k} S_{k,n} + W_{k,n} \tag{2.18}$$

where the attenuation factor α and the time-varying phase shift factor γ_k are given by

$$\alpha = \text{sinc}\left[\delta f (T - T_{CP})\right] \tag{2.19}$$

$$\gamma_k = \pi \delta f [(2k+1)T + T_{CP}] + \phi \tag{2.20}$$

and the additional noise term due to ICI, $W_{k,n}$, is

$$W_{k,n} = \sum_{\substack{n'=0 \\ n' \neq n}}^{N-1} S_{k,n'} \text{sinc}\left[(n' - n) + \delta f (T - T_{CP})\right] e^{j[\pi \delta f ((2k+1)T + T_{CP}) + \pi(n'-n) + \phi]} \tag{2.21}$$

From the expressions above, it can be seen that the complex symbols transmitted by subcarrier with index n will only be received by the same subcarrier index if a frequency offset less than half the subcarrier frequency spacing is present. The result from having larger frequency offsets can be viewed as a shift in some positions in the frequency direction, and thus the complex symbols conveyed in subchannel n will appear in the subchannel given by $\text{round}(n + \delta f / \Delta f)$, still affected by a frequency offset equal to the difference between $\delta f / \Delta f$ and the nearest integer, where $\delta f / \Delta f$ is the normalized frequency offset. The function $\text{round}(m)$ rounds m to the nearest integer.

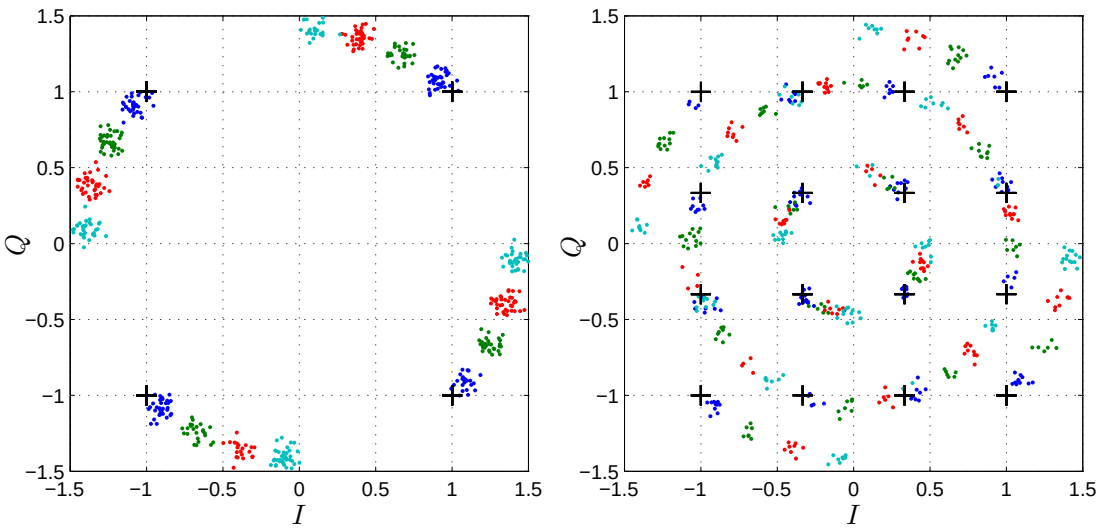

(a) OFDM/QPSK. (b) OFDM/16-QAM.

FIGURE 2.16: Constellations of four consecutive (a) OFDM/QPSK and (b) OFDM/16-QAM symbols affected by a frequency offset of $\delta f = \Delta f/30$ and a phase offset of $\phi = 0$.

Figure 2.16 shows the phase rotation due to carrier frequency offset described by (2.18). Here, two constellations of 4 consecutive OFDM symbols with time indexes $k = 0, 1, 2, 3$ are depicted for QPSK and 16-QAM signals and for a normalized frequency offset of $1/30$. As it can be seen, the received complex symbols are phase shifted by factor $\gamma_k, k = 0, 1, 2, 3$. Although not clearly seen, they are also affected by factor α. The ICI term, $W_{k,n}$, can be clearly identified by its noisy cloud shape that induces a degradation of the received signal, and consequently, in its SNR. Additionally, the constellation rotation due to both frequency and phase offsets can also be viewed as phase distortion from a multipath channel. When a multipath channel is present, the complex symbols conveyed in each subcarrier are affected by both attenuation and phase rotation factors given by the frequency response of the channel. Consequently, it is not possible to distinguish phase rotations induced by CFO and multipath channels and, thus, they can be jointly compensated using a common equalization process (see chapter 6) [81].

In Figure 2.17 it is depicted the contribution of the ICI term, $W_{k,n}$, as a function of the subcarrier index difference $n' - n$. As expected, the contribution of this term increases with the normalized frequency offset, $\delta f/\Delta f$, i.e., with the increasing of the frequency offset, and decreases with the subcarrier spacing.

OFDM based systems are very sensitive to frequency offset errors. When a large

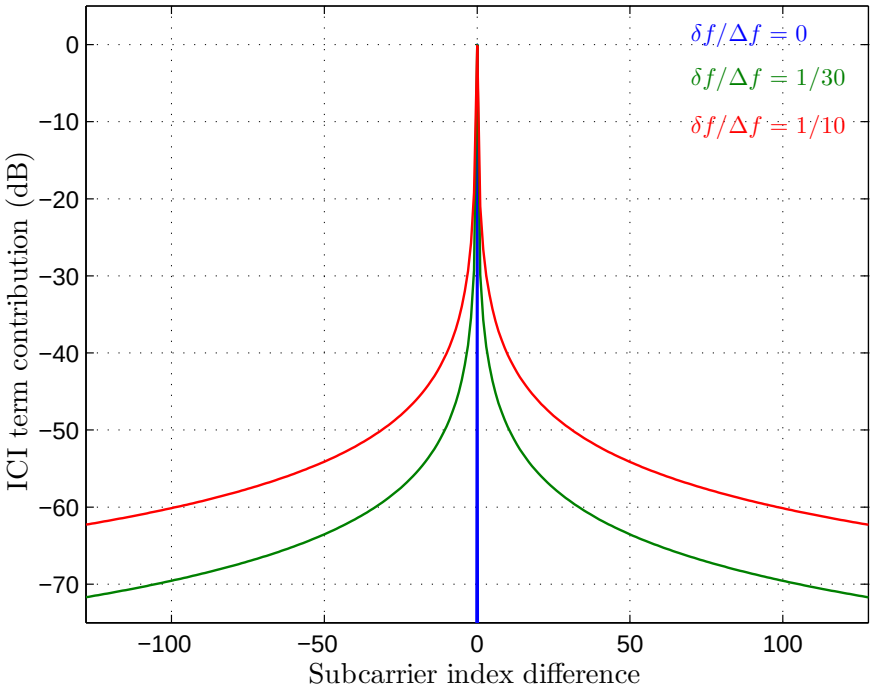

FIGURE 2.17: ICI term contribution power relative to its maximum as a function of subcarrier index for normalized frequency offsets of 0, 1/30 and 1/10.

number of subcarriers is used, its frequency spacing decreases (for the same signal bandwidth), thus making the OFDM signal even more susceptible to carrier frequency offset errors and performance degradation.

2.3.2.2 Symbol timing errors

The use of a cyclic prefix has also an important role in time synchronization. A symbol timing error occurs when the receiver does not know the exact arrival time instant of the OFDM symbols in order to apply the FFT.

Mathematically, a symbol timing error is viewed as a shift in the integration interval of the matched filter bank in (2.6). Considering a symbol timing error of $0 < \delta t < T_{CP}$, i.e., no ISI between consecutive OFDM symbols due to timing errors is present, the received complex modulated symbols are given by [45, 68, 82]

$$\begin{aligned} R_{k,n} &= \int_{kT+\delta t}^{(k+1)T-T_{CP}+\delta t} \tilde{r}(t) g_n^*(t - kT - \delta t) dt \\ &= S_{k,n} e^{j2\pi \frac{n}{T-T_{CP}} \delta t} \end{aligned} \tag{2.22}$$

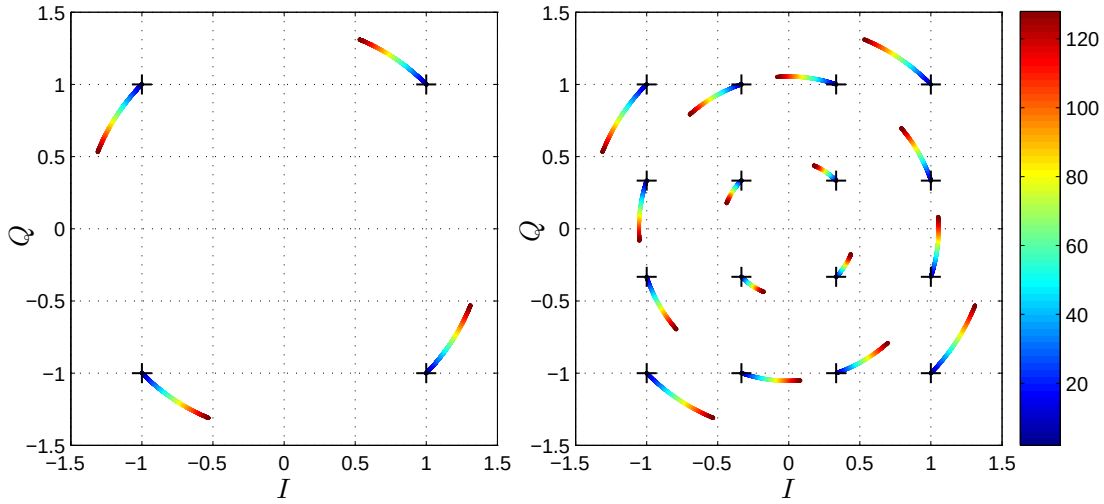

(a) OFDM/QPSK. (b) OFDM/16-QAM.

FIGURE 2.18: Constellations of (a) OFDM/QPSK and (b) OFDM/16-QAM signals with 128 subcarriers affected by a symbol timing error of $\delta t = T_{CP}/500$.

Therefore, a symbol timing error of $0 < \delta t < T_{CP}$ only introduces a pure and different phase rotation for each subcarrier. The phase rotation suffered by the complex modulated signal conveyed by the first subcarrier is zero, $n = 0$, and increases linearly until reaching the maximum phase rotation for the last subcarrier, $n = N - 1$. If symbol timing errors are smaller than the length of the cyclic prefix, the receiver is capable to capture the OFDM symbol in a region where it appears cyclic, thus preserving orthogonality.

Figure 2.18 shows the effect of symbol timing errors in QPSK and 16-QAM constellations conveyed by an OFDM signal with 128 subcarriers. Markers '+' indicate the original position of the complex modulated symbol, before being affected by timing errors. The *colorbar* indicates the subcarrier index, where the dark blue color represents the first subcarrier, $n = 0$, whereas the dark red represents the last, $n = N - 1$. In this case the symbol timing error is considerably small, hence, the received complex modulated symbols are only affected by a constant phase rotation that can be easy compensated by an equalizer at the receiver.

Summarizing, small symbol timing errors can be easily compensated by the channel equalizer, still preserving orthogonality. In a worst scenario, where a symbol timing error exceeds the cyclic prefix length, the receiver integration period overlaps adjacent OFDM symbols, resulting in interference between consecutive OFDM symbols. As a

result, the received complex modulated symbols are corrupted by ISI from adjacent OFDM symbols and ICI due to the fact that orthogonality between subcarriers is lost.

2.4 Summary

In this chapter, we have introduced the OFDM concept that will be used through the rest of this thesis. Both the continuous and discrete time implementation structures for the transmitter and receiver were presented. We have also covered the main elements of an OFDM communications system. Subsequently, the impact of both nonlinear distortion and time/frequency errors was addressed.

In the following chapters we will focus on the development of receivers and a channel estimator structure suitable for nonlinearly distorted and faded OFDM systems as well as an extensive performance assessment of the considered system. Finally, a case study concerning the applicability of the detailed techniques to a radio-over-fiber system is presented.

Chapter 3

Optimum OFDM receiver for memoryless nonlinear systems

3.1 Introduction

In the previous chapter we have introduced the OFDM basics that will be used throughout this thesis. Also, we have briefly discussed the impact of IMPs in an OFDM transmission.

In this chapter we derive the optimum receiver structure in terms of error probability for nonlinearly distorted OFDM signals in AWGN. First, we start by describing the power-series equivalent baseband representation of bandpass nonlinear channels in section 3.2. In section 3.3 the optimum receiver is analytically derived which includes a sufficient statistics extractor and a maximum likelihood sequence estimator (MLSE). In section 3.3.3, an algorithm that iteratively searches for the transmitted vector that maximizes the likelihood in the neighborhood of a first estimate given by a conventional receiver is presented.

3.2 Memoryless bandpass nonlinear systems

A bandpass nonlinearity can be defined as a system whose spectrum is centered at a certain frequency in which the input signal is centered as well. The term *memoryless* implies that the output of the system depends only on the input signal at the present

instant only. Furthermore, it also implies that the input signal bandwidth is so narrow that the transfer characteristics of the system is frequency independent. Nonetheless, the presence of a nonlinearity in a system has generally the effect of increasing the bandwidth of the input signal. As a consequence, a sampling rate increase must be performed in order to avoid aliasing distortion. It is also expected that when a bandpass input signal centered at f_c is considered, the output of a nonlinear system will exhibit several spectral components around frequencies kf_c, $k = 0, 1, \cdots$ [69, 83, 84].

Modeling these systems is of great interest because they allow a characterization of several devices often encountered in radio-frequency transmissions. Additionally, for input signals with multi-carrier characteristics like OFDM, the nonlinear bandpass channel modeling is of great interest since intermodulation products are a major source of degradation.

First, we will derive a lowpass representation of memoryless bandpass nonlinear systems by using an analytical approach [83, 84]. In the following subsection, we will consider that our nonlinearity can be given by a "power series" and a more direct and straightforward approach is described, which will be adopted through the rest of our work[1].

3.2.1 Analytical approach

Let us consider a narrowband bandpass input signal $x(t)$ given by (see Appendix A and (A.26))

$$\begin{aligned} x(t) &= A_x(t)\cos\left(2\pi f_c t + \theta_x(t)\right) \\ &= A_x(t)\cos\left(\Theta_x(t)\right) \end{aligned} \tag{3.1}$$

where $A_x(t)$ and $\theta_x(t)$ are both real-valued baseband signals representing the modulated envelope and phase of $x(t)$, respectively, and f_c is the carrier frequency of the signal.

Consider now a memoryless nonlinearity whose input-output characteristic is represented by $f(\cdot)$. The output of the nonlinearity for an input signal given by (3.1)

[1] Another well known model for nonlinearities and specially for high power amplifiers (HPAs) such as traveling-wave tubes (TWTs) and solid state amplifiers (SSAs) is the Saleh model.

is

$$y(t) = f\left[A_x(t)\cos\left(\Theta_x(t)\right)\right] \tag{3.2}$$

From (3.2), it can be seen that the output of the nonlinearity is a periodic function of $\Theta_x(t)$ and can be expanded in a Fourier series given by

$$y(t) = a_0 + \sum_{k=1}^{\infty}\left[a_k\cos(k\Theta_x(t)) + b_k\sin(k\Theta_x(t))\right] \tag{3.3}$$

where a_k and b_k are called the Fourier coefficients and, by definition, are real-valued given by

$$a_k \triangleq \frac{1}{\pi}\int_{-\pi}^{\pi} f\left[A_x(t)\cos\left(\Theta_x(t)\right)\right]\cos(k\Theta_x)d\Theta_x \tag{3.4}$$

and

$$b_k \triangleq \frac{1}{\pi}\int_{-\pi}^{\pi} f\left[A_x(t)\cos\left(\Theta_x(t)\right)\right]\sin(k\Theta_x)d\Theta_x \tag{3.5}$$

From (3.3) and the definition of $\Theta_x(t)$ given by (3.1) we can see that the output of the memoryless nonlinearity exhibits several harmonics of the fundamental frequency, kf_c, $k = 0, 1, \cdots$. A *zonal filter* must be used so we can eliminate all frequency components but the so-called first-zone, i.e., the spectral components of $y(t)$ that fall near the fundamental frequency of the input bandpass signal ($k = 1$), which are usually the ones of interest (see Figure 3.1). By doing so, the output of the nonlinear system given by (3.3) reduces to

$$\begin{aligned} y(t) &= a_1\cos\left(2\pi f_c t + \theta_x(t)\right) + b_1\sin\left(2\pi f_c t + \theta_x(t)\right) \\ &= F[A_x(t)]\cos\left(2\pi f_c t + \theta_x(t) + \Phi[A_x(t)]\right) \end{aligned} \tag{3.6}$$

where $F[A_x(t)] = \sqrt{a_1^2 + b_1^2}$ and $\Phi[A_x(t)] = -\arctan\left(b_1/a_1\right)$.

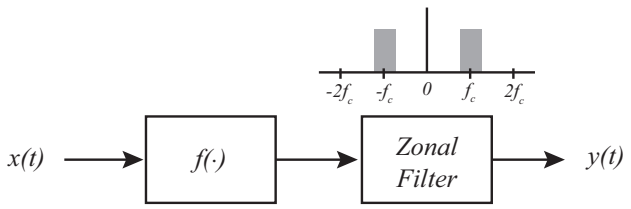

FIGURE 3.1: Block diagram representation of the bandpass nonlinear channel model.

Thus, in terms of complex envelope notation (see appendix A), the first-zone output is given by

$$\begin{aligned}\tilde{y}(t) &= F[A_x(t)]e^{j(\theta_x(t)+\Phi[A_x(t)])} \\ &= \tilde{x}(t)\frac{F[A_x(t)]}{A_x(t)}e^{j\Phi[A_x(t)]} \\ &= \tilde{x}(t)\tilde{G}[A_x(t)]\end{aligned} \tag{3.7}$$

where $\tilde{G}[\cdot]$ can be viewed as the lowpass-equivalent input-output characteristic of the nonlinearity and the relation between $x(t)$ and its complex envelope $\tilde{x}(t)$ is given by

$$x(t) = \Re\left\{\tilde{x}(t)e^{j2\pi f_c t}\right\} \tag{3.8}$$

As it can be seen, the memoryless bandpass nonlinearity can be modeled by a time-domain input-output characteristic that has a very direct implementation. Functions $F[\cdot]$ and $\Phi[\cdot]$ are usually called the AM/AM and AM/PM characteristics of the nonlinear channel, respectively, since they represent the amplitude and phase nonlinear distortions of the system. It is important to note that the analytic derivation of both AM/AM and AM/PM characteristics performed in this section are only for memoryless bandpass channels. Despite the 'apparent' AM/PM conversion it can be shown that for any "ordinary" function $f(\cdot)$ the Fourier coefficient b_1 is always zero. In other words, if a nonlinearity is only modeled by means of a real-valued ordinary function, the complex envelope of the output of the nonlinearity does not suffers from AM/PM distortion [83].

3.2.2 Power series approach

It is known that a Taylor series expansion can be used to approximate a given function. In other words, it is possible to characterize a strictly memoryless nonlinearity by a polynomial model, namely a power series, i.e., [84]

$$\begin{aligned}y(t) &= \sum_{l=0}^{\infty} c_l[x(t)]^l \\ &\approx \sum_{l=0}^{L} c_l[x(t)]^l\end{aligned} \tag{3.9}$$

where c_l are the power series coefficients and L is the maximum nonlinear order considered. Let us consider an input bandpass signal $x(t)$, centered at frequency f_c and expressed in terms of complex envelope (see appendix A)

$$\begin{aligned} x(t) &= \Re\left\{\tilde{x}(t)e^{j2\pi f_c t}\right\} \\ &= \frac{1}{2}\left[\tilde{x}(t)e^{j2\pi f_c t} + \tilde{x}^*(t)e^{-j2\pi f_c t}\right] \end{aligned} \tag{3.10}$$

where $\tilde{x}(t)$ and $\tilde{x}^*(t)$ are the complex envelope of $x(t)$ and its complex conjugate, respectively. By substituting (3.10) in (3.9), and considering a nonlinearity of maximum order L, the output of the memoryless nonlinearity can be approximated by the following power series

$$\begin{aligned} y(t) &\approx \sum_{l=0}^{L} c_l [x(t)]^l \\ &= \sum_{l=0}^{L} c_l \left[\frac{1}{2}\tilde{x}(t)e^{j2\pi f_c t} + \frac{1}{2}\tilde{x}^*(t)e^{-j2\pi f_c t}\right]^l \end{aligned} \tag{3.11}$$

Using the binomial theorem, it is possible to expand $[x(t)]^l$ and rewrite it as

$$[x(t)]^l = \frac{1}{2^l}\sum_{m=0}^{l}\binom{l}{m}[\tilde{x}(t)]^m[\tilde{x}^*(t)]^{l-m}e^{j2\pi(2m-l)f_c t} \tag{3.12}$$

where

$$\binom{l}{m} = \frac{l!}{m!(l-m)!} \tag{3.13}$$

Since we have considered a zonal filter after the nonlinearity, all frequency components that do not fall near the fundamental frequency f_c are eliminated (see Figure 3.1). In fact, only terms for $2m-l = \pm 1$, i.e., for l odd, fall in the transmission band centered at f_c. Hence, and regarding (3.10), the output of a system given by (3.11) after zonal filtering is given by

$$\begin{aligned} y(t) &= \sum_{i=1}^{(L+1)/2} \frac{1}{2^{2i-1}}\binom{2i-1}{i} c_{2i-1}\left[[\tilde{x}(t)]^i[\tilde{x}^*(t)]^{i-1}e^{j2\pi f_c t} + [\tilde{x}(t)]^{i-1}[\tilde{x}^*(t)]^i e^{-j2\pi f_c t}\right] \\ &= x(t)\sum_{i=1}^{(L+1)/2} \frac{1}{2^{2i-2}}\binom{2i-1}{i} c_{2i-1}|\tilde{x}(t)|^{2i-2} \end{aligned} \tag{3.14}$$

In terms of complex envelope notation, the output of the bandpass nonlinearity, $\tilde{y}(t)$, reduces to

$$\begin{aligned}\tilde{y}(t) &= \tilde{x}(t) \sum_{i=1}^{(L+1)/2} \tilde{c}_{2i-1} |\tilde{x}(t)|^{2i-2} \\ &= \tilde{x}(t) \tilde{G}\left[A_x(t)\right]\end{aligned} \tag{3.15}$$

where

$$\tilde{c}_{2i-1} = \frac{1}{2^{2i-2}} \binom{2i-1}{i} c_{2i-1} \tag{3.16}$$

and $|\tilde{x}(t)| \equiv A_x(t)$.

The input-output relation given by (3.15) is often denoted as *strictly* memoryless since the output signal depends only on the input signal at the same time instant. As previously stated, in this scenario where the nonlinearity is modeled by means of an ordinary function $f(\cdot)$, only the AM/AM distortion phenomena is in fact modeled [85–87]. However, experimental measurements obtained from nonlinear elements show that nonlinear phase distortion phenomena also exist. Therefore, if AM/PM distortion is intended to be considered in the modelization procedure, a second function must be added in order to model that distortion. In this scenario, the nonlinearity is said to be *quasi-memoryless*, i.e., the bandwidth of the signal is considered to be much smaller than that of the device and that only short-term memory effects are present [83, 87], and both AM/AM and AM/PM can be modeled using complex coefficients in the power series [86–89]. Thus, from (3.15), the AM/AM conversion can be given by $\left|\tilde{G}\left[A_x(t)\right]\right|$ whereas the AM/PM is described by $\angle\tilde{G}\left[A_x(t)\right]$, i.e.,

$$\left|\tilde{G}\left[A_x(t)\right]\right| \equiv F\left[A_x(t)\right] = \left|\sum_{i=1}^{(L+1)/2} \tilde{c}_{2i-1} \left[A_x(t)\right]^{2i-2}\right| \tag{3.17}$$

$$\angle\tilde{G}\left[A_x(t)\right] \equiv \Phi\left[A_x(t)\right] = \angle\left[\sum_{i=1}^{(L+1)/2} \tilde{c}_{2i-1} \left[A_x(t)\right]^{2i-2}\right] \tag{3.18}$$

Note that AM/PM conversion depends only on $A_x(t)$. Note also that for real coefficients $\tilde{c}_{2i-1}$, the bandpass nonlinearity introduces only AM/AM conversion whereas for complex coefficients an AM/PM conversion is present.

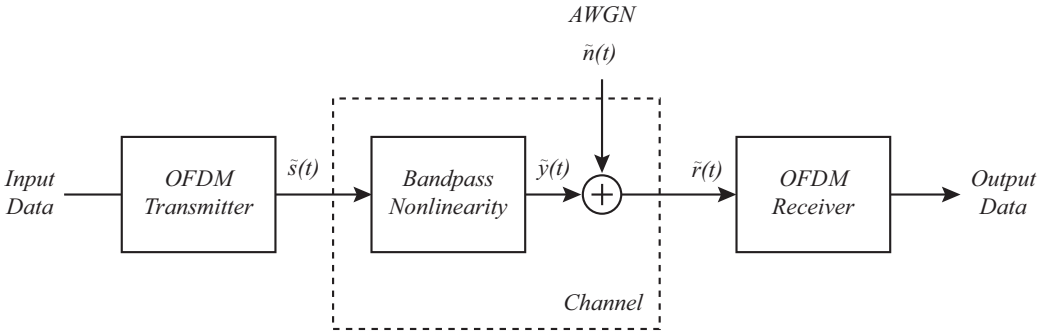

FIGURE 3.2: Equivalent baseband OFDM communications system model.

The power series approach has the advantage to offer a simple way to describe a nonlinearity and to allow us to directly obtain the harmonic levels in terms of coefficients, providing a straightforward method for implementation. When quasi-memoryless conditions are not verified, then, more elaborate models such as the Volterra series approach must be used [86, 87].

3.3 Optimum receiver structure derivation

In this section, we derive the structure of the receiver that minimizes the probability of making an error when considering a nonlinearly distorted OFDM signal corrupted by additive white Gaussian noise (AWGN) [84, 90, 91]. Additionally, we show that it can be divided in two parts: an optimum demodulator that extracts all the relevant information of the received signal followed by a detector which uses that information to optimally estimate the transmitted symbols in the minimum probability of error sense. Moreover, to reduce the large computational cost of the optimum receiver, we also present an iterative algorithm.

In Figure 3.2 it is depicted the block diagram of the system under consideration, which is composed by an OFDM transmitter, a memoryless bandpass nonlinear channel followed by an AWGN source and an OFDM receiver. From (2.14) we can write the complex envelope of $s(t)$ as

$$\tilde{s}(t) = \sum_{k=-\infty}^{\infty} \sum_{n=0}^{N-1} S_{k,n} g_n(t - kT) \tag{3.19}$$

where $g_n(t)$ are orthonormal time-limited basis functions given by

$$g_n(t) = \begin{cases} \dfrac{1}{\sqrt{T - T_{CP}}} e^{j\frac{2\pi n(t-T_{CP})}{T-T_{CP}}}, & 0 \leq t \leq T \\ 0, & \text{otherwise,} \end{cases} \tag{3.20}$$

and $S_{k,n}$ is the complex transmitted symbol in time slot k and subchannel n, T is the total OFDM symbol duration, T_{CP} is the cyclic prefix duration and N is the number of OFDM subcarriers. Note that the complex symbols conveyed by each subcarrier can be of any type of digital amplitude or phase modulation like M-QAM or M-PSK and are considered to be zero-mean and statistically independent. The channel noise $\tilde{n}(t)$ is a zero-mean white Gaussian noise process with PSD N_0 (W/Hz).

Considering an arbitrary time slot k, it is assumed that the signal $s(t)$ is defined over the interval $kT < t < (k+1)T$ and that the received signal $r(t)$ is observed by the receiver in the same interval. The aim of the receiver is to observe the received signal for each time slot k and to provide the best estimate possible of the transmitted symbols vector.

Considering the equivalent lowpass representation of a bandpass nonlinearity of order L given by (3.15), the complex envelope of the nonlinearly distorted OFDM signal corrupted by AWGN is given by

$$\begin{aligned} \tilde{r}(t) &= \sum_{i=1}^{(L+1)/2} \tilde{c}_{2i-1} \tilde{s}(t) |\tilde{s}(t)|^{2i-2} + \tilde{n}(t) \\ &= \tilde{y}(t) + \tilde{n}(t) \end{aligned} \tag{3.21}$$

where $\tilde{y}(t)$ is the complex envelope of nonlinearly distorted OFDM signal given by

$$\begin{aligned} \tilde{y}(t) = \sum_{k=-\infty}^{\infty} \sum_{i=1}^{(L+1)/2} \tilde{c}_{2i-1} \sum_{n_1=0}^{N-1} \cdots \sum_{n_{2i-1}=0}^{N-1} S_{k,n_1} \cdots S_{k,n_i} S^*_{k,n_{i+1}} \cdots S^*_{k,n_{2i-1}} \\ \times \frac{1}{(T - T_{CP})^{i-1}} g_{n_1+\cdots+n_i-n_{i+1}-\cdots-n_{2i-1}}(t - kT) \end{aligned} \tag{3.22}$$

Note that there is only one summation operator over time slot k in (3.22) due to the time-limited nature of the basis functions.

The first part of the receiver is the signal demodulator. As previously stated in

chapter 2, the demodulator can be described by a set of matched filters or, alternatively, by a set of correlators. Since the transmitted OFDM signal is distorted by the nonlinear channel, several IMPs will arise and fall both inside and outside the bandwidth of the original signal. In order to fully recover the information conveyed in the distorted signal, it is necessary to extract and demodulate all IMP components. To do so, we must project the received signal onto a broader set of orthonormal basis functions $\{g_n^*(t-kT), n = \cdots, -1, 0, 1, \cdots\}$ in order to extract the sufficient statistics, rather than onto only N basis functions as described in chapter 2 where an ideal channel was considered. This allows us to extract all the information that is relevant for the decision of which complex symbol was transmitted [69, 91]. Therefore, the sufficient statistics in time slot k and subchannel n are obtained by multiplying the received signal $\tilde{r}(t)$ by the basis function $g_n^*(t-kT)$ and integrating it from $kT + T_{CP}$ to $(k+1)T$, i.e.,

$$\begin{aligned} R_{k,n} &= \int_{kT+T_{CP}}^{(k+1)T} \tilde{r}(t) g_n^*(t-kT) dt \\ &= Y_{k,n} + N_{k,n} \end{aligned} \tag{3.23}$$

where $Y_{k,n}$ and $N_{k,n}$ are, respectively, given by

$$\begin{aligned} Y_{k,n} &= \int_{kT+T_{CP}}^{(k+1)T} \tilde{y}(t) g_n^*(t-kT) dt \\ &= \frac{\tilde{c}_1}{(T-T_{CP})^0} \sum_{n_1=0}^{N-1} S_{k,n_1} \delta(n_1 - n) \\ &\quad + \frac{\tilde{c}_3}{(T-T_{CP})^1} \sum_{n_1=0}^{N-1} \sum_{n_2=0}^{N-1} \sum_{n_3=0}^{N-1} S_{k,n_1} S_{k,n_2} S_{k,n_3}^* \delta(n_1 + n_2 - n_3 - n) \\ &\quad + \cdots \\ &\quad + \frac{\tilde{c}_L}{(T-T_{CP})^{(L-1)/2}} \sum_{n_1=0}^{N-1} \cdots \sum_{n_L=0}^{N-1} S_{k,n_1} \cdots S_{k,n_{(L+1)/2}} S_{k,n_{(L+3)/2}}^* \cdots S_{k,n_L}^* \\ &\quad \times \delta(n_1 + \cdots + n_{(L+1)/2} - n_{(L+3)/2} - \cdots - n_L - n) \end{aligned} \tag{3.24}$$

and

$$N_{k,n} = \int_{kT+T_{CP}}^{(k+1)T} \tilde{n}(t) g_n^*(t-kT) dt \tag{3.25}$$

for $n = \cdots, -1, 0, 1, \cdots$ and where $\delta(\cdot)$ represents the Kronecker delta product. Note that $N_{k,n}$ is a sample value of an independent and circularly symmetric complex Gaussian

RV[2] with zero-mean and PSD N_0.

As it can be seen from (3.24), the complex symbol $Y_{k,n}$ in time slot k and subchannel n is composed by the summation of several terms. The first term can be easily identified as the linear distortion in which the complex transmitted symbol $S_{k,n}$ suffers from an attenuation and/or phase shift depending on whether the coefficient $\tilde{c}_1$ is real (AM/AM) or complex (AM/PM). The second and subsequent terms are contributions from the third and higher order IMPs. Note that, although not clearly identified, desensitization and compression terms are also included in the second and subsequent terms (see chapter 2). In chapter 5 a more detailed analysis regarding the IMPs terms and their effect on the transmission performance is presented.

By taking into account that the complex envelope of the additive white Gaussian noise $\tilde{n}(t)$ is zero-mean and has a power spectral density N_0, the mean and variance of the RV $N_{k,n}$ are given by

$$\mathrm{E}[N_{k,n}] = \int_{kT+T_{CP}}^{(k+1)T} \mathrm{E}[\tilde{n}(t)]g_n(t-kT)dt = 0 \tag{3.26}$$

$$\begin{aligned}\mathrm{E}[N_{k,n}N_{k,m}^*] &= \int_{kT+T_{CP}}^{(k+1)T}\int_{kT+T_{CP}}^{(k+1)T} \mathrm{E}[\tilde{n}(t_1)\tilde{n}^*(t_2)]g_n(t_1-kT)g_m^*(t_2-kT)dt_1dt_2 \\ &= 2N_0\delta(n-m)\end{aligned} \tag{3.27}$$

Note that the statistical properties of the real and imaginary parts of the white complex Gaussian noise equals the ones of the real and imaginary parts of $N_{k,n}$. Consequently, the real and imaginary parts of $N_{k,n}$ are also independent, zero-mean and with power spectral densities N_0. Therefore, the probability density function of the circular symmetric complex Gaussian RV $N_{k,n}$ is given by [69, 71, 92]

$$\begin{aligned}p(N_{k,n}) &= \frac{1}{2\pi\sigma_{\Re\{N_{k,n}\}}\sigma_{\Im\{N_{k,n}\}}} e^{-\frac{\sigma^2_{\Re\{N_{k,n}\}}\left(\Re\{N_{k,n}\}-\mathrm{E}[\Re\{N_{k,n}\}]\right)^2+\sigma^2_{\Im\{N_{k,n}\}}\left(\Im\{N_{k,n}\}-\mathrm{E}[\Im\{N_{k,n}\}]\right)^2}{2\sigma^2_{\Re\{N_{k,n}\}}\sigma^2_{\Im\{N_{k,n}\}}}} \\ &= \frac{1}{2\pi N_0} e^{-\frac{|N_{k,n}|^2}{2N_0}}\end{aligned} \tag{3.28}$$

[2] A complex-valued Gaussian RV $Z = X + jY$ is circularly symmetric if its real and imaginary parts are statistically independent and identically distributed (iid) with zero mean, i.e., if and only if X and Y are jointly Gaussian with equi-probability density contours around 0. In other words, a complex Gaussian RV Z is circularly symmetric if $e^{j\phi}Z$ has the same distribution of Z for all ϕ.

3.3.1 Sufficient statistics extractor

Consider now the received complex symbols given by 3.23, 3.24 and 3.25. Assuming an odd nonlinearity of order L with coefficients $c_1, c_3, \cdots, c_L \neq 0$ and $c_i = 0$ for $i > L$, then $Y_{k,n}$ is non-zero only for $n = -1/2(L-1)(N-1), \cdots, 1/2(L+1)(N-1)$ and zero otherwise. In other words, $R_{k,n}$ can be written as

$$R_{k,n} = \begin{cases} Y_{k,n} + N_{k,n}, & n = -1/2(L-1)(N-1), \cdots, 1/2(L+1)(N-1) \\ N_{k,n}, & \text{otherwise} \end{cases} \tag{3.29}$$

From 3.29, it can be seen that a broad set of $L(N-1)+1$ orthonormal basis functions $\{g_n^*(t-kT), n = -1/2(L-1)(N-1), \cdots, 1/2(L+1)(N-1)\}$ is mandatory to extract all signal components and IMPs that fall nearby the original signal's bandwidth.

It is now important to prove that the received symbols using this new set of $L(N-1)+1$ basis functions contain all relevant data from $\tilde{r}(t)$ necessary for ML detection, i.e., that they still represent the set of sufficient statistics. First, we should rewrite 3.21 considering now the new set of basis functions. The received signal can now be given

$$\tilde{r}(t) = \tilde{r}_1(t) + \tilde{r}_2(t) \tag{3.30}$$

where

$$\tilde{r}_1(t) = \tilde{y}(t) + \tilde{n}_p(t) \tag{3.31}$$

represents the part of $\tilde{r}(t)$ that is extracted by the set of $L(N-1)+1$ basis functions, $\tilde{n}_p(t)$ is the part of the noise process that is extracted using that same set and

$$\tilde{r}_2(t) = \tilde{n}(t) - \tilde{n}_p(t) \tag{3.32}$$

is a function that can be viewed as the remainder term of the noise process that is not projected. Note that $\tilde{r}_2(t)$ is not zero due to the impossibility of projecting the entire noise process $\tilde{n}(t)$ onto a set of finite orthonormal basis functions. Since $\tilde{n}(t)$ is Gaussian with zero mean, it follows that $\tilde{r}_2(t)$ is also Gaussian with zero mean and independent of the transmitted symbols.

From the theorem of irrelevance [69, 91], the optimum receiver may disregard $\tilde{r}_2(t)$ if and only if $\tilde{r}_2(t)$ when conditioned on $\tilde{r}_1(t)$ is statistically independent of $\tilde{s}(t)$ and $\tilde{r}_1(t)$, i.e., in terms of probability density functions (PDF), if and only if

$$p\left(r_2|r_1, s\right) = p(r_2) \tag{3.33}$$

The condition given by (3.33) is true if the cross-covariance of $\tilde{r}_2(t)$ and $\tilde{r}_1(t)$ equals zero for all time instants t. From the definition of cross-covariance (e.g. [69]),

$$\Sigma_{XY} = \mathrm{E}\left[XY\right] - \mathrm{E}[X]\mathrm{E}[Y] \tag{3.34}$$

and knowing that $\tilde{r}_2(t)$ is zero-mean and that the AWGN term has a PSD N_0, the cross-covariance of $\tilde{r}_1(t)$ and $\tilde{r}_2(t)$ in fact reduces to

$$\begin{aligned}\Sigma_{r_1 r_2} &= \mathrm{E}\left[\tilde{r}_1(\tau)\tilde{r}_2^*(t)\right] \\ &= \mathrm{E}\left[\tilde{n}_p(\tau)\tilde{n}^*(t)\right] - \mathrm{E}\left[\tilde{n}_p(\tau)\tilde{n}_p^*(t)\right] \\ &= 0, \quad \forall t, \tau\end{aligned} \tag{3.35}$$

Indeed, the remainder noise process $\tilde{r_2}(t)$ is statistically independent of $\tilde{r}_1(t)$ and therefore $\left\{R_{k,-1/2(L-1)(N-1)}, \cdots, R_{k,1/2(L+1)(N-1)}\right\}$ represents the set of sufficient statistics, i.e., it contains all information necessary for the ML detection.

3.3.2 Maximum likelihood sequence estimation

As previously stated, the goal of the optimum receiver is to minimize the error probability of the estimate. From a different point of view, we can say that the optimum detector looks for the received symbols at each time slot k and outputs the estimate of the transmitted symbols that maximize the probability of a correct decision [69, 71, 84, 90].

Let us consider the vector of transmitted complex symbols in time slot k $\mathbf{S}_k = \left[S_{k,0}, S_{k,1}, \cdots, S_{k,N-1}\right]^T$ and the corresponding vector of received complex symbols in the same time slot $\mathbf{R}_k = \left[R_{k,-1/2(L-1)(N-1)}, \cdots, R_{k,1/2(L+1)(N-1)}\right]^T$ that also represents the set of sufficient statistics[3].

[3]Since the OFDM symbol in time slot k is independent from those in slot $k-1$ and $k+1$, we will hereafter omit parameter k from vectors designations and consider that the hereafter analysis is for an arbitrary time slot k.

It is assumed that each OFDM subchannel conveys M-PSK/M-QAM signal constellations, where M is the size of the constellation. Nevertheless, the following analysis can also be applied to any kind of digital modulation schemes. The OFDM symbol error probability can be obtained by averaging the probability of error of all subchannels. Alternatively, we can also derive the probability of error by defining it as

$$\begin{aligned} P(e) &= \sum_{i=1}^{M^N} P\left(e|\mathbf{S}^{(i)}\right) P\left(\mathbf{S}^{(i)}\right) \\ &= \sum_{i=1}^{M^N} \left[1 - P\left(c|\mathbf{S}^{(i)}\right)\right] P\left(\mathbf{S}^{(i)}\right) \end{aligned} \tag{3.36}$$

where $P\left(e|\mathbf{S}^{(i)}\right)$ and $P\left(c|\mathbf{S}^{(i)}\right)$, $i = 1, \cdots, M^N$ are the probability of a decision error and a correct decision, respectively, given that the vector $\mathbf{S}^{(i)}$ was transmitted, $P\left(\mathbf{S}^{(i)}\right)$ denotes the *a priori* probability of the transmitted vector $\mathbf{S}^{(i)}$, and 'i' identifies each one of the M^N different possible symbol combinations that can be transmitted.

An alternative interpretation of the OFDM signal transmission can be performed by means of its geometric representation. The transmitted vector $\mathbf{S}$ can be viewed as an N-dimensional vector in an N-dimensional Euclidean space. The set of sufficient statistics $\mathbf{R}$ obtained by projecting the received signal onto a set of $L(N-1)+1$ basis functions can also be interpreted as a vector in an $[L(N-1)+1]$-Euclidean space. Analogously, 'i' in (3.36) can also be interpreted as the identifier of the Region $\mathcal{Z}_i$ that represents one of the M^N partitions of the multi-dimensional space. Therefore, a correct decision given $\mathbf{S}^{(i)}$ occurs whenever the received vector $\mathbf{R}$ falls in the decision region $\mathcal{Z}_i$, i.e.,

$$P\left(c|\mathbf{S}^{(i)}\right) = P\left(\mathbf{R} \in \mathcal{Z}_i|\mathbf{S}^{(i)}\right) \tag{3.37}$$

The conditional probability of a correct decision given $\mathbf{S}^{(i)}$, can be obtained by integrating over region $\mathcal{Z}_i$ the corresponding conditional probability density function (PDF), i.e.,

$$P\left(c|\mathbf{S}^{(i)}\right) = \int_{\mathcal{Z}_i} p\left(\mathbf{R}|\mathbf{S}^{(i)}\right) d\mathbf{R} \tag{3.38}$$

Thus, by substituting (3.38) in (3.36), the average probability of error is

$$\begin{aligned} P(e) &= \sum_{i=1}^{M^N} \left[1 - \int_{\mathcal{Z}_i} p\left(\mathbf{R}|\mathbf{S}^{(i)}\right) d\mathbf{R}\right] P\left(\mathbf{S}^{(i)}\right) \\ &= 1 - \sum_{m=1}^{M^N} P\left(\mathbf{S}^{(i)}\right) \int_{\mathcal{Z}_i} p\left(\mathbf{R}|\mathbf{S}^{(i)}\right) d\mathbf{R} \end{aligned} \tag{3.39}$$

We can see from (3.39) that in order to minimize the probability of error, we should select an estimate of the transmitted complex symbol $\hat{\mathbf{S}} = \mathbf{S}^{(i)}$ that maximizes $P\left(\mathbf{S}^{(i)}\right) p\left(\mathbf{R}|\mathbf{S}^{(i)}\right)$.

Using Bayes' rule, we can write the following condition [69, 71, 92]

$$P\left(\mathbf{S}^{(i)}\right) p\left(\mathbf{R}|\mathbf{S}^{(i)}\right) = P\left(\mathbf{S}^{(i)}|\mathbf{R}\right) p\left(\mathbf{R}\right) \tag{3.40}$$

where the conditional probabilities $P\left(\mathbf{S}^{(i)}|\mathbf{R}\right)$ are the posterior probabilities, i.e., the probabilities of a correct decision based on the observation of the vector $\mathbf{R}$, and the PDF $p\left(\mathbf{R}\right)$ is given by

$$p\left(\mathbf{R}\right) = \sum_{i=1}^{M^N} p\left(\mathbf{R}|\mathbf{S}^{(i)}\right) P\left(\mathbf{S}^{(i)}\right) \tag{3.41}$$

It is possible to observe that the estimate of the transmitted vector $\hat{\mathbf{S}}$ that minimizes the probability of error given by (3.39) also maximizes the right hand side (RHS) of (3.40). Since $p\left(\mathbf{R}\right)$ does not depend on the transmitted symbol, the optimum decision rule can be finally stated through the following equivalent rules

$$\hat{\mathbf{S}} = \arg\max_{\mathbf{S}^{(i)}} P\left(\mathbf{S}^{(i)}|\mathbf{R}\right) \tag{3.42}$$

$$\hat{\mathbf{S}} = \arg\max_{\mathbf{S}^{(i)}} P\left(\mathbf{S}^{(i)}\right) p\left(\mathbf{R}|\mathbf{S}^{(i)}\right) \tag{3.43}$$

where $\arg\max$ represents the argument of the maximum, i.e., the argument for which the given function attains its maximum. Both decision rules are called the *maximum a posteriori* probability (MAP) criterion [90, 91].

The conditional PDF $p\left(\mathbf{R}|\mathbf{S}^{(i)}\right)$, $i = 1, 2, \cdots, M^N$, is often called the *likelihood function* and denoted by $L\left(\mathbf{R}|\mathbf{S}^{(i)}\right)$. Moreover, for equi-probable *a priori* transmitted symbols vectors with $P\left(\mathbf{S}^{(i)}\right) = 1/\left(M^N\right), \forall i = 1, 2, \cdots, M^N$, we may restate and

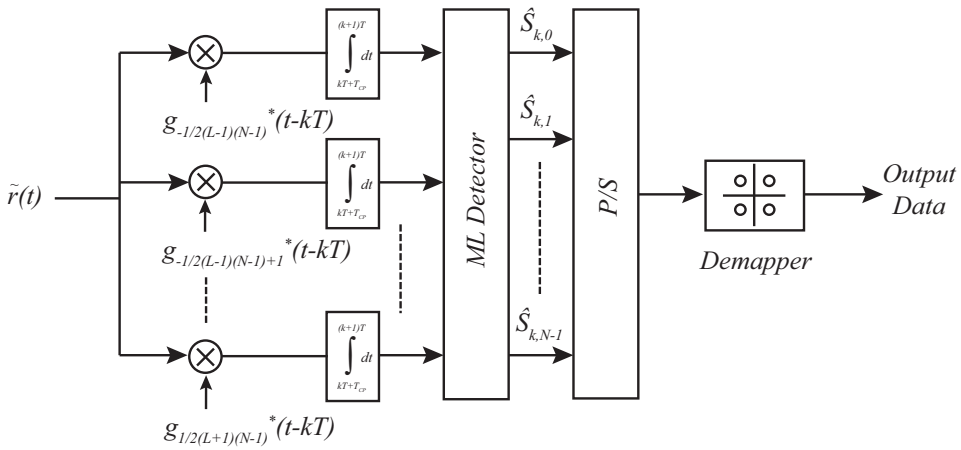

FIGURE 3.3: Equivalent lowpass representation of the OFDM optimum receiver structure.

simplify (3.43) as

$$\hat{\mathbf{S}} = \arg\max_{\mathbf{S}^{(i)}} L\left(\mathbf{R}|\mathbf{S}^{(i)}\right) \tag{3.44}$$

The decision criterion rule in (3.43) is based on maximizing the likelihood function for equally likely *a priori* probabilities and is called the *maximum likelihood* (ML) criterion. Unless stated otherwise, we will always consider hereafter equal *a priori* probabilities for the transmitted complex symbols.

Finally, we can state that the optimum decision is the one that for a given received vector $\mathbf{R} = [R_{k,-1/2(L-1)(N-1)}, \cdots, R_{k,1/2(L+1)(N-1)}]^T$ representing a set of sufficient statistics, it estimates the transmit vector $\hat{\mathbf{S}} = [\hat{S}_{k,0}, \cdots, \hat{S}_{k,N-1}]^T$ that maximizes the likelihood function. Figure 3.3 depicts the lowpass equivalent structure of the optimum OFDM receiver structure in terms of error probability.

Let us now define the likelihood function for our particular case. In the presence of a complex AWGN channel, the likelihood function is expressed as

$$L\left(\mathbf{R}|\mathbf{S}^{(i)}\right) = \frac{1}{\pi^{(L(N-1)+1)}\det\left(\Sigma_{\mathbf{R}|\mathbf{S}^{(i)}}\right)} e^{-\left(\mathbf{R}-\mathrm{E}\left[\mathbf{R}|\mathbf{S}^{(i)}\right]\right)\Sigma^{-1}_{\mathbf{R}|\mathbf{S}^{(i)}}\left(\mathbf{R}-\mathrm{E}\left[\mathbf{R}|\mathbf{S}^{(i)}\right]\right)^H} \tag{3.45}$$

where $(\cdot)^H$ denotes the conjugate transpose and matrix $\Sigma_{\mathbf{R}|\mathbf{S}^{(i)}}$ represents the covariance of random vector $\mathbf{R}$ conditioned to transmitted vector $\mathbf{S}^{(i)}$ and is defined as

$$\Sigma_{\mathbf{R}|\mathbf{S}^{(i)}} \triangleq \mathrm{E}\left[\left(\mathbf{R} - \mathrm{E}\left[\mathbf{R}|\mathbf{S}^{(i)}\right]\right)\left(\mathbf{R} - \mathrm{E}\left[\mathbf{R}|\mathbf{S}^{(i)}\right]\right)^H |\mathbf{S}^{(i)}\right] \tag{3.46}$$

Note that the conditional expectation $\mathrm{E}\left[\mathbf{R}|\mathbf{S}^{(i)}\right]$ reduces to the vector of nonlinearly distorted complex received symbols for the referred transmitted sequence, $\mathbf{Y}\left(\mathbf{S}^{(i)}\right)$, given by (3.24)) since $\mathrm{E}\left[N_{k,n}\right] = 0, \forall n$. Consequently, the covariance matrix (3.46) reduces to

$$\begin{aligned}\Sigma_{\mathbf{R}|\mathbf{S}^{(i)}} &= \mathrm{E}\left[\left(\mathbf{R}-\mathbf{Y}\left(\mathbf{S}^{(i)}\right)\right)\left(\mathbf{R}-\mathbf{Y}\left(\mathbf{S}^{(i)}\right)\right)^H|\mathbf{S}^{(i)}\right] \\ &= \mathrm{E}\left[\mathbf{N}\mathbf{N}^H\right] \\ &= 2N_0\mathbf{I}_{[L(N-1)+1]}\end{aligned} \tag{3.47}$$

where $\mathbf{N} = [N_{k,-1/2(L-1)(N-1)}, \cdots, N_{k,1/2(L+1)(N-1)}]^T$ and $\mathbf{I}_{[L(N-1)+1]}$ is the identity matrix of size $L(N-1)+1$.

Substituting (3.47) in (3.45), the likelihood function reduces to

$$L\left(\mathbf{R}|\mathbf{S}^{(i)}\right) = \frac{1}{(2\pi N_0)^{L(N-1)+1}} e^{-\frac{\left\|\mathbf{R}-\mathbf{Y}\left(\mathbf{S}^{(i)}\right)\right\|^2}{2N_0}} \tag{3.48}$$

where $\|\cdot\|$ denotes the norm of a vector. Usually, it is common to work with the natural logarithm of the likelihood function. The log-likelihood function is then given by

$$\begin{aligned}l\left(\mathbf{R}|\mathbf{S}^{(i)}\right) &= \ln\left[L\left(\mathbf{R}|\mathbf{S}^{(i)}\right)\right] \\ &= -[L(N-1)+1]\ln(2\pi N_0) - \frac{1}{2N_0}\left\|\mathbf{R}-\mathbf{Y}\left(\mathbf{S}^{(i)}\right)\right\|^2\end{aligned} \tag{3.49}$$

Note that the logarithm is a monotonic function and that the likelihood function is always non-negative. Thus, the use of the log-likelihood function in the ML criterion is equivalent to the use of the likelihood function.

Since the first term of (3.49) is constant, it is irrelevant for the estimation process and can be discarded. The log-likelihood function is maximum when the norm in (3.49) or, equivalently, the Euclidean distance between vectors $\mathbf{R}$ and $\mathbf{Y}\left(\mathbf{S}^{(i)}\right)$ given by

$$D\left(\mathbf{R}, \mathbf{Y}\left(\mathbf{S}^{(i)}\right)\right) = \left\|\mathbf{R}-\mathbf{Y}\left(\mathbf{S}^{(i)}\right)\right\|^2 \tag{3.50}$$

is minimized. The estimate of the transmitted sequence given by (3.44) can now be rewritten as

$$\begin{aligned}\hat{\mathbf{S}} &= \arg\min_{\mathbf{S}^{(i)}} \left\| \mathbf{R} - \mathbf{Y}\left(\mathbf{S}^{(i)}\right) \right\|^2 \\ &= \arg\min_{\mathbf{S}^{(i)}} \sum_{n=n_{min}}^{n_{max}} \left| R_{k,n} - Y_{k,n}\left(\mathbf{S}^{(i)}\right) \right|^2\end{aligned} \tag{3.51}$$

Note that $n_{min} = -1/2(L-1)(N-1)$ and $n_{max} = 1/2(L+1)(N-1)$.

In conclusion, the optimum ML detector computes the $L(N-1)+1$ Euclidean distances given by (3.50) for all M^N possible transmitted vectors $\mathbf{S}^{(i)}, \quad i = 1, \cdots, M^N$, compares them and selects the transmitted vector that produces the smallest Euclidean distance.

3.3.3 Iterative ML detection algorithm

The ML detection algorithm previously derived compensates for the performance degradation induced by the nonlinear channel. In fact, it estimates the original transmitted vector and guarantees the maximum performance achievable in terms of error probability. However, an ideal ML receiver demands a huge computational effort when a high number of subcarriers and/or constellation size are used.

The ideal ML detector evaluates (3.44) for every possible data vectors $\mathbf{S}^{(i)}$, $i = 1, \cdots, M^N$, where M and N are the constellation size and the number of subcarriers, respectively, resulting in a complexity of order $O\left(M^N\right)$. Putting it in numbers, (3.44) must be evaluated 256, 65536 and 2×10^{19} times when a BPSK constellation is used to modulate 8, 16 and 64 subcarriers, respectively. This exponential rise of the number of evaluations makes the ideal ML detection impracticable when M and/or N are large.

In order to reduce the large computational cost, we will also use an iterative estimation algorithm based on the one proposed by Nishijima *et al.* [93, 94] that instead of evaluating all M^N possible transmitted sequences, it evaluates (3.44) for a restricted group of data vectors $\mathbf{S}^{(i)}$ that are in the neighborhood of the estimate given by the conventional OFDM receiver. Furthermore, this process can be repeated iteratively in order to refine and minimize the probability of error.

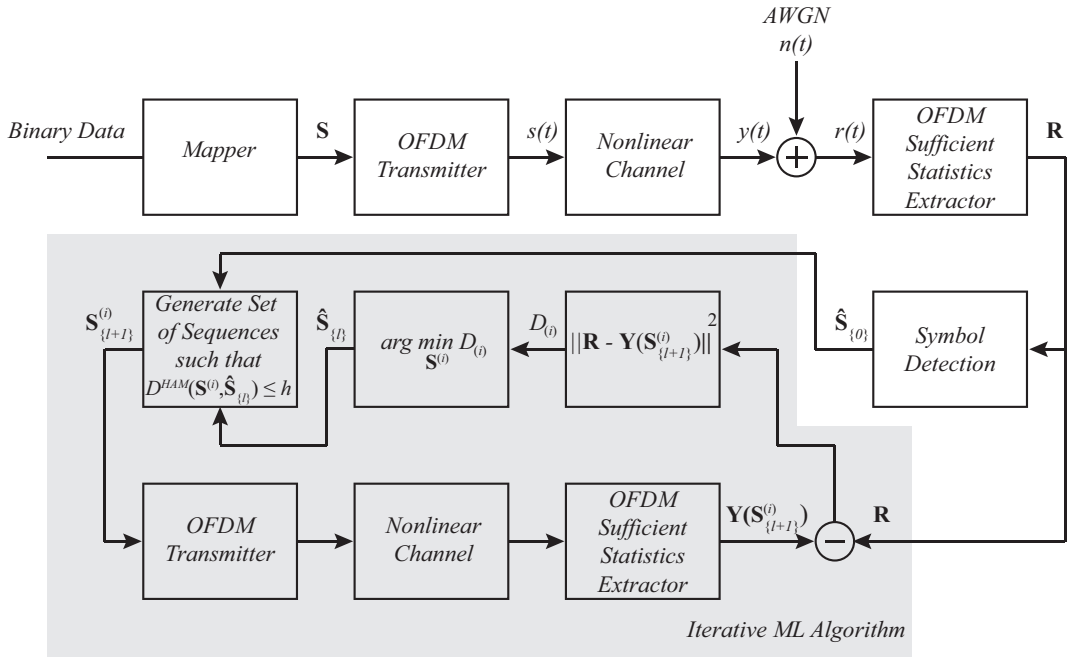

FIGURE 3.4: Block diagram of the iterative ML algorithm.

The iterative algorithm proposed by Nishijima *et al.* can be seen as sub-optimum since it only takes into account the vector of symbols obtained by a set of correlators matched only to the frequencies of the original N OFDM subcarriers, i.e., it only computes (3.50) $KN+1$ times for each iteration, where K is the number of bits per symbol. Thus, it only takes into account IMPs that fall inside the original signal's band and does not extract the set of sufficient statistics necessary to feed to the optimum detector. Moreover, it only evaluates (3.50) for data vectors $\mathbf{S}^{(i)}$ whose binary sequences differ only in one bit (Hamming distance of one) from the binary sequence of the previous iteration. Later, Rodrigues *et al.* [95] have proposed the use of the set of sufficient statistics in order to optimize the algorithm. We will now introduce a modification to the iterative algorithm and will consider the evaluation of data vectors that are within a region with a Hamming distance greater than one. Note that iteration 'zero' is always given by the conventional OFDM receiver, i.e., the starting point for this algorithm is always the same, independently of the Hamming distance parameter that is chosen and given by a simple conventional receiver. In chapter 5, the iterative algorithm will also be evaluated with a proposed modification where iteration 'zero' is given by the linear MMSE receiver derived in chapter 4, rather than by the conventional receiver.

The block diagram of the iterative ML algorithm is represented in Figure 3.4. First,

the received signal, $\tilde{r}(t)$, passes through a set of $L(N-1)+1$ matched filters or correlators matched to every possible frequency components and extracts the sufficient statistics vector, $\mathbf{R}$. The first estimate of the transmitted symbol sequence, $\hat{\mathbf{S}}_{\{0\}}$, is obtained by using a conventional receiver and is used as the start point for the iterative algorithm. Then, for the $l+1$ iteration, the sequence generator produces a set of all symbol sequences that are up to a certain Hamming distance of 'h' far from $\hat{\mathbf{S}}_{\{l\}}$. The set of possible estimates of the original transmitted sequence is given by

$$\left\{ \mathbf{S}^{(i)}_{\{l+1\}}, \quad i = 1, \cdots, \sum_{j=1}^{h} \binom{KN}{j} : D^{HAM}\left(\mathbf{S}^{(j)}, \hat{\mathbf{S}}_{\{l\}}\right) \leq h, \quad j = 1, \cdots, M^N \right\} \quad (3.52)$$

where $D^{HAM}(\cdot,\cdot)$ denotes the Hamming distance between two vectors and K is the number of bits per symbol. Since the universe of possible transmitted vectors is now much more restricted than when considering all M^N possibilities, the evaluation of the ML rule given by (3.44) has now an associated complexity cost of order $O\left[1 + l\sum_{j=1}^{h}\binom{KN}{j}\right]$. In fact, for $h = 1$, the sets given by (3.52) are composed by $\left\{\mathbf{S}^{(1)}_{\{l+1\}}, \cdots, \mathbf{S}^{(KN)}_{\{l+1\}}\right\}$ which are the KN sequences that are closest (only differing by one bit) to the estimate vector from the previous iteration. Similarly, for $h = NK$, the number of vectors rises to $2^{KN} - 1$, which corresponds to all possible transmitted sequences. This scenario is in fact the ideal ML estimation process.

The set of possible transmitted vectors are then applied to a replica of the transmitter, nonlinear channel and sufficient statistics extractor, which generates the output symbol sequences $\left\{\mathbf{Y}\left(\mathbf{S}^{(i)}_{\{l+1\}}\right), \quad i = 1, \cdots, \sum_{j=1}^{h}\binom{KN}{j}\right\}$. Then, the estimator computes the Euclidean distances between the original received vector $\mathbf{R}$ (also representing the sufficient statistics) and all generated sequences $\mathbf{Y}\left(\mathbf{S}^{(i)}_{\{l+1\}}\right)$ and chooses the sequence $\mathbf{S}^{(i)}_{\{l+1\}}$ responsible for the minimum Euclidean distance. This procedure is iteratively repeated in order to improve the performance. It is important to note that the algorithm converges to a local optimum solution after a certain number of iterations and that the optimum ML solution is not guaranteed.

3.4 Summary

In this chapter we have derived the structure of the optimum receiver for nonlinearly distorted OFDM signal in AWGN. The optimum receiver consists of a set of correlators or a set of filters matched to every possible frequency component of the nonlinearly distorted OFDM signal responsible for the extraction of a set of sufficient statistics followed by a maximum likelihood (ML) detector. In order to bypass complexity issues, we have also adopted an iterative procedure rather than the optimal exhaustive one associated with ML detection. The algorithm evaluates the sufficient statistics produced by all data vectors that are at a user defined Hamming distance from the estimate given by the previous iteration and outputs the one that maximizes the likelihood function. Note that the first estimate is always given by a conventional receiver. The algorithm is designed to converge to the global optimum estimate if a Hamming distance of M^N is chosen.

In the next chapter, we derive the structure of the minimum mean-squared error (MMSE) linear receiver for nonlinearly distorted OFDM signals in the presence of AWGN.

Chapter 4

The MMSE OFDM receiver for memoryless nonlinear channels

4.1 Introduction

In the previous chapter, we have presented the optimum receiver in terms of error probability for nonlinearly distorted OFDM. However, its high computational complexity associated with the ML detection can make it difficult to implement, specially in real-time applications. Additionally, an algorithm that, with the aid of the set of sufficient statistics, iteratively searches for the OFDM symbol that maximizes the likelihood function in the neighborhood of a first estimate given by a conventional receiver was also presented.

In this chapter we propose and evaluate the structure of the receiver that minimizes a specific metric, namely the mean-squared value of the error signal (MMSE). The implementation of this receiver is intended to be simpler than the ML receiver. We start by introducing the MSE cost function in section 4.2. Then, in section 4.3 the structure of the receiver for nonlinearly distorted OFDM signals is analytically derived. In section 4.4 its performance in terms of MSE is evaluated and compared with simulation results. An LMS based adaptive algorithm to estimate and iteratively adjust the coefficients of the MMSE receiver is also presented.

4.2 Minimum mean-squared error cost function

In statistics, a common quality measure indicator used to quantify how much deviated are the values given by an estimator from the "true" ones is the mean-squared error (MSE). The MSE corresponds in fact to the expected value of the quadratic error between values given by a parameter, θ, and its estimator, $\hat{\theta}$ [69, 71]. Thus, the MSE, ξ, is mathematically defined as

$$\begin{aligned} \xi &\triangleq \mathrm{E}[e_{\hat{\theta}}^2] \\ &= \mathrm{E}\left[(\hat{\theta} - \theta)^2\right] \end{aligned} \tag{4.1}$$

where e_θ is the error of the estimator $\hat{\theta}$.

The minimum mean-squared error (MMSE) estimator is then defined as the estimator with which the minimum of the cost function given by (4.1) is achieved.

We will now derive the structure of a receiver that processes the nonlinearly distorted OFDM signal contaminated with noise given by (3.21) and (3.22) in a linear fashion in order to optimize the performance metric MSE.

4.3 MMSE receiver structure derivation

Let us consider the structure of the MMSE receiver for nonlinearly distorted OFDM signals in the presence of AWGN. In opposite to the ML receiver which is more complex in terms of computation but also optimum in terms of error minimization, here we consider a simpler linear receiver structure given by the linear MMSE. We take its structure to consist of a bank of N linear filters with impulse responses $\{u_n(t) : n = 0, \cdots, N-1\}$ as depicted in Figure 4.1. By doing so, we consider that the nth branch of the linear receiver outputs an estimate of the transmitted symbol conveyed by subcarrier n, $\hat{S}_{k,n}$. The objective is to determine the set of linear filters impulse responses that minimize the overall linear MSE.

So, each filter is designed to output an estimate of the transmitted symbol, $\hat{S}_{k,n}$, conveyed in a specific subcarrier at a specific sampling instant $t_k = t_0 + kT$, where t_0 is a constant time delay, which is related with the sampling instant, and T is the

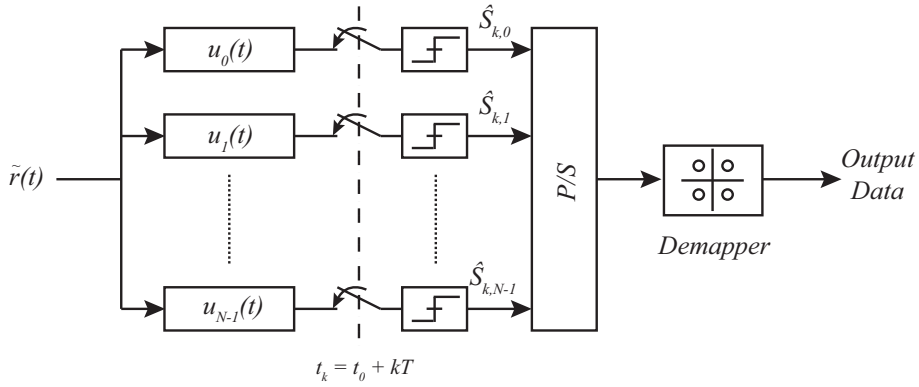

FIGURE 4.1: Structure of the linear MMSE OFDM receiver.

OFDM symbol period. Therefore, the estimate of the transmitted symbol conveyed in subcarrier n and time slot k is

$$\begin{aligned}\hat{S}_{k,n} &= [\tilde{r}(t) * u_n(t)]_{t=t_k} \\ &\triangleq \int_{-\infty}^{+\infty} u_n(\tau)\tilde{r}(t_k - \tau)d\tau\end{aligned} \tag{4.2}$$

Ideally, the condition for an optimal result by the receiver is to have $\hat{S}_{k,n} = S_{k,n}$, $n = 0, 1, \cdots, N-1$. Any deviation from this condition results in an error given by

$$e_{k,n} = S_{k,n} - \hat{S}_{k,n} \tag{4.3}$$

By substituting the error signal given by (4.3) in (4.1), we can now write the cost function to be minimized as

$$\begin{aligned}\xi &= \mathrm{E}\left[\left\|\mathbf{S}_k - \hat{\mathbf{S}}_k\right\|^2\right] \\ &= \sum_{n=0}^{N-1} \xi_n\end{aligned} \tag{4.4}$$

where $\mathbf{S}_k = [S_{k,0}, S_{k,1}, \cdots, S_{k,N-1}]^T$ is the vector of transmitted symbols in time slot k, $\hat{\mathbf{S}}_k = \left[\hat{S}_{k,0}, \hat{S}_{k,1}, \cdots, \hat{S}_{k,N-1}\right]^T$ is the vector of estimates of the transmitted symbols in time slot k and ξ_n is the MSE associated with subcarrier n given by

$$
\begin{aligned}
\xi_n &= \mathrm{E}\left[\left|S_{k,n} - \hat{S}_{k,n}\right|^2\right] \\
&= \mathrm{E}\left[\left|S_{k,n} - \int_{-\infty}^{+\infty} u_n(\tau)\tilde{r}(t_k - \tau)d\tau\right|^2\right] \\
&= \mathrm{E}\left[|S_{k,n}|^2 + \int_{-\infty}^{+\infty}\int_{-\infty}^{+\infty} u_n(\tau_1)u_n^*(\tau_2)\tilde{r}(t_k - \tau_1)\tilde{r}^*(t_k - \tau_2)d\tau_1 d\tau_2\right. \\
&\quad \left. - \int_{-\infty}^{+\infty} u_n(\tau_1)S_{k,n}^*\tilde{r}(t_k - \tau_1)d\tau_1 - \int_{-\infty}^{+\infty} u_n^*(\tau_2)S_{k,n}\tilde{r}^*(t_k - \tau_2)d\tau_2\right]
\end{aligned}
\tag{4.5}
$$

Let us now focus on the derivation of the MSE associated with each subcarrier. By representing the complex envelope of the received OFDM signal, $\tilde{r}(t)$, as a sum of nonlinear distorted and white Gaussian noise components, $\tilde{y}(t)$ and $\tilde{n}(t)$, respectively (see (3.21)), (4.5) can be rewritten and expanded to

$$
\begin{aligned}
\xi_n &= \mathrm{E}\left[|S_{k,n}|^2\right] \\
&\quad + \int_{-\infty}^{+\infty}\int_{-\infty}^{+\infty} u_n(\tau_1)u_n^*(\tau_2)\left\{\mathrm{E}\left[\tilde{y}(t_k - \tau_1)\tilde{n}^*(t_k - \tau_2)\right] + \mathrm{E}\left[\tilde{y}^*(t_k - \tau_2)\tilde{n}(t_k - \tau_1)\right]\right. \\
&\quad \left. + \mathrm{E}\left[\tilde{y}(t_k - \tau_1)\tilde{y}^*(t_k - \tau_2)\right] + \mathrm{E}\left[\tilde{n}(t_k - \tau_1)\tilde{n}^*(t_k - \tau_2)\right]\right\} d\tau_1 d\tau_2 \\
&\quad - \int_{-\infty}^{+\infty} u_n(\tau_1)\left\{\mathrm{E}\left[S_{k,n}^*\tilde{y}(t_k - \tau_1)\right] + \mathrm{E}\left[S_{k,n}^*\tilde{n}(t_k - \tau_1)\right]\right\} d\tau_1 \\
&\quad - \int_{-\infty}^{+\infty} u_n^*(\tau_2)\left\{\mathrm{E}\left[S_{k,n}\tilde{y}^*(t_k - \tau_2)\right] + \mathrm{E}\left[S_{k,n}\tilde{n}^*(t_k - \tau_2)\right]\right\} d\tau_2
\end{aligned}
\tag{4.6}
$$

From the observation of (4.6), it is possible to make some simplifications and considerations. The first term of (4.6) is the mean square of the transmitted symbols, which is considered to be known and equal to σ_S^2 for all n. Also, the first term of the third line is the auto-correlation function of the signal $\tilde{y}(t)$ and the second term of the third line is the auto-correlation function of the signal $\tilde{n}(t)$.

Consequently, by virtue of the statistical properties of $S_{k,n}$, $\tilde{y}(t)$ and $\tilde{n}(t)$, the expectations in (4.6) are given by

$$\mathrm{E}\left[\tilde{n}(t_k-\tau_1)\tilde{n}^*(t_k-\tau_2)\right] = 2N_0\delta(\tau_2-\tau_1) \tag{4.7}$$

$$\mathrm{E}\left[\tilde{y}(t_k-\tau_1)\tilde{n}^*(t_k-\tau_1)\right] = 0, \quad \forall n, t_k \tag{4.8}$$

$$\mathrm{E}\left[\tilde{y}^*(t_k-\tau_2)\tilde{n}(t_k-\tau_1)\right] = 0, \quad \forall n, t_k \tag{4.9}$$

$$\mathrm{E}\left[S^*_{k,n}\tilde{n}(t_k-\tau_1)\right] = 0, \quad \forall n, t_k \tag{4.10}$$

$$\mathrm{E}\left[S_{k,n}\tilde{n}^*(t_k-\tau_2)\right] = 0, \quad \forall n, t_k \tag{4.11}$$

Therefore, substituting (4.7), (4.8), (4.9), (4.10) and (4.11) into (4.6), we may reduce the MSE associated with subcarrier n to

$$\begin{aligned}\xi_n = \sigma_S^2 &+ \int_{-\infty}^{+\infty}\int_{-\infty}^{+\infty} u_n(\tau_1)u_n^*(\tau_2)E\left[\tilde{y}(t_k-\tau_1)\tilde{y}^*(t_k-\tau_2)\right]d\tau_1 d\tau_2 \\ &+ 2N_0\int_{-\infty}^{+\infty} u_n(\tau_1)u_n^*(\tau_1)d\tau_1 \\ &- \int_{-\infty}^{+\infty} u_n(\tau_1)\mathrm{E}\left[S^*_{k,n}\tilde{y}(t_k-\tau_1)\right]d\tau_1 - \int_{-\infty}^{+\infty} u_n^*(\tau_2)\mathrm{E}\left[S_{k,n}\tilde{y}^*(t_k-\tau_2)\right]d\tau_2\end{aligned} \tag{4.12}$$

Using calculus of variations [84, 96] it is possible to find the set of complex functions $u_n(t)$ that minimize the overall MSE $\xi(u_0(t),\cdots,u_{N-1}(t)) = \xi_0(u_0(t)) + \cdots + \xi_{N-1}(u_{N-1}(t))$. From the Fréchet differential of (4.12),

$$\frac{d}{d\alpha}\left[\xi_n(u_n(t)+\alpha h(t))\right]_{\alpha=0} = 0, \quad \forall h(t) \tag{4.13}$$

where $n = 0,\cdots,N-1$, it follows that the optimal linear filter responses satisfy the set of integral equations

$$\begin{aligned}\int_{-\infty}^{+\infty} u_n(\tau')\mathrm{E}\left[\tilde{y}^*(t_k-\tau)\tilde{y}(t_k-\tau')\right]d\tau' + 2N_0u_n(\tau) \\ = \mathrm{E}\left[S_{k,n}\tilde{y}^*(t_k-\tau)\right], \quad n = 0,1,\cdots,N-1\end{aligned} \tag{4.14}$$

or, equivalently,

$$\begin{aligned}\int_{-\infty}^{+\infty} u_n^*(\tau')\mathrm{E}\left[\tilde{y}(t_k-\tau)\tilde{y}^*(t_k-\tau')\right]d\tau' + 2N_0u_n(\tau) \\ = \mathrm{E}\left[S^*_{k,n}\tilde{y}(t_k-\tau)\right], \quad n = 0,1,\cdots,N-1\end{aligned} \tag{4.15}$$

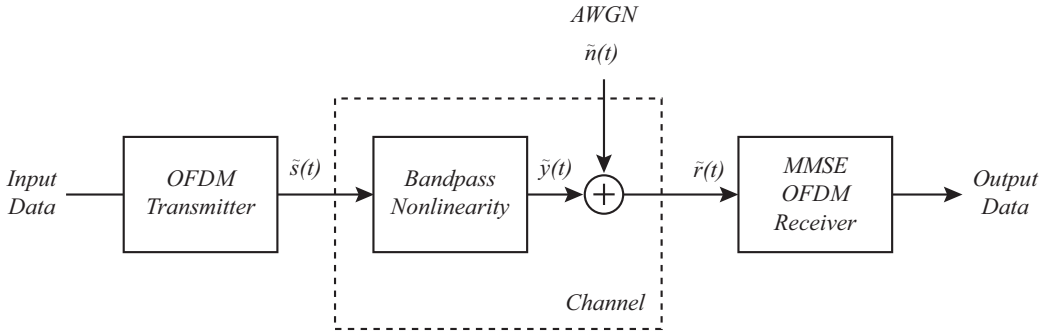

FIGURE 4.2: Equivalent baseband OFDM communications system model.

In order to obtain the impulse responses $\{u_n(t), n = 0, 1, \cdots, N-1\}$, we must first derive both the integral and the expected value in the left-hand side (LHS) and right-hand side (RHS), respectively, of (4.14) (or (4.15)). Note that no assumptions on the bandpass channel properties nor its output, $\tilde{y}(t)$, were made yet. We shall now introduce our system model.

Let us consider again the OFDM communications system model represented in Figure 4.2. Similarly to what was presented in chapter 3, $\tilde{s}(t)$ and $\tilde{r}(t)$ represent the complex envelope of the transmitted and received OFDM signals, respectively, given by

$$\tilde{s}(t) = \sum_{k=-\infty}^{+\infty} \sum_{n=0}^{N-1} S_{k,n} g_n(t - kT) \tag{4.16}$$

where

$$g_n(t) = \begin{cases} \dfrac{1}{\sqrt{T - T_{CP}}} e^{j\frac{2\pi n(t-T_{CP})}{T-T_{CP}}}, & 0 \leq t \leq T \\ 0, & \text{otherwise,} \end{cases} \tag{4.17}$$

and $S_{k,n}$ is the complex transmitted symbol in time slot k and subcarrier n, N is the number of OFDM subcarriers, T is the OFDM symbol duration and T_{CP} is the OFDM cyclic prefix duration. It is considered that the signal is distorted by a nonlinearity represented by its equivalent lowpass signal given by

$$\tilde{y}(t) = \sum_{i=1}^{(L+1)/2} \tilde{c}_{2i-1} \tilde{s}(t) |\tilde{s}(t)|^{2i-2} \tag{4.18}$$

where L and $\tilde{c}_i$ represent the nonlinearity order and its coefficients, respectively, followed by an AWGN source represented by $\tilde{n}(t)$.

By substituting (4.16) in (4.18), the complex envelope of the output of the bandpass nonlinearity is then given by

$$\begin{aligned}\tilde{y}(t) = & \frac{\tilde{c}_1}{(T-T_{CP})^0} \sum_{k=-\infty}^{+\infty} \sum_{n_1=0}^{N-1} S_{k,n_1} g_{n_1}(t-kT) \\ & + \frac{\tilde{c}_3}{(T-T_{CP})^1} \sum_{k=-\infty}^{+\infty} \sum_{n_1=0}^{N-1} \sum_{n_2=0}^{N-1} \sum_{n_3=0}^{N-1} S_{k,n_1} S_{k,n_2} S^*_{k,n_3} g_{n_1+n_2-n_3}(t-kT) \\ & + \cdots \\ & + \sum_{k=-\infty}^{\infty} \frac{\tilde{c}_L}{(T-T_{CP})^{(L-1)/2}} \sum_{n_1=0}^{N-1} \cdots \sum_{n_L=0}^{N-1} S_{k,n_1} \cdots S_{k,n_1} \cdots S_{k,n_{(L+1)/2}} \\ & \times S^*_{k,n_{(L+3)/2}} \cdots S^*_{k,n_L} g_{n_1+\cdots+n_{(L+1)/2}-n_{(L+3)/2}-\cdots-n_L}(t-kT)\end{aligned} \tag{4.19}$$

We are now ready to derive the structure of the linear MMSE receiver for nonlinearly distorted OFDM signals. To do so, and taking in consideration that the transmitted symbols in time slot k_1 are independent of the ones in time slot k_2, with $k_1 \neq k_2$, (4.19) is used to obtain the integrals and expected values in the RHS and LHS of (4.14), respectively[1],

$$\begin{aligned}& \mathrm{E}\left[S_{k,n}\ \tilde{y}^*(t_k-t)\right] \\ & \quad = \frac{\tilde{c}_1^*}{(T-T_{CP})^0} \sum_{n_1} \mathrm{E}\left[S_{k,n} S^*_{k,n_1}\right] g^*_{n_1}(t_0-t) \\ & \quad + \frac{\tilde{c}_3^*}{(T-T_{CP})^1} \sum_{n_1} \sum_{n_2} \sum_{n_3} \mathrm{E}\left[S_{k,n} S^*_{k,n_1} S^*_{k,n_2} S_{k,n_3}\right] g^*_{n_1+n_2-n_3}(t_0-t) \\ & \quad + \cdots\end{aligned} \tag{4.20}$$

and

[1]The summation operators will now be simplified in order to make their representation easier. Therefore, the following summation operators are equivalent: $\sum_{n_i} \equiv \sum_{n_i=0}^{N-1}$ and $\sum_k \equiv \sum_{k=-\infty}^{\infty}$.

$$
\begin{aligned}
&\int_{-\infty}^{+\infty} u_n(\tau')\mathrm{E}\left[\tilde{y}^*(t_k-\tau)\tilde{y}(t_k-\tau')\right]d\tau' \\
&= \frac{\tilde{c}_1\tilde{c}_1^*}{(T-T_{CP})^0}\sum_{n_1}\sum_{n_2}\mathrm{E}\left[S_{k,n_1}S_{k,n_2}^*\right] \\
&\quad \times g_{n_2}^*(t_0-\tau)\int_{-\infty}^{+\infty} u_n(\tau')g_{n_1}(t_0-\tau')d\tau' \\
&\quad + \frac{\tilde{c}_3\tilde{c}_1^*}{(T-T_{CP})^1}\sum_{n_1}\sum_{n_2}\sum_{n_3}\sum_{n_4}\mathrm{E}\left[S_{k,n_1}S_{k,n_2}S_{k,n_3}^*S_{k,n_4}^*\right] \\
&\quad \times g_{n_4}^*(t_0-\tau)\int_{-\infty}^{\infty} u_n(\tau')g_{n_1+n_2-n_3}(t_0-\tau')d\tau' \\
&\quad + \frac{\tilde{c}_1\tilde{c}_3^*}{(T-T_{CP})^1}\sum_{n_1}\sum_{n_2}\sum_{n_3}\sum_{n_4}\mathrm{E}\left[S_{k,n_1}S_{k,n_2}^*S_{k,n_3}^*S_{k,n_4}\right] \\
&\quad \times g_{n_2+n_3-n_4}^*(t_0-\tau)\int_{-\infty}^{+\infty} u_n(\tau')g_{n_1}(t_0-\tau')d\tau' \\
&\quad + \frac{\tilde{c}_3\tilde{c}_3^*}{(T-T_{CP})^2}\sum_{n_1}\sum_{n_2}\sum_{n_3}\sum_{n_4}\sum_{n_5}\sum_{n_6}\mathrm{E}\left[S_{k,n_1}S_{k,n_2}S_{k,n_3}^*S_{k,n_4}^*S_{k,n_5}^*S_{k,n_6}\right] \\
&\quad \times g_{n_4+n_5-n_6}^*(t_0-\tau)\int_{-\infty}^{+\infty} u_n(\tau')g_{n_1+n_2-n_3}(t_0-\tau')d\tau' \\
&\quad + \cdots, \quad n=0,1,\cdots,N-1
\end{aligned}
\tag{4.21}
$$

Note that the expression

$$
\int_{-\infty}^{+\infty} u_n(\tau')g_m(t_0-\tau')d\tau', \quad \forall n,m \tag{4.22}
$$

in (4.21) also represents the inner product between $u_n^*(t)$ and $g_m(t_0-t)$. In fact, by choosing an appropriate set of impulse responses $u_n(t)$, the integral expression in (4.22) can also be seen as the orthonormal condition given by (2.5) and be simplified. Assuming that the nonlinearity exhibits nonlinear behavior of maximum order L (L is odd) and by letting $u_n(t)$ be given by a summation of $L(N-1)+1$ functions[2] of $g_i^*(t_0-t)$ affected by a constant coefficient $\alpha_{i,n}$, i.e.,

$$
u_n(t) = \sum_{i=i_{min}}^{i_{max}} \alpha_{i,n} g_i^*(t_0-t) \tag{4.23}
$$

[2] A set of $L(N-1)+1$ functions was chosen because it extracts the sufficient statistics of the nonlinearly distorted OFDM signal (see section 3.3.1).

where $i_{min} = -1/2(L-1)(N-1)$ and $i_{max} = 1/2(L+1)(N-1)$, the integral in (4.22) reduces to a summation of inner products given by

$$\begin{aligned}
&\int_{-\infty}^{+\infty} \left[\sum_{i=i_{min}}^{i_{max}} \alpha_{i,n} g_i^*(t_0-\tau') \right] g_m(t_0-\tau') d\tau' \\
&\quad = \sum_{i=i_{min}}^{i_{max}} \alpha_{i,n} \int_{kT+T_{CP}}^{(k+1)T} g_i^*(t_0-\tau') g_m(t_0-\tau') d\tau' \\
&\quad = \sum_{i=i_{min}}^{i_{max}} \alpha_{i,n} \delta(i-m), \quad m = -1/2(L-1)(N-1), \cdots, 1/2(L+1)(N-1)
\end{aligned} \tag{4.24}$$

Substituting (4.24) in (4.21), the LHS of (4.14) becomes

$$\begin{aligned}
&\int_{-\infty}^{+\infty} u_n(\tau') E\left[\tilde{y}^*(t_k-\tau)\tilde{y}(t_k-\tau')\right] d\tau' + 2N_0 u_n(\tau) \\
&= \sum_{i=i_{min}}^{i_{max}} \alpha_{i,n} \frac{\tilde{c}_1 \tilde{c}_1^*}{(T-T_{CP})^0} \sum_{n_1} \sum_{n_2} \mathrm{E}\left[S_{k,n_1} S_{k,n_2}^*\right] g_{n_2}^*(t_0-\tau)\delta(i-n_1) \\
&\quad + \sum_{i=i_{min}}^{i_{max}} \alpha_{i,n} \frac{\tilde{c}_3 \tilde{c}_1^*}{(T-T_{CP})^1} \sum_{n_1} \sum_{n_2} \sum_{n_3} \sum_{n_4} \mathrm{E}\left[S_{k,n_1} S_{k,n_2} S_{k,n_3}^* S_{k,n_4}^*\right] \\
&\quad \times g_{n_4}^*(t_0-\tau)\delta(i-n_1-n_2+n_3) \\
&\quad + \sum_{i=i_{min}}^{i_{max}} \alpha_{i,n} \frac{\tilde{c}_1 \tilde{c}_3^*}{(T-T_{CP})^1} \sum_{n_1} \sum_{n_2} \sum_{n_3} \sum_{n_4} \mathrm{E}\left[S_{k,n_1} S_{k,n_2}^* S_{k,n_3}^* S_{k,n_4}\right] \\
&\quad \times g_{n_2+n_3-n_4}^*(t_0-\tau)\delta(i-n_1) \\
&\quad + \sum_{i=i_{min}}^{i_{max}} \alpha_{i,n} \frac{\tilde{c}_3 \tilde{c}_3^*}{(T-T_{CP})^2} \sum_{n_1} \sum_{n_2} \sum_{n_3} \sum_{n_4} \sum_{n_5} \sum_{n_6} \mathrm{E}\left[S_{k,n_1} S_{k,n_2} S_{k,n_3}^* S_{k,n_4}^* S_{k,n_5}^* S_{k,n_6}\right] \\
&\quad \times g_{n_4+n_5-n_6}^*(t_0-\tau)\delta(i-n_1-n_2+n_3) \\
&\quad + \cdots + \sum_{i=i_{min}}^{i_{max}} 2N_0 \alpha_{i,n} g_i^*(t_0-\tau), \quad n = 0, 1, \cdots, N-1
\end{aligned} \tag{4.25}$$

By combining the LHS and RHS of (4.14) given by (4.25) and (4.20), respectively, we can now write the integral equation as

$$\sum_{i=i_{min}}^{i_{max}} \alpha_{i,n} \mathrm{E}\left[Y_{k,i} Y_{k,m}^*\right] + 2N_0 \alpha_{m,n} = \mathrm{E}\left[S_{k,n} Y_{k,m}^*\right] \tag{4.26}$$

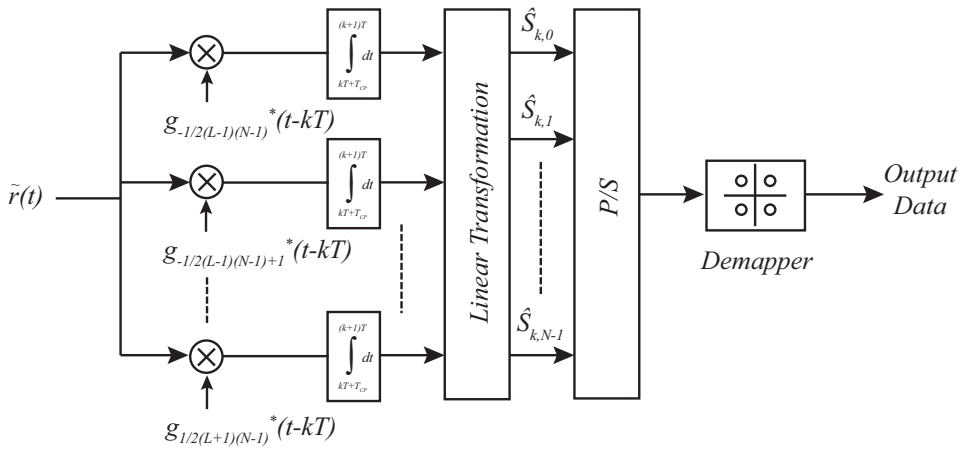

FIGURE 4.3: Alternative structure of the MMSE OFDM receiver.

for $m = -1/2(L-1)(N-1), \cdots, 1/2(L+1)(N-1)$, where the RV $Y_{k,i}$ is given by (3.24).

The impulse responses coefficients $\alpha_{i,n}$ can now be obtained by solving (4.26). In order to simplify the representation of the set of linear equations, we can aggregate and write them as matrices. Thus, by considering vectors $\mathbf{S}_k = [S_{k,0}, \cdots, S_{k,N-1}]^T$, $\mathbf{Y}_k = \left[Y_{k,-1/2(L-1)(N-1)}, \cdots, Y_{k,1/2(L+1)(N-1)}\right]^T$ and the identity matrix of size $L(N-1)+1$, $\mathbf{I}_{[L(N-1)+1]}$, we observe that the N impulse responses, $u_n(t)$, can be determined by simply finding the $[L(N-1)+1] \times N$ elements of the matrix of coefficients $\alpha_{i,n}$, $\mathbf{M}_\alpha$, given by

$$\mathbf{M}_\alpha \equiv [\alpha_{i,n}]_{i,n} = \left[\mathrm{E}\left[\mathbf{Y}_k \mathbf{Y}_k^H\right] + 2N_0 \mathbf{I}_{[L(N-1)+1]}\right]^{-1} \mathrm{E}\left[\mathbf{Y}_k^* \mathbf{S}_k^T\right] \tag{4.27}$$

The estimate of the vector of transmitted symbols, $\hat{\mathbf{S}}_k$, can be obtained by convolution of $\tilde{r}(t)$ and $u_n(t)$ or, equivalently, by simply applying a linear transformation to the sufficient statistics vector, i.e.,

$$\hat{\mathbf{S}}_k = \mathbf{M}_\alpha^T \mathbf{R}_k \tag{4.28}$$

Interestingly, we can appreciate the architecture of the linear MMSE receiver for nonlinearly distorted OFDM signals corrupted by AWGN from two view points. On the one hand, we can see the MMSE receiver as consisting of a set of linear filters given by (4.23) and (4.27) (see also Figure 4.1). On the other hand, we can see the linear MMSE receiver as consisting of two stages (see Figure 4.3): the first stage consists of a set of correlators or a set of filters matched to every possible frequency component in the nonlinearly distorted OFDM signal. This stage computes the set of sufficient

statistics. The second stage is a simple linear transformation which is solely defined by the coefficients in (4.27). In this sense, the architecture of the linear MMSE receiver is identical to the architectures of the maximum likelihood receiver derived in chapter 3 where the ML detector is substituted by the linear transformation and the decision devices.

Let us now focus on how to analytically determine the elements of $\mathbf{M}_\alpha$ given by (4.27).

4.3.1 Analytical computation of the matrix $\mathbf{M}_\alpha$

In order to obtain the matrix of coefficients $\mathbf{M}_\alpha$ given by (4.27), it is necessary to derive the expectation values of $\mathrm{E}\left[\mathbf{Y}_k\mathbf{Y}_k^H\right]$ and $\mathrm{E}\left[\mathbf{Y}_k^*\mathbf{S}_k^T\right]$.

The expectation value $\mathrm{E}\left[\mathbf{Y}_k\mathbf{Y}_k^H\right]$ is a square matrix of size $L(N-1)+1$ and its elements are given by

$$
\begin{aligned}
\mathrm{E}\left[Y_{k,i}Y_{k,m}^*\right] = & \frac{|c_1|^2}{(T-T_{CP})^0}\sum_{n_1}\sum_{n_2}\mathrm{E}\left[S_{k,n_1}S_{k,n_2}^*\right]\delta(i-n_1)\delta(m-n_2) \\
& + \frac{c_1c_3^*}{(T-T_{CP})^2}\sum_{n_1}\sum_{n_2}\sum_{n_3}\sum_{n_4}\mathrm{E}\left[S_{k,n_1}S_{k,n_2}^*S_{k,n_3}^*S_{k,n_4}\right] \\
& \times\delta(i-n_1)\delta(m-n_2-n_3+n_4) \\
& + \frac{c_3c_1^*}{(T-T_{CP})^2}\sum_{n_1}\sum_{n_2}\sum_{n_3}\sum_{n_4}\mathrm{E}\left[S_{k,n_1}S_{k,n_2}S_{k,n_3}^*S_{k,n_4}^*\right] \\
& \times\delta(i-n_1-n_2+n_3)\delta(m-n_4) \\
& + \frac{|c_3|^2}{(T-T_{CP})^4}\sum_{n_1}\sum_{n_2}\sum_{n_3}\sum_{n_4}\sum_{n_5}\sum_{n_6}\mathrm{E}\left[S_{k,n_1}S_{k,n_2}S_{k,n_3}^*S_{k,n_4}^*S_{k,n_5}^*S_{k,n_6}\right] \\
& \times\delta(i-n_1-n_2+n_3)\delta(m-n_4-n_5+n_6) \\
& + \cdots
\end{aligned}
\tag{4.29}
$$

Similarly, the expectation value $\mathrm{E}\left[\mathbf{Y}_k^*\mathbf{S}_k^T\right]$ is a matrix with elements given by

$$\begin{aligned}\mathrm{E}\left[S_{k,n}Y_{k,m}^*\right] = & \frac{c_1^*}{(T-T_{CP})^0}\sum_{n_1}\mathrm{E}\left[S_{k,n}S_{k,n_1}^*\right]\delta(m-n_1) \\ & + \frac{c_3^*}{(T-T_{CP})^1}\sum_{n_1}\sum_{n_2}\sum_{n_3}\mathrm{E}\left[S_{k,n}S_{k,n_1}^*S_{k,n_2}^*S_{k,n_3}\right] \\ & \times\delta(m-n_1-n_2+n_3) \\ & + \cdots\end{aligned} \tag{4.30}$$

It can be seen that these expressions reduce to the computation of the summation of expectations of products of equiprobable symbols S_{k,n_i}.

Taking into consideration that the transmitted symbols conveyed in a specific subcarrier are independent of the ones conveyed by the remain subcarriers[3], the expectations in (4.29) and (4.30) can be simplified using the multiplicative property of the expected value for the product of independent RVs

$$\mathrm{E}\left[S_{k,n_1}\cdots S_{k,n_i}S_{k,n_1}^*\cdots S_{k,n_m}^*\right] = \prod_{n=0}^{N-1}\mathrm{E}\left[(S_{k,n})^{a_n}(S_{k,n}^*)^{b_n}\right], \quad \forall i,m \tag{4.31}$$

where a_n and b_n denote the number of elements of the form $S_{k,n}$ and $S_{k,n}^*$, respectively.

Considering equiprobable symbols from a M-PSK constellation schemes of the set $\left\{Ae^{j\left(\pi\frac{2i+1}{M}-\pi/2\right)}\right\}$ for $i=0,1,\cdots,M-1$, where M denotes the size of the constellation, the expectation values are given by [84]

$$\mathrm{E}\left[(S_{k,n})^{a_n}(S_{k,n}^*)^{b_n}\right] = \begin{cases} A^{a_n+b_n}, & \text{if } a_n-b_n=\pm 2iM, \quad i=0,1,\cdots \\ -A^{a_n+b_n}, & \text{if } a_n-b_n=\pm(2i+1)M, \quad i=0,1,\cdots \\ 0, & \text{otherwise}\end{cases} \tag{4.32}$$

For M-QAM constellation schemes with equally likely symbols taken from an alphabet given by $\left\{\pm(2i+1)A\pm j(2k+1)A;\ i,k=0,1,\cdots,\sqrt{M}/2-1\right\}$, where M denotes the size of the constellation, a generic expression is not derived since it is dependent on M. Nonetheless, for the specific case of a 16-QAM constellation, the expectations in the

[3]Note that when coding/decoding operations are present, the complex symbols conveyed by different subcarriers may not be independent. In our analysis, we do not consider coded OFDM signals.

RHS (4.31) are given by

$$\begin{aligned}\mathrm{E}\left[(S_{k,n})^{a_n}(S_{k,n}^*)^{b_n}\right] = \frac{1}{4}A^{a_n+b_n}\Big\{&\left(\sqrt{2}\right)^{a_n+b_n}\cos\left[(a_n-b_n)\arctan(1/1)\right]\\ &+\left(\sqrt{10}\right)^{a_n+b_n}\cos\left[(a_n-b_n)\arctan(1/3)\right]\\ &+\left(\sqrt{10}\right)^{a_n+b_n}\cos\left[(a_n-b_n)\arctan(3/1)\right]\\ &+\left(\sqrt{18}\right)^{a_n+b_n}\cos\left[(a_n-b_n)\arctan(3/3)\right]\Big\}\end{aligned} \tag{4.33}$$

if $a_n - b_n = \pm 2i, i = 0, 1, \cdots$, and zero otherwise.

By observing (4.32) and (4.33), we can note that the expected value of a product of equiprobable symbols equals zero when $a_n - b_n$ is odd. This result indicates that the expected value of RV $Y_{k,n}$, i.e., its mean, is zero for all n. Therefore, the expectation values given by (4.29) and (4.30) can be seen as the covariance matrix of RV vector $\mathbf{Y}_k$ and the cross-covariance of RV vector $\mathbf{Y}_k$ and $\mathbf{S}_k$, respectively. Note that the computation complexity of the analytical derivation of the matrix of coefficients $\mathbf{M}_\alpha$ and, consequently, the impulse responses of the linear filters $u_n(t)$ increases with the number of OFDM subcarriers, N, the size of the constellation, M, and the nonlinear order of the channel, L.

To identify the operating point of a nonlinear element it is common to use the power back-off (BO). This well known parameter can be defined at the output (OBO) or input (IBO) of the given nonlinear element by, respectively, [33]

$$\text{OBO [dB]} = 10\log_{10}\left(\frac{P_{out,max}}{P_{out,0}}\right) \tag{4.34}$$

$$\text{IBO [dB]} = 10\log_{10}\left(\frac{P_{in,max}}{P_{in,0}}\right) \tag{4.35}$$

where $P_{out,max}$ and $P_{out,0}$ are the maximum power and the average output signal power, respectively, of the nonlinear channel under consideration. Similarly, $P_{in,max}$ and $P_{in,0}$ are the input power corresponding to the maximum output power and the average power of the signal at the input. The BO measure is associated with the degree of nonlinear strength, i.e., for high BO values the impact of the nonlinearity in the signal is low and vice-versa.

The maximum power at the output of the nonlinear element was determined by

injecting a sinusoidal signal with amplitude A into the nonlinearity and filtering its output to eliminate all harmonics but the one that fall at the fundamental frequency. Then, by varying its amplitude A, a local maximum of the output power was found. Analytically this local maximum is found by differentiating the expression for the output power of the sinusoidal signal [97]. The input amplitude that originates the maximum output power, $A_{[P_{out,max}]}$, and its correspondent maximum input and output powers are given by

$$A_{[P_{out,max}]} = \sqrt{-\frac{4c_1}{9c_3}} \Rightarrow \begin{cases} P_{in,max} = -\dfrac{2c_1}{9c_3} \\ P_{out,max} = -\dfrac{8c_1^3}{81c_3} \end{cases} \tag{4.36}$$

In order to validate the MMSE receiver model described above we have used Matlab/C++ as a calculator to solve and to compute the analytical expressions for the expectation values given by (4.29) and (4.30), as well as the linear transformation $\mathbf{M}_\alpha$ given by (4.27). To do so, we have considered OFDM signals with parameters $T = 4\,\mu$s and $T_{CP} = 800\,$ns and a third-order nonlinear channel characteristic given by (3.21) with polynomial coefficients given by $c_1 = 1$, $c_2 = 0$, $c_3 = -0.20$ and $c_i = 0$ for $i > 3$. Note that the following analysis can be performed considering different OFDM parameters, nonlinear channel orders and also AM/PM distortion.

The covariance of two RVs is a measure of how they change together. When the covariance is equal to zero, it is said that RVs are uncorrelated. Nevertheless, two RVs that are said to be uncorrelated are not necessarily statistically independent. Orthogonal condition is assured if the expected value of the product of two RVs equals zero [69]. Since the RV vectors under study, $\mathbf{Y}_k$ and $\mathbf{S}_k$, have zero mean, the zero-valued elements of the (cross-)covariance matrices indicate that the RVs are both uncorrelated and orthogonal.

For representative purposes, OFDM/BPSK signals with 16 subcarriers and a relatively low output back-off (OBO) value of 2 dB was considered. In Figure 4.4 it is depicted the matrix $\mathrm{E}\left[\mathbf{Y}_k\mathbf{Y}_k^H\right]$ that represents the covariance matrix of the vector $\mathbf{Y}_k$. For a better understanding of the results, a parameterized version is also plotted in Figure 4.5. Note that, it is possible to divide the covariance matrix elements in three main groups. The first, and the most expressive, is the one given by elements $\mathrm{E}\left[Y_{k,i}Y_{k,i}^*\right]$ for $i = 0, \cdots, N-1$ which represent the variance of RV $Y_{k,i}$. Note that these RVs are the ones extracted using the bank of N correlators that match the original signal frequency

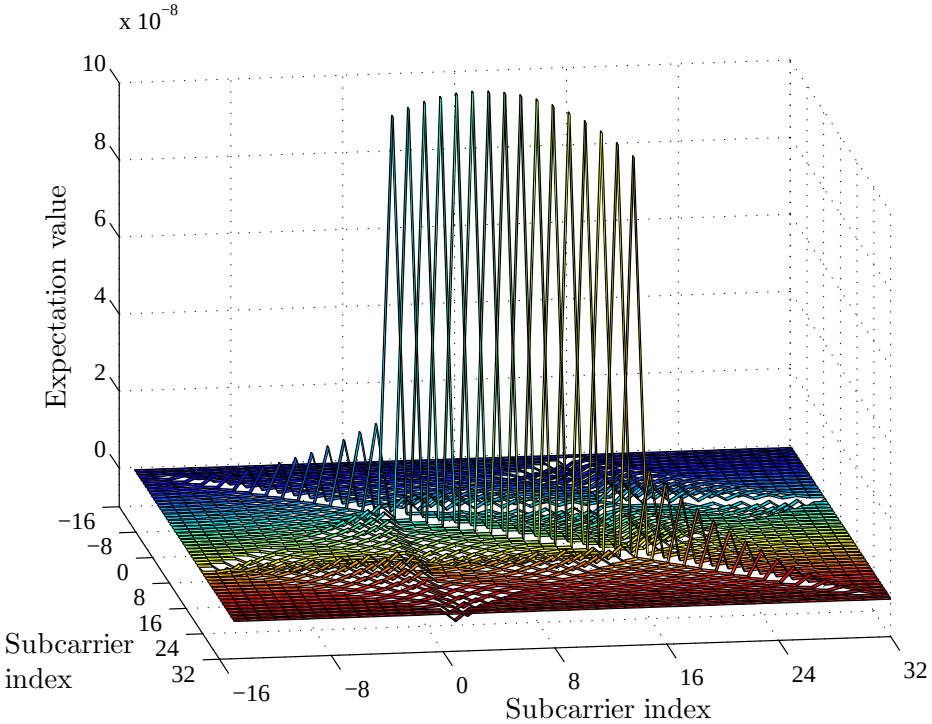

FIGURE 4.4: Covariance matrix of the vector $\mathbf{Y}_k$ for OFDM/BPSK signals with 16 subcarriers and an OBO value of 2 dB.

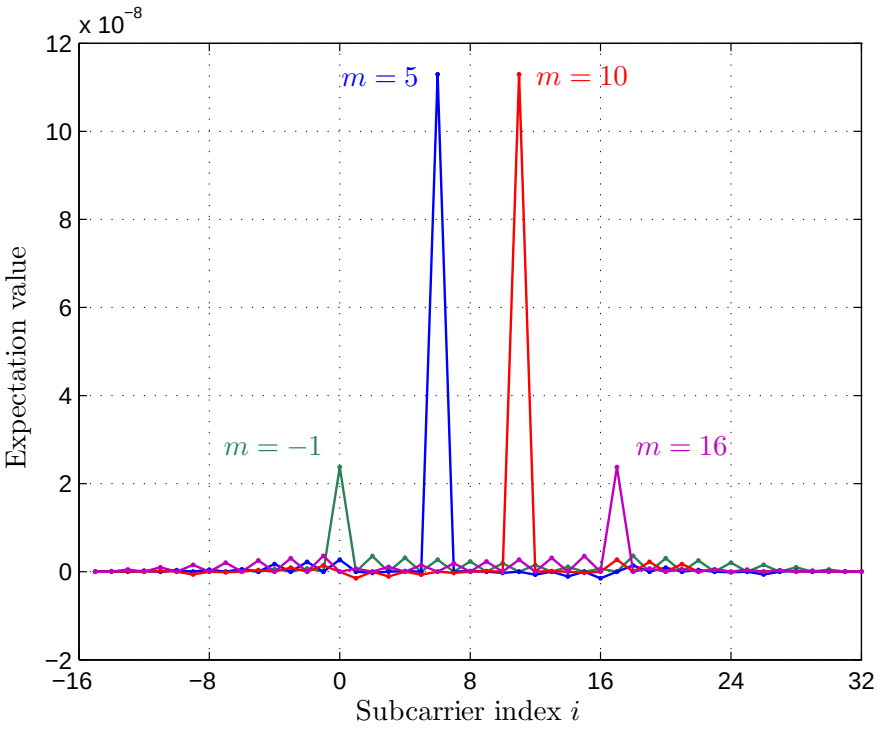

FIGURE 4.5: Expectation values $\mathrm{E}\left[Y_{k,i}Y^*_{k,m}\right]$, with $i = -15, \cdots, 30$ and parameterized in m, for OFDM/BPSK signals with 16 subcarriers and an OBO value of 2 dB.

components. It can be seen that the variance of RVs with indexes near the center is higher than the variance of the ones at the edge. This expected result can be justified by the fact that the number of IMPs generated by the nonlinearity is higher at the center of the signal's bandwidth, thus increasing its variance. The second group is composed by elements $\mathrm{E}\left[Y_{k,i}Y_{k,i}^*\right]$ for $i = -1/2(L-1)(N-1), \cdots, -1$ and $i = N, \cdots, 1/2(L+1)(N-1)$. These elements represent the variance of IMPs components that are out-of-band. The third group of elements are the remaining covariance elements given by $\mathrm{E}\left[Y_{k,i}Y_{k,m}^*\right]$ for $i, m = -1/2(L-1)(N-1), \cdots, 1/2(L+1)(N-1)$ and $i \neq m$. Note that the second and third group have non-zero elements only due to the existence of the nonlinear channel and the IMPs that fall in and outside the signal's bandwidth. By definition, these non-zero covariance elements indicate that these complex received symbols are no longer uncorrelated.

Similarly, in Figures 4.6 and 4.7 it is depicted the cross-covariance matrix of the vectors $\mathbf{Y}_k$ and $\mathbf{S}_k$. From this result it can be seen that the cross-covariance between a given transmitted symbol in subcarrier n and a received symbol in subcarrier i is maximum when $i = n$. Due to IMPs generated by the nonlinearity, there are also non-zero expectation values for $i \neq n$.

To obtain the linear transformation given by matrix $\mathbf{M}_\alpha$ in (4.27) it is assumed that the AWGN PSD level is known and equal to N_0. A representation of the matrix composed by the α values is given in Figure 4.8. Here we have considered $N_0 = 6.3 \times 10^{-9}$ W/Hz which corresponds to an SNR per bit of 10 dB. By combining a conventional OFDM receiver with the capability to extract a set of sufficient statistics and the linear transformation given by matrix $\mathbf{M}_\alpha$, an estimate of the transmitted vector that minimizes the overall MSE is obtained.

It is important to note that if other polynomial coefficients are considered, the covariance values are also expected to change, i.e., for stronger nonlinearities (higher $|c_3/c_1|$ ratios) it is expected higher covariance values. Yet, as it can be seen from (4.29) and (4.30), the indexes responsible for zero (or non-zero) covariance elements remain unchanged since it only depends on the expectation value of the product of complex transmitted symbols S_{k,n_i}.

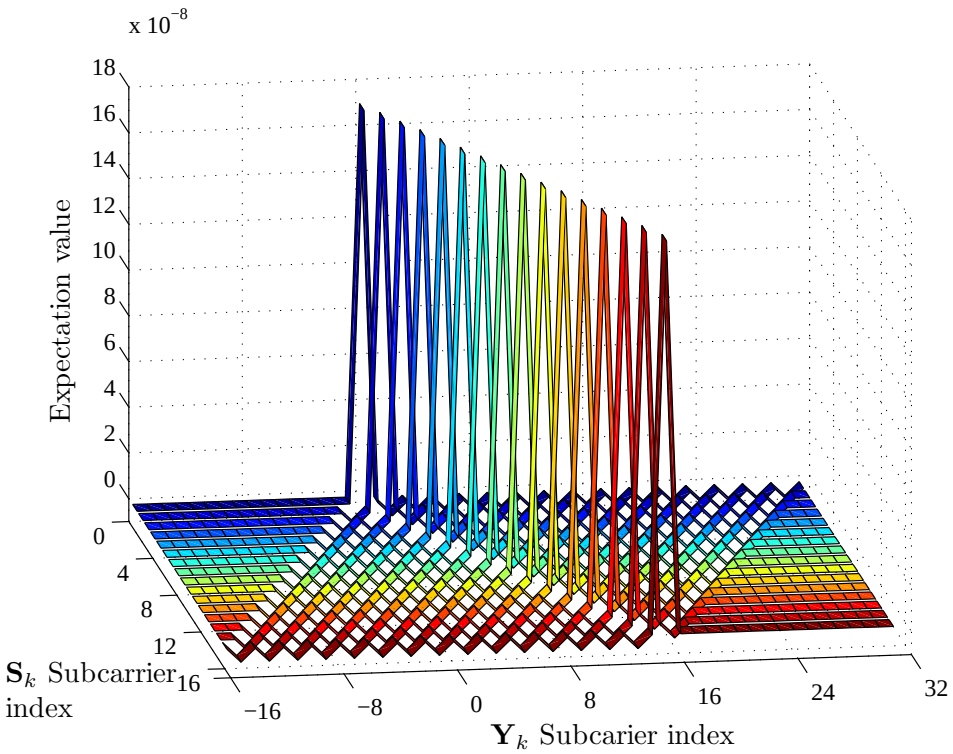

FIGURE 4.6: Cross-covariance matrix of the vectors $\mathbf{Y}_k$ and $\mathbf{S}_k$ for OFDM/BPSK signals with 16 subcarriers and an OBO value of 2 dB.

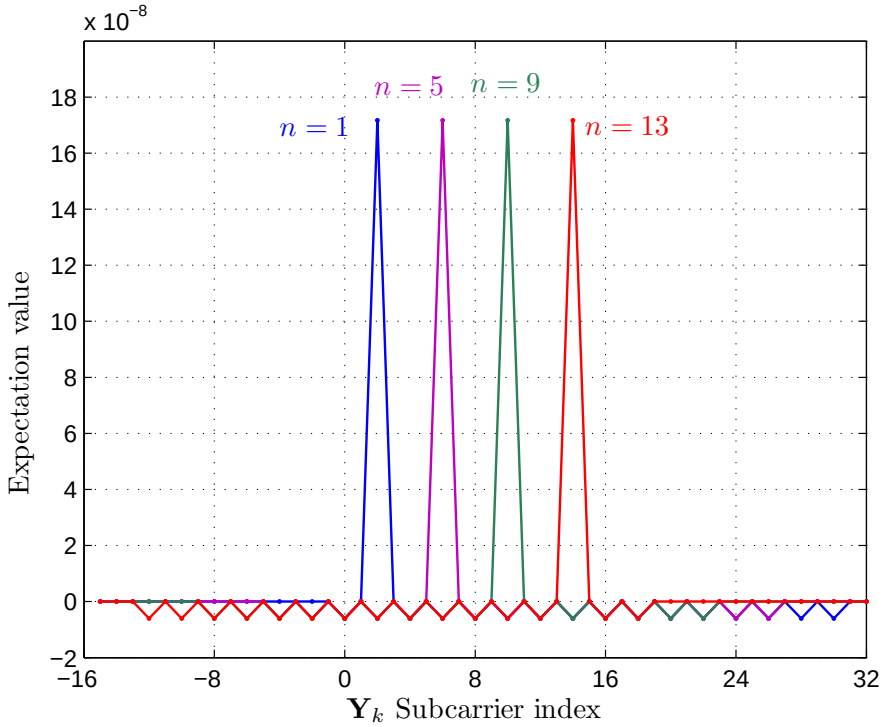

FIGURE 4.7: Expectation values $\mathrm{E}\left[S_{k,n}Y^*_{k,m}\right]$, with $m = -15, \cdots, 30$ and parameterized in n, for OFDM/BPSK signals with 16 subcarriers and an OBO value of 2 dB.

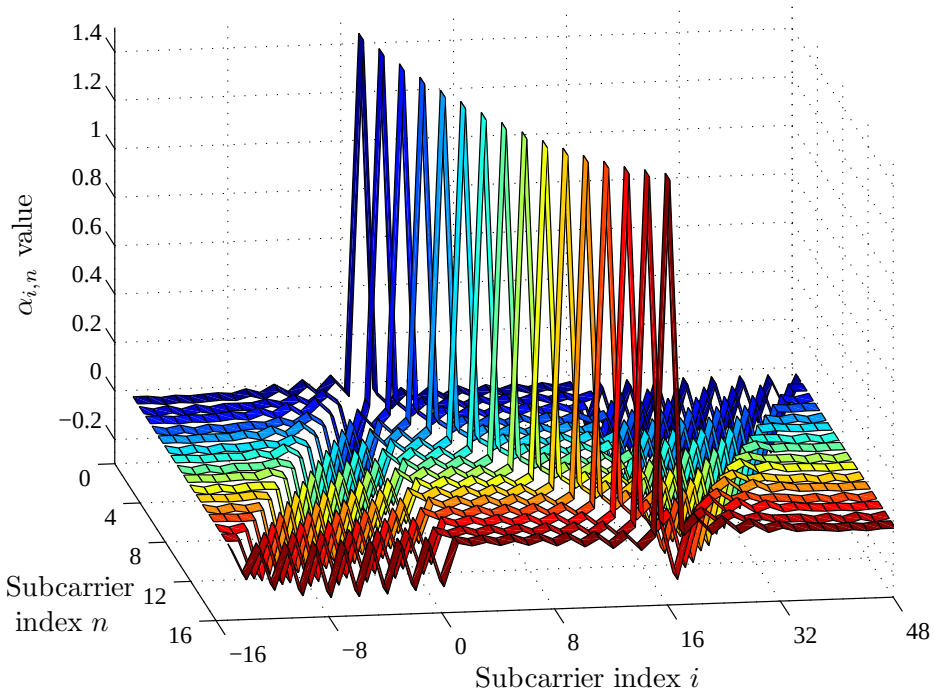

FIGURE 4.8: Matrix of coefficients α for OFDM/BPSK signals with 16 subcarriers, an OBO value of 2 dB and considering AWGN PSD $N_0 = 6.3 \times 10^{-9}$ W/Hz.

4.4 Performance evaluation

In order to evaluate the MMSE structure derived above, we have used analytical expressions for the MSE when a conventional receiver is considered and also the ones for the minimum MSE. For comparison purposes we have also obtained simulation results through Monte Carlo techniques.

For a conventional OFDM receiver, the analytical MSE expression for subcarrier n before the demapper block is obtained by considering $\hat{\mathbf{S}}_k = \mathbf{R}_k$ in (4.4) and is given by

$$\xi_n^{conv} = \mathrm{E}\left[|S_{k,n}|^2\right] + \mathrm{E}\left[|Y_{k,n}|^2\right] + 2N_0 - 2\Re\left\{\mathrm{E}\left[S_{k,n}Y_{k,n}^*\right]\right\} \tag{4.37}$$

whereas for the linear MMSE equalizer, the analytical minimum MSE expression for subcarrier n is obtained by considering $\hat{\mathbf{S}}_k = \mathbf{M}_\alpha^T \mathbf{R}_k$ and is given by

$$\begin{aligned}\xi_n^{min} = \mathrm{E}\left[|S_{k,n}|^2\right] &+ \sum_i \sum_l \alpha_{i,n}\alpha_{l,n}^* \mathrm{E}\left[Y_{k,i}Y_{k,l}^*\right] \\ &+ 2N_0 \sum_i |\alpha_{i,n}|^2 - 2\Re\left\{\sum_l \alpha_{l,n}^* \mathrm{E}\left[S_{k,n}Y_{k,l}^*\right]\right\}\end{aligned} \tag{4.38}$$

where all summations run from $-1/2(L-1)(N-1)$ to $1/2(L+1)(N-1)$. The total MSE in both cases is computed by simply performing the summation of (4.37) and (4.38) for $n = 0, 1, \cdots, N-1$ and adding.

We have considered OFDM/M-PSK and OFDM/16-QAM signals with different number of subcarriers and the following parameters: $T = 4\,\mu$s, $T_{CP} = 800\,$ns. The nonlinearity was chosen to be a third-order nonlinearity given by (3.21) with polynomial coefficients given by $c_1 = 1$, $c_2 = 0$, $c_3 = -0.20$ and $c_i = 0$ for $i > 3$. Simulation results were obtained using Matlab/C++ through Monte Carlo techniques. Analytical results were computed using Matlab/C++ as a numerical calculator.

Figure 4.9 shows the MSE as a function of the OBO for OFDM/BPSK signals with 16 subcarriers for two AWGN PSD levels. Both simulation and analytical results are verified to be in good agreement. As expected, both MSE curves decrease as the OBO increases. This behavior is even more pronounced for the lowest AWGN PSD level. In this case, the nonlinear noise is dominant, therefore, as the OBO increases, the overall noise level decreases.

In Figure 4.10 it is depicted the MSE for different SNR per bit values and OFDM constellation schemes for OFDM signals with 16 subcarriers. Again, results show that MSE values for both receivers decrease as the SNR per bit increases. Results also show that the minimum MSE decreases even more rapidly, which may suggest an increase of performance for the MMSE receiver. Yet, both minimum MSE and the MSE given by a conventional receiver tend to a given value except the ones for the minimum MSE case and OFDM/BPSK modulation scheme, which continue decaying beyond the SNR per bit of 18 dB. This result suggests that for this OBO value the total MSE is mainly due to IMD for SNR per bit values higher than 18 dB and that the MMSE receiver for OFDM/BPSK signals is actually capable of reducing it beyond that level.

In order to understand how both MSE of conventional receiver and minimum MSE decay with the size of constellation, it is represented in Figure 4.11 its relation considering two OBO values.

In Figure 4.12 it is depicted the MSE as a function of the number of subcarriers for OFDM/BPSK signals for an SNR per bit of 20 dB and considering different OBO values. Overall results show that both minimum MSE and MSE associated with the

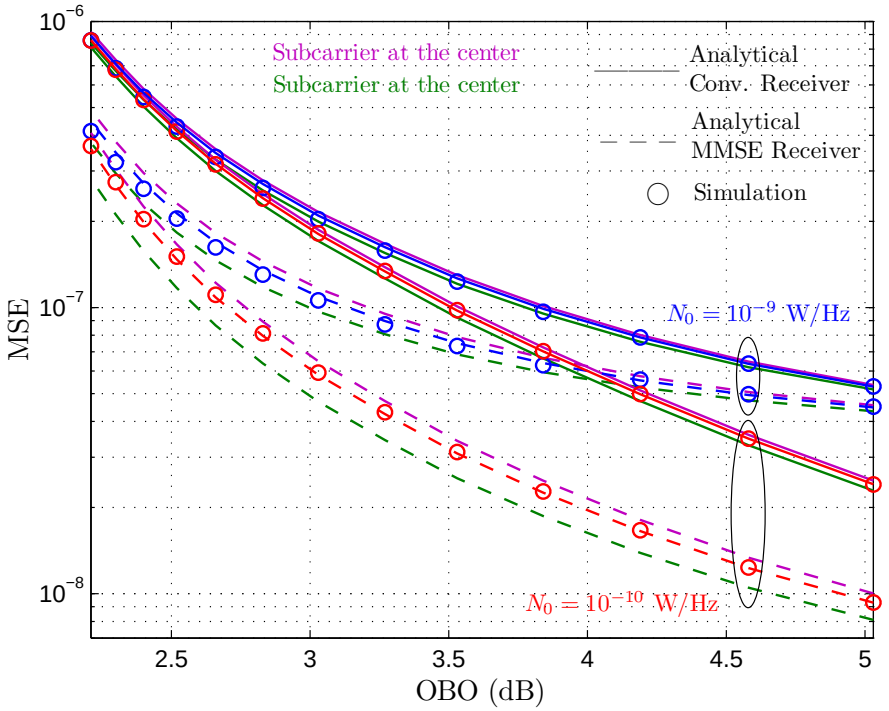

FIGURE 4.9: Analytical and simulated mean-squared errors as function of OBO for OFDM/BPSK signals with 16 subcarriers and for two AWGN PSD levels.

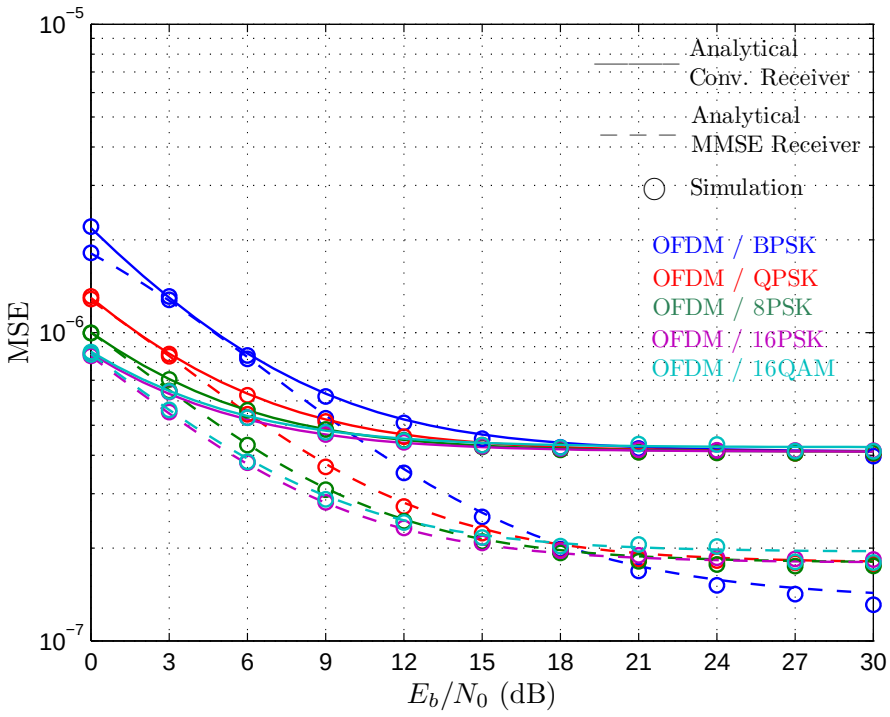

FIGURE 4.10: Analytical and simulated mean-squared errors as function of the SNR per bit for OFDM/M-PSK and OFDM/16QAM signals with 16 subcarriers for an OBO value of 2.5 dB.

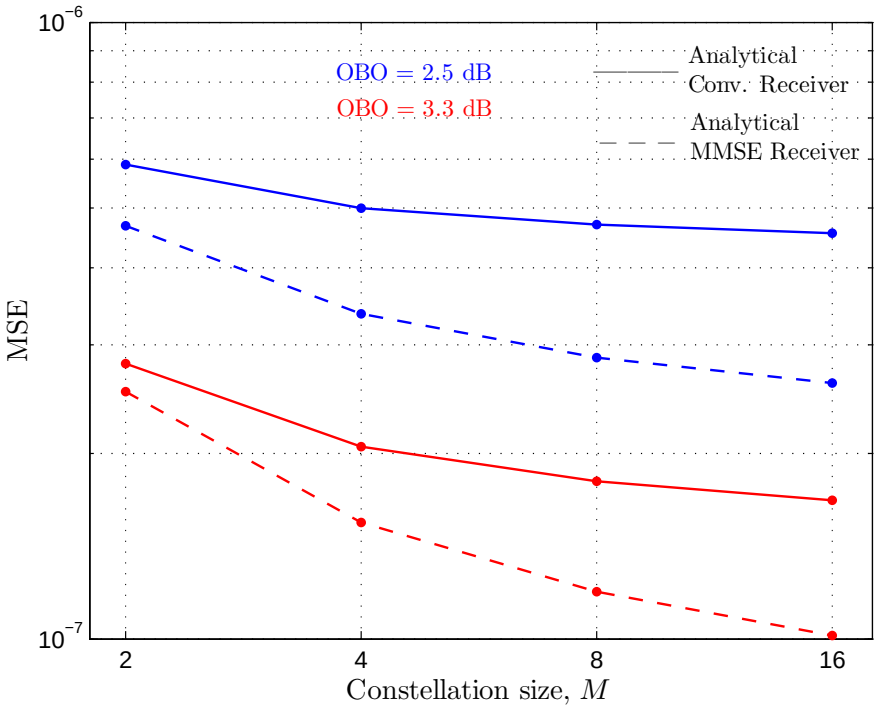

FIGURE 4.11: Analytical mean-squared errors as a function of the size of constellation, M, for OFDM/M-PSK signals with 16 subcarriers, a SNR per bit of 10 dB and for two OBO values.

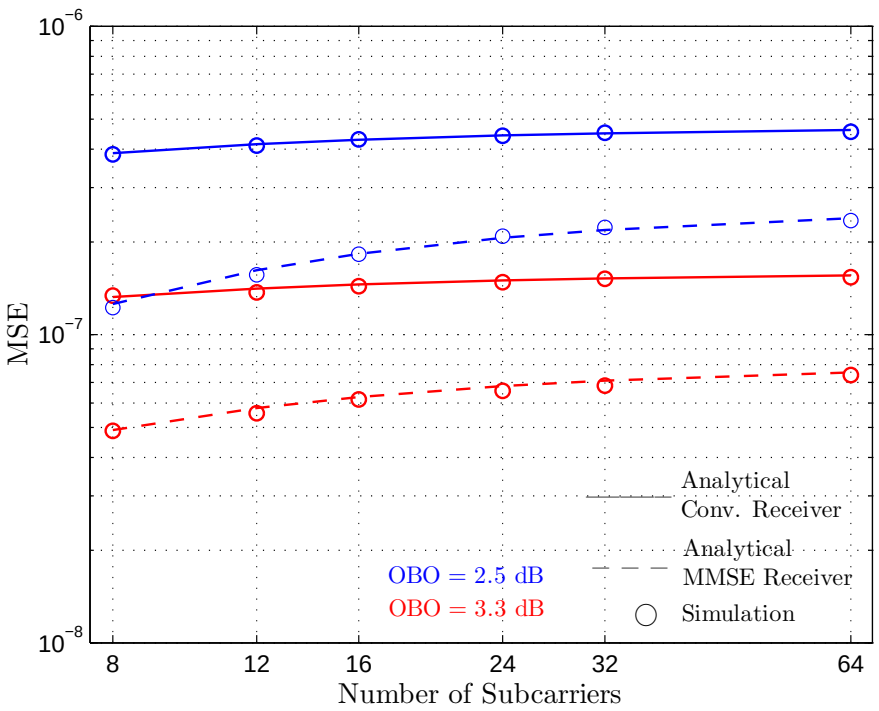

FIGURE 4.12: Analytical and simulated mean-squared errors as a function of the number of subcarriers for OFDM/BPSK signals for different OBO values and a SNR per bit of 20 dB.

conventional receiver increase with the number of subcarriers used, irrespective of the OBO value. Nevertheless, results also show that both MSE curves seem to tend to a certain value.

In conclusion, results for the MMSE receiver show an improvement in terms of MSE for the conventional receiver, specially when considering OFDM/BPSK signals and high SNR per bit levels (see Figure 4.10). Yet, it can also be seen that it is relatively small. Nevertheless, let us focus on its performance. It can be explained by analyzing both covariance and cross-covariance matrices given by Figures 4.4 and 4.6. The covariance results show that there is a considerable number of non-zero values for symbols conveyed by different subcarriers and between the received and transmitted symbols, which indicates a certain amount of correlation between them. This non-zero information, which arises from the fact that IMD is present, is of great importance for the MMSE receiver performance since it represents useful information that is actually used to obtain a better estimate of the transmitted symbols. However, results for OFDM/QPSK and higher schemes showed that, for a third order nonlinearity, the cross-correlation between received complex symbols conveyed by different subcarriers and also with the transmitted complex symbols are very low, indicating that for these modulation schemes, the correlation is very low and that there is no additional and useful information to help to improve the estimation process of the MMSE receiver.

4.4.1 Adaptive algorithms for the MMSE receiver

Although its derivation gives us the optimum result in terms of MMSE, the computational effort to derive and calculate the analytical expression of the matrix of coefficients $\mathbf{M}_\alpha$ may be substantial since it involves the computation of the covariance and cross-covariance matrices of nonlinear functions and consequently the computation of several summations of (4.31), (4.32) and (4.33), as well as matrix inversion operations. Additionally, the optimum MMSE filter design also implies the knowledge of the nonlinear channel input-output characteristic (or to be able to estimate it) as well as statistics of the AWGN and signal sources. Moreover, the linear transformation obtained maintains its optimality in terms of MSE if the transmission link characteristics stay invariant over time.

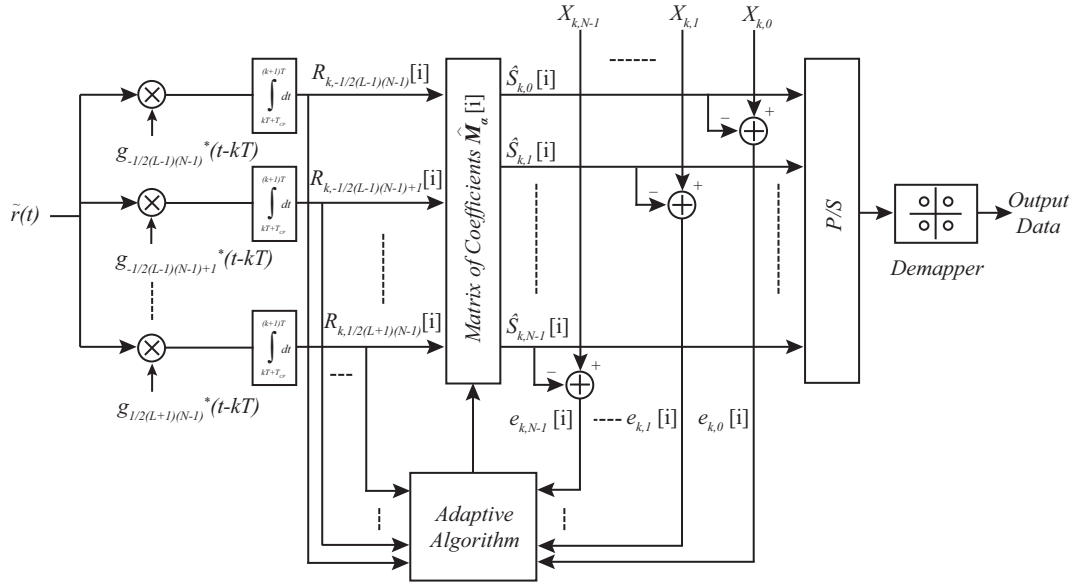

FIGURE 4.13: MMSE OFDM receiver with adaptive structure for estimation and adjustment of the matrix of coefficients $\mathbf{M}_\alpha$.

To alleviate the complexity of the analytical optimum MMSE filter design and to make it robust to channel and noise/signal sources characteristics variations, adaptive equalization algorithms like the least mean squares (LMS) and the recursive least squares (RLS) can be used.

Adaptive algorithms are used to estimate and adjust the matrix of coefficients $\mathbf{M}_\alpha$ without the need to *a priori* know the characteristics of the channel. Instead, it assumes the availability of a desired response usually given by a training sequence that is transmitted through the channel and is also available at the receiver side [71]. After the iterative training process, the adaptive algorithm can present one of two behaviors: the coefficients of the adaptive equalizer are maintained fixed after the training sequence stage; or, the adaptive algorithm adopts a decision directed approach were the desired response, heretofore given by the training sequence, is now given by the set of received complex symbols. By adopting the decision directed approach, the adaptive algorithm has the ability to track small channel variations.

The structure of the adaptive equalizer used is shown in Figure 4.13. Note that the set $\{X_{k,0}, X_{k,1}, \cdots, X_{k,N-1}\}$ represents the desired signal given by both a training sequence and the received complex symbols in the decision directed operation. We will now derive the algorithm used to adjust the coefficients $\alpha_{i,j}$ that compose the linear transformation matrix $\mathbf{M}_\alpha$.

4.4.1.1 Least mean square algorithm

The LMS algorithm is an adaptive algorithm introduced by Widrow and Hoff in 1960 that minimizes the instantaneous value of the cost function given by (4.1) by means of an iterative process. It is based on the steepest descent algorithm, also known as gradient descent, to find a local minimum of the cost function [69].

From the previous analytical derivation of the MMSE, it was demonstrated that the estimate of the vector of transmitted symbols, $\hat{\mathbf{S}}_k$, can be determined by simply applying a linear transformation to the received vector of complex symbols that also represent the sufficient statistics (see (4.28)). Thus, the error signal in subchannel n given by (4.3) can be written as

$$\begin{aligned} e_{k,n} &= S_{k,n} - \hat{S}_{k,n} \\ &= S_{k,n} - \left[\sum_{j=j_{min}}^{j_{max}} \alpha_{j,n} R_{k,j} \right], \quad n = 0, \cdots, N-1 \end{aligned} \tag{4.39}$$

where $j_{min} = -1/2(L-1)(N-1)$ and $j_{max} = 1/2(L+1)(N-1)$.

By using vector and matrix notations, the error signal vector is given by

$$\begin{aligned} \mathbf{e}_k &= \mathbf{S}_k - \hat{\mathbf{S}}_k \\ &= \mathbf{S}_k - \mathbf{M}_\alpha^T \mathbf{R}_k \end{aligned} \tag{4.40}$$

and the MSE function used as cost function to be minimized is

$$\xi = \mathrm{E}\left[\left\| \mathbf{S}_k - \mathbf{M}_\alpha^T \mathbf{R}_k \right\|^2 \right] \tag{4.41}$$

In the steepest descent algorithm no matrix inversion operation is needed to compute the matrix of coefficients $\mathbf{M}_\alpha$. It begins by arbitrarily choosing a starting matrix at iteration $i = 0$, $\mathbf{M}_\alpha[0]$. Then, a gradient vector is computed by varying coefficient matrix elements, $\alpha_{j,n}$, in the opposite direction of the gradient. In mathematical terms,

$$\mathbf{M}_\alpha[i+1] = \mathbf{M}_\alpha[i] - \frac{\mu_{LMS}}{2} \Delta\xi \tag{4.42}$$

where μ_{LMS} represents the step size parameter, also known as adaptation constant,

$\mathbf{M}_\alpha[i+1]$ is the coefficient matrix at the $(i+1)th$ iteration and Δ represents the gradient operator. The gradient of the cost function given by the MSE, ξ, is given by

$$\Delta\xi = -2\mathrm{E}\left[\mathbf{e}_k\mathbf{R}_k^H\right] \tag{4.43}$$

where the error signal $\mathbf{e}_k$ is given by (4.40). Thus, from (4.42) and (4.43), the steepest descent algorithm for adjusting the coefficient matrix reduces to

$$\mathbf{M}_\alpha[i+1] = \mathbf{M}_\alpha[i] + \mu_{LMS}\mathrm{E}\left[\mathbf{e}_k\mathbf{R}_k^H\right] \tag{4.44}$$

The iterative computation of the matrix $\mathbf{M}_\alpha$ implies the knowledge of the gradient given by (4.43). To overcome that, the LMS algorithm uses an estimative of the gradient given by its instantaneous value. Therefore, the LMS estimate of the matrix $\mathbf{M}_\alpha$ on the $(i+1)th$ iteration is given by

$$\hat{\mathbf{M}}_\alpha^{LMS}[i+1] = \hat{\mathbf{M}}_\alpha^{LMS}[i] + \mu_{LMS}\left[\mathbf{e}_k\mathbf{R}_k^H\right]_{k=i} \tag{4.45}$$

Note that during the training process stage, the estimate matrix $\hat{\mathbf{M}}_\alpha$ is updated at each iteration. Moreover, each time slot k also corresponds to one iteration. Equations (4.45) and (4.40) constitute the iterative LMS algorithm for adaptive equalization. Note that the LMS algorithm never finds the exactly minimum point of the cost function. Rather, it follows a zig-zag path towards the minimum point and once steady-state conditions are reached and the actual MSE value is below a given threshold, it acquires a random and noise-like behavior around the minimum point [71].

The stability and convergence speed of the LMS iterative algorithm are highly dependent of the step size chosen. A very low step size leads to a very low excess MSE, i.e., to a residual noise with a low variance, but also to a very slow convergence speed. On the other hand, a high step size speeds up convergence but can lead to a high excess MSE. Moreover, divergence of the iterative process can occur for high step sizes.

To overcome the high sensibility of the LMS algorithm to the scaling of received signal vector $\mathbf{R}_k$, the variant named normalized LMS (NLMS) is commonly used. With NLMS, the received signal vector is normalized by its power. The NLMS estimate of

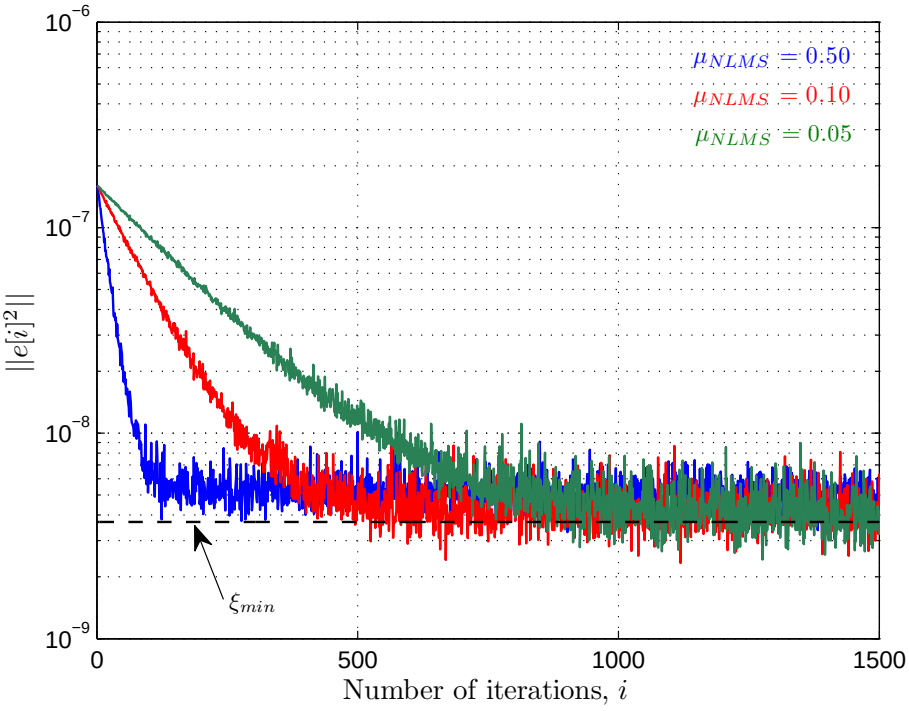

FIGURE 4.14: Estimation squared error as a function of the number of iterations for OFDM/BPSK signals with 16 subcarriers and for an OBO value of 3 dB. The dashed line represents the analytical minimum mean-squared error.

the matrix $\mathbf{M}_\alpha$ equation is given by

$$\hat{\mathbf{M}}_\alpha^{NLMS}[i+1] = \hat{\mathbf{M}}_\alpha^{NLMS}[i] + \mu_{NLMS}\frac{\left[\mathbf{e}_i\mathbf{R}_i^H\right]}{\left[\mathbf{R}_i^H\mathbf{R}_i\right]} \tag{4.46}$$

where $0 < \mu_{NLMS} < 2$.

To examine the behavior of the NLMS we have considered again OFDM signals with $T = 4\,\mu$s and $T_{CP} = 800$ ns and a third-order nonlinear channel characteristic given by (3.21) with polynomial coefficients given by $c_1 = 1$, $c_2 = 0$, $c_3 = -0.20$ and $c_i = 0$ for $i > 3$. Simulation results were obtained using Matlab/C++.

In Figure 4.14 it is depicted averaged learning curves for the NLMS adaptive algorithm when considering different step sizes. Learning curves are plots of the MSE as a function of time or iteration. Estimates of the squared error for each iteration i, $\|e[i]\|^2$, were obtained by averaging 100 learning curves [98]. The dashed line represents the MMSE values analytically obtained (see (4.38) and Figure 4.9). The signal was chosen to be OFDM/BPSK with 16 subcarriers and for an OBO value of 3 dB. Results show that the squared error tends to its minimum as the number of iterations increase.

Moreover, it can also be seen that the convergence speed increases with the step size. Nevertheless, the excess squared error is smaller when smaller step sizes are used.

4.5 Summary

In this chapter, we have derived the structure of the MMSE receiver for nonlinearly distorted OFDM signals in the presence of AWGN. We have shown that the MMSE receiver simply reduces to a set of correlators matched to every possible frequency components followed by a linear transformation. Moreover, it can be said that after the computation of the expected values, its usage and implementation are simple since it only adds a matrix product operation to a conventional OFDM receiver capable to extract a set of sufficient statistics.

Subsequently, we have developed analytical expressions to obtain the coefficients of the linear transformation for OFDM signals conveying either M-PSK and 16-QAM modulated complex symbols in each subchannel. Nevertheless, they can also be expanded to generic M-QAM modulations.

Then, an analytical and by means of simulation evaluation of the MSE metric using both the conventional and the derived structure was conducted.

Finally, we have also proposed an LMS based adaptive algorithm to iteratively estimate and adjust the coefficients of the linear transformation. Note that this approach introduces a significant simplification to the analytical computation of the coefficients. Moreover, the adaptive algorithm has the ability to track small channel variations and do not need to know *a priori* several link characteristics.

In the next chapter, we perform an analysis of the impact of intermodulation distortion in OFDM communication systems. Also, an extensive performance assessment of the conventional, ML, iterative ML algorithm and MMSE receivers is performed by means of simulation for a nonlinear transmission.

Chapter 5

Receivers performance assessment

5.1 Introduction

In previous chapters we have derived both the optimum ML receiver and the optimum linear receiver in terms of MSE for nonlinearly distorted OFDM signals in AWGN where each subchannel conveys complex symbols from M-PSK and M-QAM constellation schemes. Also, an ML algorithm that, with the aid of the set of sufficient statistics, iteratively searches for the OFDM symbol that maximizes the likelihood function in the neighborhood of a first estimate given by a conventional receiver was also presented and discussed. Moreover, we have developed analytical expressions for the linear MMSE receiver and it was shown that it reduces to a conventional OFDM receiver followed by a linear transformation.

In this chapter we start by introducing and describing the nonlinear channel characteristics and concepts that are used through this chapter. Then, an analytical and simulation analysis of the impact of the nonlinear channel on the transmission of OFDM signals is addressed. In particular, the impact of the IMD term and both compression and desensitization terms in the received constellation is evaluated. In sections 5.3 and 5.4, an extensive performance assessment of all OFDM receivers previously derived is performed and their results are discussed. In sections 5.5 and 5.6, we present an analysis of the degradation induced by an AWGN noise source before the nonlinear channel (as occurs in RF uplink systems) and also the degradation when an unknown frequency offset between the receiver and transmitter is present. Additionally, the impact of these

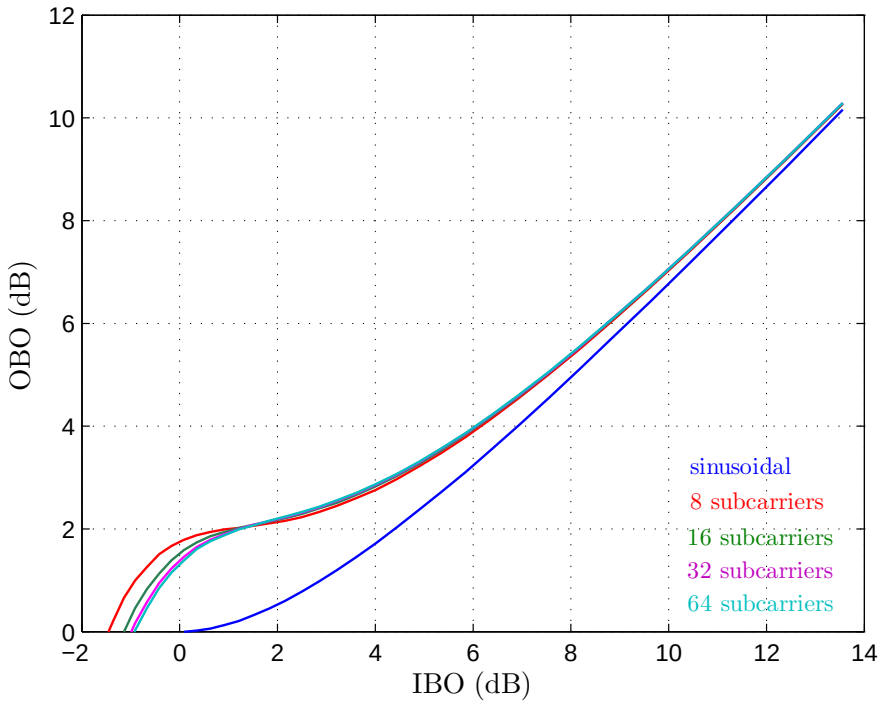

FIGURE 5.1: Output back-off as a function of the input back-off for a third-order nonlinearity with $c_1 = 1$, $c_2 = 0$ and $c_3 = -0.20$, OFDM/BPSK signals and considering different number of subcarriers.

impairments on the optimality of the ML receiver is also discussed and simulation results are presented.

Finally, section 5.7 summarizes the main results of this chapter.

5.2 Intermodulation distortion analysis

Let us consider a memoryless bandpass nonlinearity given by a power series of maximum order L. As it was derived in section 3.2.2, its equivalent complex envelope representation after first-zone filter can be written as

$$\tilde{y}(t) = \tilde{c}_1 \tilde{x}(t) + \tilde{c}_3 \left|\tilde{x}(t)\right|^2 \tilde{x}(t) + \cdots + \tilde{c}_L \left|\tilde{x}(t)\right|^{L-1} \tilde{x}(t) \tag{5.1}$$

Although the following analysis is independent of the order of the nonlinearity, as well as of its coefficients, we will consider a polynomial approximation up to the third order, i.e., with coefficients $\tilde{c}_i = 0, i > 3$, for the upcoming analysis.

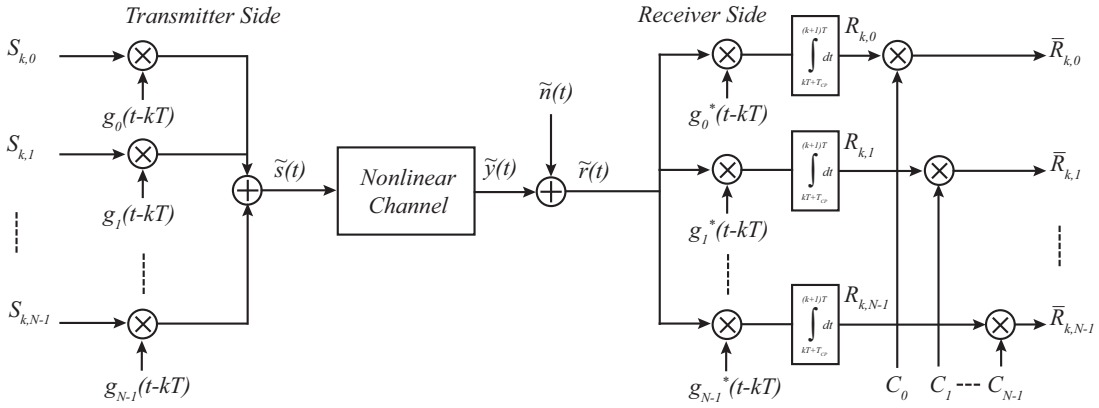

FIGURE 5.2: Equivalent baseband model used to study the impact of nonlinearities in OFDM signals transmissions.

In Figure 5.1 it is depicted the relation between the OBO and IBO for a nonlinearity given by (5.1) and considering OFDM/BPSK signals. Note that when OBO decreases to zero, there is a slightly difference between curves that can be explained by the fact that the number of IMPs increase with the number of subcarriers. Note also that IBO and OBO are not jointly equal to zero except when only a sinusoidal signal is considered.

In order to allow an efficient utilization of the available transmit power, it is desirable to operate the nonlinear element at a low BO. However, when operating at such a very nonlinear region of the input-output characteristic, the excessive distortion causes IMP components to fall inside and nearby the signals' band, spreading the shape of the signal spectrum and inducing a significant degradation to the signal as well as to adjacent channels (if any).

Let us now focus on the impact of the nonlinear element on the OFDM transmission system. To do so, we will consider the equivalent baseband transmission scheme depicted in Figure 5.2. Here, $\tilde{s}(t)$ represents the complex envelope of an OFDM signal, $\tilde{y}(t)$ represents the output of the baseband equivalent nonlinear channel, $\tilde{r}(t)$ represents the complex envelope of the received OFDM signal and $\tilde{n}(t)$ represents the complex envelope of an additive white Gaussian noise source with PSD N_0. To partly compensate the effects of the bandpass nonlinearity, namely attenuation and/or phase rotation, each complex received symbol is equalized by means of a complex automatic gain control (CAGC) C_n.

In chapter 3 we have derived the received complex symbols vector in time slot k, $\mathbf{R}_k = [R_{k,0}, R_{k,1}, \cdots, R_{k,N-1}]^T$, where each complex received symbol is given by

$$R_{k,n} = Y_{k,n} + N_{k,n} \tag{5.2}$$

and $Y_{k,n}$ and $N_{k,n}$ are, respectively, the complex symbol corrupted only by the nonlinear channel and a sample value of an independent and circularly symmetric complex Gaussian RV due to the presence of the AWGN source.

Consider now a generic OFDM signal transmission where each subchannel conveys a complex symbol that corresponds to a point i from a constellation of size M, $i = 1, \cdots, M$, of a single or multi-level digital modulation scheme. By denoting $R^i_{k,n}$ as the received complex symbol in time slot k and subchannel n conditioned to a transmitted complex symbol $S^i_{k,n}$, we can write it as the following sum

$$R^i_{k,n} = D^i_{k,n} + W^i_{k,n} + N_{k,n} \tag{5.3}$$

where the term $D^i_{k,n}$ is a deterministic quantity that represents the useful received complex symbol and $W^i_{k,n}$ is the intermodulation distortion (IMD) random quantity from the nonlinearity.

Thus, the useful received complex symbol is given by

$$\begin{aligned} D^i_{k,n} = & \frac{\tilde{c}_1}{(T - T_{CP})^0} S^i_{k,n} + \frac{\tilde{c}_3}{(T - T_{CP})^1} S^i_{k,n} S^i_{k,n} S^{i*}_{k,n} \\ & + \cdots \\ & + \frac{\tilde{c}_L}{(T - T_{CP})^{(L-1)/2}} S^i_{k,n} \left| S^i_{k,n} \right|^{(L-1)} \end{aligned} \tag{5.4}$$

where the first term is the linear contribution, the second term is the third-order contribution and the following terms are contributions from higher order IMP terms that are generated only considering subchannel n. These specific IMPs are called the *compression* of the linear term (see chapter 2).

The IMD term at subcarrier n that accounts the remaining IMPs, $W^i_{k,n}$, is often denoted as *nonlinear noise* and is given by

$$\begin{aligned} W^i_{k,n} = & \frac{\tilde{c}_1}{(T-T_{CP})^0} \sum_{\substack{n_1=0 \\ n_1 \neq n}}^{N-1} S_{k,n_1} \delta(n_1 - n) \\ & + \frac{\tilde{c}_3}{(T-T_{CP})^1} \sum_{\substack{n_1=0 \\ n_1,n_2,n_3 \neq n,n,n}}^{N-1} \sum_{n_2=0}^{N-1} \sum_{n_3=0}^{N-1} S_{k,n_1} S_{k,n_2} S^*_{k,n_3} \delta(n_1 + n_2 - n_3 - n) \\ & + \cdots \\ & + \frac{\tilde{c}_L}{(T-T_{CP})^{(L-1)/2}} \sum_{\substack{n_1=0 \\ n_1,\cdots,n_L \neq n,\cdots,n}}^{N-1} \cdots \sum_{n_L=0}^{N-1} S_{k,n_1} \cdots S_{k,n_{(L+1)/2}} S^*_{k,n_{(L+3)/2}} \cdots S^*_{k,n_L} \\ & \times \delta(n_1 + \cdots + n_{(L+1)/2} - n_{(L+3)/2} - \cdots - n_L - n) \end{aligned} \tag{5.5}$$

Note that for a high number of subcarriers, the number of IMPs increases drastically and as well as the nonlinear distortion. Although some authors consider that the nonlinear noise may be modeled as a Gaussian process, it was demonstrated that due to the heavy tails of the IMD distribution the approximation is not always valid [97].

The mean value of the IMD term, $\overline{W}^i_n$, is given by taking its expectation value

$$\begin{aligned} \overline{W}^i_n \triangleq & \mathrm{E}\left[W^i_{k,n}\right] \\ = & \frac{\tilde{c}_3}{(T-T_{CP})^1} \sum_{\substack{n_1=0 \\ n_1,n_2,n_3 \neq n,n,n}}^{N-1} \sum_{n_2=0}^{N-1} \sum_{n_3=0}^{N-1} \mathrm{E}\left[S_{k,n_1} S_{k,n_2} S^*_{k,n_3} | S^i_{k,n}\right] \delta(n_1 + n_2 - n_3 - n) \\ & + \cdots \\ & + \frac{\tilde{c}_L}{(T-T_{CP})^{(L-1)/2}} \sum_{\substack{n_1=0 \\ n_1,\cdots,n_L \neq n,\cdots,n}}^{N-1} \cdots \sum_{n_L=0}^{N-1} \mathrm{E}\left[S_{k,n_1} \cdots S_{k,n_{(L+1)/2}} S^*_{k,n_{(L+3)/2}} \cdots S^*_{k,n_L} | S^i_{k,n}\right] \\ & \times \delta(n_1 + \cdots + n_{(L+1)/2} - n_{(L+3)/2} - \cdots - n_L - n) \end{aligned} \tag{5.6}$$

So, the received symbol in time slot k and subchannel n conditioned to the transmitted symbol $S^i_{k,n}$ can be rewritten as

$$R^i_{k,n} = D^i_{k,n} + \overline{W}^i_n + {}^{zm}W^i_{k,n} + N_{k,n} \tag{5.7}$$

where ${}^{zm}W^i_{k,n} = W^i_{k,n} - \overline{W}^i_n$ corresponds to the zero-mean IMD term.

Similarly to the analysis performed in section 4.3.1, by taking into consideration that the N subcarriers are independent, it can be stated that the transmitted symbols conveyed in a given subchannel are also independent of the ones conveyed by the remain subchannels. Therefore, the conditional expectations in (5.6) can be simplified using the multiplicative property of the expected value operator for independent RVs [84]

$$\mathrm{E}\left[S_{k,n_1}\cdots S_{k,n_{(L+1)/2}}S^*_{k,n_{(L+3)/2}}\cdots S^*_{k,n_L}|S^i_{k,n}\right] = \\ = (S^i_{k,n})^{a_n}(S^{i*}_{k,n})^{b_n}\prod_{\substack{m=0\\ m\neq n}}^{N-1}\mathrm{E}\left[(S_{k,m})^{a_m}(S^*_{k,m})^{b_m}\right] \quad (5.8)$$

where a_m and b_m denote the number of elements of the form $S_{k,m}$ and $S^*_{k,m}$, respectively.

Expectations in the RHS of (5.8) are given by (4.32) when considering the transmission of equally likely complex symbols of M-PSK constellation scheme, whilst (4.33) is specific for the 16-QAM signal transmission.

In a similar fashion it is possible to analytically compute the variance of the nonlinear noise, ${\sigma^i_n}^2 = \mathrm{E}\left[\left|W^i_{k,n} - \overline{W}^i_n\right|^2\right]$, using (5.5), (5.6) and (5.8).

Note that the mean value of the IMD term in subcarrier n, $\overline{W}^i_n$, is given by the desensitization terms, i.e., the terms that are used to describe the transfer of energy from one subchannel to another. The desensitization terms are given by subcarrier combinations of the form $(n'+n-n')$ with $n, n' = 0, \cdots, N-1$ and $n \neq n'$, when a third-order nonlinearity is considered [72, 99]. Moreover, in constant modulus modulation formats such as M-PSK where all symbols have the same energy, the amplitude of the desensitizations terms is constant and, consequently, for a given transmitted symbol, they are deterministic. On the other hand, complex symbols from multilevel modulation schemes can have different energy levels. So, when what is conveyed by the others subchannels is unknown, the desensitization terms cannot be determined.

In order to investigate the effect of intermodulation distortion in the transmission of OFDM signal, we use Matlab/C++ to perform several simulations accordingly to the scheme depicted in Figure 5.2. Here, the AWGN source was shut off so we can analyze only the impact of the nonlinear channel. The complex transmitted symbols where chosen to be M-PSK and M-QAM with up to 16 constellation points, the OFDM

symbol period was set to $T = 4\,\mu$s and the OFDM cyclic prefix set to $T_{CP} = 0.8\,\mu$s. Different back-off values as well as different number of subcarriers were also considered. Analytical results of the nonlinear noise statistics were obtained using Matlab/C++ as a numerical calculator.

The channel is considered to be a third-order nonlinearity with AM/AM and AM/PM characteristics given by complex power series coefficients[1] $\tilde{c}_1 = 1 + j0$, $\tilde{c}_2 = 0$, $\tilde{c}_3 = -0.18 + j0.13$ and $\tilde{c}_i = 0$ for $i > 3$. Note that the referred complex power series coefficients can also be seen as a third order approximation of the polar AM/AM and AM/PM characteristics given, respectively, by (see (3.17) and (3.18))

$$F[|\tilde{s}(t)|] = 1 - \frac{3}{4}0.20\,|\tilde{s}(t)|^2 \tag{5.9}$$

$$\Phi[|\tilde{s}(t)|] = 0.20\,|\tilde{s}(t)|^2 \tag{5.10}$$

In Figures 5.3 and 5.4 it is depicted the power spectra density for OFDM/QPSK signals with 16 and 64 subcarriers, respectively, considering three OBO values. It can be seen that when OBO decreases, the power of the IMPs outside the signal's band increase drastically. Nevertheless, several IMPs also fall inside the band. The out-of-band distortion slowly decays with frequency due to the fact that the number of IMPs reaches its maximum at the center frequency of the OFDM signal. Note also that the IMPs are confined to the band $[f_c - 3B/2, f_c + 3B/2]$ because the channel model considered is a third order nonlinearity. Moreover, observation of both Figures also shows that the impact of the nonlinearity in the PSD is higher for the OFDM signal with 64 subcarriers. Again, this is explained by the fact that the number of IMPs increases with the number of subcarriers (see chapter 2).

Let us now look carefully to the received OFDM signal before the CAGC and how IMD affects the modulated signal conveyed. For a fair comparison and interpretation of the results when different OBO operating points and number of subcarriers are considered, the amplitude of the received signal is normalized by the amplitude of the transmitted signal. Figures 5.5(a) and 5.6(a) show the normalized received constellation for OFDM/QPSK and OFDM/16-QAM signals with 64 subcarriers in the presence

[1]For this generic analysis we consider that both AM/AM and AM/PM distortions are present. Consequently, the nonlinearity is considered not to be strictly memoryless and given by a complex power series (see section 3.2.2).

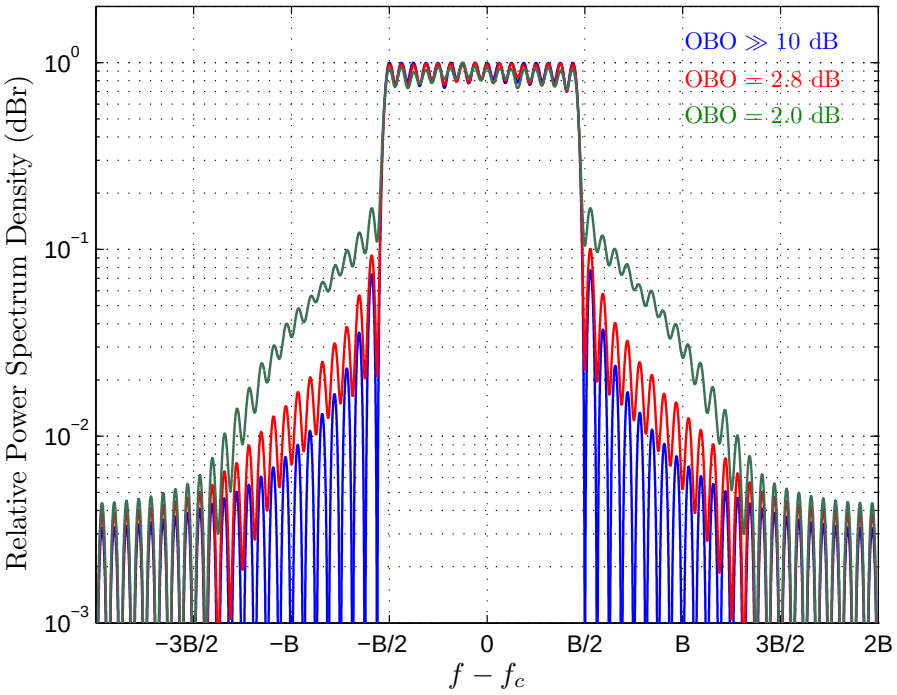

FIGURE 5.3: Power spectrum density comparison for different OBO values and considering OFDM/QPSK signals with 16 subcarriers.

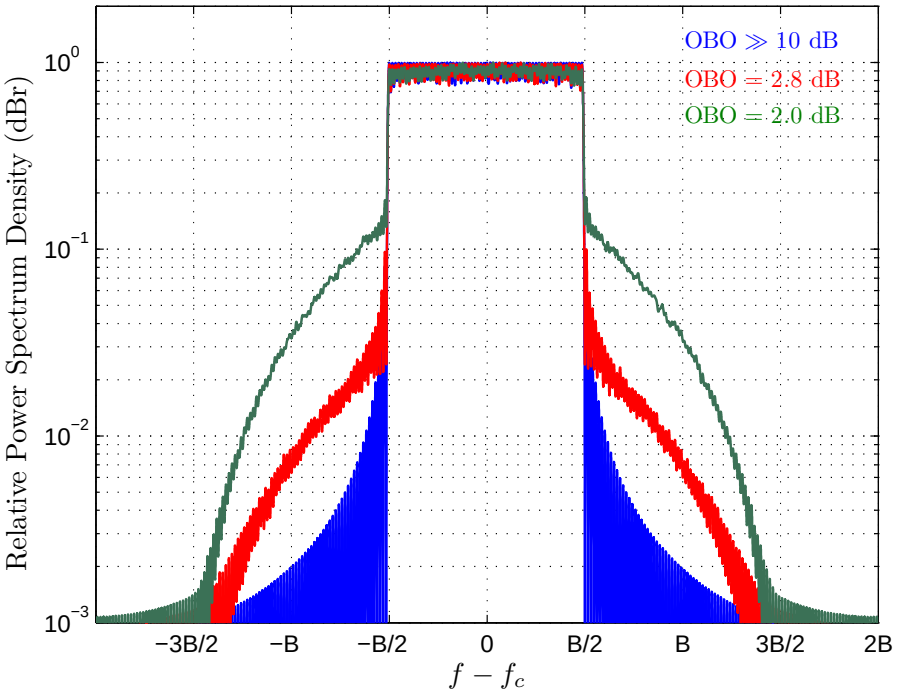

FIGURE 5.4: Power spectrum density comparison for different OBO values and considering OFDM/QPSK signals with 64 subcarriers.

of the same AM/AM and AM/PM characteristics. Note that both constellations were obtained taking into account the complex symbols conveyed by all N subcarriers. Different output back-off values as well as ideal constellation points positions are represented. Furthermore, it is also represented in Figures 5.5(b) and 5.6(b) the normalized averaged constellation points analytically given by the deterministic received symbol, $D^i_{k,n}$, affected by the mean of the IMD term, $\overline{W}^i_n$ (see (5.7)). Note that the noisy-like received constellations are only due to nonlinear distortion and that no other noise sources were added. Results clearly show how strong the inband distortion can be and its impact in the received signal constellation. When low OBO values are considered, both received QPSK and 16-QAM constellations show that OFDM signals are strongly distorted, despite not being clearly perceptible from their spectra. As expected, the AM/AM conversion increases with the signal's power and a clear cloud-like shape due to the nonlinear noise term is present. Also, it is possible to identify the attenuation induced by the AM/AM conversion. Moreover, the AM/PM conversion shows to be stronger for low OBO values, inducing a phase rotation and a critical cross-talk between in-phase and quadrature components.

In order to evaluate the weight of the various IMPs that form the received signal, Figure 5.7(a) shows the deterministic compression gain terms affected by the desensitization terms in a constellation representation for OFDM/QPSK signals with an OBO value of 3 dB and considering different number of subcarriers. It is also represented in Figure 5.7(b) the received constellation points conditioned to a transmitted symbol i where all the main terms are represented by colors. Similar results for OFDM/16-QAM signals are also depicted in Figure 5.8. Several important conclusions can be taken from these results. Figures show that the mean of the received constellation points can be analytically determined by knowing only the compression gain and desensitizations terms. It can also be seen that for constant modulus modulation formats (like M-PSK), the averaged constellation is in fact deterministic, as it was previously stated, and practically independent on the number of subcarriers used. On the other hand, results for OFDM/16-QAM signals show that the desensitization terms are highly dependent on the number of subcarriers. This can be explained by the fact that for a given OBO, the amplitude of the transmitted complex symbols varies inversely with the number

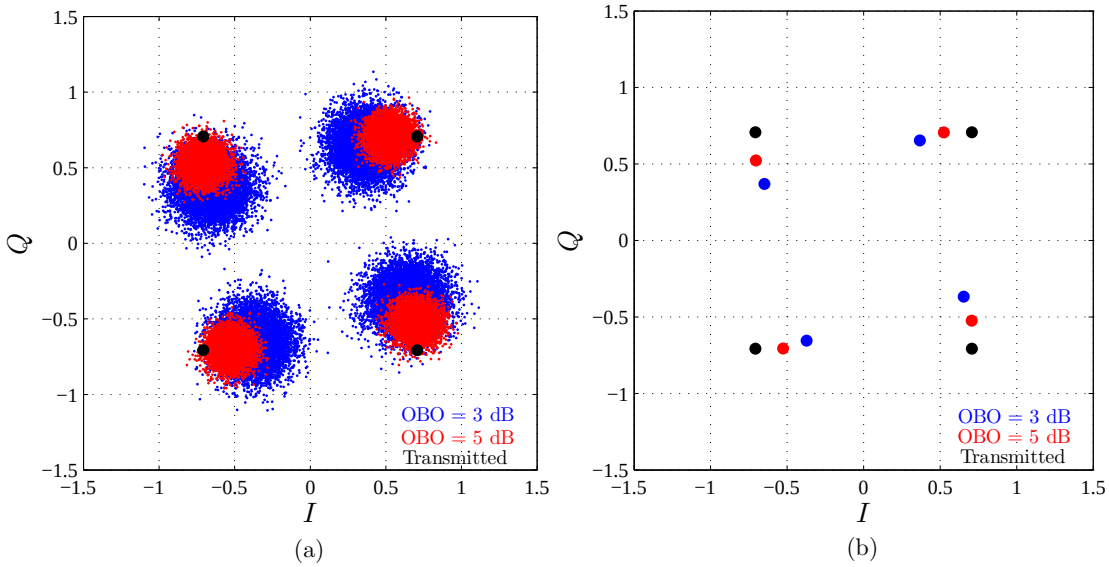

FIGURE 5.5: (a) Received constellation and (b) received averaged constellation for different OBO values considering OFDM/QPSK signals with 64 subcarriers.

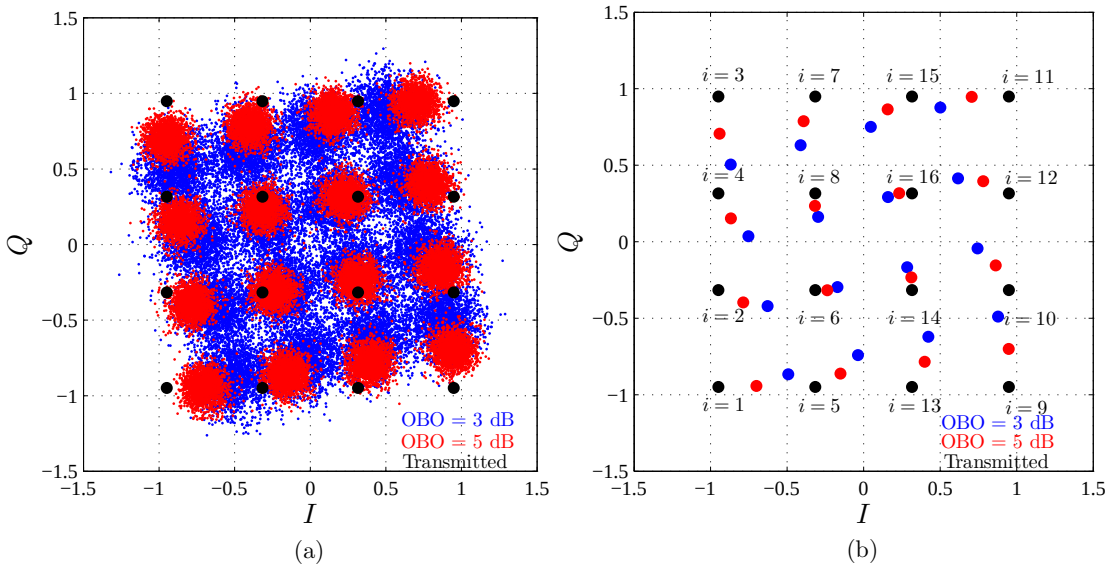

FIGURE 5.6: (a) Received constellation and (b) received averaged constellation for different OBO values considering OFDM/16-QAM signals with 64 subcarriers.

of subcarriers used and so does the energy of the complex symbols conveyed in each subchannel. Results also show that the gain compression contribution has a negligible influence in the received signal, contrary to the desensitization contributions. From a careful inspection of the IMD cloud shape given by Figure 5.8(b), it is also possible to observe a slight distortion of the in-phase and quadrature components.

Figure 5.9 depicts simulation and analytical results of the normalized amplitude

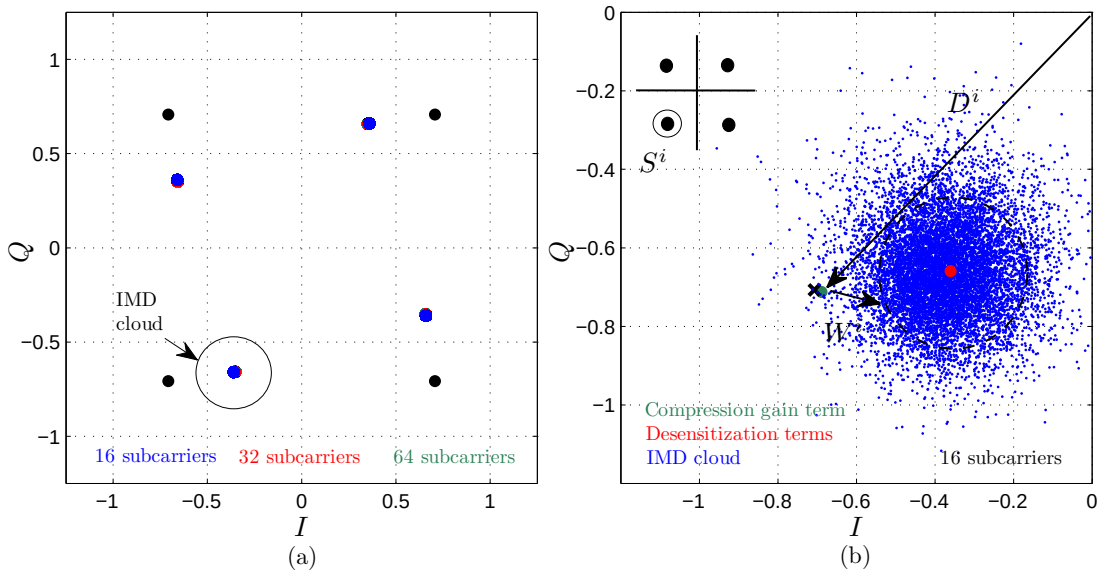

FIGURE 5.7: Deterministic compression gain term affected by desensitization terms in a (a) constellation representation and (b) received constellation point conditioned to a transmitted symbol $S^i_{k,n}$ (right), for OFDM/QPSK signals with an OBO value of 3 dB and different number of subcarriers.

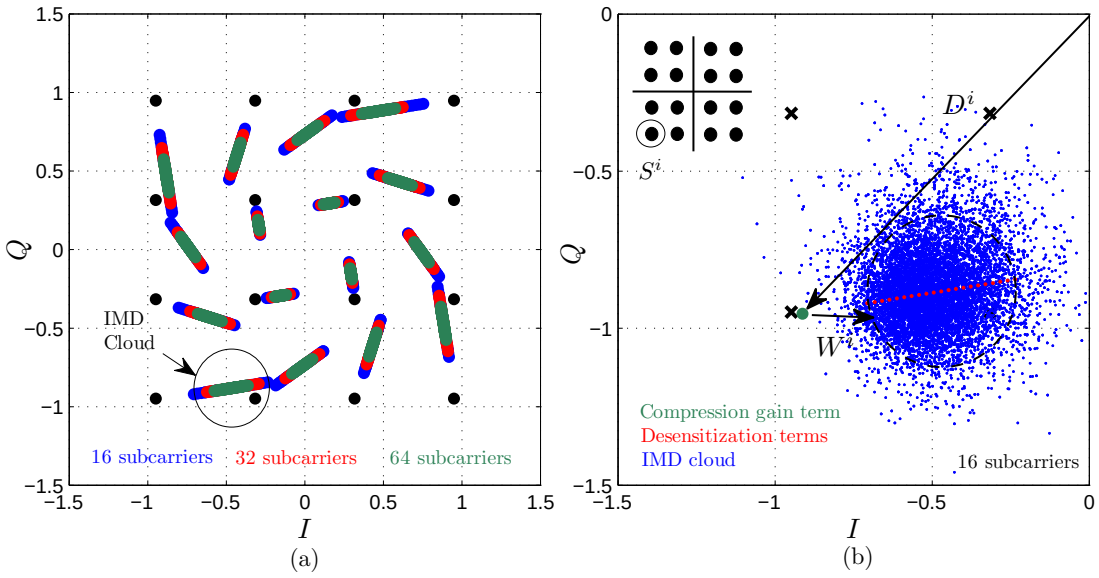

FIGURE 5.8: Deterministic compression gain term affected by desensitization terms in a (a) constellation representation and (b) received constellation point conditioned to a transmitted symbol $S^i_{k,n}$ (right), for OFDM/16-QAM signals with an OBO value of 3 dB and different number of subcarriers.

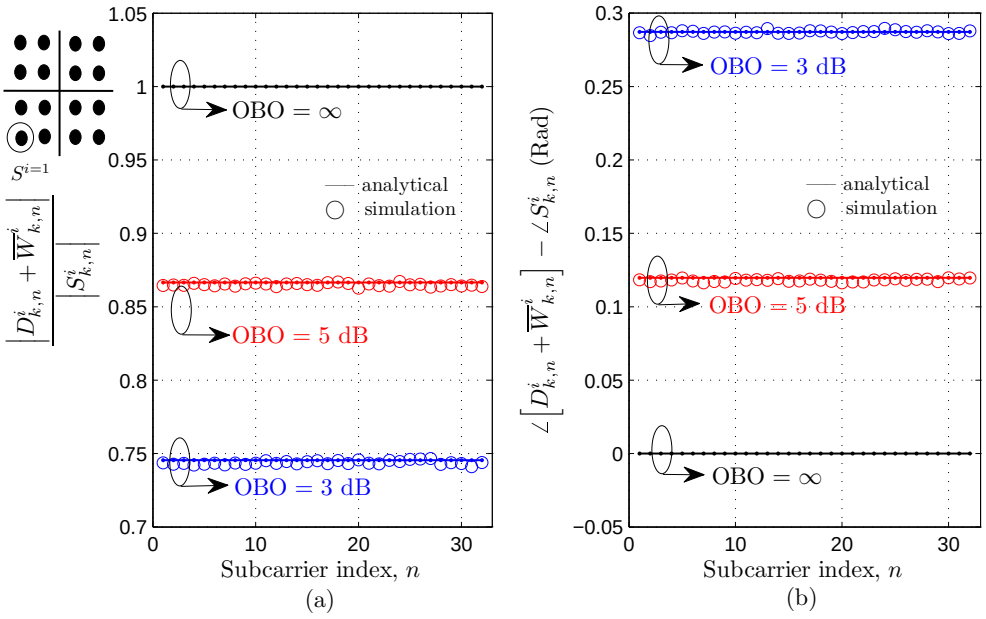

FIGURE 5.9: Simulation and analytical results of the (a) normalized amplitude and (b) phase of the averaged received complex symbol conditioned and relative to a specific transmitted symbol $S^i_{k,n}$ as a function of the subcarrier index for different OBO values and OFDM/16-QAM signals with 64 subcarriers.

and phase of the averaged received complex symbol conditioned and relative to a given transmitted symbol as a function of the subcarrier index for OFDM/16-QAM signals and considering different OBO values. Simulation results were obtained by transmitting 10^4 OFDM symbols and conditioning a specific subcarrier n to a symbol $S^i_{k,n}$. Both analytical and simulation results show to be in agreement. So, it can be concluded that attenuation and phase rotation of the received constellation are independent of the subchannel in which it is conveyed. Similar results for different number of subcarriers and for OFDM/QPSK signals were also obtained.

In Figure 5.10 it is assessed if the normalized averaged received complex symbol is dependent on the transmitted symbol. Again, the same procedure as the previously described was used to obtain the simulation results. Analytical results show that in fact there is a slight difference that increases with the input signals' power. This dependency on the transmitted symbol point is explained by the multilevel nature of the 16-QAM and its effect on the desensitization terms. For single level modulations like QPSK it was both analytically and by means of simulations verified that the normalized averaged received complex symbol is independent of the transmitted symbol $S^i_{k,n}$. This result suggests that the decision boundaries to amplitude modulation schemes could be optimized to

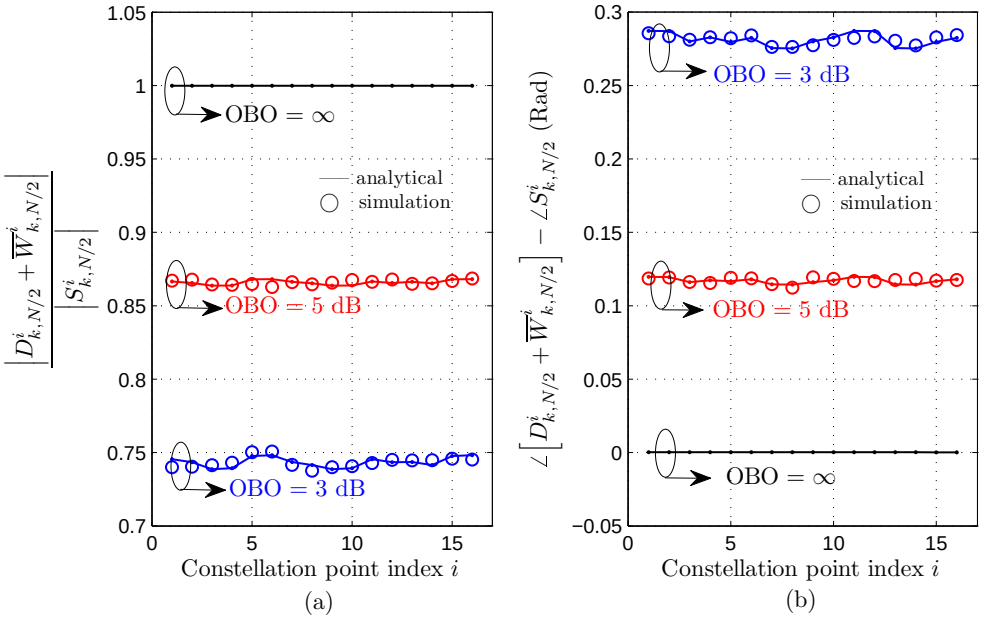

FIGURE 5.10: Simulation and analytical results of the (a) relative amplitude and (b) phase of the averaged received complex symbol conveyed in subchannel $N/2$ as a function of the constellation point index for different OBO values and OFDM/16-QAM signals with 64 subcarriers.

minimize the error rate.

In order to address the dependency of the normalized averaged received constellation on the number of subcarriers used, it is shown in Figure 5.11 both analytical calculations and simulation results for OFDM/16-QAM using different OBO values. Results were obtained by averaging both amplitude and phase of the normalized received complex symbol conditioned and relative to all possible transmitted complex symbols and for the subcarrier index $N/2$. Equal results for M-PSK modulations were obtained, suggesting that both amplitude and phase of the received constellation averaged over all possible transmitted complex symbols, $S^i_{k,n}, \forall i = 1, \cdots, M$, are independent of its size M and shape. Moreover, Figure 5.11 shows that there is a slight dependency on the number of subcarriers used, especially for a low number of subcarriers. Yet, as the number of subcarriers increase, results show that the dependency turns out to dilute.

So, from the previously obtained results, it is reasonable to define a CAGC coefficient given by

$$C = \left[\frac{1}{M} \sum_{i=1}^{M} \left(\frac{\mathrm{E}\left[R^i_{k,n}\right]}{S^i_n} \right) \right]^{-1}, \quad \forall n = 0, \cdots, N-1 \tag{5.11}$$

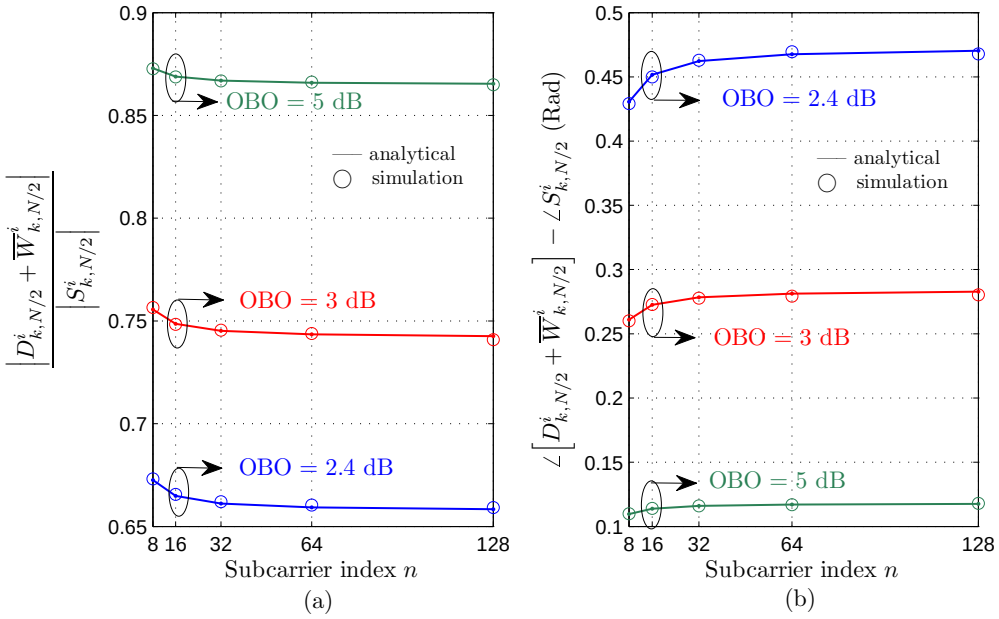

FIGURE 5.11: Simulation and analytical results of the (a) relative amplitude and (b) phase of the averaged received complex symbol conveyed in subchannel $N/2$ as a function of the number of the number of subcarriers for different OBO values considering OFDM/16-QAM signals.

Figure 5.12 shows analytical results for the amplitude and phase of the CAGC coefficient as a function of the output back-off for OFDM/16-QAM signals and considering different number of subcarriers. Note that the results given by Figure 5.12 are also applicable to M-PSK modulation schemes since both amplitude and phase of the normalized received symbols were found to be independent of both size and shape of the constellation. Moreover, the CAGC coefficient is normalized to the amplitude of the transmitted signal.

In conclusion, the normalized averaged received constellation of OFDM signals is independent of the subchannel index in which data is conveyed. Regarding the variance of the IMD nonlinear noise, as it can be seen from Figures 5.5 and 5.6 it is expected that it increases with the input signal power.

In order to obtain the variance of the nonlinear noise, several simulations were conducted. First, simulations of OFDM transmissions to obtain received symbols conditioned to all possible transmitted complex symbols $S^i_{k,n}, i = 1, \cdots, M$ were performed and their variance was evaluated. Since all possible transmitted symbols are equiprobable, the overall variance can be calculated by averaging all M variances evaluated for

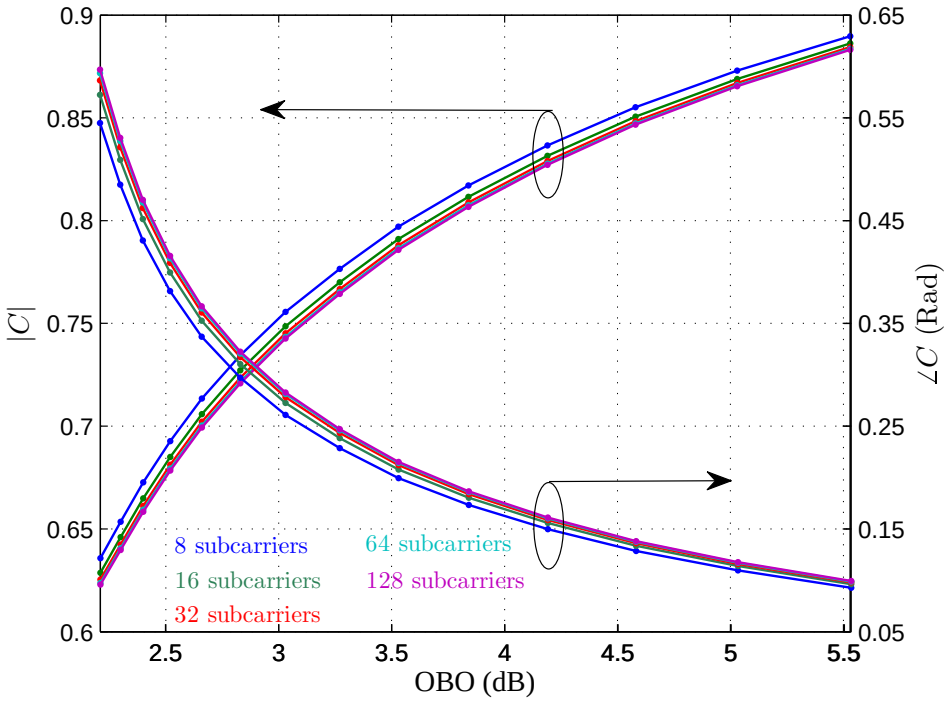

FIGURE 5.12: Amplitude and phase of the CAGC coefficient as a function of the output back-off for OFDM/16-QAM signals with 8, 16, 32, 64 and 128 subcarriers.

each subchannel. To make possible their comparison, the received symbols are normalized to the input signal's amplitude and respective CAGC coefficient. In Figure 5.13 it is represented the variance of the received symbol which also corresponds to the variance of the IMD term, $W_{k,n}$, around its mean as a function of the number of subcarriers for OFDM/16-QAM and OFDM/QPSK signals. Moreover, the results considered are for the in-phase component of the nonlinear noise and for subchannels at the center and edge, where the number of IMPs is the highest and the lowest, respectively. As expected, the variance of the IMD term increases as the OBO value decreases. Results also show that the subchannel at the center is more affected by the IMD. Additionally, an important result that is obtained from the Figure is that the variance depends on the number of subcarriers used. In fact, as the number of subcarriers increases, the variance of the IMD term also increases, due to the increase of IMPs. This result suggests that the impact of the nonlinearity increases as the number of subcarriers increase. Simulations results in terms of bit error rate concerning the effect of the number of subcarriers will be discussed ahead in section 5.3.4. Regarding the difference between QPSK and 16-QAM schemes, results show that when a low number of subcarriers is used the variance of

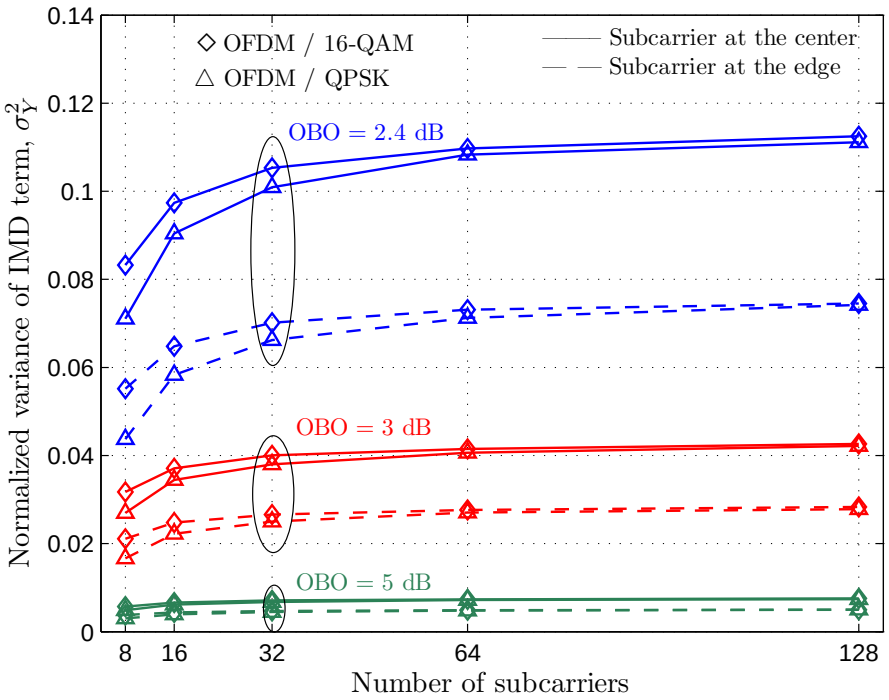

FIGURE 5.13: Normalized variance of the in-phase component of the IMD term in both subchannels at the center and edge as a function of the number of subcarriers for OFDM/16QAM and OFDM/QPSK signals and considering different OBO values.

the IMD term is higher for the 16-QAM case. Yet, they both tend to the same value as the number of subcarriers increase. Since both modulation formats are circularly symmetrical, identical results for the quadrature component of the nonlinear noise were also obtained.

To study the impact of the size of constellation on the normalized variance of the IMD term, Figure 5.14 shows its behavior for OFDM/M-PSK signals considering different OBO values as well as number of subcarrier used. Again, the same simulation procedure described above was conducted. Note that the variance is taken after affecting the received signal by its respectively CAGC coefficient and normalized to the transmitted signal's amplitude. Figure 5.14 also reports both the in-phase and quadrature components of the IMD term. It can be seen that the overall variance does not change with the size of constellation. The BPSK case is considered particular because it is not circular symmetric, which explains the difference on the variance of both components.

In Figures 5.15 and 5.16 it is represented the behavior of the in-phase and quadrature components of the normalized variance as a function of the transmitted complex

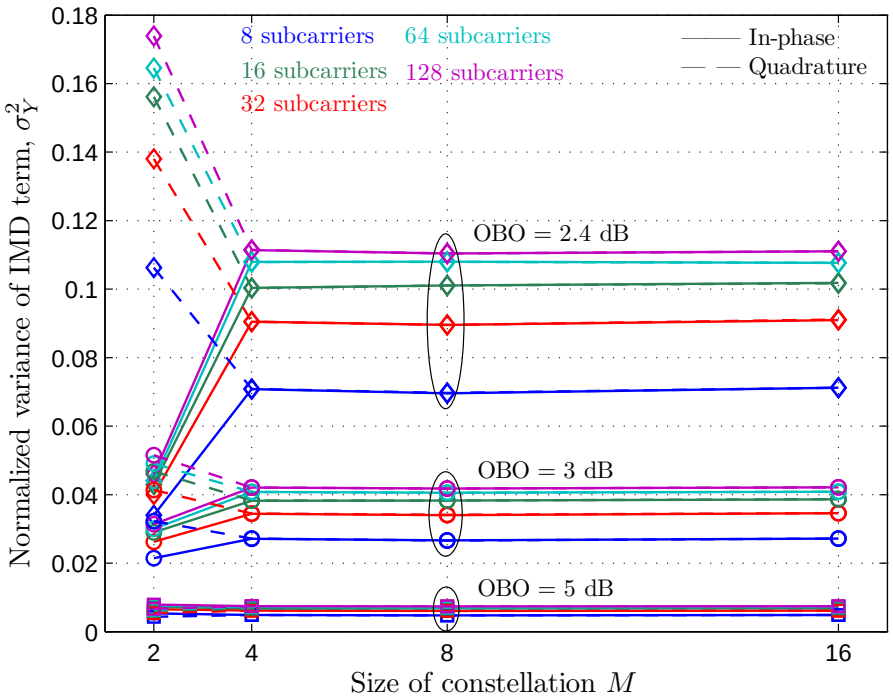

FIGURE 5.14: Normalized variance of the in-phase component of the IMD term in the subchannel at the center as a function of the size of constellation, M, for OFDM/M-PSK signals and considering different OBO values.

symbol $S^i_{k,n}$ for OFDM/16-QAM and OFDM/QPSK signals, respectively. Results for the OFDM/16-QAM case show that the in-phase and quadrature components of the variance are not equal. Interestingly, its behavior starts to show very pronounced maximum and minimum peaks as the number of subcarriers used decrease. Moreover, results show that maximum peaks occur at constellation point indexes that correspond to the edges of the constellation. This behavior is observed for all OBO values considered. Furthermore, results also suggest that the received constellation cloud starts to warp and to distort non-uniformly in terms of in-phase and quadrature components when a low number subcarriers is used. Note that this effect has already been previously referred (see Figure 5.6). For the OFDM/QPSK case, a constant variance of both in-phase an quadrature components for all constellation points is reported. Nevertheless, it has been shown that OFDM/16-QAM and OFDM/QPSK have their received constellation warp and that the distribution of the in-phase and quadrature components start to be asymmetric and to have a non-zero skew, especially when a low number of subcarriers is used [97].

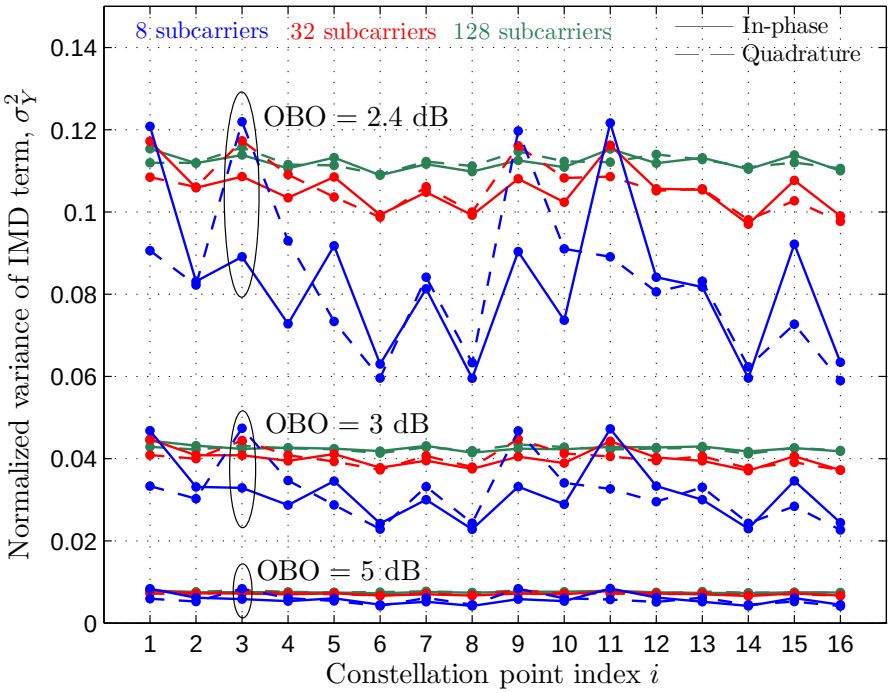

FIGURE 5.15: Normalized variance of the IMD term in the subchannel at the center as a function of the constellation point index, i, for OFDM/16-QAM signals and considering different OBO values and number of subcarriers used.

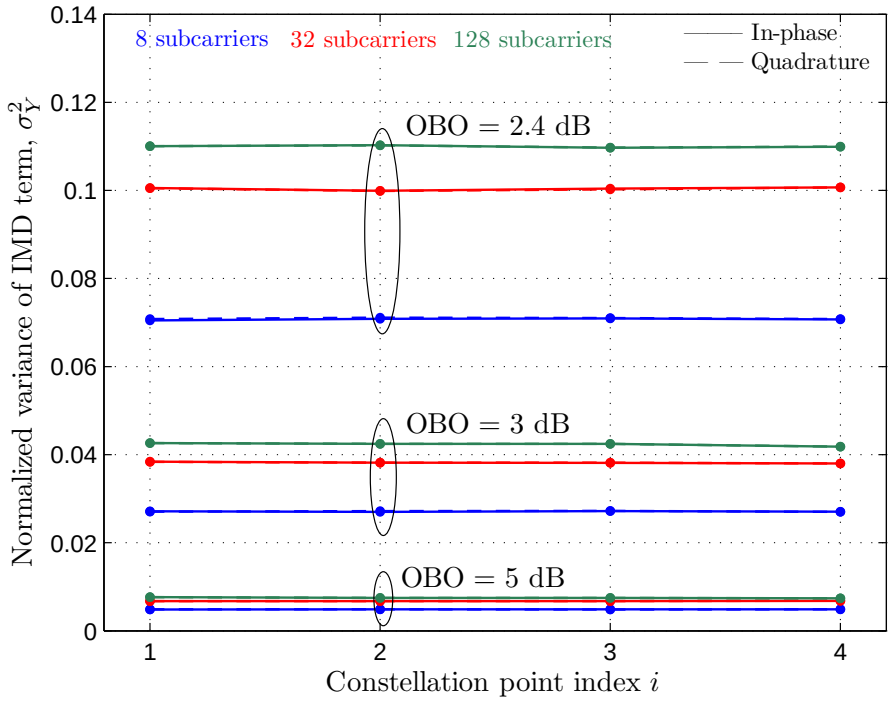

FIGURE 5.16: Normalized variance of the IMD term in the subchannel at the center as a function of the constellation point index, i, for OFDM/QPSK signals and considering different OBO values and number of subcarriers used.

5.3 ML receiver performance assessment

In the following sections we will use Matlab/C++ to conduct a series of simulations in order to evaluate the performance of the ML receiver. The OFDM signal has the following general characteristics: $T = 4\,\mu$s, $T_{CP} = 800\,$ns with different number of subcarriers and OBO levels. The complex symbols conveyed in each subchannel are chosen to be modulated as M-PSK signals taking values of $\left\{Ae^{j\left(\pi\frac{2i+1}{M}-\pi/2\right)}; i = 0, \cdots, M-1\right\}$, where M denotes the size of the PSK constellation, as well as the multilevel modulation 16-QAM. It is also assumed Gray coding for constellations with $M > 2$. The channel is considered to be a third-order nonlinearity with AM/AM characteristic given by power series coefficients $c_1 = 1$, $c_2 = 0$ and $c_3 = -0.20$. The equivalent baseband transmission setup is considered to be the one depicted in Figure 3.2, or equivalently the one given by Figure 5.2 where the structure of a conventional OFDM receiver is also represented. Simulation results for the ML receiver described in section 3.3.2 are also obtained for OFDM/BPSK signal transmissions only up to 16 subcarriers due to the very high simulation time associated when $N\log_2(M) > 16$. Finally, the OFDM receiver based on the iterative ML algorithm represented in Figure 3.4 is also considered.

As previously verified in section 5.2, the variance of the IMD term conveyed in subchannels at the center of the band is higher than the ones conveyed in subchannels at the edge. This behavior of the nonlinear noise level can be explained by knowing that the number of IMPs that fall at the center of the band is higher (see Figures 2.13 and 2.14). Thus, it is also expected the error probability of a modulated signal conveyed at a specific subchannel to follow the same behavior. Figure 5.17 depicts error probability estimates as a function of the subcarrier index for OFDM/BPSK signals with 64 subcarriers, an SNR per bit of 10 dB and different OBO values. Results for both conventional and iterative ML algorithm are presented. From the observation of the Figure 5.17 it can be seen that in fact the error probability reaches its maximum at the center of the OFDM band when a conventional receiver is considered. Results also show that the iterative ML algorithm exhibits a similar behavior. Yet, the difference between error probabilities obtained in subcarriers at the center and at the edge appears to decrease with the number of iterations used. In fact, for an OBO value of 3.3 dB and an SNR per bit of 10 dB, Figure 5.17 shows that the BER for the five iterations ML algorithm

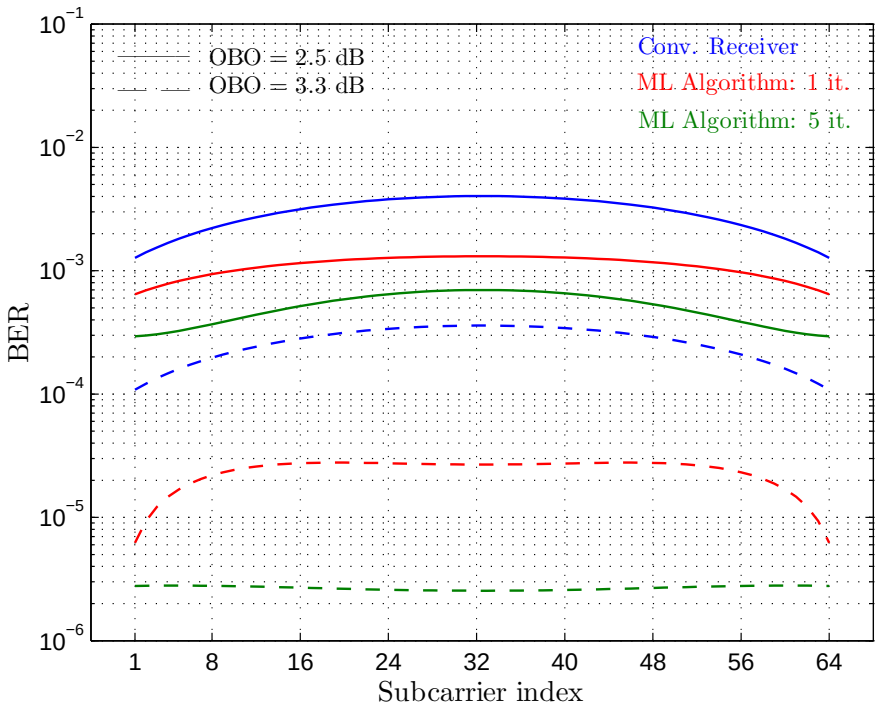

FIGURE 5.17: Bit error rate versus subcarrier index for OFDM/BPSK signals with 64 subcarriers, an SNR per bit of 10 dB and different OBO values. Results for both conventional receiver and iterative ML algorithm are presented.

as a function of the subcarrier index is practically constant. So, preliminarily results for the iterative ML algorithm suggest that its performance in terms of error probability improves with the number of iterations used. Moreover, it is also observed that the improvement in terms of performance of the ML algorithm relative to the conventional receiver varies with the OBO value.

A detailed analysis of the error probability performance of nonlinearly distorted OFDM signals, demodulated and detected by both conventional and ML receivers, will be performed in the following sections.

5.3.1 Impact of the output back-off

In Figure 5.18 it is depicted the error probability performance for the iterative ML algorithm in comparison with the conventional and ML receivers as a function of the OBO for OFDM/BPSK signals with 16 and 64 subcarriers. The AWGN PSD levels were chosen so both OFDM signals could have the same E_b/N_0 at each OBO value. Also, several iterations are considered for the ML algorithm. Equivalent results for an

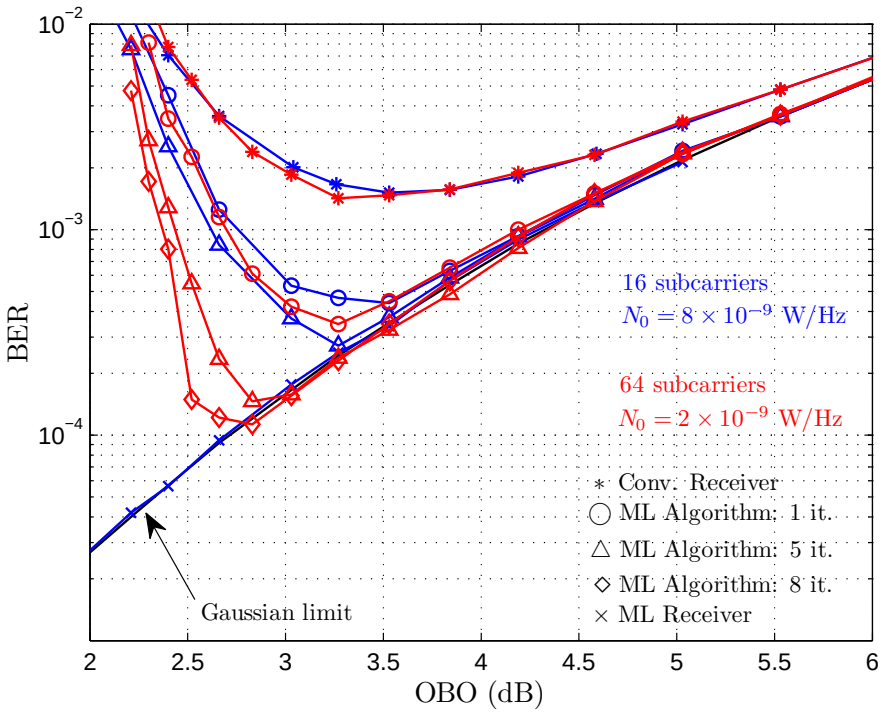

FIGURE 5.18: Bit error rate vs output back-off for OFDM/BPSK signals with 16 and 64 subcarriers and AWGN PSDs of 8×10^{-10} W/Hz and 2×10^{-10} W/Hz, respectively. Results for conventional, iterative ML and optimum ML receivers are presented.

SNR per bit 3 dB above the previous ones are shown in Figure 5.19. Note that when the number of iterations of the algorithm is zero, it corresponds to the conventional receiver. The Gaussian limits were obtained using the complementary error function (erfc) for the E_b/N_0 value at each OBO. These curves indicate the theoretical minimum BER values if a linear channel was considered.

Results show that for high OBO values, the AWGN noise contribution is dominant and, as expected, the error probability performances of both conventional and iterative ML receivers are similar. When OBO decreases, the nonlinear noise increases and after reaching a certain operating point, it starts to dominate over the AWGN. Due to the nature of the ML algorithm, part of nonlinear noise is seen as useful information, hence, it is used to optimally estimate the transmitted complex symbols vector. An analysis of the obtained results allow us to say that the iterative ML algorithm outperforms the conventional receiver and that the gap in performance seems to increase with the decrease of the AWGN noise level. Moreover, it can also be seen that both minimum BER level and corresponding OBO value decrease with the number of iterations used. For very

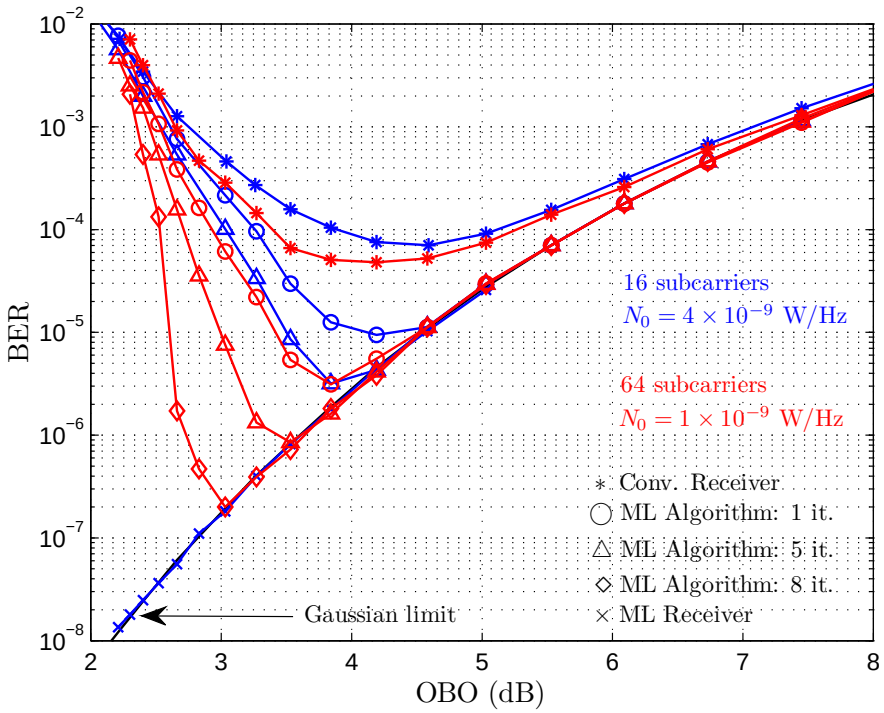

FIGURE 5.19: Bit error rate vs output back-off for OFDM/BPSK signals with 16 and 64 subcarriers and AWGN PSDs of 4×10^{-10} W/Hz and 1×10^{-10} W/Hz, respectively. Results for conventional, iterative ML and optimum ML receivers are presented.

low OBO values the nonlinear noise reaches an unbearable level and the performance of both receivers start to degrade rapidly and to converge.

Results for the ML receiver are only shown for the 16 subcarriers scenario since for 64 subcarriers it would be impossible to simulate due to its extremely high time consuming nature. For this case, it can be seen that the performance of the ML receiver equals the Gaussian limit.

From the observation of both Figures 5.18 and 5.19 we can also conclude that BERs of both conventional and iterative ML receiver for OFDM signals with 64 subcarriers are lower than the corresponding BERs for the 16 subcarriers case. Moreover, the OBO value for which the BER is minimum seems to decrease as the number of subcarriers increase. From these results it is possible to determine the OBO value that provides the minimum BER value for each receiver structure. This operating point can be see as optimum and the best to use when considering a constant AWGN level. On the other hand, if the goal is to operate with a BER level no higher than a given value, than, it can be seen that by using the ML algorithm, a wider OBO range is tolerable, i.e., it allows

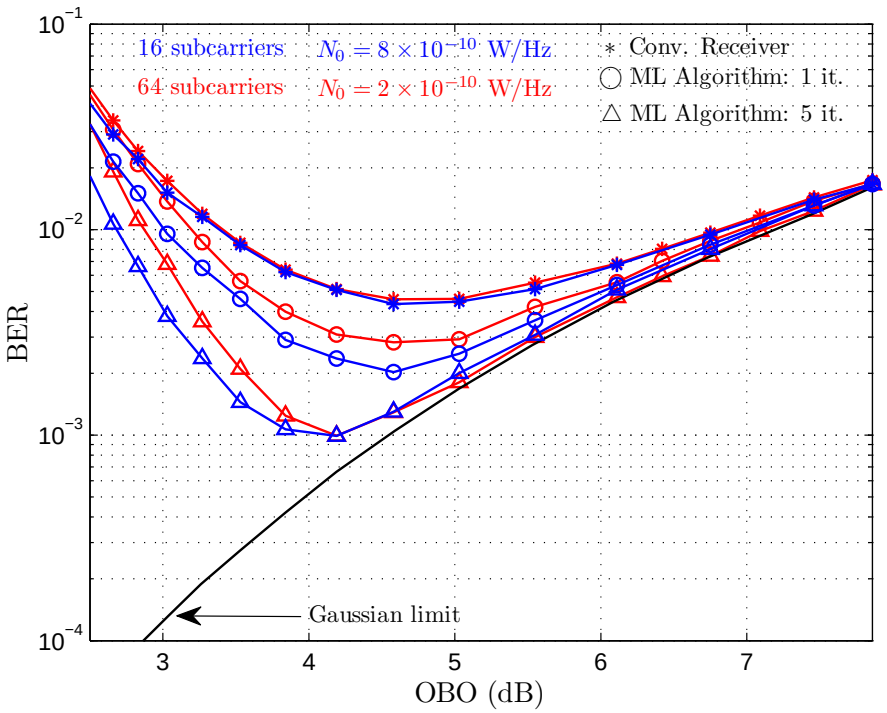

FIGURE 5.20: Bit error rate vs output back-off for OFDM/16-QAM signals with 16 and 64 subcarriers and AWGN PSDs of 8×10^{-10} W/Hz and 2×10^{-10} W/Hz, respectively. Results for conventional and iterative ML receivers are presented.

the transmission of OFDM signals with higher dynamic ranges. The OBO operating point that provides the best trade-off in terms of degradation for a specific BER level will be a subject of study in an upcoming section.

Equivalent results for OFDM/16-QAM signals are depicted in Figures 5.20 and 5.21. Results show that for the highest AWGN PSD level (Figure 5.20) the BERs of all receivers are similar for both 16 and 64 subcarriers cases, whereas for the lowest AWGN PSD level (Figure 5.21) the error probability performances for the 64 subcarriers case better than the ones of the 16 subcarriers case. Nevertheless, the gap in terms of performance between the iterative ML algorithm and the conventional receiver appears to increase as the AWGN PSD level decreases.

5.3.2 Impact of the AWGN PSD

To show the impact of the AWGN PSD level in the error probability performance we consider OFDM signals with 16 subcarriers conveying different modulation schemes as

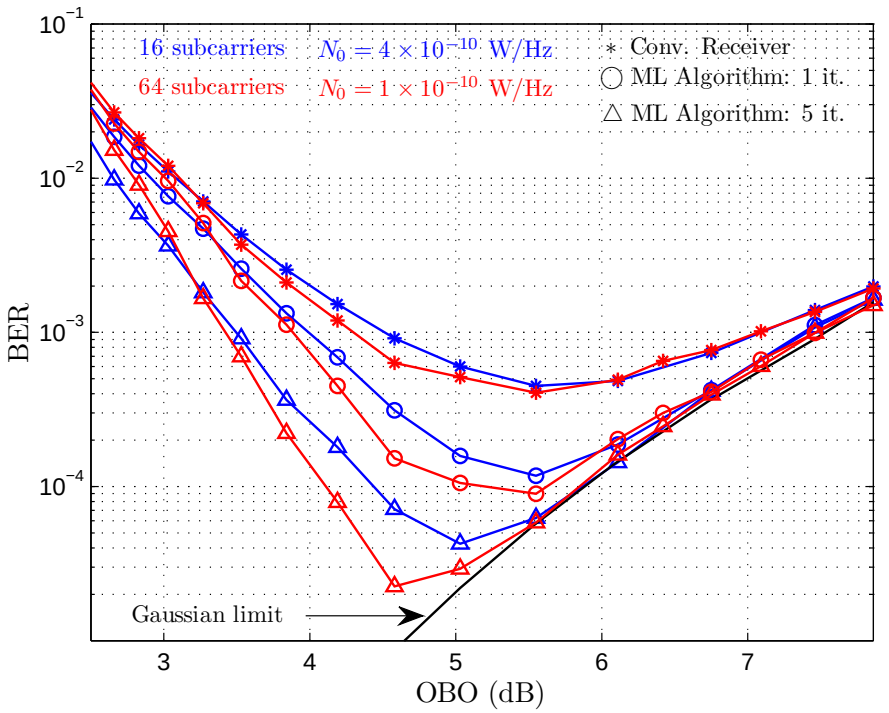

FIGURE 5.21: Bit error rate vs output back-off for OFDM/16-QAM signals with 16 and 64 subcarriers and AWGN PSDs of 4×10^{-10} W/Hz and 1×10^{-10} W/Hz, respectively. Results for conventional and iterative ML receivers are presented.

well as OBO values. In Figures 5.22 and 5.23 it is depicted the results for OFDM/BPSK/QPSK and OFDM/8-PSK transmissions, respectively, whereas in Figure 5.24 it is depicted the OFDM/16-PSK/16-QAM transmission cases. As expected, the error probability performances of both receivers, conventional and ML algorithm with one or five iterations, increase with the ratio E_b/N_0. Again, results show a significant improvement when the ML algorithm with one or five iterations are considered. Moreover, even for relatively low SNR per bit values values, the error probability performance curves for the ML algorithm with one and, even clearly, five iterations starts to deviate from the ones given by the conventional receiver.

The results from Figures 5.22, 5.23 and 5.24 also show that, as it was previously stated, the gap between performance curves seems to increase inversely with the noise power. Nevertheless, the behavior of BER curves suggest that they eventually tend asymptotically to a specific value.

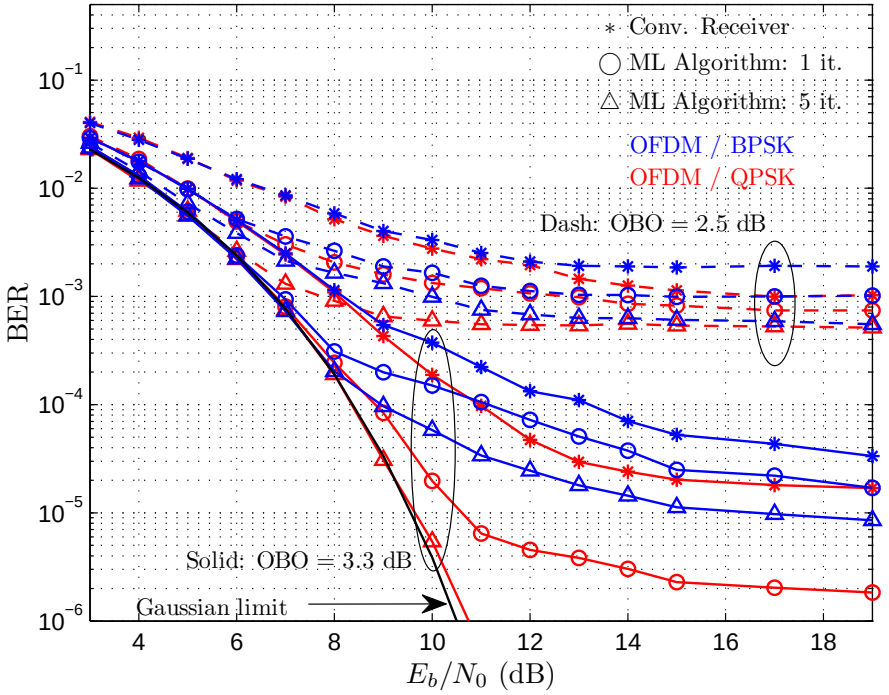

FIGURE 5.22: Bit error rate versus E_b/N_0 for OFDM/BPSK and OFDM/QPSK signals with 16 subcarriers, considering different back-offs and number of iterations for the iterative ML algorithm.

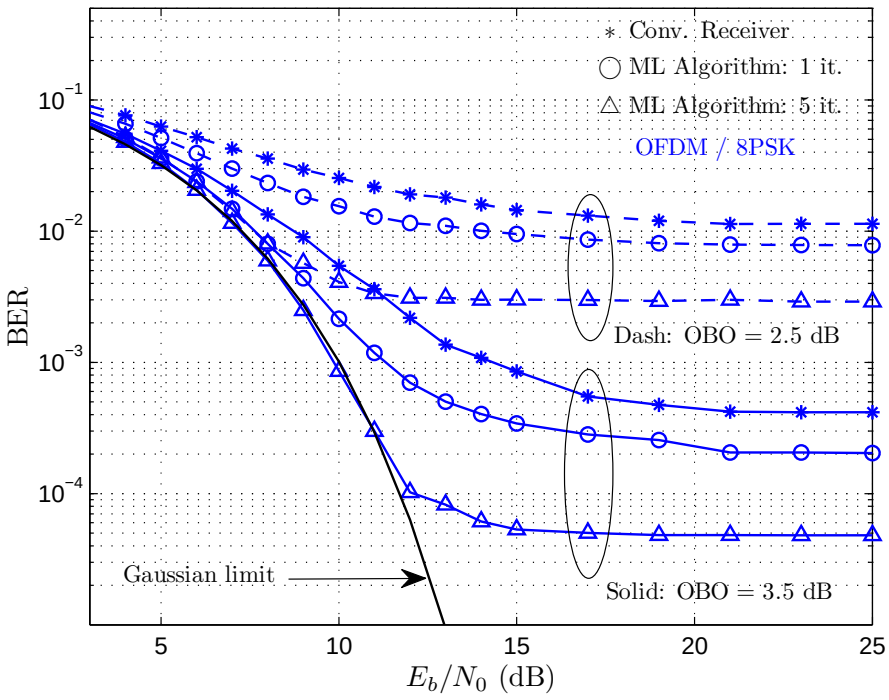

FIGURE 5.23: Bit error rate versus E_b/N_0 for OFDM/8-PSK signals with 16 subcarriers, considering different back-offs and number of iterations for the iterative ML algorithm.

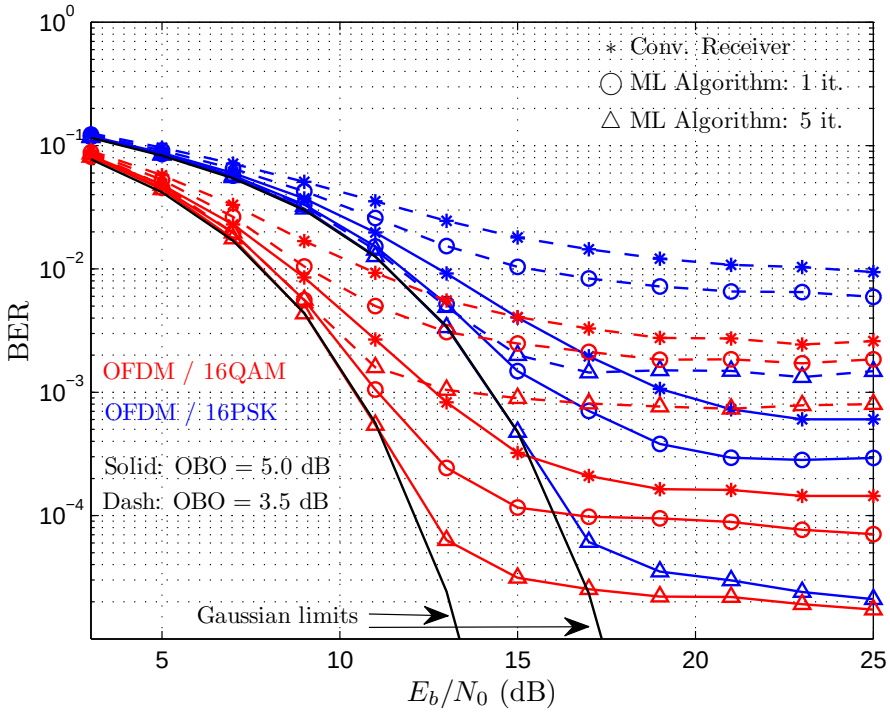

FIGURE 5.24: Bit error rate versus E_b/N_0 for OFDM/16-PSK and OFDM/16-QAM signals with 16 subcarriers and considering different back-offs and number of iterations for the iterative ML algorithm.

5.3.3 Optimum nonlinear operation point

As it was previously stated and discussed, the effects of nonlinearities can be minimized by working at high OBO values, i.e., at a linear region of the nonlinear element. However, such option is not always the one of interest and an efficient use of the available transmit power should be performed. From the discussion of the previous results it is possible to conclude that an optimum operating point, in terms of error probability performance, for both conventional and iterative ML algorithm receivers may exist. In this context, a well-known performance figure used is the total degradation (TD) as a function of the output (or input) back-off. The total degradation parameter is defined as [100, 101]

$$\mathrm{TD[dB]} = \left[\left(\frac{E_b}{N_0}\right)_{NL} - \left(\frac{E_b}{N_0}\right)_{L}\right] + \mathrm{OBO} \tag{5.12}$$

where $\left(\frac{E_b}{N_0}\right)_{NL}$ is the required SNR per bit in decibels at the input of the threshold detector to obtain a fixed BER for a given OBO value and $\left(\frac{E_b}{N_0}\right)_{L}$ is the required SNR per bit in decibels to obtain the same fixed BER in absence of nonlinearity. In other

words, it is the sum of the OBO and the increment in the SNR per bit to achieve a given BER with respect to the case of a linear channel. The optimum operating point is defined as the best trade-off between the maximum output power and the minimum signal degradation due to nonlinear distortion. So, the optimum operating point at a given BER level is the one that minimizes the total degradation given by (5.12).

Figures 5.25 and 5.26 show the total degradation for OFDM/M-PSK signals with 16 subcarriers and for $M = 2, 4, 8, 16$. Results for the conventional receiver and for the iterative ML algorithm considering different number of iterations evaluated for a target BER of 10^{-3} are presented. Note that the black line corresponds to the linear channel scenario. As expected, for high OBO values, the total degradation of both receivers and modulation schemes conveyed in subchannels tend to the degradation level of the linear channel. When OBO decreases, the nonlinear noise increases and the total degradation decreases but at a lower rate until the optimum point at which the degradation reaches its minimum is achieved. After that point, all curves asymptotically tend to infinity at certain OBO values, meaning that the nonlinear noise level dominates over the AWGN source and that those transmission cases do not achieve the BER target of 10^{-3}.

Let us focus on the behavior of both conventional and iterative ML algorithm receivers. While the conventional receiver performance starts to deviate from the pure Gaussian channel case at a relatively high OBO value, the degradation associated with the ML algorithm continues pursuing its minimum located at a lower OBO. Yet, after reaching its optimum operating point, results show that degradation increases at a much higher slope rate, comparatively to the degradation curve of the conventional receiver. Thus, when working near the optimum operating point, the iterative ML algorithm demands a tighter OBO control in order to be at the minimum total degradation point. Results from Figures 5.25 and 5.26 indicate that both the operating point and total degradation decrease with the number of iterations used. Similar results for OFDM signals with 64 subcarriers are also presented in Figures 5.27 and 5.28.

Another interesting result that has been discussed previously is the gap between performance curves. From Figures 5.25 through 5.28 it is clear that there is an improvement in terms of degradation when the ML algorithm is used. Moreover, results seem to indicate that the gap between the conventional receiver and the five iterations

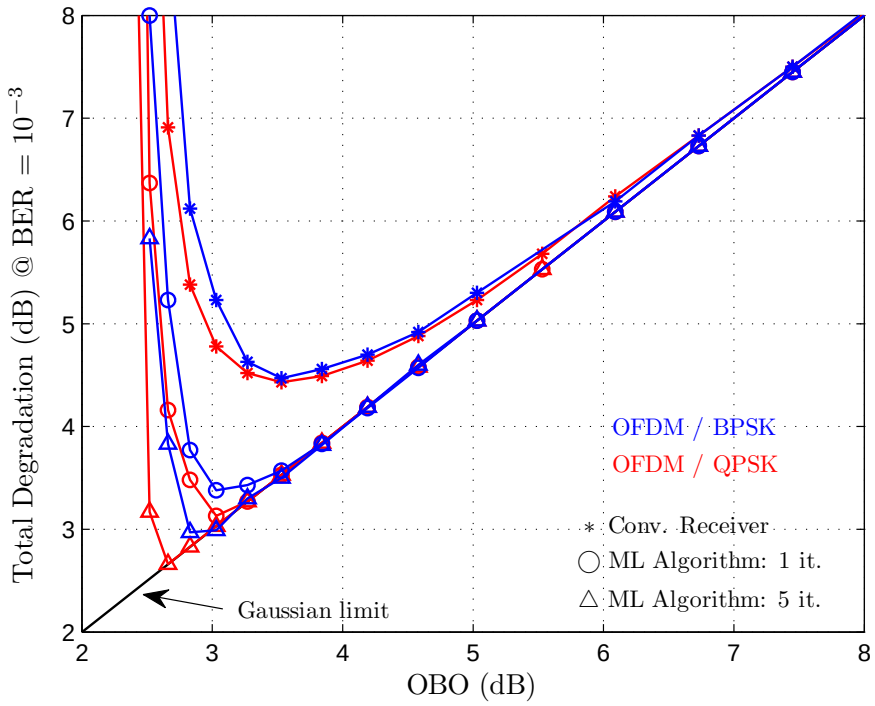

FIGURE 5.25: Total degradation versus output back-off for both OFDM/BPSK and OFDM/QPSK signals with 16 subcarriers when considering both conventional receiver and iterative ML algorithm. Results for a bit error rate target of 10^{-3}.

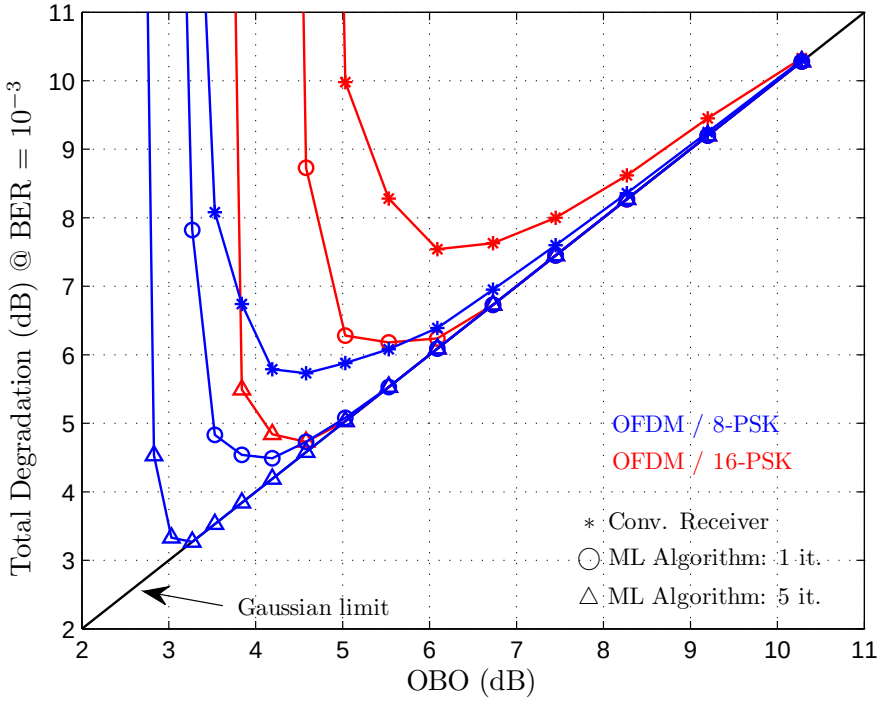

FIGURE 5.26: Total degradation versus output back-off for both OFDM/8-PSK and OFDM/16-PSK signals with 16 subcarriers when considering both conventional receiver and iterative ML algorithm. Results for a bit error rate target of 10^{-3}.

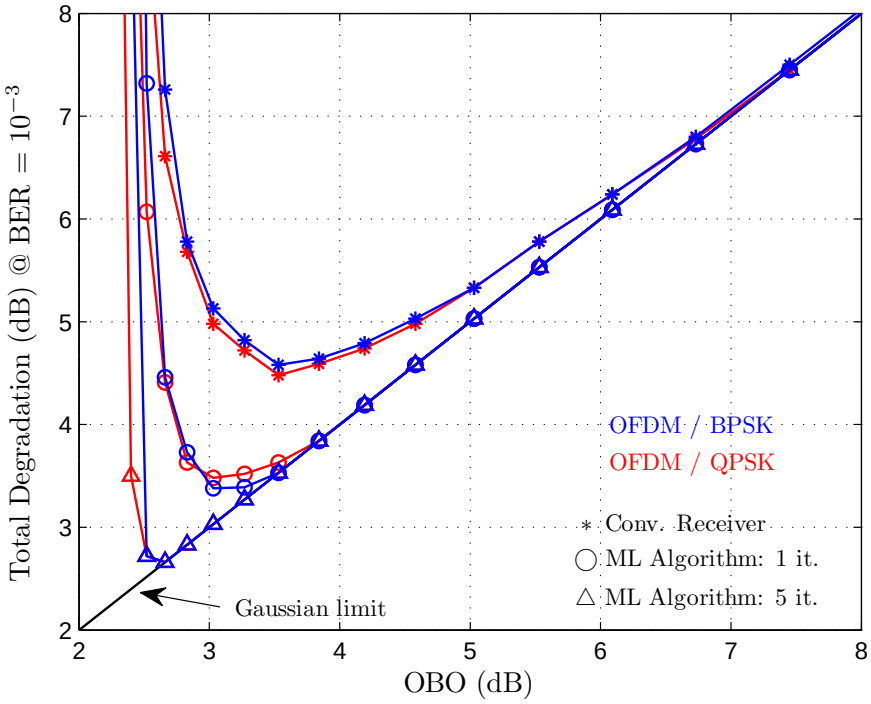

FIGURE 5.27: Total degradation versus output back-off for both OFDM/BPSK and OFDM/QPSK signals with 64 subcarriers when considering both conventional receiver and iterative ML algorithm. Results for a bit error rate target of 10^{-3}.

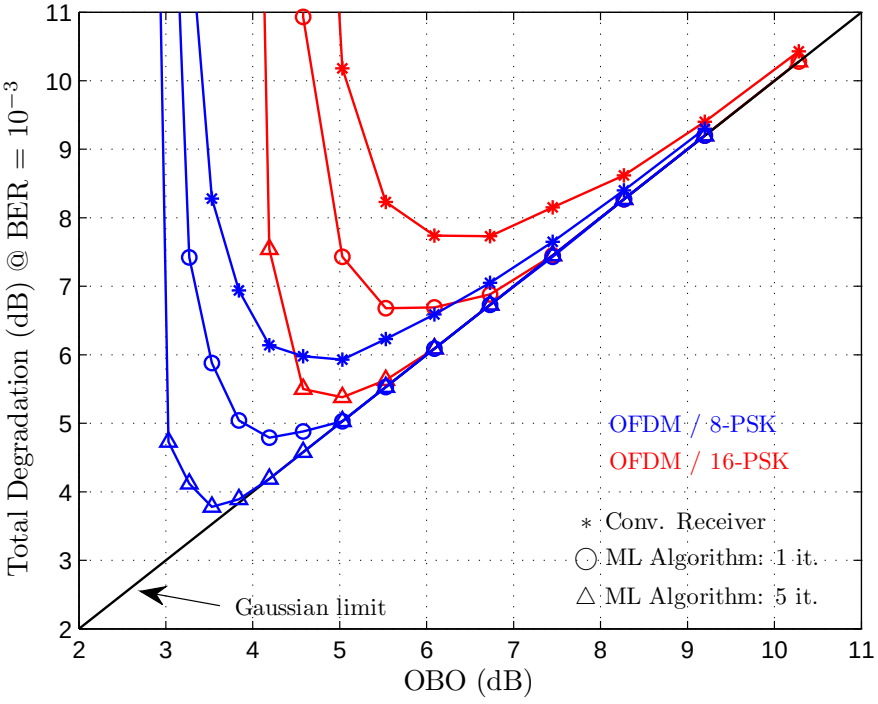

FIGURE 5.28: Total degradation versus output back-off for both OFDM/8-PSK and OFDM/16-PSK signals with 64 subcarriers when considering both conventional receiver and iterative ML algorithm. Results for a bit error rate target of 10^{-3}.

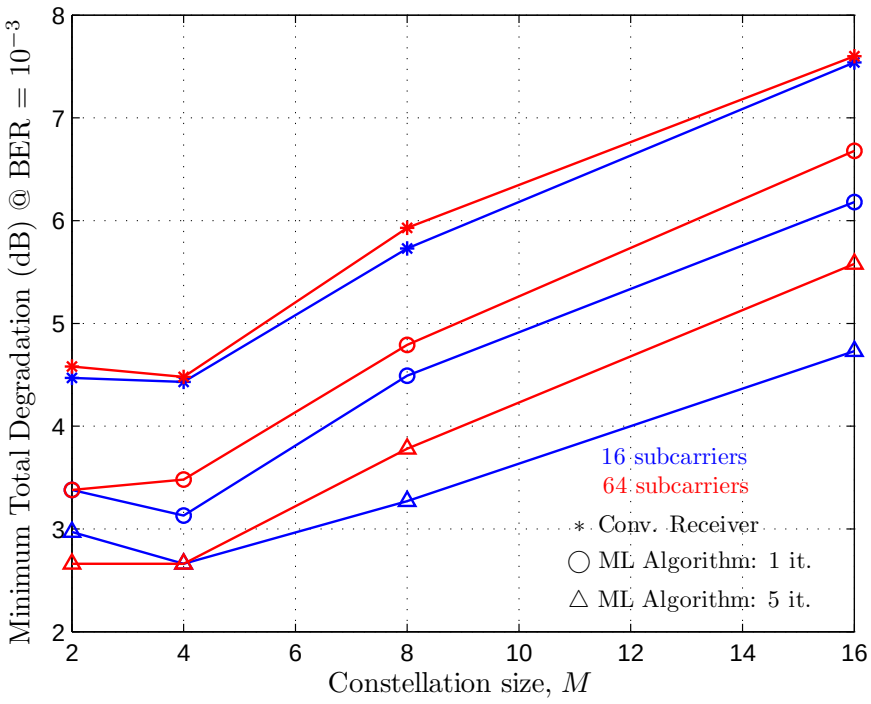

FIGURE 5.29: Minimum (and optimum) total degradation versus size of constellation for OFDM/M-PSK signals with 16 and 64 subcarriers when considering both conventional receiver and iterative ML algorithm. Results for a bit error rate target of 10^{-3}.

ML algorithm increases with the size of constellation. To understand better how both minimum degradation point and corresponding OBO value change, their minimum (and optimum) values are, respectively, depicted in Figures 5.29 and 5.30 as functions of the size of constellation. From the observation of both Figures, it can be concluded that the OFDM/QPSK modulation is the one that provides the best performance in terms of minimum total degradation for both conventional and iterative ML algorithm. Nonetheless, the difference for the OFDM/BPSK modulation scheme is practically negligible. For M-PSK constellations with size $M > 4$, the results show that minimum degradation and corresponding OBO value start to increase. So, as the constellation size increases, the optimum operating point increases and so does the minimum total degradation. This behavior was found to be identical for both receivers. Furthermore, for the BER target of 10^{-3}, Figures suggest that in general OFDM signals with 16 subcarriers produce slight better results than with 64 subcarriers, in terms of minimum total degradation.

One of the most important results that can be extracted from total degradation plots is the gain improvement that the ML algorithm brings to the link transmission,

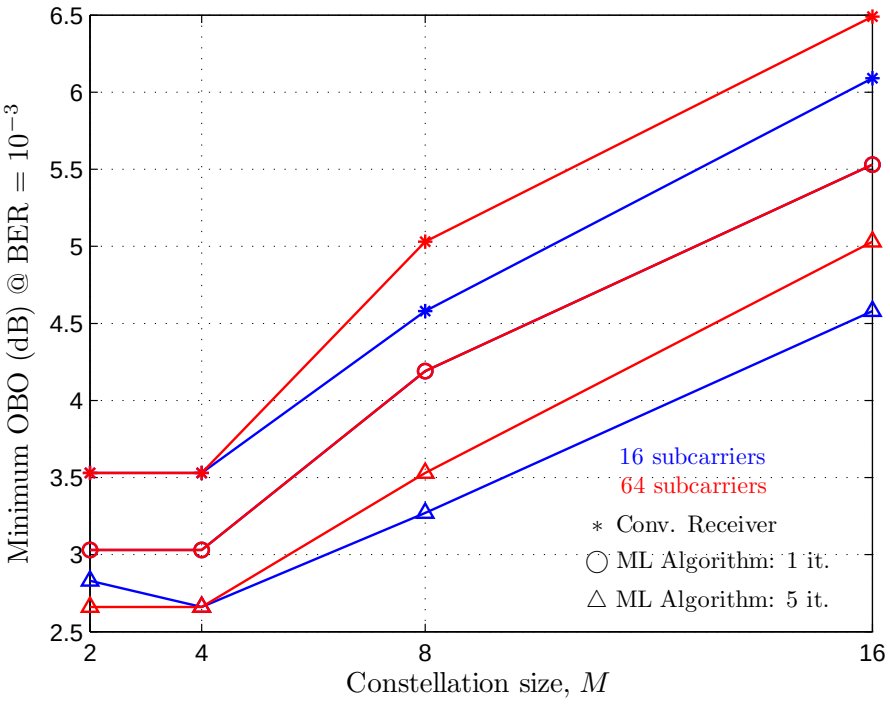

FIGURE 5.30: Minimum (and optimum) output back-off versus size of constellation for OFDM/M-PSK signals with 16 and 64 subcarriers when considering both conventional receiver and iterative ML algorithm. Results for a bit error rate target of 10^{-3}.

relatively to the conventional receiver. For instance, results for OFDM/8-PSK signals show that the minimum total degradations when considering the conventional receiver, iterative ML algorithm with one and 5 iterations are approximately 5.7 dB to 4.5 dB and 3.3 dB, leading to a reduction of 2.4 dB in signal power degradation. In other words, the ML algorithm provides us a link gain margin of 2.4 dB that can be used to relax noise receiver requirements or, equivalent, to allow an additional attenuation in the transmission link. Alternatively, it can also be seen that OFDM/16-PSK signals jointly with the ML algorithm provides the same degradation as the OFDM/BPSK signals detected by a conventional receiver, allowing a higher bit rate.

In Table 5.1 it is summarized the minimum total degradation improvements obtained when a five iterations ML algorithm is used relative to the conventional receiver. It is important to note that if a lower BER target was considered, say 10^{-4}, we would expect even more pronounced link gain margins. This result can be extrapolated from the ones given by Figures 5.18 through 5.24. Some preliminary simulation results of TD were in fact obtained for a BER of 10^{-4} only to a specific case so we could confirm it. Yet, due

TABLE 5.1: Minimum degradation improvements for the five iterations ML algorithm.

		Minimum Degradation Gain (dB)
OFDM/BPSK	N = 16	1.50
	N = 64	1.92
OFDM/QPSK	N = 16	1.77
	N = 64	1.82
OFDM/8-PSK	N = 16	2.46
	N = 64	2.15
OFDM/16-PSK	N = 16	2.81
	N = 64	2.02

to the very high simulation time that TD results demand we decided to present only the ones for a BER of 10^{-3}.

5.3.4 Influence of the number of subcarriers used

As it was previously referred in sections 5.3.1 and 5.3.3, the error probability performance of nonlinearly distorted OFDM signals varies with the number of subcarriers used. Furthermore, in section 5.2, we have seen that the variance of the IMD component of the nonlinearly distorted OFDM signal increases with the number of subcarriers used. In this section we present simulation results for both conventional and iterative ML receiver for OFDM/M-PSK signals considering different number of subcarriers.

In Figures 5.31 and 5.32 it is depicted the error probability performance for OFDM/BPSK signals as a function of the number of subcarriers used for SNR per bit values of 5 dB and 10 dB, respectively. Results are presented for OBO values of 3.3 dB and 2.5 dB. Results show that when a conventional receiver is considered, the BER increases slightly with number of subcarriers for a low E_b/N_0 value of 5 dB. However, for an SNR per bit of 10 dB, the BER for an OBO value of 2.5 dB is practically constant, while for an OBO of 3.3 dB a worst number of OFDM subcarriers in terms of BER seems to arise around 12 and 16. In fact, as the SNR per bit increases even further, it was already demonstrated that there is indeed a worst number of subcarriers in terms of BER [102]. This behavior can be explained by analyzing the properties of the IMD component of

the nonlinearly distorted OFDM signal. It has been shown that the heaviness of the tails of the IMD distribution diminishes by increasing the number of subcarriers [102]. On the other hand, the variance of the IMD increases with the number of subcarriers used. While the former effect induces a decrease of the error rate, the later implies an increase of the error probability rate. Therefore, a worst number of subcarriers in terms of error probability performance is expected, independently of the OBO value and specially for high SNR per bit values.

Let us focus now on the error probability performance of the iterative ML algorithm. From the observation of Figures 5.31 and 5.32, we can see that its behavior is highly dependent on the SNR per bit and OBO values. Results show that for an SNR per bit value of 5 dB, the BER of the ML algorithm with one iteration increases with the number of subcarriers following the tendency of the conventional receiver, whereas with five iterations a decreasing BER is reported. On the other hand, for an OBO value of 3.3 dB, the five iterations ML algorithm seems to produce nearly optimum BER results by following the Gaussian limit BER. Similar results are also reported for the one iteration case, specially when the number of subcarriers is considered to be bellow 24. For higher number of subcarriers the BER starts to increase.

For an SNR per bit of 10 dB (Figure 5.32), the BER of the iterative ML algorithm has distinguishable behaviors depending on the OBO value. In fact, for an OBO value of 2.5 dB, it can be seen that the BER diminishes with the number of subcarriers. Yet, its performance is still 100 times worst than the optimum error rate given by the Gaussian limit. On the other hand, for an OBO value of 3.3 dB, the results show the same behavior previously referred for the conventional receiver with a very well pronounced worst number of subcarriers case at around 12 and 16, independently on the number of iterations used. Nevertheless, the results for the five iterations case practically equals the ones of the optimum receiver for a number of subcarriers of 8, 32 and above.

Equivalent results for OFDM/16-PSK signals are also plotted in Figures 5.33 and 5.34 but for SNR per bit values of 15 dB and 25 dB, respectively. Results for the lower SNR per bit value given by Figure 5.33 show that both conventional and iterative ML algorithm have similar performance curves to the ones given by OFDM/BPSK signals in Figure 5.31. On the other hand, for a relatively high SNR per bit value of 25 dB

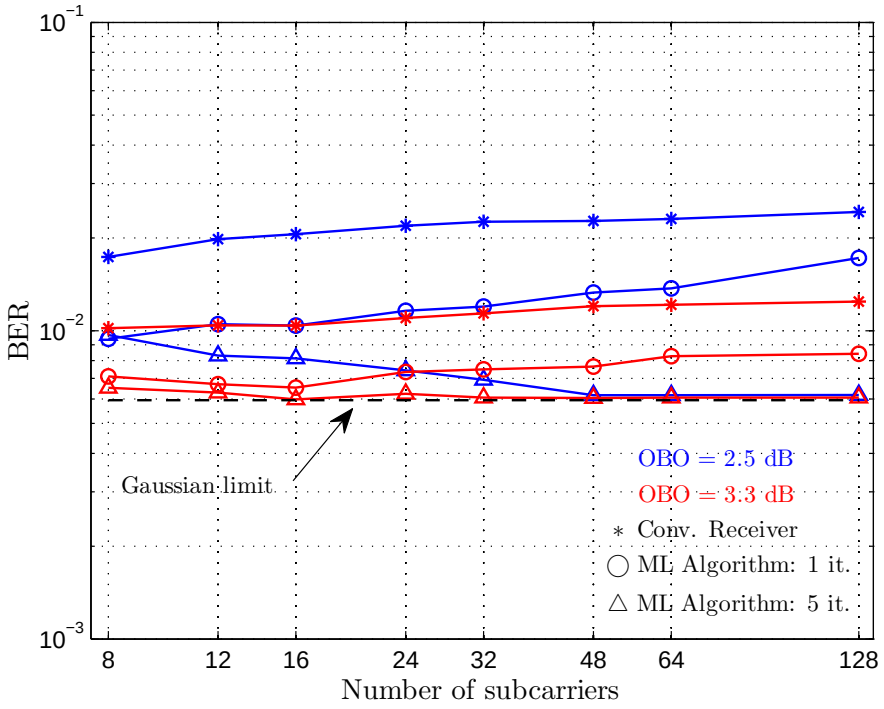

FIGURE 5.31: Bit error rate as a function of the number of subcarriers for an OFDM/BPSK signal with $E_b/N_0 = 5\,\text{dB}$ and various OBO values.

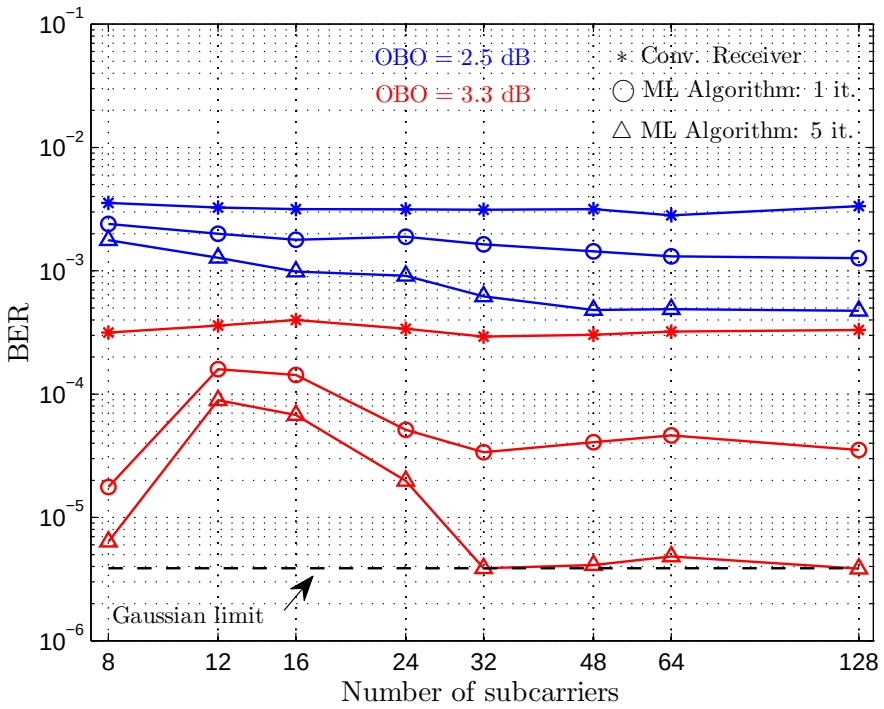

FIGURE 5.32: Bit error rate as a function of the number of subcarriers for an OFDM/BPSK signal with $E_b/N_0 = 10\,\text{dB}$ and various OBO values.

(Figure 5.34), BER results for the conventional receiver show that the same behavior of a worst number of subcarriers is only observed when a high OBO value of 5.0 dB is considered. Yet, a very pronounced worst case is not reported. This behavior is again explained by the properties of the IMD component. As previously stated, the variance of the IMD component increases with the number of subcarriers (see Figure 5.14) while the heaviness of the tails of its distribution decreases. By increasing the size of the constellation it is likely that the correlation between the various IMP terms that fall in a particular OFDM subchannel diminishes, increasing the speed of convergence to a Gaussian distribution. Regarding the performance of the ML algorithm, the results show that the BER performance also have a worst number of subcarriers around 24 and 32 for a one iteration receiver and around 32 and 48 for a five iterations receiver.

Furthermore, results also show that the gap in terms of BER between both receivers decreases as the number of subcarriers increase.

In conclusion, BER results from both modulation schemes show that the iterative ML algorithm follow the same behavior of a worst number of subcarriers, similarly to what happens when a conventional receiver is considered. This suggests again that the iteration 'zero' given by the conventional receiver may be a serious performance limiting factor. Moreover, for a 16-PSK modulation scheme, and contrary to what happens for the BPSK, we can conclude that its performance relative to the one of the conventional receiver seems not to increase with the number of subcarriers. Nevertheless, the results indicate that the iterative ML receiver always outperforms the conventional one and also that it performs better for high SNR per bit values.

5.3.5 Performance impact of both size of search region and number of iterations used

We will now study the impact in terms of error probability performance of the region size in which the iterative ML algorithm searches for the minimum BER. By proving a wider search area to the iterative ML algorithm, it is expected a better estimate of the transmitted vector in terms of error probability. Figure 5.35 depicts the results of BER for OFDM/BPSK signals with 16 subcarriers and three OBO values as a function of the size search region (Hamming distance). Additionally, only one iteration of the

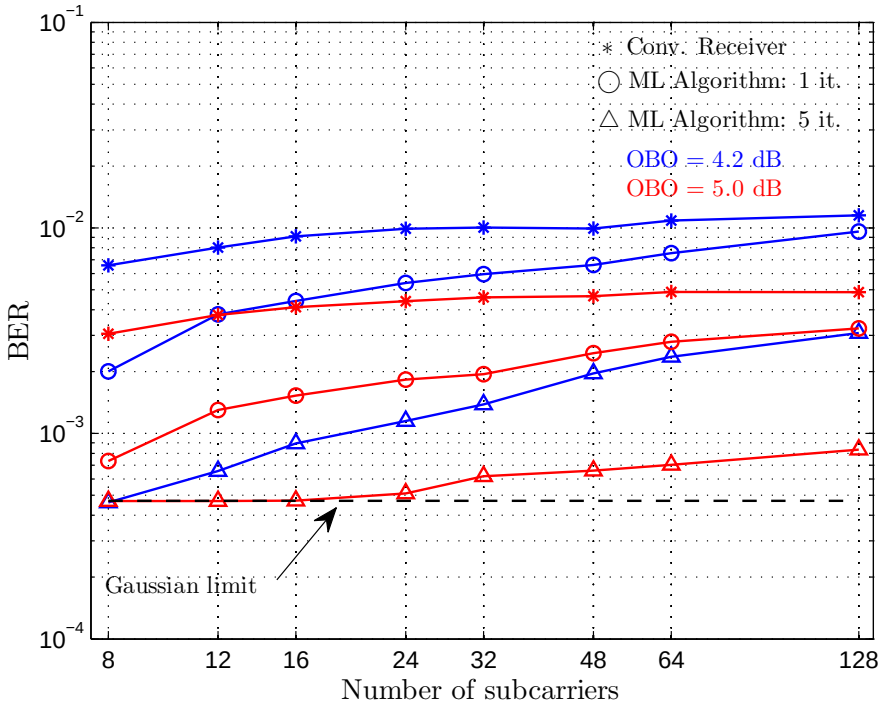

FIGURE 5.33: Bit error rate as a function of the number of subcarriers for an OFDM/16-PSK signal with $E_b/N_0 = 15\,\text{dB}$ and various OBO values.

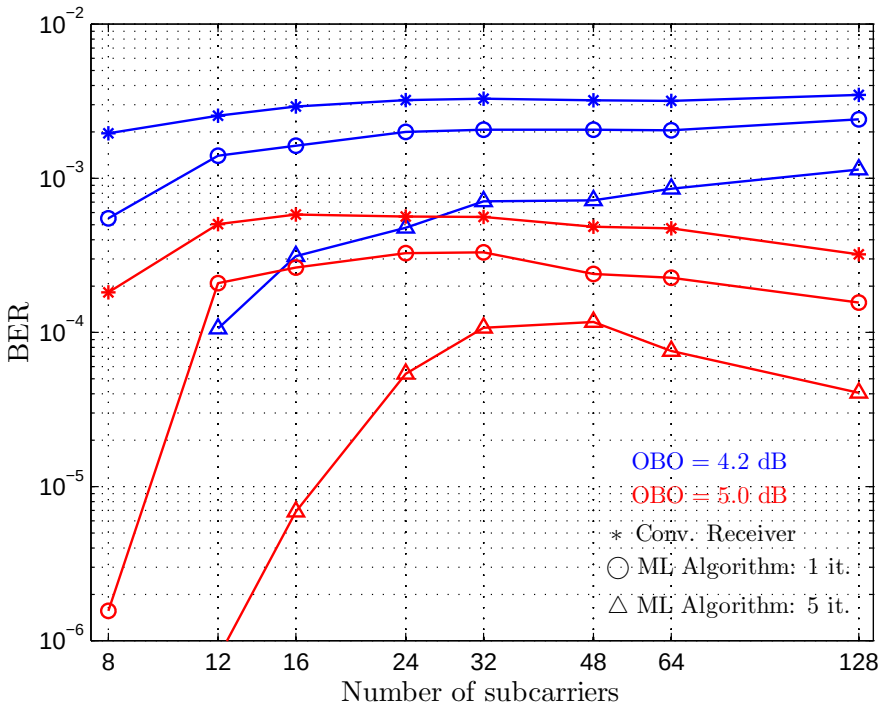

FIGURE 5.34: Bit error rate as a function of the number of subcarriers for an OFDM/16-PSK signal with $E_b/N_0 = 25\,\text{dB}$ and various OBO values.

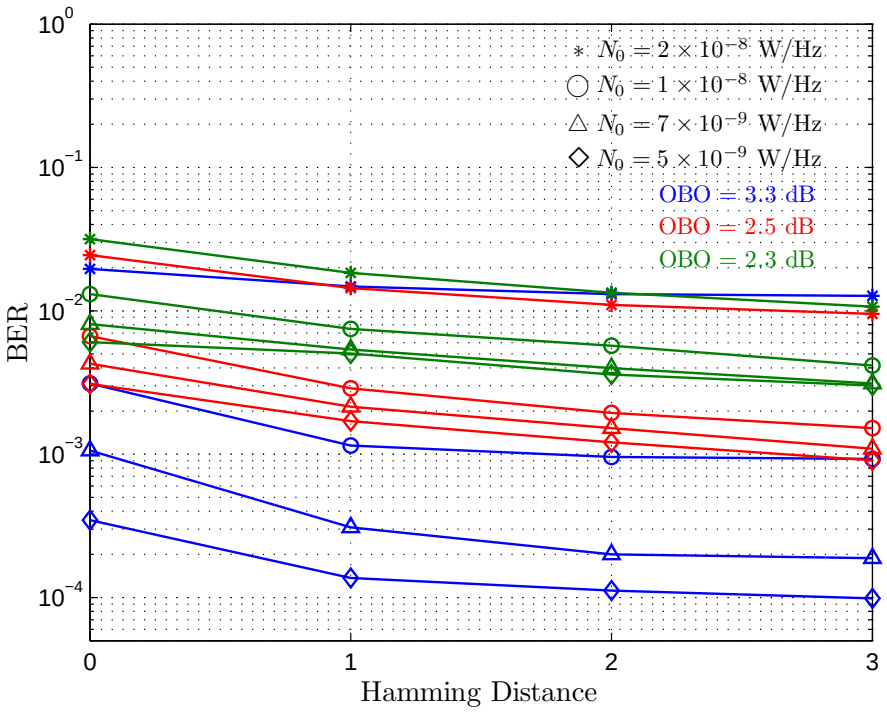

FIGURE 5.35: Bit error rate versus size of the search region for the iterative ML algorithm considering OFDM/BPSK signals with 16 subcarriers and different OBO and AWGN PSD values.

ML algorithm is considered. From the observation of the results, we can conclude that the wider the search region, the better estimate of the transmitted vector. Moreover, a careful observation shows that for an OBO value of 3.3 dB there is a considerable decrease of BER as the Hamming distance increases from zero to one. However, for Hamming distances greater than one, the improvement is minimal. This behavior which is common to all AWGN PSD levels considered suggests that the local minimum was achieved and that no further improvement in terms of error probability is obtained by increasing the search region size. On the other hand, for lower OBO values, it can be seen that the error probability performance continues to improve even further as the search region expands. This performance improvement can be explained by the following: as previously stated, the strength of IMPs that fall inside the signal's bandwidth originating the nonlinear noise increases inversely with the OBO; additionally, the lower the AWGN PSD level, the greater is the dominance of the nonlinear noise over it. Since the iterative ML algorithm uses this noise-like signal to obtain a better estimate of the transmitted vector, when the nonlinear distortion increases it is acceptable to say that there is an

increased difficulty in finding the best estimate. Consequently, by increasing the size of the region where the algorithm is allowed to search, we also increase the possibility for the algorithm to find an estimate responsible for a higher likelihood value.

Figures 5.36 and 5.37 show the error probability performance of the iterative ML algorithm as a function of the number of iterations used considering different SNR per bit values. The results given are for OFDM/BPSK signals with 16 subcarriers and OBO values of 3.3 dB and 2.5 dB, respectively. Furthermore, it is depicted the error probability performance of the algorithm for search region sizes expanded to a Hamming distance of one ($h = 1$) and three ($h = 3$). Note that the iteration 'zero' of the ML algorithm is equivalent to signal detection using a conventional receiver, therefore there is no difference in error probability performance for both search region sizes. From these set of results we can extract several interesting conclusions. As expected, when the number of iterations increase, the algorithm with a larger search region outperforms the other one since it searches for the best estimate in a wider search area. Also, it can be seen that the convergence speed for both Hamming distances ($h = 1$ and $h = 3$) is faster when considering low SNR per bit values.

Let us now focus on Figure 5.36 which corresponds to an OBO value of 3.3 dB. The fast convergence speed, specially for low SNR per bit values, is mainly due to the fact that the AWGN dominates over the distortion introduced by the nonlinearity, and so there is no significant improvement for both search regions. In fact, all cases depicted except one, have their BER converging to the AWGN BER level, meaning that their results converge to the ones of the optimum receiver. The case that do not converges is the one for the highest SNR per bit case considered. Here, the nonlinear noise dominates over the AWGN and the algorithm could not reach the minimum BER in the number of iterations considered.

With respect to the difference between the results for Hamming distances of one and three, Figure 5.36 shows that after just one iteration, the results of the algorithm with $h = 3$ equal the ones for the optimum receiver for all cases except for the highest SNR per bit, whereas the algorithm with $h = 1$ needs two to four iterations to achieve the same result.

In Figure 5.37 it is depicted equivalent results for a lower OBO value. At first, one

may expect that the BER performance of the iterative ML algorithm would also increase with the nonlinear distortion. However, it is not guaranteed that the iterative algorithm converges to the global minimum and a local minimum is more likely. From the observation of Figure 5.37, for low OBO values the distortion level from the nonlinearity is high enough to dominate over the AWGN and to prevent the iterative algorithm to improve its performance above a certain SNR per bit. Despite all BER curves converge after one and three iterations for the smallest and wider search region receivers, respectively, only the ones for the lowest SNR per bit converge to the optimum BER level. Nevertheless, and contrary to what happened for an OBO value of 3.3 dB, the BER curves for the ML algorithm using search regions of Hamming distances of three always outperforms the ones for the smaller search region cases. These interesting results indicate that the first vector estimates given by the algorithm are critical and that when a larger search region is considered, the algorithm choses a considerable better local minimum with just one iteration than when considering a search region universe consisting of possible estimative vectors that differ by only one bit.

Equivalent results for OFDM/BPSK signals with 64 subcarriers are presented in Figures 5.38 and 5.39. From the observation of the results for OFDM/BPSK signals with 16 and 64 subcarriers depicted in Figures 5.36 through 5.39, several important conclusions can be drawn. First of all, it can be seen that when considering 64 subcarriers the number of iterations needed to achieve a constant error probability is higher. Regarding the results for an OBO value of 3.3 dB plotted in Figure 5.38, and contrary to what was observed for the 16 subcarriers case, the $h = 3$ algorithm is capable of reaching the AWGN BER level after two iterations for all SNR per bit levels considered. Moreover, results show that, for the highest SNR per bit case, the algorithm with the smallest search region with eight iterations does not even outperforms the algorithm with just one iteration and the wider search region.

With respect to the results for an OBO value of 2.5 dB, the steady-state BER level is not achieved with less than nine and three iterations for search regions of Hamming distances of one and three, respectively. In the origin of this result is the higher number of IMPs that are generated due to the higher number of subcarriers used. Therefore, the results suggest that the local minimum of the error probability was not achieved

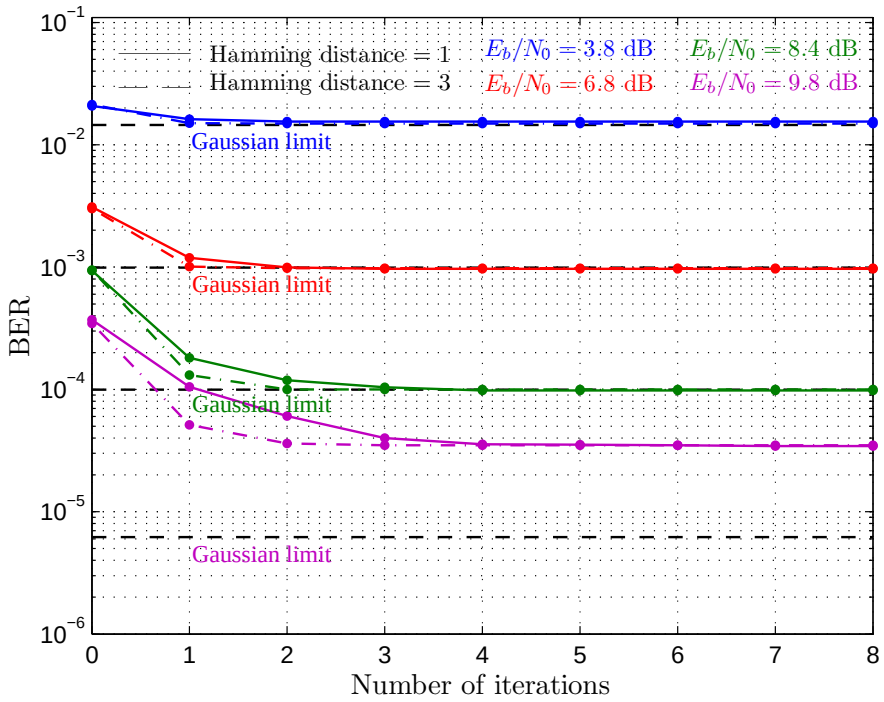

FIGURE 5.36: Bit error rate vs. number of iterations of the iterative ML algorithm for an OFDM/BPSK signal with 16 subcarriers, OBO = 3.3 dB and considering different AWGN PSD values.

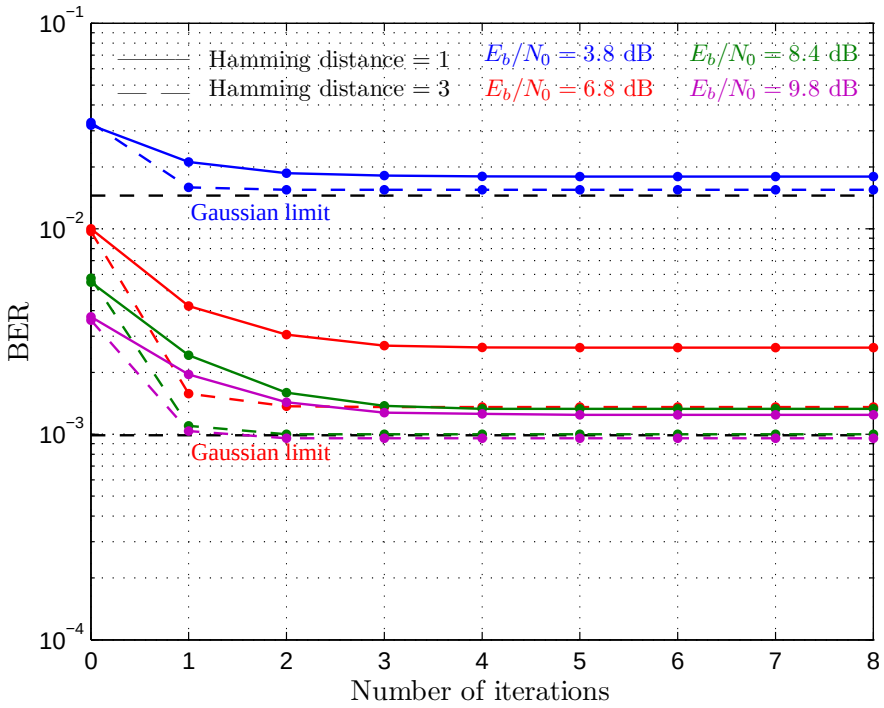

FIGURE 5.37: Bit error rate vs. number of iterations of the iterative ML algorithm for an OFDM/BPSK signal with 16 subcarriers, OBO = 2.5 dB and considering different AWGN PSD values.

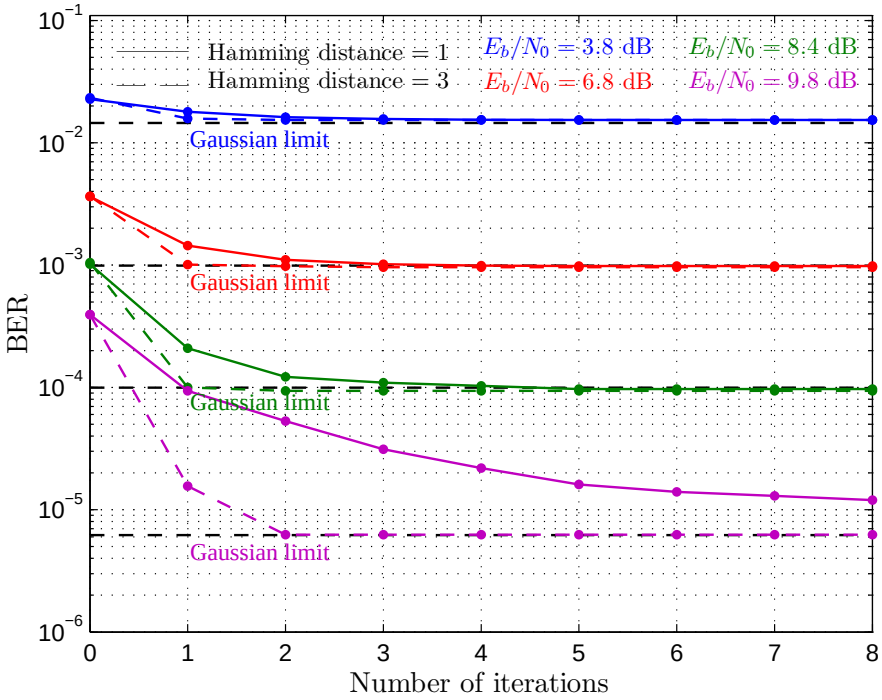

FIGURE 5.38: Bit error rate vs. number of iterations of the iterative ML algorithm for an OFDM/BPSK signal with 64 subcarriers, OBO = 3.3 dB and considering different AWGN PSD values.

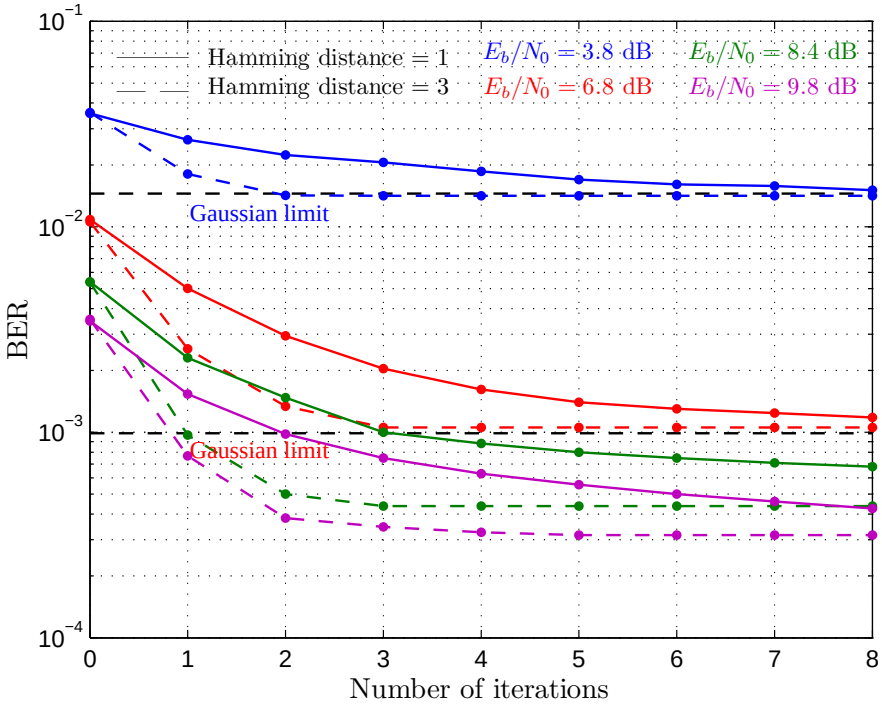

FIGURE 5.39: Bit error rate vs. number of iterations of the iterative ML algorithm for an OFDM/BPSK signal with 64 subcarriers, OBO = 2.5 dB and considering different AWGN PSD values.

yet and that if a higher number of iterations was used, an improvement in terms of bit error rate is expected. Contrary to what was observed for the 16 subcarriers case, the results for an OBO of 2.5 dB suggest that error probabilities when considering an ML algorithm that computes a Hamming distance of one are likely to tend to the ones for a Hamming distance of three. Nevertheless, the results for eight iterations of the former still underperform the ones for two iterations of the later. It is also interesting to note that results for 64 subcarriers outperform the ones for 16 subcarriers, specially when high SNR per bit values are considered.

5.4 MMSE receiver performance assessment

Similarly to what was performed in section 5.3, we will now evaluate in terms of bit error probability the performance of the proposed MMSE receiver derived in chapter 4. The OFDM signal parameters and nonlinear channel characteristics were again considered to be the ones given in section 5.3.

Figures 5.40 and 5.41 show the performance in terms of bit error rate as a function of the number of subcarriers used for OFDM/BPSK signals with OBO values of 3.3 dB and 2.5 dB, respectively, and an SNR per bit of 10 dB. We have considered results for both conventional and MMSE receivers, as well as a proposed combination between the MMSE and the iterative ML algorithm. In this jointly MMSE/iterative ML receiver, the received signal passes first through the linear transformation given by matrix $\mathbf{M}_\alpha$ and then the iterative ML algorithm takes place, i.e., the first estimate of this jointly receiver, which is the starting point of the ML algorithm, is given by the MMSE receiver rather by the conventional one. Therefore, it is expected that this iterative hybrid receiver will follow a different path through the minimum error probability search than the 'original' iterative ML algorithm. For comparison purposes, BER performance curves for the iterative ML algorithm are also depicted.

From the observation of the results we can conclude that the use of the linear transformation improves in a significant way the error probability performance when a low number of subcarriers is considered. In fact, for an OBO value of 2.4 dB it even outperforms the results given by the iterative ML algorithm. Yet, as the number of subcarriers

used increases, the error probability performance of the MMSE receiver tends to decrease and to approximate with the ones given by the conventional receiver. This can be explained by the fact that when N is large, the central limit theorem ensures that an OFDM signal tends to a cyclo-stationary zero-mean Gaussian stochastic process and reducing the existing correlation among various IMDs that fall at a particular OFDM subchannel. Thus, although improvements in terms of MSE were observed in section 4.4, the impact of the linear transformation in the probability of error decreases with the number of subcarriers used.

Results for the jointly MMSE/iterative ML are quite interesting. We can conclude that they outperform the ones given by the stand-alone iterative ML algorithm. In fact, results show that the jointly MMSE/iterative ML has the error probability performance behavior of the MMSE receiver when a low number of subcarriers is considered and also the behavior of the iterative ML algorithm when the number of subcarriers is high, requiring only a linear transformation, i.e., by combining both, the overall performance is a mixture of the best individual algorithm performances.

The results for an OBO value of 3.3 dB (Figure 5.40) show that the BER of the MMSE/ML algorithm with five iterations is almost flat and no worst case was reported. Furthermore, an improvement of more than 10 times is reported for 12 and 16 subcarriers cases, comparatively to the BER given by the iterative ML algorithm. For an OBO value of 2.5 dB, this improvement factor was found to be nearly 20 times for the 8 subcarriers case. Modulations with larger constellations were also considered and simulated but their results showed that the BER performance of the MMSE are very close to the ones given by the conventional receiver and that no significant gain is achieved. Again, this can be explained by the critical reduction of the correlation among the various IMPs, which reduces drastically the performance of the linear transformation. Therefore, and also from the results provided by Figures 5.40 and 5.41, we will concentrate on results for OFDM/BPSK signals with relatively low number of subcarriers.

Let us now focus on the performance of both MMSE receiver and jointly MMSE/ML algorithm for OFDM/BPSK signals with 8 and 16 subcarriers. Since the MMSE receiver is a linear transformation, it is possible to use semi-analytic simulations under certain

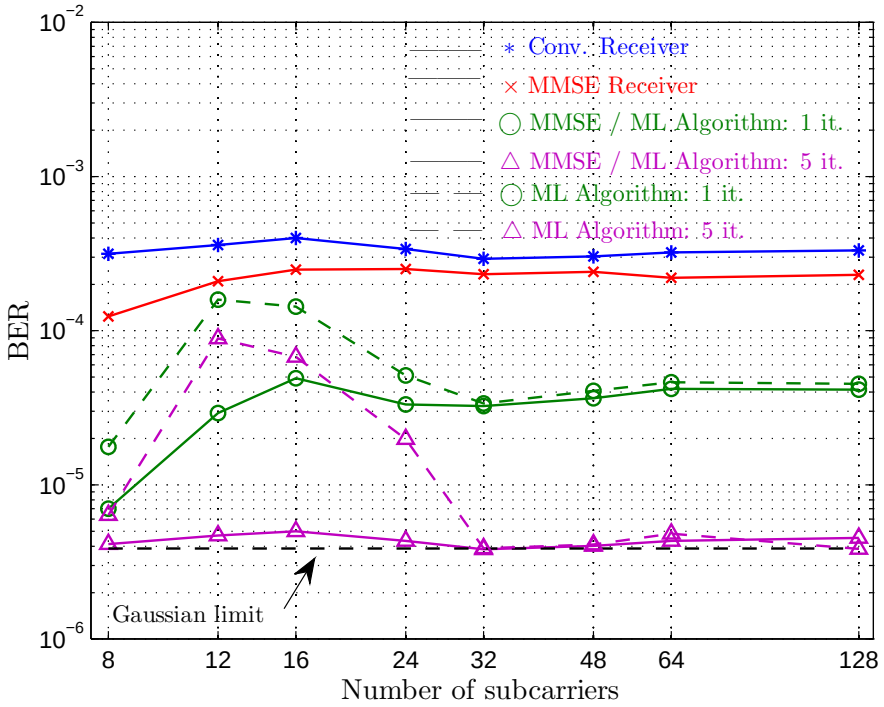

FIGURE 5.40: Bit error rate versus number of subcarriers used for OFDM/BPSK signals with an OBO value of 3.3 dB and SNR per bit of 10 dB. Results considering several OFDM receivers are presented.

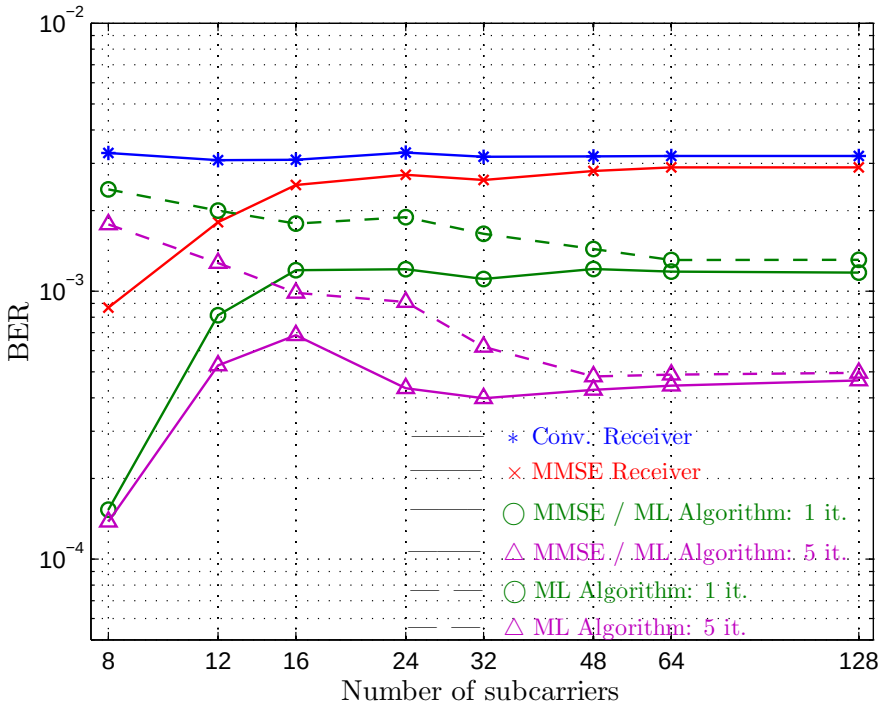

FIGURE 5.41: Bit error rate versus number of subcarriers used for OFDM/BPSK signals with an OBO value of 2.5 dB and SNR per bit of 10 dB. Results considering several OFDM receivers are presented.

circumstances to obtain performance results for very low BER levels, otherwise impossible to obtain by simple Monte Carlo techniques.

A semi-analytic method is a combination of analytical and simulation tools that take advantage of some *a priori* knowledge or assumptions to produce a BER estimation with a considerable simulation run-time reduction [83, 103]. In our case, it is assumed that the PSD of the AWGN source is known and equal to N_0. In order to estimate the BER we need to separate our problem in two parts. First, we deal with the noiseless signal component at the output of the nonlinear channel by means of simulation, i.e., several simulations considering the nonlinear channel and with the AWGN source disabled are conducted to produce 2^{KN} vectors $\mathbf{Y} = [Y_{k,-1/2(N-1)(L-1)}, \cdots, Y_{k,1/2(N-1)(L+1)}]^T$ that corresponds to all possible combinations for an OFDM signal where N subchannels convey vectors of symbols $\mathbf{S} = [S_{k,0}, S_{k,1}, \cdots, S_{k,N-1}]^T$ and where $S_{k,n}$ can take any value from a constellation of size $M = 2^K$. Then, the analytic part takes place and an equivalent noise source substitutes the "real" AWGN source before the decision block. The BER estimation is done by integrating the known noise PDF centered at each simulated noiseless complex symbol received. Since we consider that transmitted complex symbols are equi-probable, the overall BER estimation is given by averaging all BER estimations. Note that the system in study is linear from the AWGN source to the decision block, thus, the Gaussian process is not corrupted. Note also that it is irrelevant if the system is linear or nonlinear prior to the AWGN source. Moreover, linearity ensures that both signal and noise components can be treated separately [83].

Figure 5.42 depicts semi-analytic results for BER considering two AWGN PSD levels chosen in order to have the same SNR per bit at each OBO value for 8 and 16 subcarriers transmissions. Results for the 16 subcarriers case show that there is a slight improvement of the minimum BER for the lowest AWGN PSD level. Moreover, the OBO value at which the BER reaches its minimum remain unaltered. However, for lower OBO values, where the BER level is not minimum, BER results show in fact a considerable difference for the ones given by the conventional receiver. Results for the 8 subcarriers case show a similar but even more pronounced behavior. For the highest noise PSD level considered it can be seen that the MMSE receiver induces a slight reduction in the minimum BER, as well as on its corresponding OBO value. However, when low noise levels are

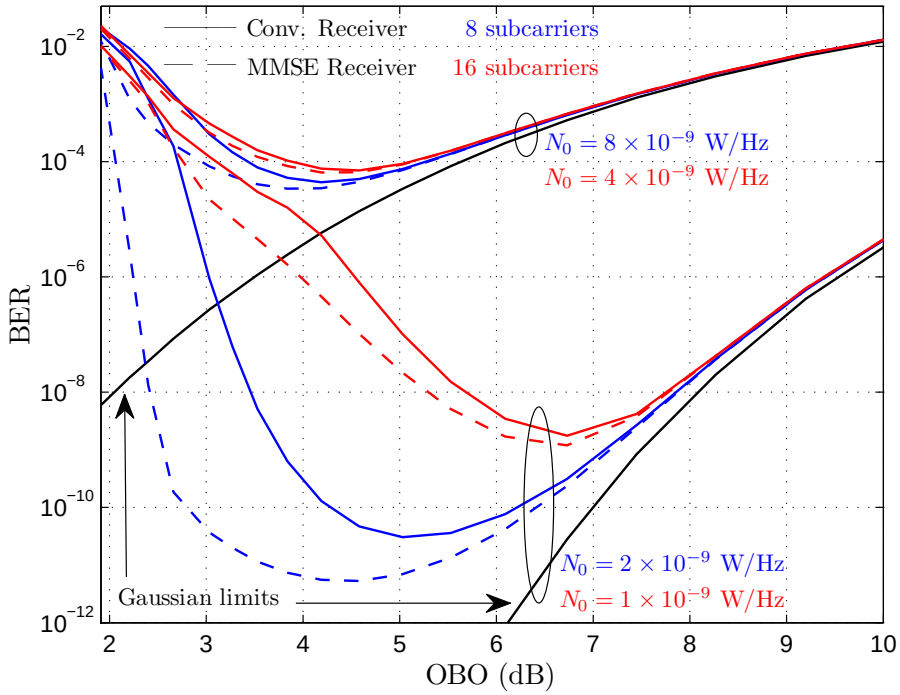

FIGURE 5.42: Semi-analytic bit error rate versus OBO value for OFDM/BPSK signals with 8 and 16 subcarriers and different AWGN PDS levels. Both OFDM signals have the same SNR per bit at each OBO value.

considered, a great impact on both minimum BER and corresponding OBO value is observed. Additionally, for even lower OBO values, the error probability performance difference increases further.

In Figure 5.43 it is depicted the BER results for all previously described receivers as a function of the SNR per bit for OFDM/BPSK signals with 8 subcarriers and OBO values of 2.5 dB and 3.3 dB. Essentially, these results confirm the ones given by Figures 5.40 and 5.41 for 8 subcarriers. As is can be seen, the difference in terms of performance between the conventional receiver and both the MMSE and jointly MMSE/iterative ML algorithm increases with the SNR per bit. Also, Figure 5.43 shows that the iterative ML algorithm is outperformed by both the MMSE receiver and MMSE/iterative ML algorithm. Moreover, the greater the SNR per bit, the greater is the difference of error probability performance between both conventional receiver and iterative ML algorithm and both MMSE receiver and MMSE/iterative ML algorithm.

Equivalent results for OFDM/BPSK signals with 16 subcarriers are plotted in Figure 5.44. As expected, the BER of the MMSE receiver has a limited performance for

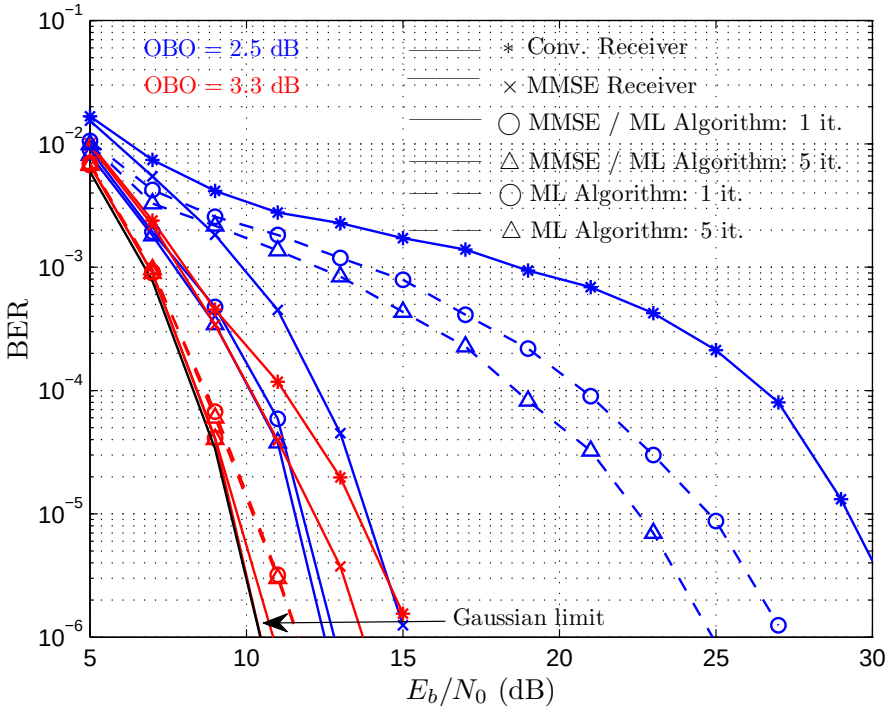

FIGURE 5.43: Bit error rate versus SNR per bit for an OFDM/BPSK with 8 subcarriers and for two OBO values. Results considering several OFDM receivers are presented.

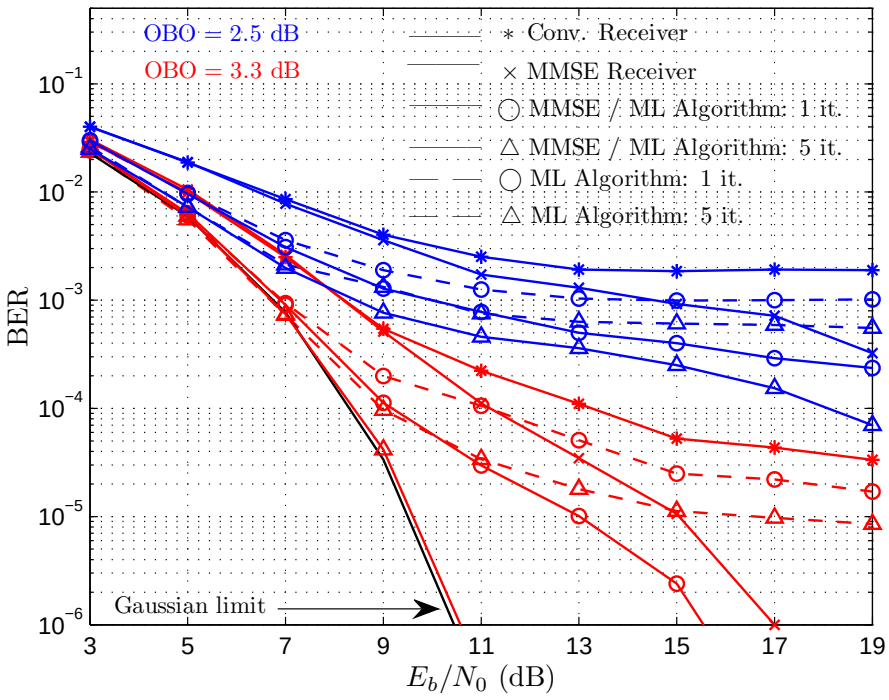

FIGURE 5.44: Bit error rate versus SNR per bit for an OFDM/BPSK with 16 subcarriers and for two OBO values. Results considering several OFDM receivers are presented.

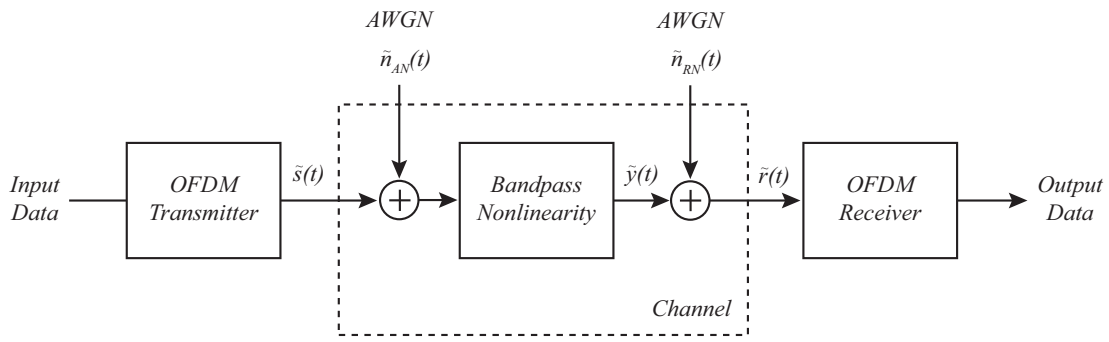

FIGURE 5.45: Equivalent baseband OFDM communication system model with the presence of antenna noise.

low SNR per bit values, comparatively to the one of the conventional receiver. However, as the SNR per bit increases, its performance outperforms the one given by the iterative ML algorithm. Finally, it is interesting to note that the performance of the MMSE/ML algorithm with five iterations outperforms all other receiver configurations, particularly the one corresponding to an OBO value of 3.3 dB which almost equals the optimum BER curve for an AWGN channel.

5.5 Analysis of the impact of an AWGN source before the bandpass nonlinearity

We will now study the impact of an AWGN source added before the nonlinearity on the OFDM signal transmission, as happens in uplink systems. Moreover, the optimality of the ML receiver structure derived in chapter 3 will also be addressed.

Consider the system model depicted in Figure 5.45 where an extra AWGN source before the nonlinearity is added. In wireless systems, this new source of noise represents the uplink noise associated with the base station antenna. Here, we consider the wireless channel to be ideal. Additionally, to clearly identify the AWGN sources, we use the terms antenna noise (AN) and receiver noise (RN) for the AWGN source that is, respectively, before and after the nonlinear channel.

Mathematically, the complex envelope of the received OFDM signal is now given by

$$\tilde{r}(t) = f[\tilde{s}(t) + \tilde{n}_{AN}(t)] + \tilde{n}_{RN}(t) \tag{5.13}$$

where $f(\cdot)$, $\tilde{n}_{AN}(t)$ and $\tilde{n}_{RN}(t)$ represent the nonlinearity lowpass equivalent, the complex envelope of the antenna noise with power spectral density N_0^{AN} and the complex envelope of the AWGN source at the receiver with power spectral density N_0^{RN}, respectively. Considering a bandpass nonlinearity of order L given by (5.1), the nonlinearly distorted OFDM signal can be written as

$$\begin{aligned}\tilde{y}(t) = \sum_{k=-\infty}^{+\infty} \Bigg\{ & \left[\tilde{c}_1 \sum_{n_1=0}^{N-1} S_{k,n_1} g_{n_1}(t-kT) + \tilde{n}_{AN}(t) \right] \\ & + \tilde{c}_3 \left[\sum_{n_1=0}^{N-1} S_{k,n_1} g_{n_1}(t-kT) + \tilde{n}_{AN}(t) \right] \left[\sum_{n_2=0}^{N-1} S_{k,n_2} g_{n_2}(t-kT) + \tilde{n}_{AN}(t) \right] \\ & \left[\sum_{n_3=0}^{N-1} S^*_{k,n_3} g^*_{n_3}(t-kT) + \tilde{n}^*_{AN}(t) \right] \Bigg\} + \tilde{c}_5 \cdots \end{aligned} \tag{5.14}$$

As expected, besides a pure AWGN term affected by the first order coefficient of the nonlinear channel, additional noisy terms arise at the output of the nonlinear channel. These undesirable terms generate a new IMD RV that is the result of intermodulation products between the OFDM signal and the antenna noise. Thus, the additional noisy-like signal denoted by $\tilde{n}'(t)$ can be defined as the resultant signal from the difference of received OFDM signals with and without considering antenna noise. Mathematically it is given by

$$\begin{aligned}\tilde{n}'(t) &= \tilde{y}(t)|_{\tilde{n}_{AN}(t)\neq 0} - \tilde{y}(t)|_{\tilde{n}_{AN}(t)=0} \\ &= \sum_{k=-\infty}^{+\infty} \tilde{c}_1 \tilde{n}_{AN}(t) + \tilde{c}_3 \left|\tilde{n}_{AN}(t)\right|^2 \tilde{n}_{AN}(t) \\ &+ \tilde{c}_3 \Bigg\{ \tilde{n}^2_{AN}(t) \sum_{n_3=0}^{N-1} S^*_{k,n_3} g^*_{n_3}(t-kT) + \left|\tilde{n}_{AN}(t)\right|^2 \sum_{n_1=0}^{N-1} S_{k,n_1} g_{n_1}(t-kT) \\ &\quad + \left|\tilde{n}_{AN}(t)\right|^2 \sum_{n_2=0}^{N-1} S_{k,n_2} g_{n_2}(t-kT) + \frac{1}{\sqrt{T-T_{CP}}} \\ &\quad \times \Bigg[\tilde{n}^*_{AN}(t) \sum_{n_1=0}^{N-1} \sum_{n_2=0}^{N-1} S_{k,n_1} S_{k,n_2} g_{n_1+n_2}(t-kT) \\ &\quad + \tilde{n}_{AN}(t) \sum_{n_1=0}^{N-1} \sum_{n_3=0}^{N-1} S_{k,n_1} S^*_{k,n_3} g_{n_1-n_3}(t-kT) \\ &\quad + \tilde{n}_{AN}(t) \sum_{n_2=0}^{N-1} \sum_{n_3=0}^{N-1} S_{k,n_2} S^*_{k,n_3} g_{n_2-n_3}(t-kT) \Bigg] \Bigg\} + \tilde{c}_5 \cdots \end{aligned} \tag{5.15}$$

Note that the first term of (5.15) is a pure Gaussian RV affected by the complex gain $\tilde{c}_1$ that corresponds to a linear component and the remaining terms are IMD components from the beat between the OFDM signal and the AWGN source.

Finally, sample values of the additional undesirable terms given by (5.15) are obtained by means of a conventional OFDM receiver structure, i.e., by multiplying $\tilde{n}'(t)$ by $g_n^*(t-kT)$ and integrating from $kT+T_{CP}$ to $(k+1)T$. Therefore,

$$N'_{k,n} = \int_{kT+T_{CP}}^{(k+1)T} \tilde{n}'(t) g_n^*(t-kT) dt \tag{5.16}$$

Obviously, in situations where this additional term is not modeled by a Gaussian process, the receiver structure described in section 3.3 is no longer optimal. By means of simulations we can infer how close (or not) from a Gaussian process this additional noise is and study the impact of the antenna noise on the OFDM signal transmission demodulated by a conventional receiver as well as its effects on the optimality of the receiver structure proposed in section 3.3. Note that the antenna noise will also affect the OBO of the signal transmission.

In order to analyze the statistical nature of RV $N'_{k,n}$, we will study the behavior and properties of the cumulative distribution function (CDF) of the process $N'_{k,n}$ which by definition is given by

$$F_X(x) \triangleq \int_{-\infty}^{x} p(t) dt \tag{5.17}$$

where $p(x)$ is the PDF of RV. Furthermore, we will also take in consideration additional and more concise information about its distribution that can be obtained by its central moments. The central moments (or the moments around the mean) of a RV describe and provide a quantitative measure of the shape of its PDF [69]. The *ith* central moment of the RV $N'_{k,n}$ is given by

$$\mu_i = \mathrm{E}\left[(N'_{k,n} - \mathrm{E}[N'_{k,n}])^i\right] \tag{5.18}$$

It can be easily seen that the first and second central moments are equal to zero and to the variance, respectively. The third and fourth central moments are used to define skewness and kurtosis of a distribution. The coefficients of skewness and kurtosis are

defined, respectively, by [104, 105]

$$\gamma_1 \triangleq \frac{\mu_3^2}{\mu_2^{3/2}} \tag{5.19}$$

$$\beta_2 \triangleq \frac{\mu_4}{\mu_2^2} \tag{5.20}$$

which correspond to the standardized third and fourth central moments of a distribution.

When referring to the shape of a distribution, skewness indicates how symmetric around the mean is the distribution. Positive/negative skewness values indicate a long right/left tail. For symmetric distributions around the mean, the skewness equals zero. The kurtosis coefficient is a measure the degree of peakedness of a distribution. It is common to define the *excess* kurtosis of a distribution as the kurtosis value relative to the one of the standard normal distribution which is equal to three. A kurtosis value higher than three indicates a flat distribution with long tails, while the opposite indicates peakedness.

To estimate both coefficients we have used Matlab/C++ to generate a large enough amount of samples $X_1, \cdots, X_K$ of the RV $N'_{k,n}$. From there, we have first obtained estimates $\hat{\mu}'_i, i = 1, 2, \cdots$ of the moments (or sample moments) around the origin $\mu'_i, i = 1, 2, \cdots$ through [83]

$$\hat{\mu}'_i = \frac{1}{K}\sum_{k=1}^{K} X_k^i, \quad i = 1, 2, \cdots \tag{5.21}$$

and then estimates $\hat{\mu}_i, i = 1, 2, \cdots$ of the central moments $\mu_i, i = 1, 2, \cdots$ up to the fourth order were obtained by using the following relations

$$\mu_1 = 0 \tag{5.22}$$

$$\mu_2 = -\mu_1'^2 + \mu'_2 \tag{5.23}$$

$$\mu_3 = 2\mu_1'^3 - 3\mu'_1\mu'_2 + \mu'_3 \tag{5.24}$$

$$\mu_4 = -3\mu_1'^4 + 6\mu_1'^2\mu'_2 - 4\mu'_1\mu'_3 + \mu'_4 \tag{5.25}$$

In a similar way, we have used Matlab/C++ to estimate the CDF of the distribution but with samples written in an increasing order, i.e., $X_k < X_{k+1}$. Therefore, the

estimative of the CDF, $\hat{F}(x)$, is obtained by the following definition [83]

$$\hat{F}_X(x) = \begin{cases} 0, & x < X_1 \\ k/K, & X_k \leq x < X_{k+1}, \quad k = 1, \cdots, K-1 \\ 1, & x \geq X_K \end{cases} \tag{5.26}$$

We will now examine the properties of the additional noise term $N'_{k,n}$. To do so, some considerations must be taken. First, it is assumed that complex symbols conveyed in subchannel n are independent from the ones conveyed in the remaining subchannels. It is also assumed that M-PSK complex symbols assume equally likely values in the set $\left\{Ae^{j\left(\pi\frac{2i+1}{M}-\pi/2\right)}; i = 0, 1, \cdots, M-1\right\}$, where M denotes the size of the constellation. Moreover, the complex transmitted symbol conveyed in subchannel index n subject to evaluation is considered to be known and set to one of the M possible constellation points, $S^i_{k,n}$. Due to M-PSK symmetry, any of the M constellation points could be chosen as the one to be conveyed in subchannel n because it does not affect the properties of the conditioned received term $N^i_{k,n}$. Therefore, all symbol conditioning is considered to be set to constellation point index $i = 0$ independently on the size of constellation. Also, due to symmetry, we will examine only the real part of the RV $N'_{k,n}$ for modulations of size $M > 2$ since both real and imaginary parts are identical. For the BPSK case, we will also examine only the real part of $N'_{k,n}$ since it is sufficient for error probability purposes [102, 106]. Regarding the subcarrier index, we will consider the signal conveyed in the subchannel at the center of the band and also the one conveyed in the subchannel at the edge, since they represent the two extreme cases in terms of number of IMPs.

The OFDM signal considered has the following general characteristics: $T = 4\,\mu$s, $T_{CP} = 800\,$ns. The M-PSK complex symbols conveyed in each subcarrier were chosen to take values from the set $\left\{Ae^{j\left(\pi\frac{2i+1}{M}-\pi/2\right)}; i = 0, 1, \cdots, M-1\right\}$. It is also assumed Gray coding for constellations with $M > 2$. The channel is considered to be a third-order nonlinearity given by a power series with coefficients $c_1 = 1$, $c_2 = 0$, $c_3 = -0.20$ and $c_i = 0$ for $i > 3$.

In Figures 5.46 and 5.47 it is depicted the CDF of the RV $N'_{k,n}$ given by (5.16) for OFDM/BPSK signals considering different number of subcarriers, an SNR per bit of

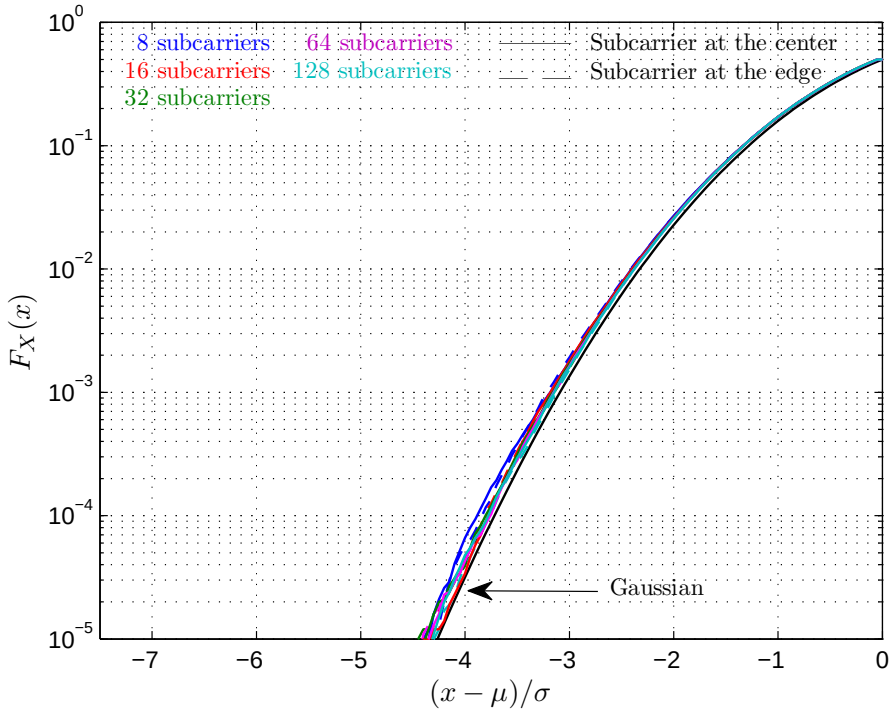

FIGURE 5.46: CDF of $N'_{k,n}$ for OFDM/BPSK signals with an SNR per bit of 5 dB and an OBO value of 2.5 dB. Results for different number of subcarriers are presented.

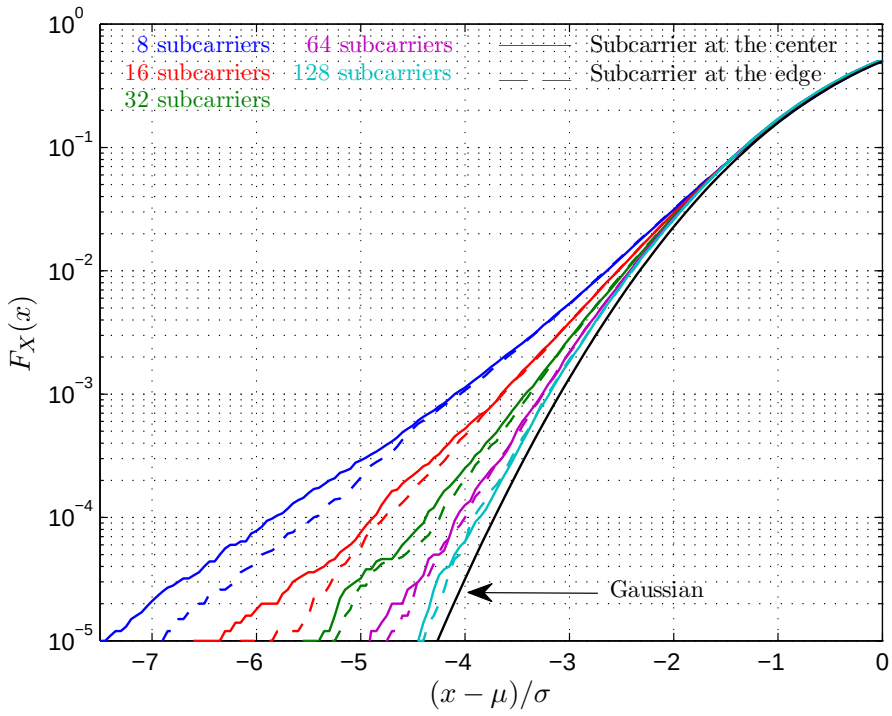

FIGURE 5.47: CDF of $N'_{k,n}$ for OFDM/BPSK signals with an SNR per bit of 5 dB and an OBO value of 1.4 dB. Results for different number of subcarriers are presented.

5 dB and OBO values of 2.5 dB and 1.4 dB, respectively. The SNR per bit corresponds to the ratio between the energy per bit of the transmitted OFDM symbols and the noise power spectral density of the antenna noise obtained immediately before the nonlinearity. The x-axis is normalized to the mean and the standard deviation. Note that these results are only respective to the additional noise term due to the antenna and that no intermodulation terms between OFDM subchannels are present. From the observation of both Figures we can infer that the additional noise term starts to deviate from a Gaussian distribution if a very low OBO value is considered. In fact, for an OBO of 2.5 dB which can be considered relatively low, the distribution of RV $N'_{k,n}$ approaches pretty well a Gaussian distribution independently on the number of subcarriers used. For a even lower OBO value of 1.4 dB, the rate of tail decay depends mainly on both the number of subcarriers used and on the location of OFDM subchannel. In conclusion, heavy-tailed distributions were obtained for lower number of subcarriers considered and subchannels on the center whereas lighter tail distributions correspond to higher number of subcarriers and subchannels on the edge of the band.

Figure 5.48 shows corresponding results for OFDM/16-PSK signals and an OBO value of 1.4 dB. It can be seen that for OFDM/16-PSK signals the distributions have slightly lighter tails than the ones for OFDM/BPSK signals. Nevertheless, results from both constellations can be considered similar, suggesting that the size of constellation do not significantly affects the distribution of RV $N'_{k,n}$. Results for an OBO value of 2.5 dB are not show since they equal the ones for OFDM/BPSK signals. Also, it was observed that results from simulations considering higher SNR per bit values have similar distributions to the ones given by Figures 5.46, 5.47 and 5.48.

Skewness and kurtosis coefficient values of RV $N'_{k,n}$ are depicted in Figure 5.49 for OFDM/BPSK and OFDM/16-PSK signals considering an OBO value of 1.4 dB and an SNR per bit of 5 dB. From the observation of the Figure it can be seen that all distributions considered do not present skewness, thus they all are symmetric distributions around the mean. Moreover, the behavior of the Kurtosis coefficient curve shows that the distribution of RV $N'_{k,n}$ has in fact long tails for low number of subcarriers, corroborating with the results from Figures 5.47 and 5.48. Yet, as the number of subcarriers increase, the kurtosis coefficient converges rapidly to the Gaussian distribution reference

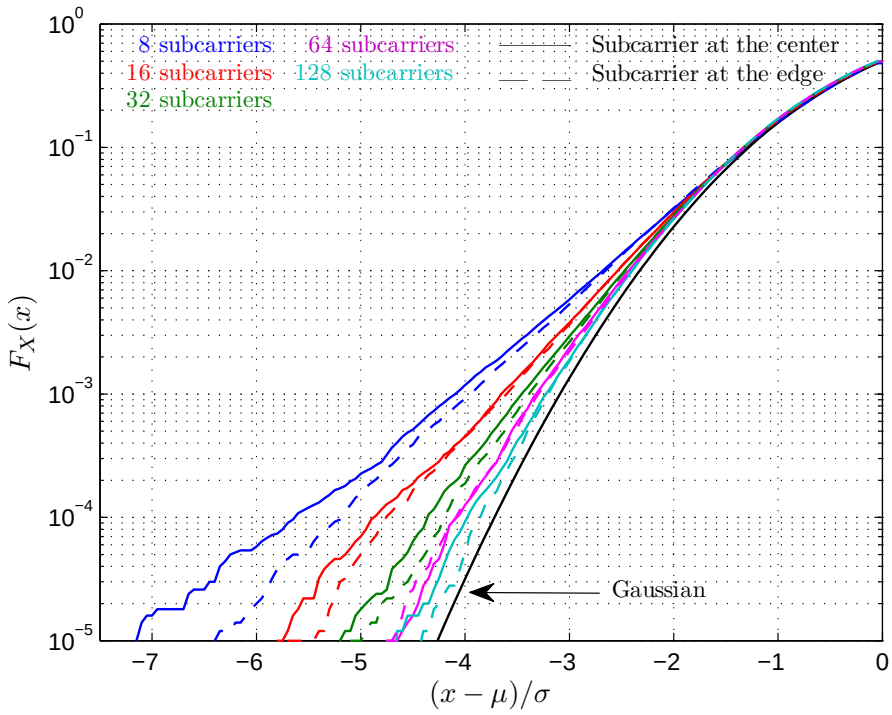

FIGURE 5.48: CDF of $N'_{k,n}$ for OFDM/16-PSK signals with an SNR per bit of 5 dB and an OBO value of 1.4 dB. Results for different number of subcarriers are presented.

value. Results for for higher OBO values are not depicted since they practically equal the ones of a Gaussian distribution.

In conclusion, we have seen from both CDF and kurtosis/skewness coefficients analysis that the additional noisy signal given by the intermodulation of antenna noise and the OFDM signal approaches well a Gaussian process for OBO values greater than 2.5 dB. Moreover, for a very low OBO value of 1.4 dB, the RV $N'_{k,n}$ also approaches a Gaussian process when a high number of subcarriers is considered. This result comes in accordance with the central limit theorem under weak dependence which says that the distribution of the sample average of a sequence of N identically distributed RVs with some degree of dependency tends to normal for a large N [92, 107]. On the other hand, if both low OBO values and number of subcarriers are considered, results show that it starts to deviate from a Gaussian distribution. Here, the IMP terms between antenna noise and OFDM signal dominate over the linear AWGN term.

To examine the effect of the antenna noise on the performance of both conventional and ML receiver we have conducted several simulations using Matlab/C++ for OFDM/BPSK signals with different number of subcarriers.

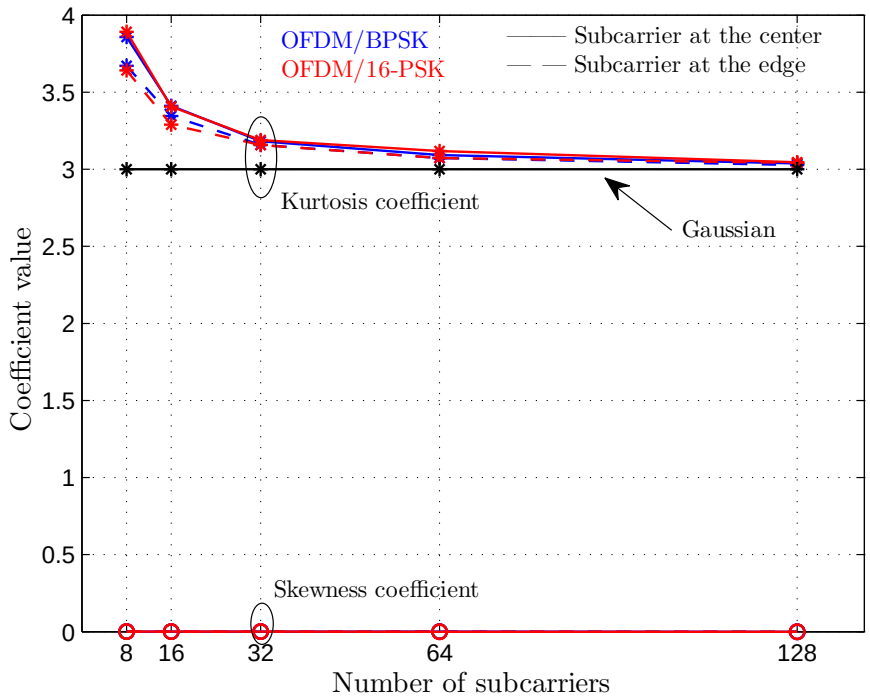

FIGURE 5.49: Kurtosis and skewness coefficient values of RV $N'_{k,n}$ for OFDM/BPSK and OFDM/16-PSK signals as a function of the number of subcarriers used for an OBO value of 1.4 dB and an SNR per bit of 5 dB.

In Figure 5.50 it is represented the performance in terms of error probability for the system depicted in Figure 5.45. Here, the receiver noise source is set to zero, so only antenna noise is present. Performance curves for the conventional, iterative ML algorithm and ML receivers are shown for OFDM/BPSK signals with 16 and 64 subcarriers and different antenna noise PSD levels. Note that in order to maintain the same SNR per bit immediately before the nonlinear channel, the antenna noise PSD for the 16 subcarrier OFDM transmission is set to four times the one for the 64 subcarrier transmission. Note also that the ML receiver previously derived is no longer optimum due to the excess noise from beat between antenna noise and OFDM signal. Performance curves for the lowest noise PSD levels for both $N = 16$ and $N = 64$ were not depicted for OBO values below 2.5 dB since they fall on top of the ones given by the higher noise PSD level.

From the observation of the Figure it can be seen that for high OBO values the linear term of the antenna noise is dominant over both the nonlinear noise and IMD antenna noise terms. Here, the error probability is mainly affected by the linear term of the antenna noise. As the OBO decreases, both nonlinear noise and IMD antenna

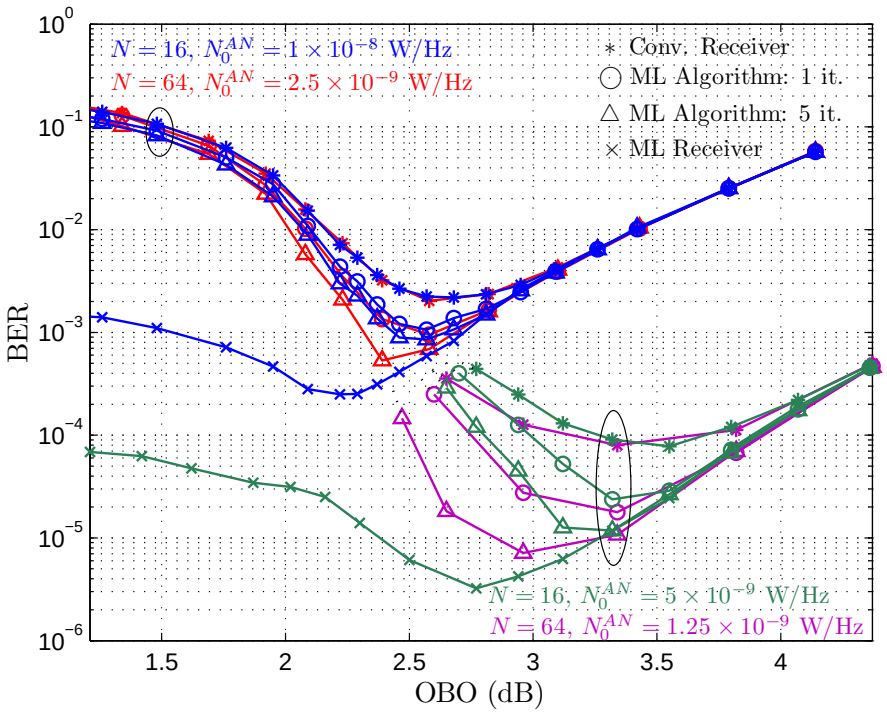

FIGURE 5.50: Bit error rate performance vs. output back-off for OFDM/BPSK signals with 16 and 64 subcarriers considering conventional, iterative ML algorithm and (non-optimum) ML receivers. Antenna noise relation is considered to be $N_0^{AN}|_{N=16} = 4N_0^{AN}|_{N=64}$ to ensure the same SNR per bit immediately before the nonlinear channel.

noise terms increase which originates a degradation in the error probability performance of all receivers. Yet, iterative ML algorithms show to be relatively robust and an improvement in terms of bit error rate is still reported. As an example, results taken from the best transmission scenario depicted in Figure 5.50 show that, comparatively to the conventional receiver, the five iterations ML algorithm is responsible for a decrease of the error probability by factors of eight and ten when 16 and 64 subcarriers are used, respectively.

In Figure 5.50 it is also depicted performance curves of the (non-optimum) ML receiver for OFDM transmissions using 16 subcarriers. Results show that the nonlinear noise is still very well compensated by the ML receiver even for very low OBO values. These results corroborate the analysis of the statistical properties of the antenna noise signal performed previously (see Figures 5.46 through 5.49). In fact, for a very low OBO value of 1.5 dB, the error probability is reduced around 100 and 2000 times for antenna noise PSD levels of 1×10^{-8} W/Hz and 5×10^{-9} W/Hz, respectively. Similar results for 64 subcarriers are not reported due to very high computational time effort.

5.6 Effect of carrier frequency and phase offsets

As previously stated in chapter 2, one of the major drawbacks of OFDM signal transmissions is their high vulnerability to frequency and phase offsets. OFDM symbol synchronization techniques have been a subject of study in the last years and are used in order to compensate frequency offsets that can be caused by local oscillator errors and Doppler spread [73–76, 108]. Here we will study the effects of carrier frequency and phase offsets in the nonlinearly distorted OFDM signal transmission system depicted in Figure 3.2.

From section 2.3.2.1, an OFDM signal with frequency and phase offsets, respectively given by δf and ϕ, can be modeled as [45, 65]

$$\tilde{r}'(t) = \tilde{r}(t)e^{j(2\pi\delta f t+\phi)} \tag{5.27}$$

So, the complex symbol conveyed in subchannel n and time slot k are given by

$$\begin{aligned} R'_{k,n} = & \frac{\tilde{c}_1}{(T-T_{CP})^0}\sum_{n_1=0}^{N-1} S_{k,n_1}\alpha_{n_1}e^{j\gamma_{k,n_1}} \\ & + \frac{\tilde{c}_3}{(T-T_{CP})^1}\sum_{n_1=0}^{N-1}\sum_{n_2=0}^{N-1}\sum_{n_3=0}^{N-1} S_{k,n_1}S_{k,n_2}S^*_{k,n_3}\alpha_{n_1+n_2-n_3}e^{j\gamma_{k,n_1+n_2-n_3}} \\ & + \cdots \\ & + \frac{\tilde{c}_L}{(T-T_{CP})^{(L-1)/2}}\sum_{n_1=0}^{N-1}\cdots\sum_{n_L=0}^{N-1} S_{k,n_1}\cdots S_{k,n_{(L+1)/2}}S^*_{k,n_{(L+3)/2}}\cdots S^*_{k,n_L} \\ & \times \alpha_{n_1+\cdots+n_{(L+1)/2}-n_{(L+3)/2}-\cdots-n_L}e^{j\gamma_{k,n_1+\cdots+n_{(L+1)/2}-n_{(L+3)/2}-\cdots-n_L}} + N_{k,n} \end{aligned} \tag{5.28}$$

where the attenuation factor α_{n_l} and the time-varying phase shift factor γ_{k,n_l} are given, respectively, by

$$\alpha_{n_l} = \text{sinc}\left[(n_l - n) + \delta f(T - T_{CP})\right] \tag{5.29}$$

$$\gamma_{k,n_l} = \pi(n_l - n) + \pi\delta f[(2k+1)T + T_{CP}] + \phi \tag{5.30}$$

For a $\delta f > 0$, the attenuation factor α_{n_l} is always nonzero, whereas for a $\delta f = 0$, it equals one for $n_l = n$, and zero otherwise.

By evaluating (5.28) it can be seen that the expression for the complex received symbol $R'_{k,n}$ contains three main terms. Following the same procedure performed in section 5.2, by denoting $R^i_{k,n}$ as the received complex symbol in time slot k and subchannel n conditioned to a transmitted complex symbol $S^i_{k,n}$, we can rewrite (5.28) as

$$R'^i_{k,n} = U'^i_{k,n} + W'^i_{k,n} + N_{k,n} \tag{5.31}$$

where the first term, $U'^i_{k,n}$, accounts the useful term in which all subcarriers suffer the same phase shift and attenuation, i.e., it is only composed by elements for $n_1, \cdots, n_L = n, \cdots, n$. Additionally, it also accounts a deterministic quantity from the nonlinearity given by the compression gain terms of the IMPs also affected by the same phase shift and attenuation factors. The second term, $W'^i_{k,n}$, for $n_1, \cdots, n_L \neq n$, represents both the ICI from the loss of orthogonality due to frequency/phase offsets and IMD from the nonlinearity. Finally, the third term, $N_{k,n}$, corresponds to AWGN.

Mathematically, the useful and overall ICI terms are, respectively, given by

$$\begin{aligned} U'_{k,n} = & \frac{\tilde{c}_1}{(T-T_{CP})^0} S_{k,n}\alpha_n e^{j\gamma_{k,n}} + \frac{\tilde{c}_3}{(T-T_{CP})^3} S_{k,n}S_{k,n}S^*_{k,n}\alpha_{n+n-n} e^{j\gamma_{k,n+n-n}} \\ & + \cdots \\ & + \frac{\tilde{c}_L}{(T-T_{CP})^{(L-1)/2}} S_{k,n}\left|S_{k,n}\right|^{(L-1)} \alpha_{\underbrace{n+\cdots+n}_{(L+1)/2}-\underbrace{n-\cdots-n}_{(L-1)/2}} \\ & \times e^{j\gamma_{k,\underbrace{n+\cdots+n}_{(L+1)/2}-\underbrace{n-\cdots-n}_{(L-1)/2}}} \end{aligned} \tag{5.32}$$

and

$$\begin{aligned} W'_{k,n} = & \frac{\tilde{c}_1}{(T-T_{CP})^0} \sum_{\substack{n_1=0 \\ n_1\neq n}}^{N-1} S_{k,n_1}\alpha_{n_1} e^{j\gamma_{k,n_1}} \\ & + \frac{\tilde{c}_3}{(T-T_{CP})^1} \sum_{\substack{n_1=0 \\ n_1,n_2,n_3\neq n,n,n}}^{N-1}\sum_{n_2=0}^{N-1}\sum_{n_3=0}^{N-1} S_{k,n_1}S_{k,n_2}S^*_{k,n_3}\alpha_{n_1+n_2-n_3} e^{j\gamma_{k,n_1+n_2-n_3}} \\ & + \cdots \\ & + \frac{\tilde{c}_L}{(T-T_{CP})^{(L-1)/2}} \sum_{\substack{n_1=0 \\ n_1,\cdots,n_L\neq n,\cdots,n}}^{N-1} \cdots \sum_{n_L=0}^{N-1} S_{k,n_1}\cdots S_{k,n_{(L+1)/2}} S^*_{k,n_{(L+3)/2}}\cdots S^*_{k,n_L} \\ & \times \alpha_{n_1+\cdots+n_{(L+1)/2}-n_{(L+3)/2}-\cdots-n_L} e^{j\gamma_{k,n_1+\cdots+n_{(L+1)/2}-n_{(L+3)/2}-\cdots-n_L}} \end{aligned} \tag{5.33}$$

In order to study the impact of a CFO in the error rate performance of both conventional and iterative ML algorithm, several simulations using Matlab/C++ were conducted.

Figures 5.51 and 5.52 depict both the in-phase and quadrature components of the received constellation for OFDM/QPSK signals with 64 subcarriers when considering a transmission through a linear ($c_1 \neq 0$ and $c_i = 0$, $i > 1$) and a third order nonlinear channels, respectively. The coefficients of the nonlinear channel and OFDM signal parameters were considered to be the same as the ones defined in previous sections. Note that the noisy-like cloud shape in Figure 5.51 is only due to CFO and the consequent loss of orthogonality. On the other hand, the distorted constellation shape in Figure 5.52 is due to both CFO and IMD from nonlinear distortion. The main difference between both received constellations are the size of the noisy cloud around the transmitted symbol and the signal attenuation from compression gain and desensitization terms. The constellation phase rotation clearly identified in both Figures increases linearly with CFO (see (5.30)).

In Figure 5.53 it is depicted the variance of the in-phase component of the received complex signal for different OBO and CFO values. The signal was set to be an OFDM/QPSK with 64 subcarriers. Note again that the only noise contributions that are present are given by the IMD term and ICI component from CFO, i.e., no AWGN source is considered. Results obtained show that the CFO affects tremendously the OFDM signal transmission. Note also that for $\delta f = 0$, the variance of the ICI is only due to the nonlinear noise. It can be seen that the effect of CFO is stronger at the center of the OFDM signal rather at the edges. This can be explained by knowing that the ICI due to loss of orthogonality is given by a summation of contributions of all subcarriers. These contributions are given by the attenuator factor α_{n_l} (see (5.29)) and rapidly decrease with subcarrier distance (see also Figure 2.17). Therefore, subcarriers at the center suffer a higher degradation due to the loss of orthogonality. Results from Figure 5.53 also show that the difference between OBO curves is constant, indicating that the variance of the received OFDM signal is given by the summation of the two ICI contributions, one from the nonlinear noise and the other from the CFO. Similar results were obtained using different M-PSK and 16-QAM modulation schemes.

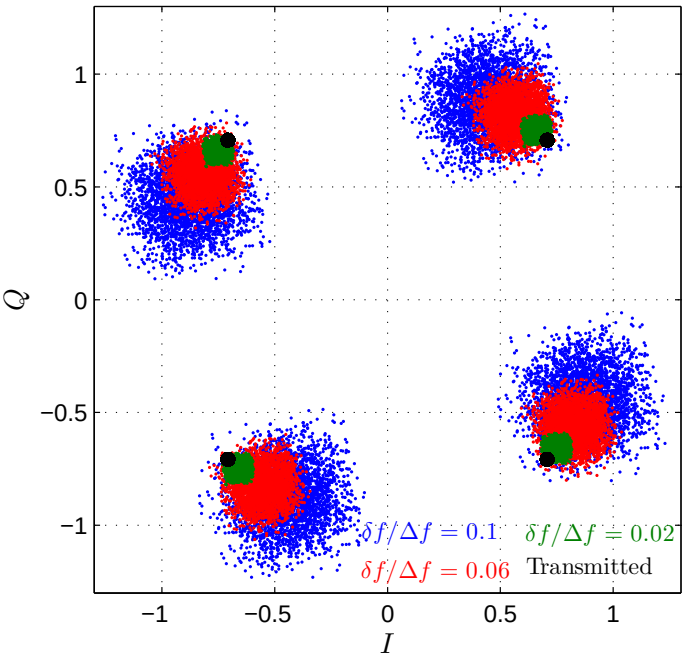

FIGURE 5.51: Received constellation when considering OFDM/QPSK signals with 64 subcarriers, a linear channel transmission and different frequency offset scenarios.

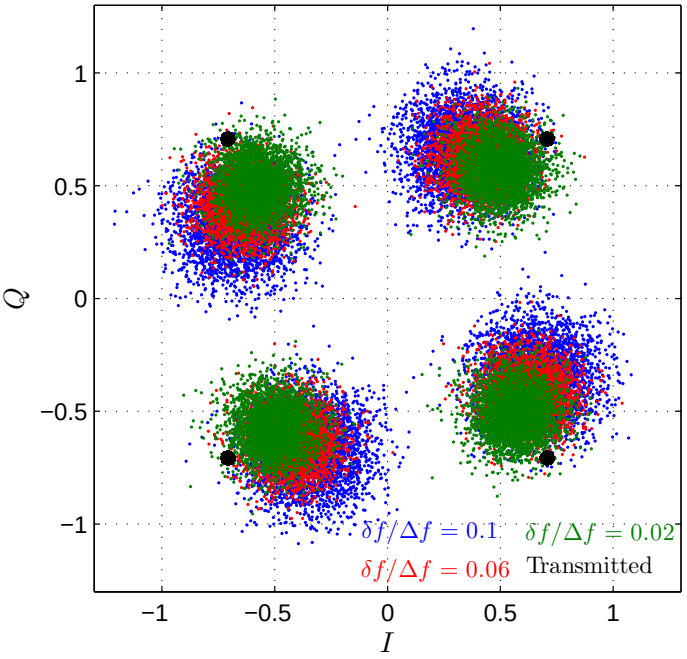

FIGURE 5.52: Received constellation when considering OFDM/QPSK signals with 64 subcarriers, an output back-off of 3 dB and different frequency offset scenarios.

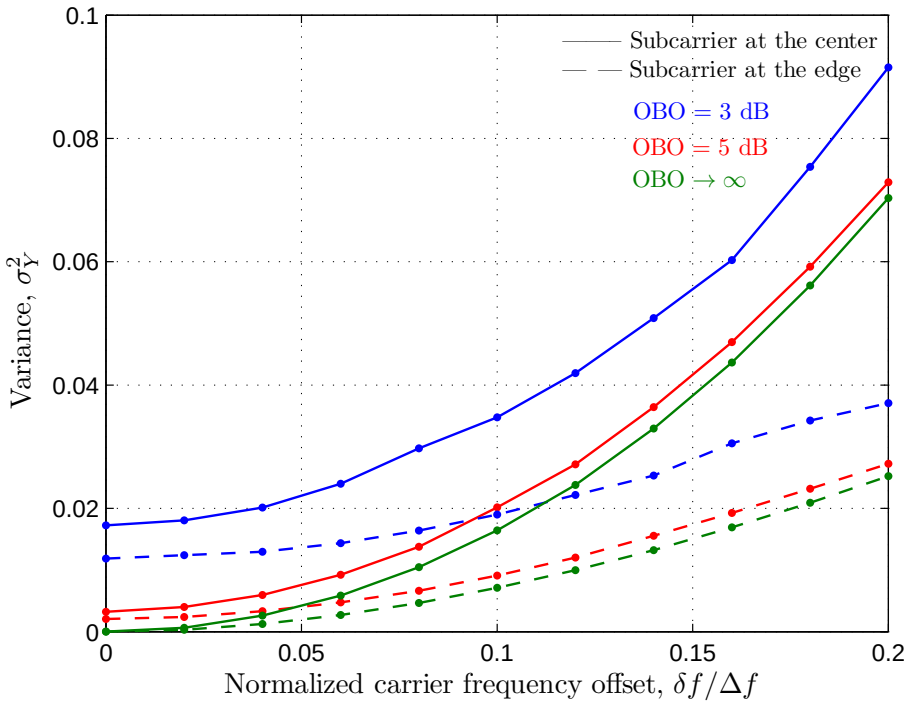

FIGURE 5.53: In-phase variance component of the received OFDM/QPSK signal as a function of carrier frequency offset. OFDM signal is considered to have 64 subcarriers and different OBO values.

Since effects of phase noise are out of the scope of this thesis and that a continuous phase shift can be well compensated at the receiver, we will set ϕ to zero and consider only the existence of a constant frequency offset at the receiver. Moreover, both the attenuation and phase rotation induced by both IMD and CFO are partly compensated considering a CAGC similar to the one given by (5.11) immediately before the conventional receiver and the iterative ML algorithm.

The effect of the CFO in the BER is plotted in Figure 5.54 for OFDM/QPSK signals with 64 subcarriers, considering an OBO value of 3 dB and two different SNR per bit values. Results were obtained using both conventional receiver and the ML algorithm with one and five iterations. Additionally, the error probability performance curve of both subcarriers at the edge and center of the signal's band are also considered for one specific case. From the observation of the Figure, it is clear that the CFO has a tremendous effect on the OFDM signal transmission. In conformance with results depicted in Figure 5.53, the performance of both receivers deteriorates as the CFO increases. When considering the conventional receiver and an SNR per bit of 10 dB, it

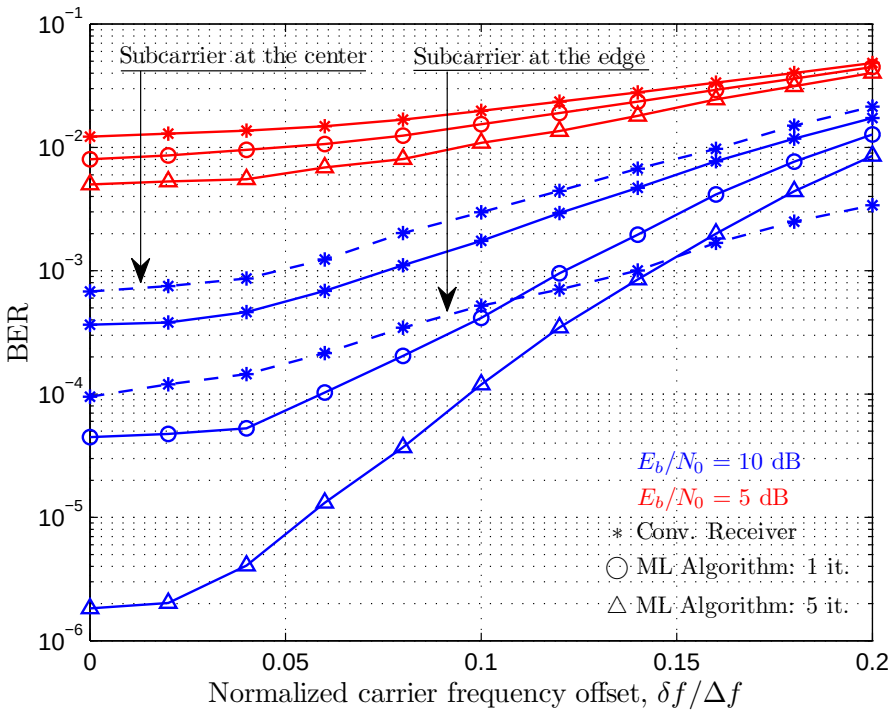

FIGURE 5.54: Bit error rate as a function of carrier frequency offset for OFDM/QPSK signals with 64 subcarriers, an OBO value of 3 dB and different SNR per bit values.

can be seen that error probability increases around five times for a CFO value of 10% the subcarrier frequency spacing. Comparatively, it increases ten and fifty times if the ML algorithm with one and five iterations, respectively, is used. Nevertheless, both iterative ML receivers exhibit a better error probability at a normalized CFO of 10% than the conventional receiver with no CFO. Interestingly, the iterative ML algorithm is quite robust to CFO and a simple one iteration for a normalized CFO of 11% yields the same bit error rate as the conventional receiver with no CFO. For the five iterations algorithm, a normalized CFO can go up to 14% and still match the conventional receiver performance for 0% CFO.

In Figure 5.55 it is depicted the total degradation (TD) as a function of the OBO for both iterative ML algorithm and conventional receivers and considering OFDM/QPSK signals with 64 subcarriers. Results for a normalized CFO of 10% are presented as well as the ones for 0% CFO also given by Figure 5.27 for comparison purposes. From the observation of the Figure it can be see that for high OBO values all receivers present a constant degradation of 1.5 dB for the 10% CFO case relativelly to the zero-offset case. Furthermore, results for the five iterations algorithm and the conventional receiver

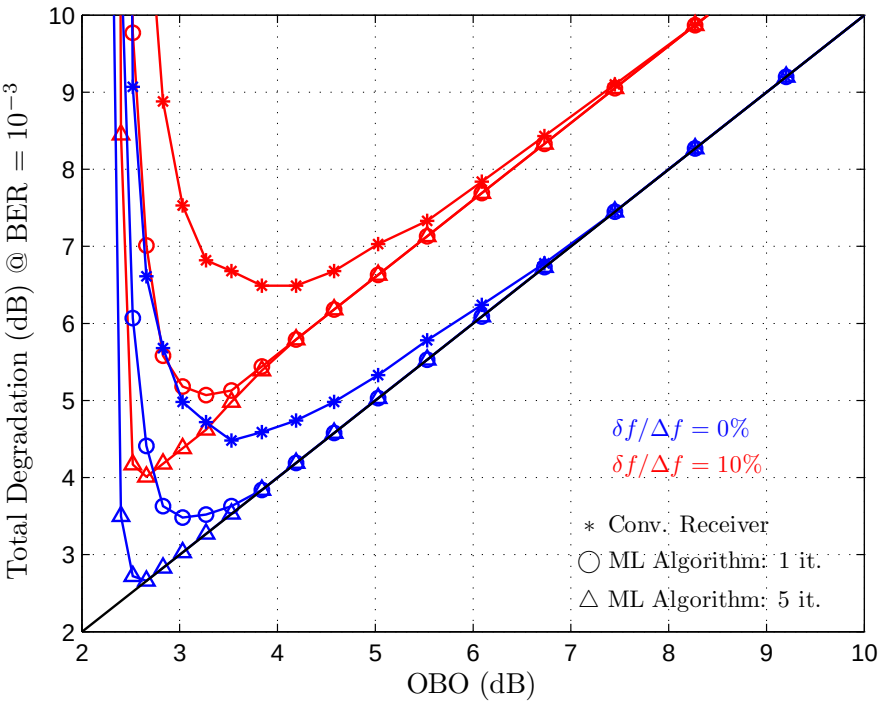

FIGURE 5.55: Total degradation versus output back-off for OFDM/QPSK signals with 64 subcarriers considering both the conventional receiver and iterative ML algorithm and different CFO values for a target BER of 10^{-3}.

also indicate maximum gains in terms of minimum TD of 1.9 dB and 2.5 dB for the 0% CFO and 10% normalized CFO, respectivelly. These interesting results indicate that for a normalized CFO of 10% and a target BER of 10^{-3}, the iterative ML is in fact capable of processing the distorted signal and exhibiting a performance gain of 0.6 dB, comparatively to the 0% CFO case.

In conclusion, the ICI from frequency offset can be viewed as an additional noise term that deteriorates the SNR. Minimum total degradation values indicate that the iterative ML algorithm processes the nonlinearly distorted corrupted by AWGN and the additional ICI term from the CFO and is still capable to increase its gain margin to the conventional receiver.

5.7 Summary

In this chapter, we have presented several results from the application of the OFDM receivers designed in chapters 3 and 4.

Initially, the nonlinear channel considered was described and, by analytical and simulations means, an analysis of the impact of nonlinearities on OFDM signals was assessed. It was reported that there is a dependency on the averaged received constellation points for amplitude constellations such as 16-QAM. Moreover, the variance of the IMD term on a given subchannel is also highly dependent on the transmitted complex symbol, suggesting that the decision boundaries to those schemes could be optimized and that post-compensation techniques that take this information into account could also be a subject of further study. Another interesting and already referred in the literature result is the increase of the variance of the IMD term with the number of subcarriers.

Subsequently, individual performances of the OFDM conventional receiver, iterative ML algorithm, ML receiver and MMSE linear transformation were studied. Simulations were conducted over a wide range of OFDM signals. We have considered different types of modulation taken from M-PSK schemes as well as the multilevel 16-QAM. Also, the impact of varying both signal power, which is closely related to the OBO, and the number of subcarriers on the error probability was analyzed for all OFDM receivers. Furthermore, we have shown that there is an optimum operating point in terms of OBO for the conventional and iterative ML receivers given by a compromise between transmit power and signal degradation and also that it is highly dependent on the size of the constellation. Different ML algorithm implementations considering various numbers of iterations and search region sizes were also discussed. In fact, it was verified that its performance is highly dependent on the search region size and number of iterations as well as on its first estimate which corresponds to the starting point of the algorithm.

Results for both the conventional receiver and the iterative ML algorithm have shown a worst performance peak for numbers of subcarriers between 12 and 24. This effect is explained by the result of two effects: the increase of the variance of the IMD term and simultaneous decrease of the heaviness of the tails of its distribution, both with the increase of the number of subcarriers.

Regarding the MMSE receiver, simulation results have shown that in fact it only produces acceptable BER improvements when OFDM signal transmissions with BPSK modulation schemes and a relatively low number of subcarriers are considered. This result suggests that when the number of IMPs is very high and the IMD term starts to

lose its correlation between subchannels, the MMSE sees its advantage neutralized. Yet, in these conditions, it largely outperforms the ML algorithm with at least five iterations by the cost of a simple linear transformation. Note that these results are for the linear MMSE receiver and that a better performance (but also an increase in complexity) would be expected if a nonlinear MMSE structure was used. Despite its relatively poor performance for signals with a high number of subcarriers, the linear MMSE receiver was a subject of study since its structure is also the basis of the channel frequency response estimator proposed in the next chapter.

Results for the proposed joint MMSE/iterative ML algorithm have shown that it outperforms all the others considered receivers. Interestingly, by using the MMSE structure as the iteration 'zero', it was found that the overall performance is a mixture of the best individual algorithm performances. Moreover, it was observed that this new algorithm is capable of compensate the performance degradation reported for 12, 16 and 24 subcarriers by both conventional and iterative ML algorithms just by the cost of a simple linear transformation.

Subsequently, the impact of an AWGN source before the nonlinear channel was also evaluated. A statistical analysis of the additional noise term given by the beat between the OFDM signal and noise was conducted. From the analysis of both CDF and kurtosis/skewness coefficients we have concluded that this additional term approaches well a Gaussian process for OBO values grater than 2.5 dB and also for OFDM signals with a large number of subcarriers. Additionally, the impact of the antenna noise on the optimality of the iterative ML algorithm was also evaluated.

Finally, the impact of the CFO in a nonlinearly distorted OFDM signal was also investigated and simulations concerning the performance behavior of both the conventional and iterative ML algorithm were performed. Results show that despite the additional noise term given by the CFO, the iterative ML algorithm is still able to process the nonlinear noise in order to minimize the total degradation and also to increase its performance relative to the one given by the conventional receiver.

In the next chapter, we investigate the use of the MMSE receiver structure derived in chapter 4 to obtain a channel estimator based on MSE minimization for nonlinearly distortion OFDM systems.

Chapter 6

Channel estimation in an uplink system configuration

6.1 Introduction

In an ideal world, a wireless channel would be just a direct link between the transmitter and the receiver, with no attenuation and delay, i.e., the received signal would be just a perfect replica of the transmitted signal. However, in the real world the transmitted signal can be severally distorted by the propagation medium.

In a wireless channel transmission, the signal is usually scattered, diffracted and reflected in several objects before reaching the antenna (see Figure 6.1). As a result, multiple versions of the signal with different delays and attenuation factors caused by different paths lengths are collected by the receivers' antenna resulting in fading. This superposition of signals leads to several constructive and destructive interferences depending on the instant time, locations of both the receiver and transmitter antennas and the channel itself. Thus, the summation of all delayed versions of the transmitted signal causes the spread of the symbol boundaries, resulting in both ISI and signal distortion of the received signal. A channel with these characteristics is said to be multipath. Moreover, a wireless channel also induces attenuation, adds noise and can cause frequency shifts if one or both the transmitter and receiver are moving.

The fading phenomena can be divided in two main groups: large-scale fading and small-scale fading [45, 109]. The former group accounts for attenuation factors relative

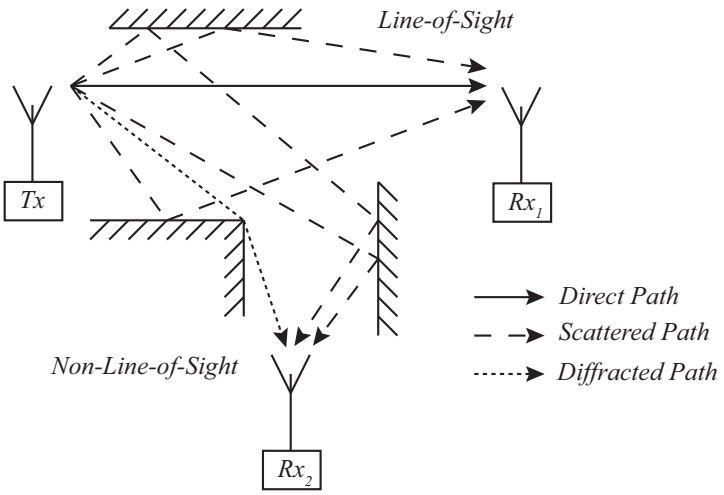

FIGURE 6.1: Illustration of multipath propagation in both LOS and NLOS transmissions.

to free-space path losses which are dependent on both frequency and distance traveled, and shadowing effects from the existence of several geometric objects in the propagation environment. The later describes the effect of constructive and destructive interferences from the multipath transmission and is usually frequency dependent.

While the large-scale fading effects are mainly considered for large cell planning, the small-scale fading is crucial in local area networks where the distortion induced are mainly from the multipath effects. Therefore, we will concentrate on the modeling of multipath channels.

In this chapter we will study the impact of bandpass nonlinear channels on the performance of faded OFDM signals. Moreover, the channel estimation operation is also a subject of study. We focus on an uplink radio transmission system where the OFDM signal is considered to be first distorted by a wireless channel and then the resultant signal passes through a nonlinear element such as an HPA or an electro-optic converter. In this scenario, the faded OFDM signal is corrupted by nonlinear noise and, consequently, both the channel estimation and equalization operations are highly hindered. Since we also focus our work on RoF systems, no signal processing and/or compensation is performed before the central station. Channel estimation techniques suitable for this scenario are not well exploited in the literature. Here we propose a new minimum mean-squared error channel frequency response estimator and its performance is compared with both perfect

and conventional zero-forcing based estimators. This estimator, designed specifically for uplink transmission scenarios, takes into account the potentially significant correlation between complex symbols conveyed by different subcarriers due to both multipath and nonlinear distortion. Additionally, a joint multipath channel and carrier frequency and constant phase offsets (CFO) estimator in the presence of nonlinearities and AWGN is also derived. The chapter is organized as follow: first, an overview on multipath channel modeling is performed; then, the equalization of faded OFDM signals corrupted by a nonlinear distortion is assessed; subsequently, the proposed MMSE channel/CFO estimator is derived and its performance is assessed by means of simulation.

6.2 Multipath channel modeling

Wireless channels can change both in time and frequency. Thus, two important channel parameters are usually defined, namely the coherence time and coherence bandwidth. The first is the duration over which it is considered that the channel is not varying significantly, i.e., it is the maximum time for which its magnitude response is still considered to be correlated with its previous value. The coherence time is closely related with the movement of the transmitter, receiver or even the environment. The faster one of them changes, the less time coherent will be the channel. Furthermore, if there is a relative movement between transmitter and receiver, different paths will have different Doppler shifts. The time coherence of the channel, T_c, is usually defined as [68, 110]

$$T_c \approx \frac{1}{f_{d,max}} = \frac{c}{\nu f_c} \cos \alpha_m \tag{6.1}$$

where $f_{d,max}$ is the maximum Doppler shift, c is the speed of light, α_m is the angle between direction of motion and received signal, ν is the relative velocity and f_c is the transmit frequency. The superposition of several Doppler shifts leads to the so-called Doppler spectrum that describes the spectral broadening caused by the movement. The channel is said to be slow fading if the coherence time is much higher than the delay requirement of the application and fast fading otherwise. Note that this classification depends on both channel characteristics and application.

The other important parameter, coherence bandwidth, is closely related with the frequency selectivity of the channel. The coherence bandwidth shows us how fast the channel changes in frequency. It is mathematically defined as the inverse of the maximum delay spread of the channel. Thus, high delay spreads corresponds to low coherence bandwidths and fast frequency fluctuations of the magnitude response. If the bandwidth of the signal is much smaller than the coherence bandwidth, the channel is said to be frequency non-selective, otherwise it is frequency selective. The maximum delay spread is defined as the total time interval during which reflections arrive with an energy level above a given threshold. The power delay profile (PDP) can assume several forms but is typically assumed to be a decreasing function of delay, i.e., [45, 68, 111, 112]

$$\Omega(\tau) \propto e^{-\tau/\tau_{rms}} \tag{6.2}$$

where τ_{rms} is the RMS delay spread. The idea behind the exponential decay model of the PDP is that the power of reflected paths decays with their delay. Usually wireless channels have delay spreads much smaller than their coherence time. In these circumstances, the channel is said to be *underspread*.

It is common to model time-variant channels as a linear filter with an impulse response (IR) given as a sum of M_p frequency flat channels [45, 68, 69, 109, 110]. So, the complex lowpass equivalent representation of the IR is given by

$$\begin{aligned} \tilde{h}(\tau, t) &= \sum_{p=0}^{M_p-1} \alpha_p(t) e^{-j\theta_p(t)} \delta(t - \tau_p(t)) \\ &= \sum_{p=0}^{M_p-1} \tilde{h}_p(t) \delta(\tau - \tau_p(t)) \end{aligned} \tag{6.3}$$

where $\tilde{h}_p(t) = \alpha_p(t) e^{-j\theta_p(t)}$ and $\tau_p(t)$ are the different path complex gains/attenuations and time delays, respectively, M_p is the total number of paths and $\delta(\cdot)$ is the Dirac delta function.

The multipath channel transfer function (TF) is obtained by performing the conversion of the impulse response (IR) to the frequency domain. Thus, by applying the

Fourier transform to the time-variant IR given by (6.3), it leads to the following frequency response

$$\begin{aligned}\tilde{H}(f,t) &= \mathcal{F}\left\{\tilde{h}(\tau,t)\right\} \\ &= \sum_{p=0}^{M_p-1} \tilde{h}_p(t) e^{-j2\pi f \tau_p(t)}\end{aligned} \tag{6.4}$$

In local area networks, the multipath channel can be considered relatively static during the transmission of a block of symbols, i.e., it is considered that the coherence time is much higher than the symbol duration, thus $\tilde{h}(\tau,t)$ is considered to be constant over a certain period of time and reduces to $\tilde{h}(\tau)$. Accordingly, both the complex gains and delays are also considered to be independent of time and simplified to $\tilde{h}_p$ and τ_p.

If a large number of paths is considered, we may assume that the complex gains $\tilde{h}_p$ are independent random variables. Moreover, it is also assumed that the two-dimensional autocorrelation function of $H(f,t)$ is both time and frequency shift invariant. Such a process is called wide-sense stationary uncorrelated scattering (WSSUS) and is commonly used to model multipath fading channels [45, 68, 113]. The central limit theorem states that as the number of paths becomes larger, the resulting sum tends to a zero-mean circularly symmetric complex Gaussian random variable. Therefore, the magnitude of the complex envelope of the received signal is in fact a Rayleigh distributed RV and its phase is uniformly distributed in $[0; 2\pi[$. This model is called Rayleigh fading and it is used in non-line-of-sight (NLOS) scenarios. When a stronger path is present (usually the line-of-sight path), at least one of the paths is modeled by a nonzero-mean RV. Hence, in LOS channels it is common to model the IR of the multipath channel using Rician distributed RVs.

In the generic LOS channel, the magnitude of the complex gains $\tilde{h}_p$ are described by the Rician PDF

$$p\left(x|\mu,\sigma\right) = \frac{x}{\sigma^2} e^{-\left(\frac{x^2+\mu^2}{2\sigma^2}\right)} I_0\left(\frac{x\mu}{\sigma^2}\right) \tag{6.5}$$

where μ and σ are the mean and the standard deviation of the RV X, respectively, and $I_0(\cdot)$ is the modified Bessel function of the first kind with order zero. The ratio $K = \mu^2/\sigma^2$ is commonly denoted as *Rician K-factor* and is the ratio of signal power between the dominant component, usually the LOS, and the scattered. Note that for

$K = 0$ the distribution in (6.5) reduces to a Rayleigh distribution and there is no dominant component, whereas for $K \gg 0$ the channel is considered to have a dominant component. Other probabilistic models describing the statistical behavior of fading channels can also be used, depending on the nature of the channel [110].

6.3 Equalization of faded OFDM signals in a nonlinear system

Because of its orthogonal multi-carrier nature, OFDM shows a good performance in multipath and fading environments. As already referred in chapter 2, the symbol period per subcarrier is considerably high and, consequently, the bandwidth of each modulated subcarrier becomes narrower than the coherence bandwidth of the channel [45]. In other words, each subcarrier experiences flat fading in multipath channels, rather than frequency selective fading. This characteristic combined with the use of a cyclic prefix avoids ISI and ICI and greatly simplifies receiver and equalizer structures.

In order to carry out simulations of faded signals, it is necessary to represent the multipath in the discrete domain. A very widely used model is the tapped delay line (TDL). The TDL model is based on the assumption that a large number of reflected paths with random and independent and uncorrelated amplitudes and phases arrive at the receiver during the time window of a single tap. Therefore, each tap contains an aggregate of paths that is considered to be sufficiently large in order to apply the central limit theorem. In Figure 6.2 an illustrative example of several frequency responses of Rayleigh distributed (NLOS) channels is depicted. Here we have considered equally spaced TDL models with 3 to 15 taps and as the number of taps increase, the delay spread also increases and the coherence bandwidth decreases. As expected, it is clearly seen that the frequency of the number of peaks and notches (valleys) increases with the delay spread. As an example, it is also depicted in Figure 6.3 a flat fading frequency response representation for each OFDM subcarrier of a frequency selective channel. Note that if the number of channel taps is low, the correlation of the channel frequency response along the frequency is considerable high.

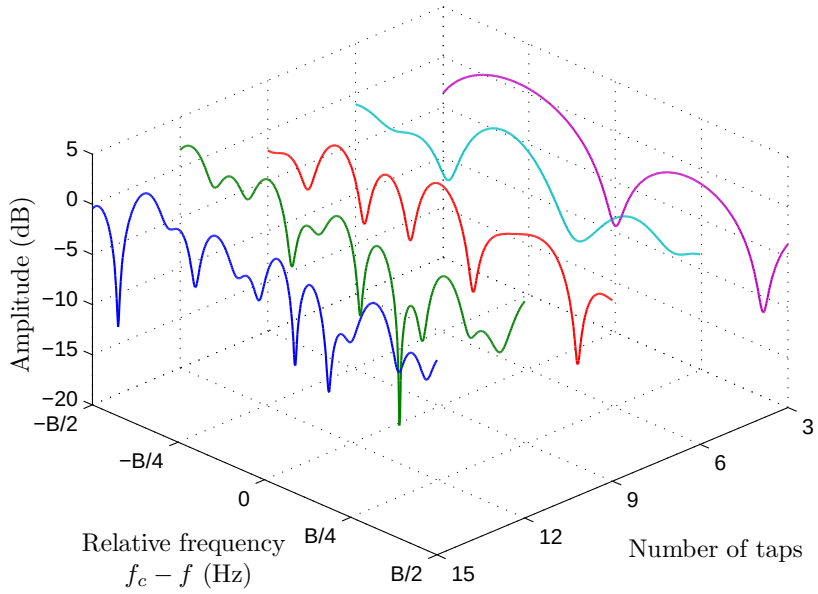

FIGURE 6.2: Illustrative example of Rayleigh distributed channel frequency responses.

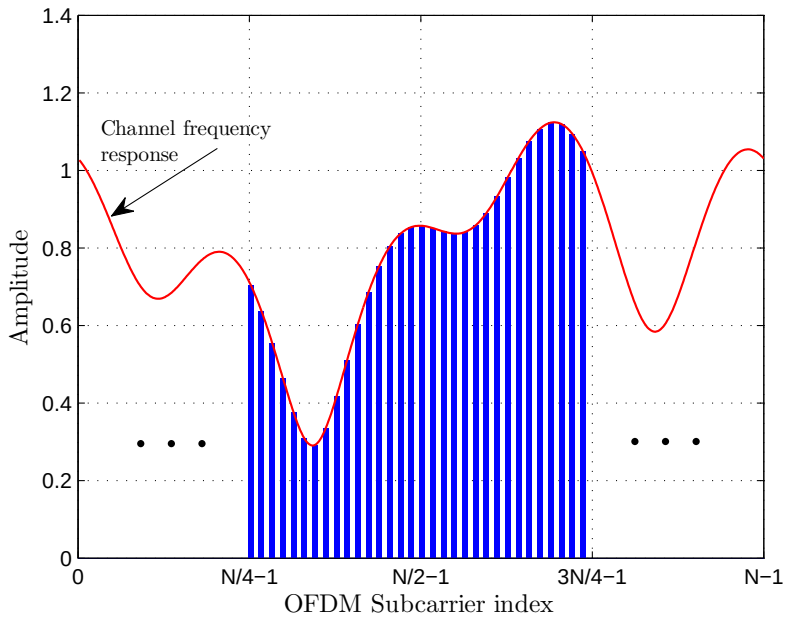

FIGURE 6.3: Illustrative representation of OFDM subcarrier flat fading frequency responses of a multipath channel.

Let us now consider our OFDM signal transmission setup. In this chapter we analyze the uplink transmission of OFDM signals. As previously stated, the OFDM signal is considered to be both linearly and nonlinearly distorted in this order by bandpass fading and a bandpass nonlinear channels. The nonlinearity is represented by the previously described power series lowpass representation given by the following input-output characteristic

$$\begin{aligned}\tilde{y}(t) &= f[\tilde{x}(t)] \\ &= \tilde{x}(t) \sum_{i=1}^{(L+1)/2} \tilde{c}_{2i-1} |\tilde{x}(t)|^{2i-2}\end{aligned} \tag{6.6}$$

where $\tilde{c}_i$ is the equivalent lowpass complex coefficient of order i and L is the maximum order (odd) of the nonlinearity.

The equivalent baseband OFDM wireless system is depicted in Figure 6.4 where $\tilde{s}(t)$ and $\tilde{x}(t)$ are the complex envelopes of the transmitted OFDM signal before and after the bandpass fading channel, respectively, $\tilde{y}(t)$ is the complex envelope of the nonlinearly distorted faded OFDM signal, $\tilde{r}(t)$ is the complex envelope of the received OFDM signal, $\tilde{n}(t)$ is the complex envelope of the AWGN with power spectral density N_0 and $\hat{\mathbf{H}}$ is the estimate vector of the multipath channel frequency response. Note that the communication system depicted in Figure 6.4 can represent a typical radio-over-fiber uplink system, where the bandpass fading represents the radio channel between the remote antenna unit and the wireless device, the bandpass nonlinearity represents the electro-optic modulator and, for last, the AWGN source, the photodiode thermal noise, respectively.

The complex envelope of the received OFDM signal is given by

$$\tilde{r}(t) = f\left[\tilde{s}(t) * \tilde{h}(t)\right] + \tilde{n}(t) \tag{6.7}$$

where '$*$' denotes the convolution.

At the receiver side, with assumptions that the bandpass multipath fading has an impulse response no longer than the OFDM cyclic prefix duration, T_{CP}, the nth subcarrier output of the kth OFDM symbol is obtained by multiplying the received OFDM

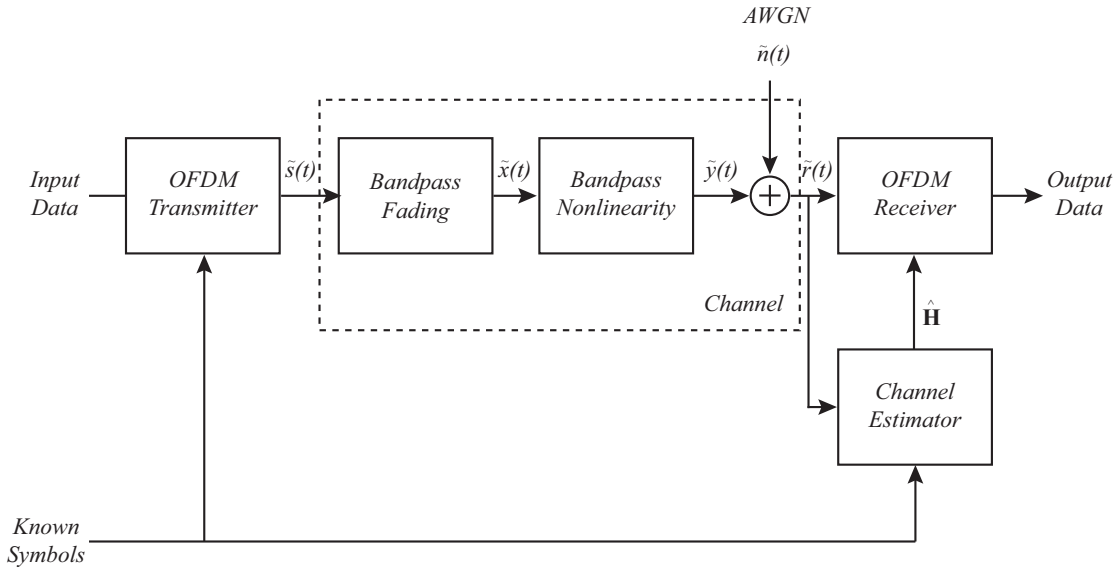

FIGURE 6.4: Equivalent baseband OFDM wireless communication model.

signal, $\tilde{r}(t)$, by the function $g_n^*(t-kT)$ and integrating from $kT+T_{CP}$ to $(k+1)T$. Thus,

$$\begin{aligned} R_{k,n} &= Y_{k,n} + N_{k,n} \\ &= \sum_{i=1}^{(L+1)/2} \frac{\tilde{c}_{2i-1}}{(T-T_{CP})^{i-1}} \sum_{k=-\infty}^{\infty} \sum_{n_1=0}^{N-1} \cdots \sum_{n_{2i-1}=0}^{N-1} H_{k,n_1} S_{k,n_1} \cdots H_{k,n_i} S_{k,n_i} \\ &\quad \times H^*_{k,n_{i+1}} S^*_{k,n_{i+1}} \cdots H^*_{k,n_{2i-1}} S^*_{k,n_{2i-1}} \delta(n_1 + \cdots + n_i - n_{i+1} - \cdots - n_{2i-1} - n) \\ &\quad + N_{k,n} \end{aligned} \tag{6.8}$$

where $H_{k,n}$ is the frequency response of the multipath fading channel in time slot k and subchannel n. Note that the vector $\mathbf{R}_k = [R_{k,-1/2(L-1)(N-1)}, \cdots, R_{k,1/2(L+1)(N-1)}]^T$ represents the set of sufficient statistics. Subsequently, this set is fed into the estimator block that outputs the frequency response channel estimate for each subchannel, $\hat{H}_{k,n}$.

Similarly to the analysis performed in 5.2, the received complex symbol conditioned to a transmitted complex symbol $S^i_{k,n}$ can be written as the sum of four main terms, i.e.,

$$R^i_{k,n} = \left[D^i_{k,n} + \overline{W}^i_n\right] + {}^{zm}W^i_{k,n} + N_{k,n} \tag{6.9}$$

where the term $D^i_{k,n}$ accounts for the quantity that represents the useful complex symbol affected by the corresponding multipath channel frequency response and by compression gain terms, the term $\overline{W}^i_n$ represents the desensitization terms and ${}^{zm}W^i_{k,n}$ represents the

intermodulation distortion (IMD) quantity.

In a conventional OFDM receiver with a one-tap equalizer, the estimate of the transmitted complex symbols, $\hat{S}_{k,n}$, is obtained by applying a zero-forcing (ZF) based equalization to the received complex symbol given by (6.8) and (6.9), i.e.,

$$\begin{aligned}\hat{S}_{k,n} &= \frac{R_{k,n}}{\hat{H}_{k,n}} \\ &= \frac{\left[D_{k,n} + \overline{W}_n\right]}{\hat{H}_{k,n}} + \frac{{}^{zm}W_{k,n}}{\hat{H}_{k,n}} + \frac{N_{k,n}}{\hat{H}_{k,n}}, \quad n = 0, 1, \cdots, N-1\end{aligned} \tag{6.10}$$

Note that for low OBO values the weight of compression and desensitization terms increases as well as the variance of the IMD term, severely affecting the estimation process. Moreover, the estimate of the transmitted symbols, given by the equalization process, will also be highly dependent on the estimate of the channel since near-zero magnitude estimates may enhance both IMD and AWGN terms.

6.4 OFDM channel estimation

As previously stated, the multipath channel can tremendously affect both amplitude and phase of a signal. In a coherent modulation scheme the phase variation must be tracked and compensated in order to recover the data stream, while for non-coherent modulations it is only necessary to estimate the fading envelope. One of the main advantages of OFDM is its potentially simple equalization and channel estimation operations [45, 68]. OFDM channel estimation techniques can be either blind or non-blind. While the former is not so much attractive since it mostly exploits the statistical properties of the channel and require a large amount of data (e.g. [114]), the later is the most commonly used. Due to the OFDM two-dimensional structure, the estimation procedures can be performed using a set of known training symbols that can be assigned to both the time and/or frequency domain. These set of symbols are inserted at specific subcarrier indexes also known as pilot subcarriers and are used to enable channel estimation.

In Figure 6.5 it is depicted the two most common pilot schemes used [115–117]. Pilot subcarriers can be inserted either in a block scheme where all (or at least the majority of the) subcarriers of a given OFDM symbol are used as pilots (see Figure 6.5(a)), or in a comb scheme where pilots are inserted in all OFDM symbols but only at specific indexes

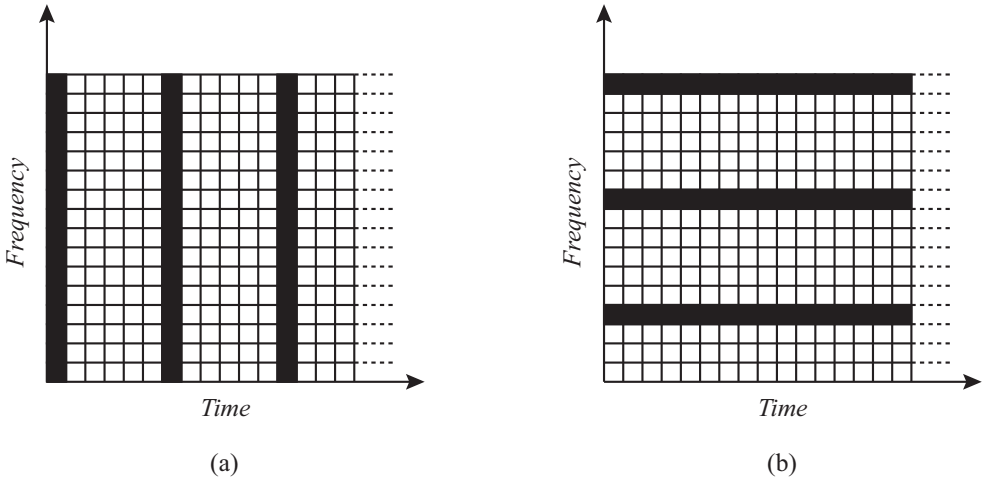

FIGURE 6.5: Representation of (a) block-type and (b) comb-type pilot subcarrier arrangements.

(see Figure 6.5(b)). The block-type scheme assumes that the channel is slow varying and thus the channel estimative is valid for a given number of consecutive OFDM symbols. On the other hand, the comb-type is mainly considered for transmissions where the channel varies significantly between two consecutive OFDM symbols. Since only some of the subcarriers are used as pilots, the channel estimate at others frequencies must be obtained using interpolation operations.

The simplest means for channel estimation in an OFDM based transmission is to use pilot-aided zero-forcing (ZF) techniques. In a linear transmission scheme, it is also called *least squares*. This technique will be briefly discussed in the following section.

In order to exploit channel statistics and to improve its performance, linear MMSE based techniques for channel estimation are continuously being studied and proposed in the literature for pilot-based schemes [115, 117–122]. In fact, LMMSE estimation techniques can use both the SNR and correlation information between subcarriers and OFDM symbols to optimize the estimation. Moreover, simplified sub-optimal methods are often considered [115, 123, 124]. A complementary approach that uses algorithms to predict the channel for subsequent time slots are also being considered [125–127].

6.4.1 Zero-forcing estimator

By transmitting known symbols at specific subcarrier indexes (pilots), the ZF estimation of the frequency response of the channel is obtained by just dividing the received pilot

symbols by the transmitted, i.e., [116, 120]

$$\begin{aligned}\hat{H}^{ZF}_{k,n_p} &= \frac{R_{k,n_p}}{S_{k,n_p}} \\ &= \frac{Y_{k,n_p}}{S_{k,n_p}} + \frac{N_{k,n_p}}{S_{k,n_p}}\end{aligned} \tag{6.11}$$

where n_p accounts for all pilot-subcarriers indexes. Note that if the transmission channel is linear, i.e., $Y_{k,n} = H_{k,n}S_{k,n}$, $n = 0, \cdots, N-1$, then $\frac{Y_{k,n_p}}{S_{k,n_p}} = H_{k,n_p}$.

From (6.11) it is evident that in nonlinearly distorted OFDM signals the ZF estimator is not the best option since the received signal can be extremely corrupted by IMD distortion. In this scenario, the ZF estimation of the channel will also be very noisy.

The ZF estimator can be used in both block-type and comb-type schemes. Nevertheless, from (6.11) it is apparent that the ZF estimation does not exploits the correlation between subcarriers and across OFDM symbols nor uses any knowledge of the channel statistics. It is usually used to obtain an initial channel estimation which is then improved using more complex estimation techniques.

We will now derive the structure of the frequency response channel estimator that minimizes the mean-squared error of the estimate vector for the OFDM communication system depicted in Figure 6.4.

6.4.2 A novel MMSE channel estimator

Let us now consider the structure of the MMSE channel estimator for both faded and nonlinearly distorted OFDM signals corrupted by AWGN. Here we derive a new channel estimator structure that processes the distorted OFDM signal in a linear fashion in order to optimize a performance metric, namely the MSE. Our linear MMSE channel estimator is a pilot-aided channel estimation technique that operates using a block-type pilot based scheme where pilots are inserted in a specific OFDM symbol and are used to estimate the frequency response of the multipath channel. Contrary to what happens with the ZF estimator and others MMSE estimators optimized only for linear distortion, our approach does not disregard the potentially significant correlation between the complex symbols conveyed by different subcarriers due to both multipath and nonlinear distortion.

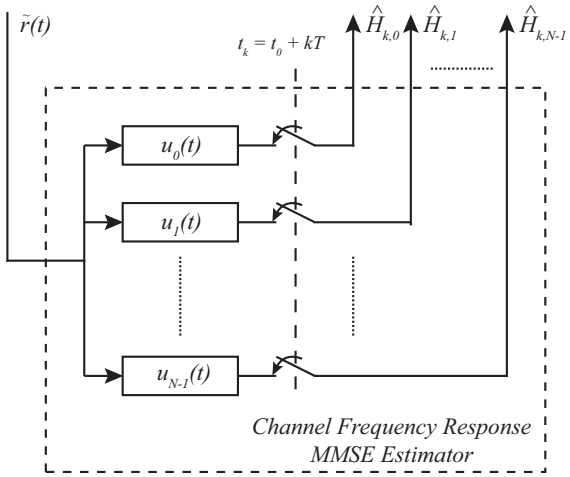

FIGURE 6.6: Structure of the channel frequency response MMSE estimator.

The multipath channel is considered to be quasi-static over a block of OFDM symbols, i.e., the coherence time is much greater than the OFDM symbol duration. This allows to use one part of the OFDM block for estimation purposes and the other for the transmission of useful data. Moreover, we will consider a TDL model for the multipath channel with its envelope following both a Rayleigh and Rician distribution[1].

A representation of the proposed channel estimator is depicted in Figure 6.6. We take the estimator to consist of a bank of N linear filters with impulse responses $u_n(t)$, $n = 0, \cdots, N-1$, that produce estimates of the frequency response of the multipath channel for each subchannel n at slot index k. Thus, the estimate of the channel complex frequency response in time slot k and subcarrier n is

$$\begin{aligned} \hat{H}_{k,n} &= [\tilde{r}(t) * u_n(t)]_{t=t_k} \\ &\triangleq \int_{-\infty}^{+\infty} u_n(\tau)\tilde{r}(t_k - \tau)d\tau \end{aligned} \tag{6.12}$$

The objective is to determine the set of linear filters impulse response that minimize the MSE of the channel estimate given by

$$\begin{aligned} \xi &= \mathrm{E}\left[\left\|\mathbf{H}_k - \hat{\mathbf{H}}_k\right\|^2\right] \\ &= \sum_{n=0}^{N-1} \xi_n \end{aligned} \tag{6.13}$$

[1]Here we will not consider the exponential decay for the PDP in order to keep the analysis more generic. Yet, its implementation is completely straightforward involving only the multiplication of the TDL impulse response by the PDP. In chapter 7, an exponential PDP will be used for the case study in radio-over-fiber systems.

where $\mathbf{H}_k = [H_{k,0}, H_{k,1}, \cdots, H_{k,N-1}]^T$ is the channel frequency response vector in time slot k, $\hat{\mathbf{H}}_k = \left[\hat{H}_{k,0}, \hat{H}_{k,1}, \cdots, \hat{H}_{k,N-1}\right]^T$ is the channel frequency response estimate vector in time slot k and ξ_n is the MSE associated with subcarrier n and is given by

$$\begin{aligned}
\xi_n &= \mathrm{E}\left[\left|H_{k,n} - \hat{H}_{k,n}\right|^2\right] \\
&= \mathrm{E}\left[|H_{k,n} - [\tilde{r}(t_k) * u_n(t_k)]|^2\right] \\
&= \mathrm{E}\left[|H_{k,n}|^2 + \int_{-\infty}^{+\infty}\int_{-\infty}^{+\infty} u_n(\tau_1)u_n^*(\tau_2)\tilde{r}(t_k-\tau_1)\tilde{r}^*(t_k-\tau_2)d\tau_1 d\tau_2\right. \\
&\quad \left. - \int_{-\infty}^{+\infty} u_n(\tau_1)H_{k,n}^*\tilde{r}(t_k-\tau_1)d\tau_1 - \int_{-\infty}^{+\infty} u_n^*(\tau_2)H_{k,n}\tilde{r}^*(t_k-\tau_2)d\tau_2\right]
\end{aligned} \tag{6.14}$$

Note that the MSE cost function to be minimized given by (6.14) is very similar to the one in chapter 4 given by (4.5). In fact, instead of the transmitted complex symbols $S_{k,n}$ we have the channel frequency responses of the corresponding subcarrier and time slot, $H_{k,n}$. Therefore, the derivation of the structure for the channel frequency response estimate that minimizes the MSE follows a similar procedure as the one in chapter 4 with particular differences.

Representing the complex envelope of the received OFDM signal, $\tilde{r}(t)$, by its nonlinearly distorted and AWGN components, $\tilde{y}(t)$ and $\tilde{n}(t)$, respectively, (6.13) can be rewritten as

$$\begin{aligned}
\xi_n &= \mathrm{E}\left[|H_{k,n}|^2\right] \\
&\quad + \int_{-\infty}^{+\infty}\int_{-\infty}^{+\infty} u_n(\tau_1)u_n^*(\tau_2)\left\{\mathrm{E}\left[\tilde{y}(t_k-\tau_1)\tilde{n}^*(t_k-\tau_2)\right] + \mathrm{E}\left[\tilde{y}^*(t_k-\tau_2)\tilde{n}(t_k-\tau_1)\right]\right. \\
&\quad \left. + \mathrm{E}\left[\tilde{y}(t_k-\tau_1)\tilde{y}^*(t_k-\tau_2)\right] + \mathrm{E}\left[\tilde{n}(t_k-\tau_1)\tilde{n}^*(t_k-\tau_2)\right]\right\} d\tau_1 d\tau_2 \\
&\quad - \int_{-\infty}^{+\infty} u_n(\tau_1)\left\{\mathrm{E}\left[H_{k,n}^*\tilde{y}(t_k-\tau_1)\right] + \mathrm{E}\left[H_{k,n}^*\tilde{n}(t_k-\tau_1)\right]\right\} d\tau_1 \\
&\quad - \int_{-\infty}^{+\infty} u_n^*(\tau_2)\left\{\mathrm{E}\left[H_{k,n}\tilde{y}^*(t_k-\tau_2)\right] + \mathrm{E}\left[H_{k,n}\tilde{n}^*(t_k-\tau_2)\right]\right\} d\tau_2
\end{aligned} \tag{6.15}$$

Note that due to the statistical properties of the signals in (6.15), the relations given by (4.7) through (4.9) are also valid. Moreover, the expected value of the product between $\tilde{n}(t)$ and $H_{k,n}$ (or their complex conjugate values) always equal zero. Again, using calculus of variations and considering a nonlinearly distorted OFDM signal given

by (6.6) and the impulse responses of the N linear filters as a summation of $L(N-1)+1$ orthonormal functions $g_i^*(t_0-t)$ affected by a constant coefficient $\beta_{i,n}$, i.e.,

$$u_n(t) = \sum_{i_{min}}^{i_{max}} \beta_{i,n} g_i^*(t_0 - t) \tag{6.16}$$

where $i_{min} = -1/2(L-1)(N-1)$ and $i_{max} = 1/2(L+1)(N-1)$, the minimization of the MSE leads to the following condition

$$\sum_{i=i_{min}}^{i_{max}} \beta_{i,n} \mathrm{E}\left[Y_{k,i} Y_{k,m}^*\right] + 2N_0 \beta_{m,n} = \mathrm{E}\left[H_{k,n} Y_{k,m}^*\right],$$
$$m = -1/2(L-1)(N-1), \cdots, 1/2(L+1)(N-1) \tag{6.17}$$

Note that the $L(N-1)+1$ orthonormal functions ensure the extraction of a set of sufficient statistics from the OFDM signal.

By substituting the impulse response of the nth branch given by (6.16) in (6.12), the estimate of the channel frequency response in time slot k and subcarrier n reduces to

$$\begin{aligned}\hat{H}_{k,n} &= \int_{-\infty}^{+\infty} \sum_{i_{min}}^{i_{max}} \beta_{i,n} g_i^*(t_0 - \tau) \tilde{r}(t_k - \tau) d\tau \\ &= \sum_{i_{min}}^{i_{max}} \beta_{i,n} \int_{-\infty}^{+\infty} \tilde{r}(t_k - \tau) g_i^*(t_0 - \tau) d\tau \\ &= \sum_{i_{min}}^{i_{max}} \beta_{i,n} R_{k,i}\end{aligned} \tag{6.18}$$

In an equivalent way, (6.17) can also be represented in the following matrix notation

$$\begin{aligned}\mathbf{M}_\beta &\equiv [\beta_{i,n}]_{[L(N-1)+1]\times[N]} \\ &= \left[\mathrm{E}\left[\mathbf{Y}_k \mathbf{Y}_k^H\right] + 2N_0 \mathbf{I}_{[L(N-1)+1]}\right]^{-1} \mathrm{E}\left[\mathbf{Y}_k^* \mathbf{H}_k^T\right]\end{aligned} \tag{6.19}$$

where $\mathbf{M}_\beta$ is the matrix of coefficients $\beta_{i,n}$ with size $L(N-1)+1$ by N, $\mathbf{I}_{[L(N-1)+1]}$ is the identity matrix of size $L(N-1)+1$ and $\mathbf{Y}_k = \left[Y_{k,-1/2(L-1)(N-1)}, \cdots, Y_{k,1/2(L+1)(N-1)}\right]^T$ is the vector of nonlinearly distorted complex symbols in time slot k. Finally, the

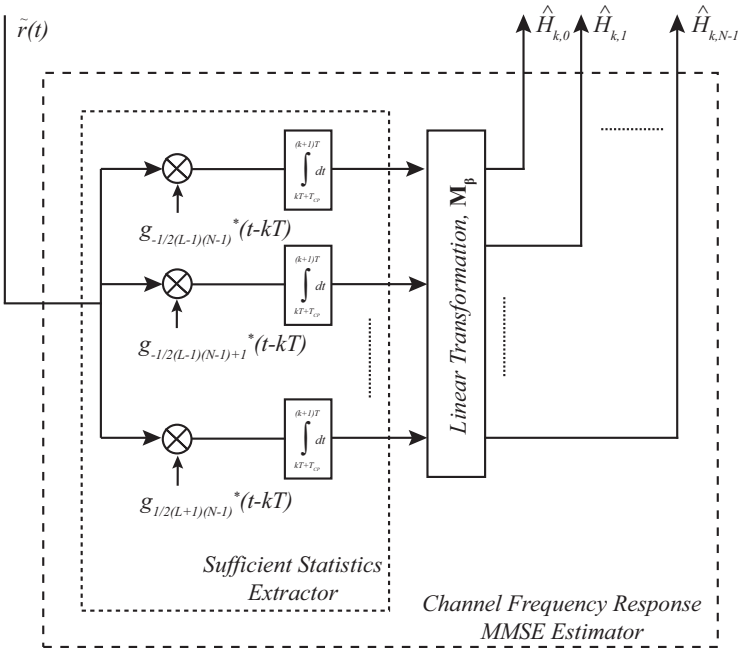

FIGURE 6.7: Alternative structure of the channel frequency response MMSE estimator.

frequency channel estimate vector is given by

$$\hat{\mathbf{H}}_k = \mathbf{M}_\beta^T \hat{\mathbf{R}}_k \tag{6.20}$$

As previously stated, the structure for the channel frequency response MMSE estimator is indeed similar to the one for the MMSE receiver for nonlinearly distorted OFDM signals derived in chapter 4. In fact, the structure depicted in Figure 6.6 representing a set of linear filters given by (6.16) can also be, alternatively, represented by a set of correlators or a set of filters matched to every possible frequency components of the nonlinearly distorted OFDM responsible for the extraction of the sufficient statistics of the signal, followed by a linear transformation defined by coefficients $\beta_{i,n}$ given by (6.17) or, in a matrix notation, by (6.19) (see Figure 6.7).

Let us now focus on the derivation of matrix of coefficients $\mathbf{M}_\beta$. To analytically compute the expectations in (6.19), we use a set of known symbols, i.e., a block-type pilot arrangement is considered. Thus, when the receiver is performing channel estimation, it is considered that the estimator knows the vector of transmitted complex symbols, $\mathbf{S}'$, and that it is used in time slot indexes k dedicated to estimation procedures. With this assumption, the elements of the matrix given by expectation value $\mathrm{E}\left[\mathbf{Y}_k \mathbf{Y}_k^H \middle| \mathbf{S}'\right]$

are given by

$$
\begin{aligned}
&\mathrm{E}\left[Y_{k,i}Y_{k,m}^{*}\middle|\mathbf{S}'\right] = \\
&= \frac{|c_1|^2}{(T-T_{CP})^0}\sum_{n_1}\sum_{n_2}\mathrm{E}\left[H_{k,n_1}H_{k,n_2}^{*}\right]S'_{n_1}S'^{*}_{n_2}\delta(i-n_1)\delta(m-n_2) \\
&\quad + \frac{c_1c_3^{*}}{(T-T_{CP})^2}\sum_{n_1}\sum_{n_2}\sum_{n_3}\sum_{n_4}\mathrm{E}\left[H_{k,n_1}H_{k,n_2}^{*}H_{k,n_3}^{*}H_{k,n_4}\right]S'_{n_1}S'^{*}_{n_2}S'^{*}_{n_3}S'_{n_4} \\
&\qquad \times\delta(i-n_1)\delta(m-n_2-n_3+n_4) \\
&\quad + \frac{c_3c_1^{*}}{(T-T_{CP})^2}\sum_{n_1}\sum_{n_2}\sum_{n_3}\sum_{n_4}\mathrm{E}\left[H_{k,n_1}H_{k,n_2}H_{k,n_3}^{*}H_{n_4}^{*}\right]S'_{n_1}S'_{n_2}S'^{*}_{n_3}S'^{*}_{n_4} \\
&\qquad \times\delta(i-n_1-n_2+n_3)\delta(m-n_4) \\
&\quad + \frac{|c_3|^2}{(T-T_{CP})^4}\sum_{n_1}\sum_{n_2}\sum_{n_3}\sum_{n_4}\sum_{n_5}\sum_{n_6}\mathrm{E}\left[H_{k,n_1}H_{k,n_2}H_{k,n_3}^{*}H_{k,n_4}^{*}H_{k,n_5}^{*}H_{k,n_6}\right] \\
&\qquad \times S'_{n_1}S'_{n_2}S'^{*}_{n_3}S'^{*}_{n_4}S'^{*}_{n_5}S'_{n_6}\delta(i-n_1-n_2+n_3)\delta(m-n_4-n_5+n_6) \\
&\quad + \cdots
\end{aligned}
\tag{6.21}
$$

In a similar way, the elements of $\mathrm{E}\left[\mathbf{Y}_k^{*}\mathbf{H}_k^{T}\middle|\mathbf{S}'\right]$ are given by

$$
\begin{aligned}
\mathrm{E}\left[H_{k,n}Y_{k,m}^{*}\middle|\mathbf{S}'\right] &= \frac{c_1^{*}}{(T-T_{CP})^0}\sum_{n_1}\mathrm{E}\left[H_{k,n}H_{k,n_1}^{*}\right]S'_{n}S'^{*}_{n_1}\delta(m-n_1) \\
&\quad + \frac{c_3^{*}}{(T-T_{CP})^1}\sum_{n_1}\sum_{n_2}\sum_{n_3}\mathrm{E}\left[H_{k,n}H_{k,n_1}^{*}H_{k,n_2}^{*}H_{k,n_3}\right] \\
&\qquad \times S'_{n}S'^{*}_{n_1}S'^{*}_{n_2}S'_{n_3}\delta(m-n_1-n_2+n_3) \\
&\quad + \cdots
\end{aligned}
\tag{6.22}
$$

To analytically obtain the expressions of the expectations of matrices $\mathrm{E}\left[\mathbf{Y}_k\mathbf{Y}_k^{H}\middle|\mathbf{S}'\right]$ and $\mathrm{E}\left[\mathbf{H}_k\mathbf{Y}_k^{H}\middle|\mathbf{S}'\right]$ it is necessary to derive the expectation of the product of complex Gaussian RVs. To do so, we must refer to the Isserlis' theorem [128] which relates the expectation of products of jointly Gaussian RVs to products of pairs of these variables.

6.4.2.1 Rayleigh fading channel case

Let us consider the case when the channel is considered to be Rayleigh fading. Here, the channel frequency responses $H_{k,n}$ follow a zero-mean complex Gaussian distribution. The Isserlis' theorem states that the expectation of the product of m even zero-mean

jointly Gaussian RVs, $\zeta_1\zeta_2\cdots\zeta_m$, is equal to the sum of all distinct ways of partitioning $\zeta_1, \zeta_2, \cdots, \zeta_m$ into pairs, while for m odd, it equals zero, irrespective of their mutual correlation, i.e., [128]

$$\mathrm{E}\left[\zeta_1\zeta_2\cdots\zeta_m\right] = \begin{cases} \sum\prod \mathrm{E}\left[\zeta_i\zeta_j\right], & m \text{ is even} \\ 0, & m \text{ is odd} \end{cases} \tag{6.23}$$

This yields $m!/\left[(m/2)!2^{(m/2)}\right]$ terms in the sum, each being the product of $m/2$ covariances. Note that $\zeta_i, i = 1, 2, \cdots, m$ can be either complex or real. From (6.21) and (6.22) we can also note that all expectations are in fact the product of m Gaussian RVs in which $m/2$ are complex conjugate. Thus, for $m = 4$ and considering the product of two Gaussian RVs and two complex conjugate Gaussian RVs, the theorem gives the following relation

$$\mathrm{E}\left[\zeta_1\zeta_2\zeta_3^*\zeta_4^*\right] = \mathrm{E}\left[\zeta_1\zeta_2\right]\mathrm{E}\left[\zeta_3^*\zeta_4^*\right] + \mathrm{E}\left[\zeta_1\zeta_3^*\right]\mathrm{E}\left[\zeta_2\zeta_4^*\right] + \mathrm{E}\left[\zeta_1\zeta_4^*\right]\mathrm{E}\left[\zeta_2\zeta_3^*\right] \tag{6.24}$$

Therefore, the computation of the product of zero-mean jointly Gaussian RVs reduces to a sum of products of pairs. Recalling the multipath impulse response model for quasi-static (slow varying) channels,

$$\tilde{h}(\tau) = \sum_{p=0}^{M_p-1} \tilde{h}_p\delta(\tau - \tau_p) \tag{6.25}$$

the equivalent Fourier pair of the discrete TDL model considering equally time spaced tap gains is given by

$$\tilde{h}[i] = \sum_{l=0}^{M_l-1} \tilde{h}_l\delta[i - l] \tag{6.26}$$

and

$$\begin{aligned} H_{k,n} \equiv \tilde{H}[n] &= DFT\{\tilde{h}[i]\} \\ &= \sum_{i=0}^{N_{DFT}-1} \tilde{h}[i]e^{-j\frac{2\pi}{N_{DFT}}in} \\ &= \sum_{l=0}^{M_l-1} \tilde{h}_l e^{-j\frac{2\pi}{N_{DFT}}ln}, n = 0, 1\cdots, N-1 \end{aligned} \tag{6.27}$$

where $M_l < N \leq N_{DFT}$, M_l is the number of taps considered and N_{DFT} is the size of the DFT. Consequently, all three possible expectations of product of pair combinations in (6.23) are given by

$$\mathrm{E}\left[H_{k,n_1}H_{k,n_2}\right] = \sum_{l_1=0}^{M_l-1}\sum_{l_2=0}^{M_l-1} \mathrm{E}\left[\tilde{h}_{l_1}\tilde{h}_{l_2}\right] e^{-j\frac{2\pi}{N_{DFT}}(l_1n_1+l_2n_2)} = 0 \tag{6.28}$$

$$\mathrm{E}\left[H^*_{k,n_1}H^*_{k,n_2}\right] = \sum_{l_1=0}^{M_l-1}\sum_{l_2=0}^{M_l-1} \mathrm{E}\left[\tilde{h}^*_{l_1}\tilde{h}^*_{l_2}\right] e^{j\frac{2\pi}{N_{DFT}}(l_1n_1+l_2n_2)} = 0 \tag{6.29}$$

$$\begin{aligned}\mathrm{E}\left[H_{k,n_1}H^*_{k,n_2}\right] &= \sum_{l_1=0}^{M_l-1}\sum_{l_2=0}^{M_l-1} \mathrm{E}\left[\tilde{h}_{l_1}\tilde{h}^*_{l_2}\right] e^{-j\frac{2\pi}{N_{DFT}}(l_1n_1-l_2n_2)} \\ &= \sum_{l=0}^{M_l-1} \mathrm{E}\left[\left|\tilde{h}_l\right|^2\right] e^{-j\frac{2\pi}{N_{DFT}}(n_1-n_2)l} \\ &= \frac{1}{M_l}\sum_{l=0}^{M_l-1} e^{-j\frac{2\pi}{N_{DFT}}(n_1-n_2)l}\end{aligned} \tag{6.30}$$

Note that the expectation $\mathrm{E}\left[\tilde{h}_{l_1}\tilde{h}^*_{l_2}\right]$ is zero for all l_1 and l_2 but for $l_1 = l_2$. Without loss of generality, we assume that the channel is normalized, i.e., $\mathrm{E}\left[\left|\tilde{h}_l\right|^2\right] = 1/M_l$, or equivalent, $\mathrm{E}\left[\left|H_{k,n}\right|^2\right] = 1$.

In Figures 6.8 and 6.9 it is depicted the normalized values for the expectation matrix (6.21) considering a 6 taps multipath channel followed by both a linear and nonlinear channel with OBO = 7.7 dB, respectively. Note that when considering a linear channel transmission, the expectation matrix reduces to the covariance of the frequency responses of the multipath channel conditioned to a known symbols vector. For an OBO value of 7.7 dB, expectation values from Figure 6.9 show that new correlations between symbols conveyed by different subcarriers indexes arise both inside and outside the signals bandwidth.

6.4.2.2 Rician fading channel case

For a Rician fading channel, it is considered that the channel has a strong LOS component, i.e., the frequency responses $H_{k,n}$ are considered to be non-zero mean complex Gaussian distributed. A simple generalization of the Isserlis' theorem for m RVs

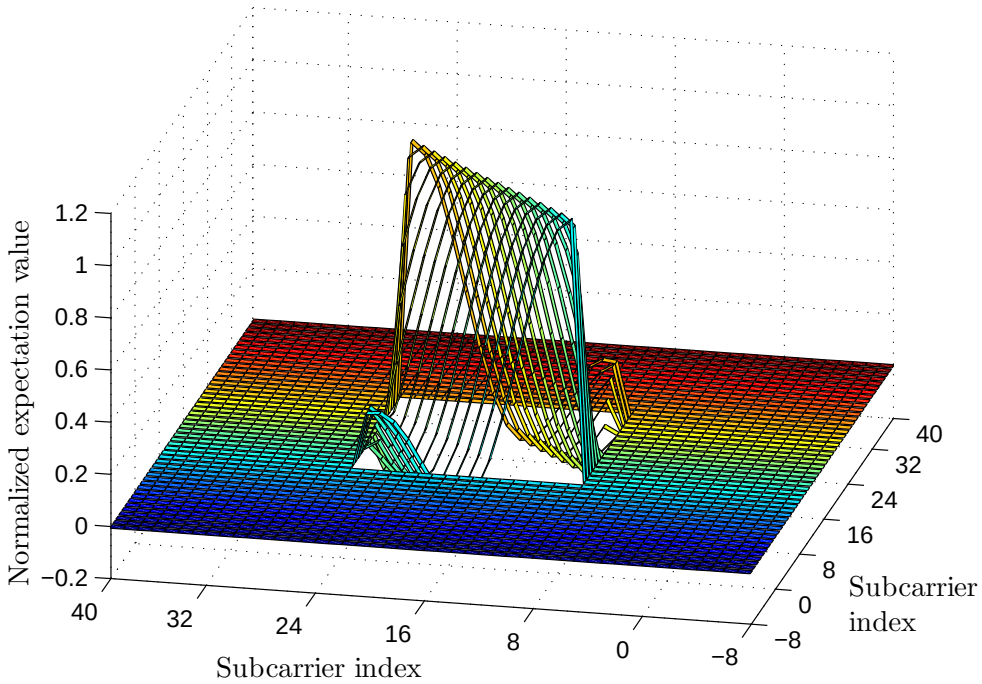

FIGURE 6.8: Normalized values for the real part of the matrix $\mathrm{E}\left[Y_{k,i}Y_{k,m}^{*}|\mathbf{S}'\right]$ considering a 6 taps multipath channel followed by a linear channel (OBO $= +\infty$) for $N = 16$.

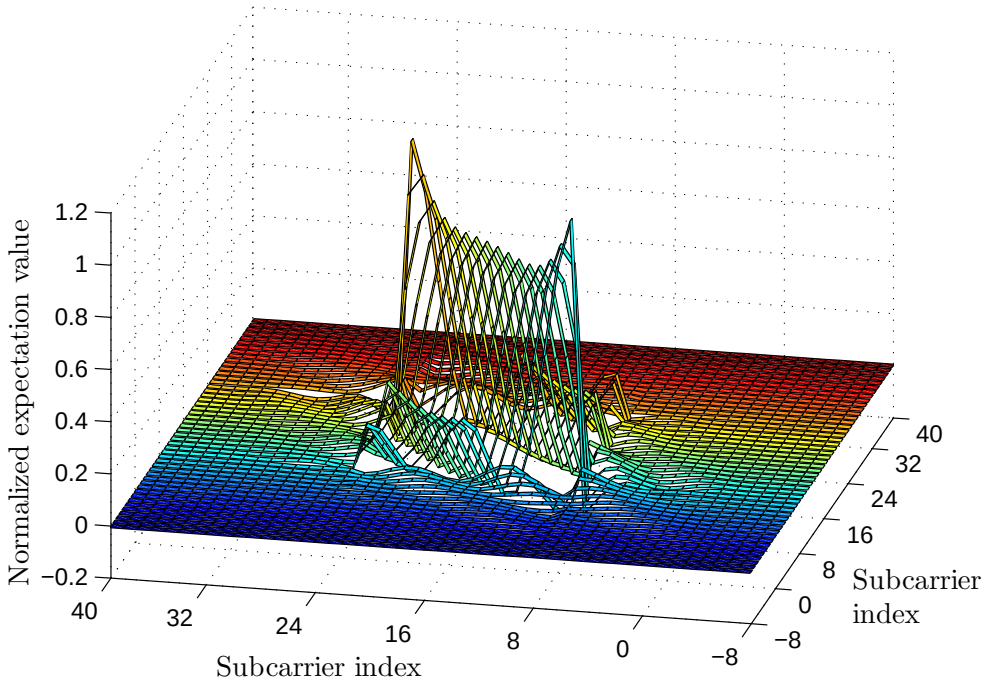

FIGURE 6.9: Normalized values for the real part of the matrix $\mathrm{E}\left[Y_{k,i}Y_{k,m}^{*}|\mathbf{S}'\right]$ considering a 6 taps multipath channel followed by a nonlinear channel for an OBO value of 7.7 dB and $N = 16$.

$\psi_1\psi_2\cdots\psi_m$ with means $\mu_1, \mu_2, \cdots, \mu_m$ leads to

$$\mathrm{E}\left[(\psi_1-\mu_1)(\psi_2-\mu_2)\cdots(\psi_m-\mu_m)\right] = \begin{cases} \sum\prod \mathrm{E}\left[(\psi_i-\mu_i)(\psi_j-\mu_j)\right], & m \text{ is even} \\ 0, & m \text{ is odd} \end{cases} \tag{6.31}$$

Consequently, and setting $\psi_i = \zeta_i + \mu_i$, from (6.31) it yields

$$\begin{aligned} \mathrm{E}\left[\psi_1\psi_2\cdots\psi_m\right] = {} & \mathrm{E}\left[\zeta_1\zeta_2\cdots\zeta_m\right] \\ & + \mu_1\mathrm{E}\left[\zeta_2\zeta_3\cdots\zeta_m\right] + \mu_2\mathrm{E}\left[\zeta_1\zeta_3\cdots\zeta_m\right] + \cdots + \mu_m\mathrm{E}\left[\zeta_1\zeta_2\cdots\zeta_{m-1}\right] + \cdots \\ & + \mu_1\mu_2\cdots\mu_{m-1}\mathrm{E}\left[\zeta_m\right] + \cdots + \mu_1\mu_3\cdots\mu_m\mathrm{E}\left[\zeta_2\right] + \mu_2\mu_3\cdots\mu_m\mathrm{E}\left[\zeta_1\right] \\ & + \mu_1\mu_2\cdots\mu_m \end{aligned} \tag{6.32}$$

Similarly to (6.24), for $m = 4$ and considering the product of two Gaussian RVs and two complex conjugate Gaussian RVs and that $\mu_i = \mu_j = \mu, \forall i, j$, (6.31) yields

$$\begin{aligned} \mathrm{E}\left[\psi_1\psi_2\psi_3^*\psi_4^*\right] = {} & \mathrm{E}\left[\zeta_1\zeta_2\right]\mathrm{E}\left[\zeta_3^*\zeta_4^*\right] + \mathrm{E}\left[\zeta_1\zeta_3^*\right]\mathrm{E}\left[\zeta_2\zeta_4^*\right] + \mathrm{E}\left[\zeta_1\zeta_4^*\right]\mathrm{E}\left[\zeta_2\zeta_3^*\right] \\ & + \mu^2\left(\mathrm{E}\left[\zeta_1\zeta_2\right] + \mathrm{E}\left[\zeta_3^*\zeta_4^*\right] + \mathrm{E}\left[\zeta_1\zeta_3^*\right] + \mathrm{E}\left[\zeta_1\zeta_4^*\right] + \mathrm{E}\left[\zeta_2\zeta_3^*\right] + \mathrm{E}\left[\zeta_2\zeta_4^*\right]\right) \\ & + \mu^4 \end{aligned} \tag{6.33}$$

Note that for $\mu = 0$, (6.32) and (6.33) reduce to the zero-mean Gaussian case given by (6.23) and (6.24), respectively, and the expectation values given by (6.28), (6.29) and (6.30) are also applicable.

6.4.3 Extension of MMSE channel estimator for OFDM signals with carrier frequency and phase offsets

As previously referred, the constellation rotation induced by both carrier frequency and constant phase offsets are not distinguishable from the random attenuation/rotation imposed by the multipath channel. Yet, the CFO induces both an attenuation to the useful received symbol and an additional ICI term due to the loss of orthogonality.

Consider again the complex envelope of the received OFDM signal affected by both offsets, $\dot{\tilde{r}}(t)$, given by (see section 5.6)

$$\dot{\tilde{r}}(t) = \tilde{r}(t)e^{j(2\pi\delta f t+\phi)} \tag{6.34}$$

where δf and ϕ are the CFO and phase offsets, respectively, we will now extend the MMSE estimator described in the previous section to also compensate the effects of both offsets. The new structure was found to be also the one represented in Figures 6.6 and 6.7. Yet, the linear transformation given by (6.19) and the expectation values $\mathrm{E}\left[\dot{\mathbf{Y}}_k\dot{\mathbf{Y}}_k^H|\mathbf{S}'\right]$ and $\mathrm{E}\left[\dot{\mathbf{Y}}_k^*\mathbf{H}_k^T|\mathbf{S}'\right]$ are now given by[2]

$$\begin{aligned}
&\mathrm{E}\left[\dot{Y}_{k,i}\dot{Y}_{k,m}^*|\mathbf{S}'\right] = \\
&= \frac{|c_1|^2}{(T-T_{CP})^0}\sum_{n_1}\sum_{n_2}\mathrm{E}\left[H_{k,n_1}H_{k,n_2}^*\right]S'_{n_1}S'^*_{n_2}\alpha_{i,n_1}\alpha^*_{m,n_2}e^{j(\gamma_{k,i,n_1}-\gamma_{k,m,n_2})} \\
&\quad + \frac{c_1c_3^*}{(T-T_{CP})^2}\sum_{n_1}\sum_{n_2}\sum_{n_3}\sum_{n_4}\mathrm{E}\left[H_{k,n_1}H_{k,n_2}^*H_{k,n_3}^*H_{k,n_4}\right]S'_{n_1}S'^*_{n_2}S'^*_{n_3}S'_{n_4} \\
&\quad \times \alpha_{i,n_1}\alpha^*_{m,n_2+n_3-n_4}e^{j(\gamma_{k,i,n_1}-\gamma_{k,m,n_2+n_3-n_4})} \\
&\quad + \frac{c_3c_1^*}{(T-T_{CP})^2}\sum_{n_1}\sum_{n_2}\sum_{n_3}\sum_{n_4}\mathrm{E}\left[H_{k,n_1}H_{k,n_2}H_{k,n_3}^*H_{k,n_4}^*\right]S'_{n_1}S'_{n_2}S'^*_{n_3}S'^*_{n_4} \\
&\quad \times \alpha_{i,n_1+n_2-n_3}\alpha^*_{m,n_4}e^{j(\gamma_{k,i,n_1+n_2-n_3}-\gamma_{k,m,n_4})} \\
&\quad + \frac{|c_3|^2}{(T-T_{CP})^4}\sum_{n_1}\sum_{n_2}\sum_{n_3}\sum_{n_4}\sum_{n_5}\sum_{n_6}\mathrm{E}\left[H_{k,n_1}H_{k,n_2}H_{k,n_3}^*H_{k,n_4}^*H_{k,n_5}^*H_{k,n_6}\right] \\
&\quad \times S'_{n_1}S'_{n_2}S'^*_{n_3}S'^*_{n_4}S'^*_{n_5}S'_{n_6}\alpha_{i,n_1+n_2-n_3}\alpha^*_{m,n_4+n_5-n_6}e^{j(\gamma_{k,i,n_1+n_2-n_3}-\gamma_{k,m,n_4+n_5-n_6})} \\
&\quad + \cdots
\end{aligned} \tag{6.35}$$

and

[2]Note that the vector of complex symbols after the nonlinearity is now affected by CFO and in order to distinguish it from the zero CFO case, we denote it by $\dot{\mathbf{Y}}_k$.

$$\begin{aligned}
\mathrm{E}\left[H_{k,n}\dot{Y}^*_{k,m}\middle|\mathbf{S}'\right] = & \frac{c_1^*}{(T-T_{CP})^0}\sum_{n_1}\mathrm{E}\left[H_{k,n}H^*_{k,n_1}\right]S'_nS'^*_{n_1}\alpha^*_{m,n_1}e^{-j\gamma_{k,m,n_1}} \\
& + \frac{c_3^*}{(T-T_{CP})^1}\sum_{n_1}\sum_{n_2}\sum_{n_3}\mathrm{E}\left[H_{k,n}H^*_{k,n_1}H^*_{k,n_2}H_{k,n_3}\right] \\
& \times S'_nS'^*_{n_1}S'^*_{n_2}S'_{n_3}\alpha^*_{m,n_1+n_2-n_3}e^{-j\gamma_{k,m,n_1+n_2-n_3}} \\
& + \cdots
\end{aligned} \tag{6.36}$$

where the attenuation factor α_{x,n_l} and the time-varying phase shift factor γ_{k,x,n_l} are given, respectively, by

$$\alpha_{x,n_l} = \mathrm{sinc}\left[(n_l - x) + \delta f(T - T_{CP})\right] \tag{6.37}$$

$$\gamma_{k,x,n_l} = \pi(n_l - x) + \pi\delta f[(2k+1)T + T_{CP}] + \phi \tag{6.38}$$

As it can be seen from (6.35) and (6.36), the expectation values of the joint carrier frequency/phase offsets and channel MMSE estimator reduces again to the computation of the expectation value of the product of complex Gaussian RVs. Therefore, its analytical computation follows the same procedure as the one described for both the Rayleigh and Rician fading channels.

6.5 Performance evaluation

In order to evaluate the MMSE channel estimator structure derived above, we will first analyze its performance in terms of MSE for different E_b/N_0 and OBO values and number of channel taps used. Additionally, a comparison with the ZF estimator performance is also presented.

Similarly to what was performed in chapter 4, we have derived analytical expressions for the MSE for both the ZF estimator and for the minimum MSE. Simulation results were also obtained through Monte Carlo techniques.

When considering a ZF channel estimator, the analytical MSE expression for subcarrier n is given by

$$\xi_n^{ZF} = \mathrm{E}\left[|H_{k,n}|^2\right] + \frac{\mathrm{E}\left[|Y_{k,n}|^2 \left|S'_n\right.\right]}{|S'_n|^2} + \frac{2N_0}{|S'_n|^2} - 2\Re\left\{\frac{\mathrm{E}\left[H_{k,n}Y^*_{k,n}\left|S'_n\right.\right]}{(S'_n)^*}\right\} \tag{6.39}$$

whereas for the linear MMSE estimator, the analytical minimum MSE expression for subcarrier n is given by

$$\begin{aligned}\xi_n^{min} = \mathrm{E}\left[|H_{k,n}|^2\right] + \sum_i \sum_l \beta_{i,n}\beta^*_{l,n}\mathrm{E}\left[Y_{k,i}Y^*_{k,l}\left|\mathbf{S}'\right.\right] \\ + 2N_0 \sum_i |\beta_{i,n}|^2 - 2\Re\left\{\sum_l \beta^*_{l,n}\mathrm{E}\left[H_{k,n}Y^*_{k,l}\left|S'_l\right.\right]\right\}\end{aligned} \tag{6.40}$$

where all summation operators run from $-1/2(L-1)(N-1)$ to $1/2(L+1)(N-1)$. The total MSE in both cases is computed by simply performing the summation of (6.39) and (6.40) for $n = 0, 1, \cdots, N-1$.

To evaluate the performance of the channel estimator structure we have considered pilot subcarriers conveying complex symbols $S'_n = Ae^{jn\pi}$ for $n = 0, 1, \cdots, N-1$. We have also considered OFDM signals with different number of subcarriers and the following parameters: $T = 4\,\mu$s, $T_{CP} = 800\,$ns. The nonlinearity was chosen to be a third-order nonlinearity given by (3.21) with polynomial odd coefficients given by $c_1 = 1$, $c_2 = 0$, $c_3 = -0.20$ and $c_i = 0$ for $i > 3$. Simulation results were obtained using Matlab/C++ through Monte Carlo techniques. Analytical results were computed using Matlab/C++ as a numerical calculator.

Figure 6.10 shows the mean-squared error as a function of the E_b/N_0 for OFDM signals with 16 subcarriers and OBO values of 4.1 dB, 7.7 dB and 10.4 dB. Results presented are for 6 taps channels and both the ZF and MMSE estimators are considered. Both simulation and analytical results are verified to be in good agreement. Results show that the MSE associated with both estimators decrease as the SNR per bit increases. As previously referred, the PSD of the AWGN source plays an important role on the channel estimation process. Furthermore, it can be seen that the MSE of the ZF estimator starts to asymptotically tend to a given MSE, while the performance of the MMSE estimator continues to decrease, indicating an increasing performance gap

between both estimators. Additionally, results also show that the MSE associated with both estimators decreases with the OBO value. Yet, the MMSE estimator outperforms the ZF.

In Figure 6.11 it is depicted the mean-squared error as a function of the OBO for OFDM signals with 16 subcarriers for E_b/N_0 values of 30 dB and 40 dB and considering channels with 3, 6 and 10 taps. Only results for the analytical MSE are given due to the good agreement between both analytical and simulation results. From an overall point of view, results show that as expected the MSE decreases inversely with the OBO. Also, it can be seen that the decrease rate associated with the ZF estimator is higher than the one of the MMSE estimator, as already reported in Figure 6.10. Moreover, results indicate that as the number of taps increase, the performance of the MMSE estimator decreases, especially for low OBO values, contrary to what is reported for the ZF estimator. The explanation of this result lies in the nature of the multipath channel frequency response and on the nonlinear channel impact. As the number of taps increase, the number of peaks and notches on its frequency response increases as well, decreasing the correlation between frequency components and explaining the decrease of performance of the MMSE estimator. Additionally, in this scenario, the PAPR of the OFDM signal is reduced comparatively to when a channel with a low number of taps is considered. Therefore, the MSE associated with the ZF decreases with the number of taps and inversely with the OBO. Another interesting result is the fact that results for the ZF estimator for both SNR per bit values of 30 dB and 40 dB are very similar, especially for OBO values lower than 10 dB, contrary to what is reported for the MMSE estimator case. This may indicate that the ZF estimator is highly dependent on the OBO.

Results of the impact of the number of subcarriers in the MSE of both estimators are given by Figure 6.12 for OBO values of 4.10 dB, 7.7 dB and 10.4 dB and SNR per bit values of 30 dB and 40 dB. Results show that there is a degradation in terms of performance as the number of subcarriers increase for the ZF estimator. This effect can be explained by the increase of the PAPR and consequently the exponential increase of the number of IMPs. Results of the MSE for the MMSE estimator show that its dependence on the number of subcarriers is much lower than for the ZF estimator. In

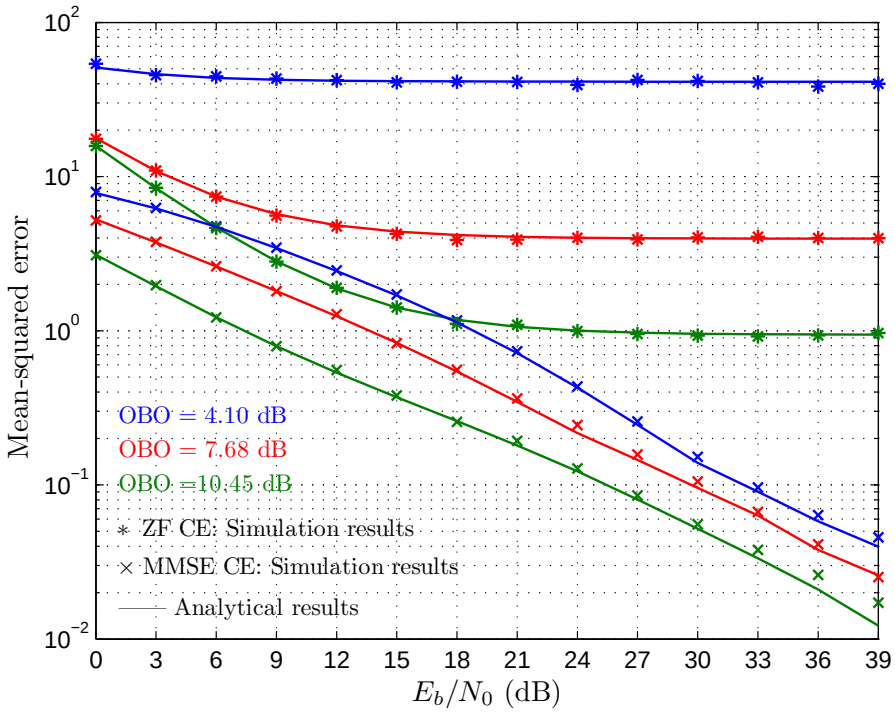

FIGURE 6.10: Analytical and simulated mean-squared errors as function of E_b/N_0 for OFDM signals with 16 subcarriers and OBO values of 4.10 dB, 7.68 dB and 10.45 dB. Results presented are for 6 taps channels.

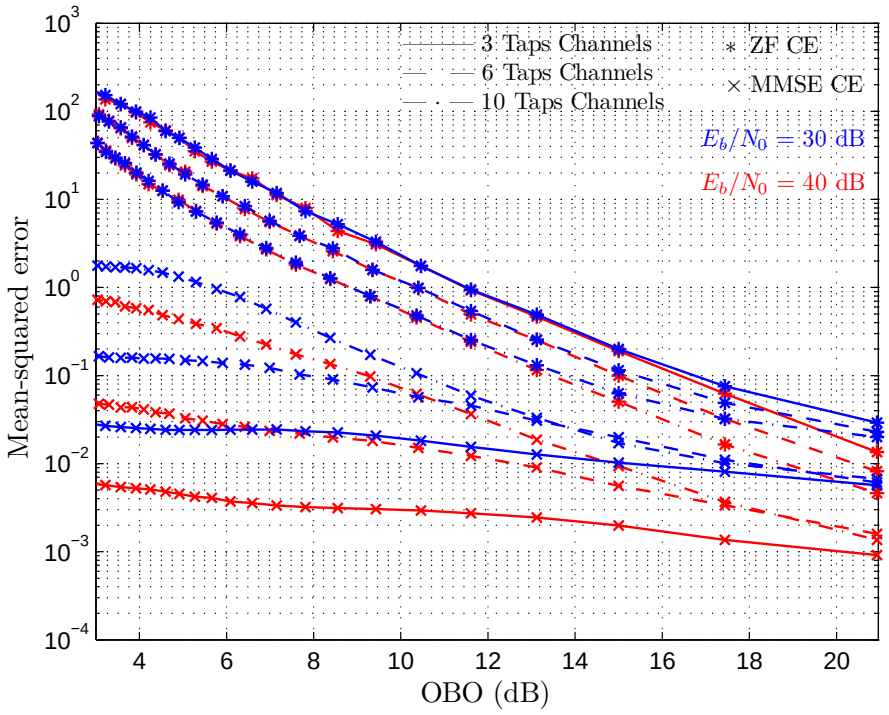

FIGURE 6.11: Mean-squared error as a function of the output back-off for OFDM signals with 16 subcarriers for E_b/N_0 values of 30 dB and 40 dB and considering channels with 3, 6 and 10 taps.

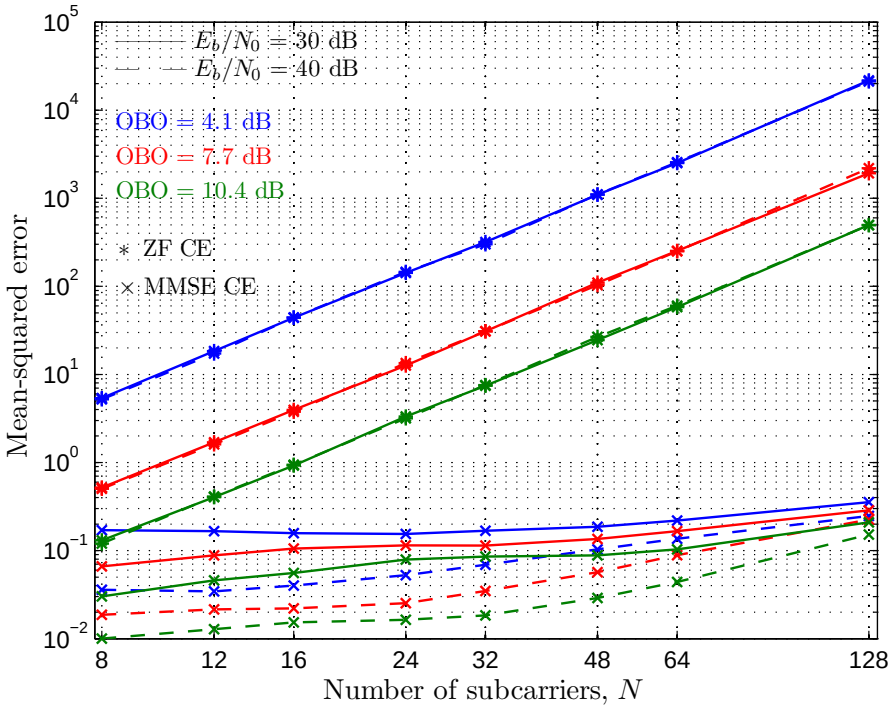

FIGURE 6.12: Mean-squared error as function of the number of subcarriers for OFDM signals with OBO values of 4.10 dB, 7.68 dB and 10.45 dB and E_b/N_0 values of 30 dB and 40 dB. Results presented are for 6 taps channels.

fact, the MSE only increases slightly when high OBO values are considered.

We will now evaluate the performance of both ZF and MMSE estimators in terms of error probability. The schematic used for the simulation is represented in Figure 6.4. Moreover, we will consider two different OFDM receivers: the conventional one-tap equalizer and the iterative ML algorithm. The former simply divides the received complex symbol in subcarrier n by the frequency response of the channel estimation in the same subcarrier frequency, while the later uses the algorithm derived in chapter 3 fed with channel estimates. Its robustness as an equalizer will be studied on the upcoming sections and a comparison with the conventional one-tap is performed.

To evaluate the performance of both equalizers we have considered that the set of known symbols $S'_n = Ae^{jn\pi}$ for $n = 0, 1, \cdots, N-1$ is used as a block-type pilot arrangement in order to estimate the frequency response of the multipath channel. Simulation results were obtained using Matlab/C++ through Monte Carlo techniques in two stages as follows: initially an OFDM symbol composed by pilot subcarriers is generated using $\mathbf{S}'$; then, the convolution between the OFDM pilot symbol and a randomly generated

multipath channel IR is performed; subsequently, the faded OFDM symbol is distorted by the nonlinearity; finally, after being corrupted by AWGN, it is used to estimate the frequency response of the multipath channel. In the second stage, a randomly OFDM symbol is generated; then, a convolution between the OFDM symbol and the multipath channel IR generated in the previous stage is performed; subsequently, the faded OFDM symbol is distorted by the nonlinearity and corrupted by AWGN; finally, with the aid of the previous estimated multipath channel frequency response and by means of an equalizer, an estimation of the transmitted complex symbols is obtained. Note that stage one is responsible for the multipath channel estimation whereas stage two is responsible for the equalization and recover of useful data. Here it is considered that the multipath channel is constant over both stages. Moreover, it is always ensured that the maximum delay of the multipath channel does not exceeds the length of the cyclic prefix, i.e., both ISI and ICI are avoided.

In the following subsections we present several results concerning the performance of the MMSE multipath channel estimator in the presence of both Rayleigh and Rician distributed channels as well as for the joint multipath/CFO estimator.

6.5.1 Rayleigh fading channel

We will first focus on the performance of both ZF and MMSE estimators jointly with the one-tap equalizer comparatively to the perfect estimator. A perfect channel estimation means that, ideally, the OFDM receiver has exact knowledge of the multipath impulse/frequency response. In Figure 6.13 it is depicted the error probability performance for faded OFDM/BPSK signals with 16 subcarriers as a function of E_b/N_0. Here we have considered OBO values of 4.1 dB, 7.7 dB and 10.4 dB and Rayleigh distributed 6 paths channels. As it can be seen, the performance of the ZF estimator in a nonlinearly distorted OFDM signal is tremendously affected, especially for relatively low OBO values. Moreover, for high OBO values its performance improves up to a certain E_b/N_0 value from which it remains constant. On the other hand, the MMSE estimator always outperforms the ZF one. In fact, as the E_b/N_0 increases it tends to the performance curve of the perfect (or ideal) channel estimator.

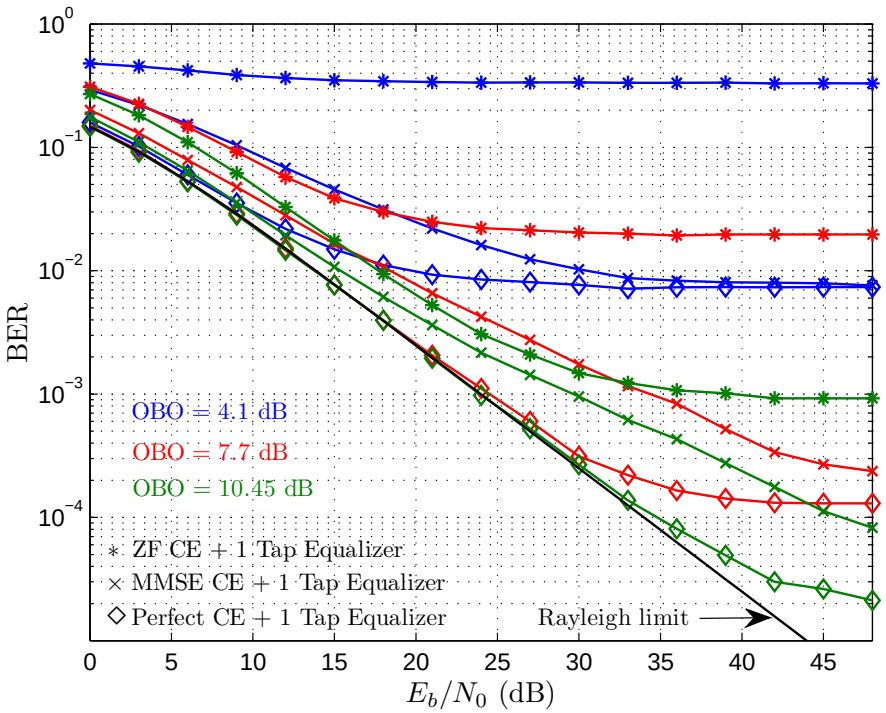

FIGURE 6.13: Bit error rate as a function of E_b/N_0 for faded OFDM/BPSK signals with 16 subcarriers, OBOs of 4.1 dB, 7.7 dB and 10.4 dB considering ZF, MMSE and perfect channel estimations and a one-tap equalizer. Results given are for 6 taps channels.

Figure 6.14 depicts the error probability as a function of the OBO for faded OFDM signals with 64 subcarriers conveying different modulation formats. Here, several results for M-PSK with constellation size $M = 2, 4, 8, 16$ and 16-QAM are considered. For comparison purposes the AWGN PSDs are considered to be $N_0/K = 2.5 \times 10^{-13}$ W/Hz, where $K = \log_2(M)$, in order to have the same SNR per bit for all modulation formats at each OBO value. In general, results show that BPSK provides the best performance and 16-PSK the worst, for all estimators. This result would also be expected if the transmission channel was linear. Moreover, results also show that the minimum bit error rate is obtained for relatively high OBO values of $12 \sim 14$ dB for perfect and MMSE channels estimators and $18 \sim 21$ dB for the ZF. It is also interesting to note that for high OBO values the MMSE estimator tends to the performance of the perfect estimator, contrary to the ZF.

The error probability performance of the one-tap equalizer for nonlinearly faded OFDM/BPSK signals with different number of subcarriers is depicted in Figure 6.15. Here we consider two OBO values of 7.7 dB and 10.4 dB, an E_b/N_0 of 40 dB and Rayleigh

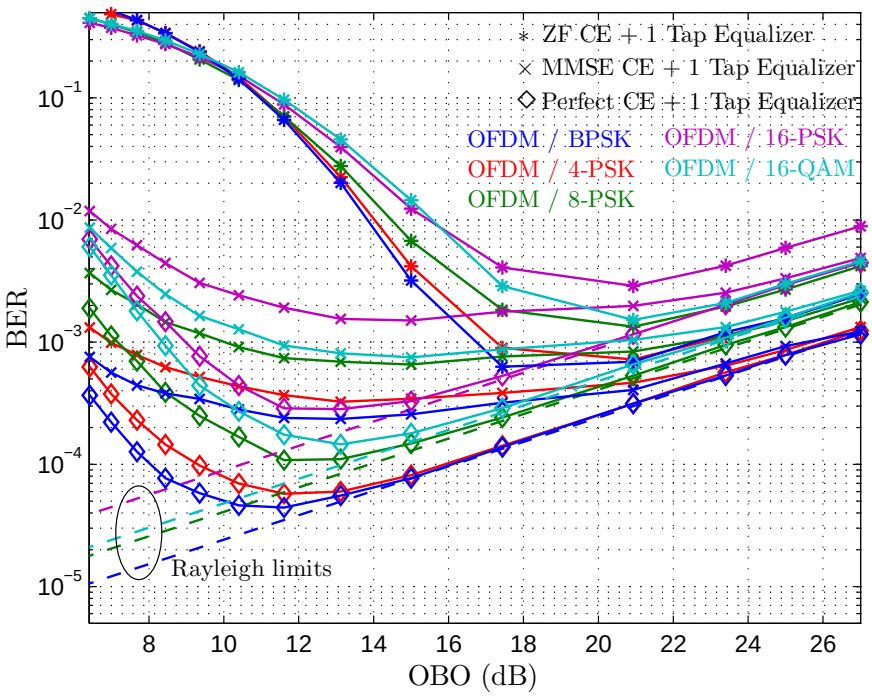

FIGURE 6.14: Bit error rate vs OBO for faded OFDM/{2,4,8,16}-PSK/16-QAM signals with 64 subcarriers and considering ZF, MMSE and ideal channel estimations and a one-tap equalizer. Results given are for 6 taps channels and AWGN PSDs of $N_0/K = 2.5 \times 10^{-13}$ W/Hz, where $K = \log_2(M)$.

distributed 6 taps channels. Results show that the MMSE estimator jointly with the one-tap equalizer have an almost flat performance behavior over the simulated number of subcarriers. Yet, for the ZF estimator, it can be seen that the error probability performance decreases drastically with N, specially for the lowest OBO value considered. However, it is interesting to note that for the OBO value of 7.7 dB and 128 subcarriers the error probability has a slight reduction comparatively to the 64 subcarriers case. This happens because in stage one, the OFDM pilot symbol is 180° inverted due to the tremendous effected of the nonlinearity and high PAPR in the gain compression and desensitization terms. In these circumstances, the ZF channel estimator produces very noisy and sign inverted estimates. Here, we have considered that the channel sign inversion is detected and corrected by the equalizer.

For the results plotted in both Figures 6.13 and 6.14 we have considered Rayleigh distributed channels with 6 taps. As previously referred, the number of taps, jointly with the nonlinear noise, affects in a significant way the estimation process. Figures 6.16 and 6.17 show the error probability performance as a function of the number of taps for

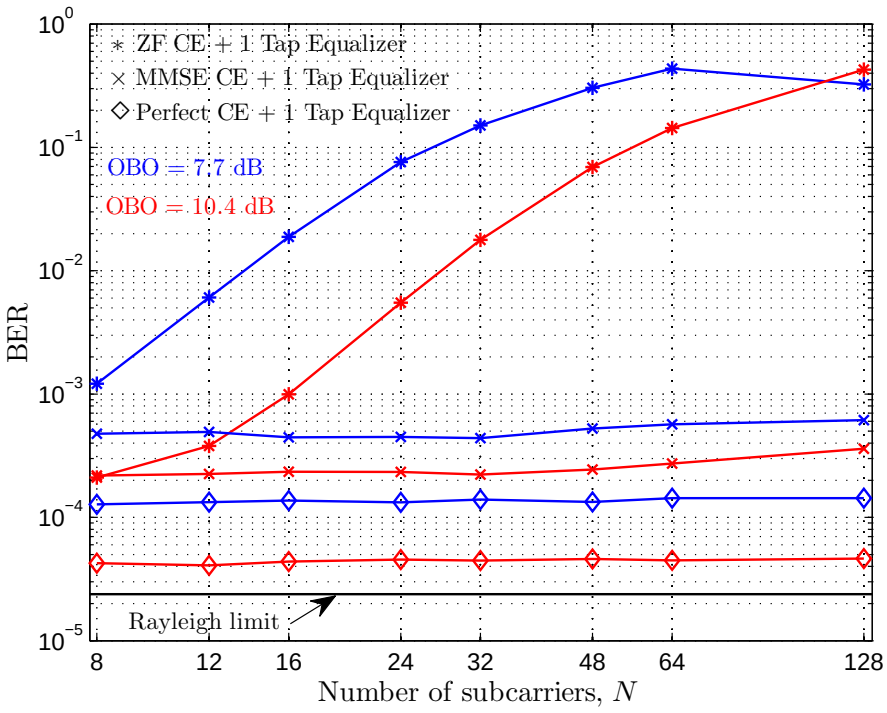

FIGURE 6.15: Bit error rate vs number of subcarrier used for faded OFDM/BPSK signals for OBO values of 7.7 dB and 10.4 dB and for an E_b/N_0 value of 40 dB considering ZF, MMSE and ideal channel estimations and a one-tap equalizer. Results for 6 taps channels.

OFDM/BPSK signals with 16 and 64 subcarriers, respectively, and with OBO values of 7.7 dB and 10.4 dB and E_b/N_0 values of 30 dB and 40 dB. From the observation of both Figures it can be seen that all three estimators show similar behaviors for 16 and 64 subcarriers. Let us now focus on each particular case. Results show that the performance of the perfect estimation jointly with the one-tap equalizer starts to decrease as the number of taps increases. This result comes from the fact that the higher the number of taps, the higher the number of peaks and notches of the frequency response of the channel and the lower is their correlation. Thus, for subcarrier indexes with near-zero frequency responses, the one-tap equalizer boosts the IMD term of the received complex symbol. In fact, it was found that the variance of the IMD term after equalization increases with the number of taps. The opposite behavior of the ZF estimator case is mainly due to the distorted channel estimation that dominates over the equalization process as previously explained (see Figure 6.11). The behavior of the MMSE estimation followed by the one-tap equalizer can be seen as a mixture of several effects. On one hand, the increase of the number of taps induces a decrease of the correlation between complex

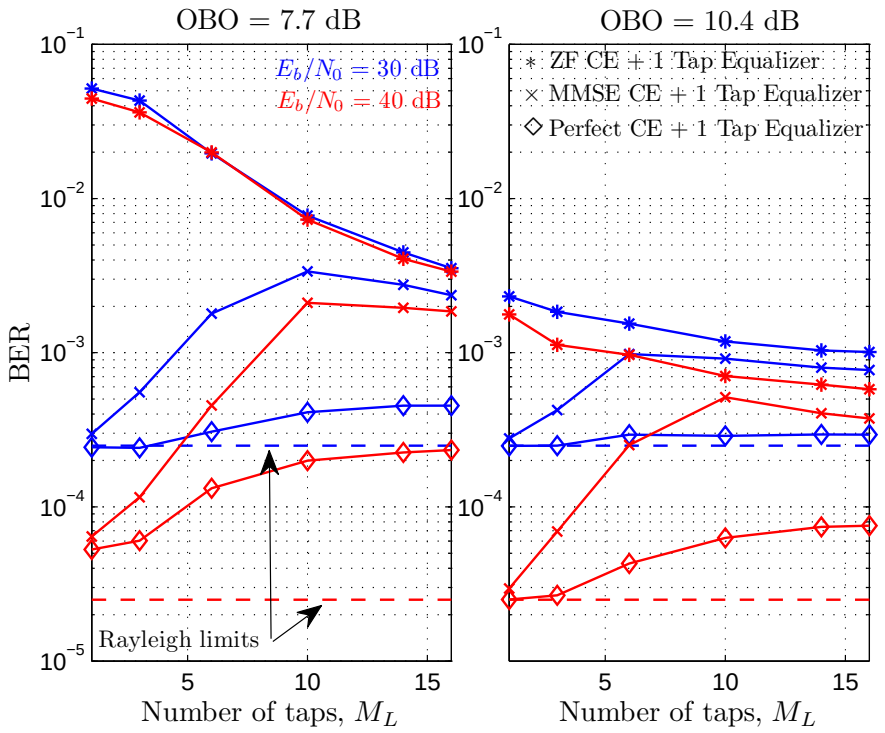

FIGURE 6.16: Bit error rate vs the number of channel taps for faded OFDM/BPSK signals with 16 subcarriers, OBOs of 7.7 dB and 10.4 dB and E_b/N_0 values of 30 dB and 40 dB considering ZF, MMSE and ideal channel estimations and a one-tap equalizer.

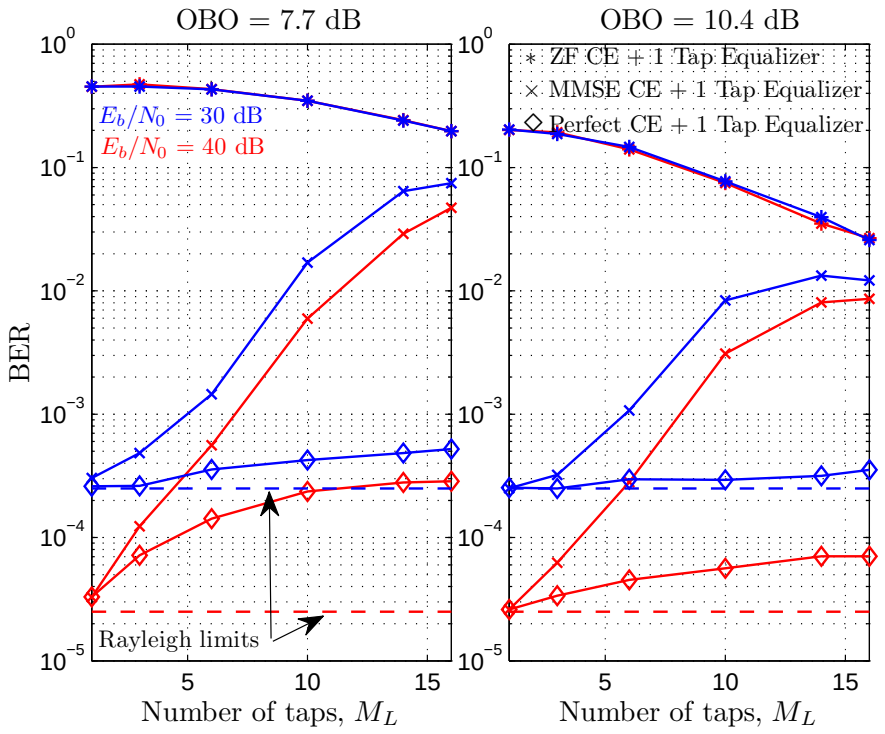

FIGURE 6.17: Bit error rate vs the number of channel taps for faded OFDM/BPSK signals with 64 subcarriers, OBOs of 7.7 dB and 10.4 dB and E_b/N_0 values of 30 dB and 40 dB considering ZF, MMSE and ideal channel estimations and a one-tap equalizer.

symbols conveyed by different subcarriers and, thus, a decrease of the performance of the estimation (see Figure 6.11). Additionally, and similarly to what happens with the perfect estimation, there is also a performance deterioration due to the boost of the IMD term at the equalization process. For the 16 subcarriers case and $M_L > 10$, the slight improvement of the error probability performance may also be related with the PAPR reduction at the one-tap equalization process.

We will now evaluate the performance of the previously defined estimators, ZF, MMSE and perfect, jointly with the iterative ML algorithm acting as an equalizer fed with channel estimates. Results for the one-tap equalizer are also present for comparison purposes.

In Figures 6.18 and 6.19 it is depicted the error probability performance as a function of the OBO for faded OFDM/BPSK signals with 16 and 64 subcarriers, respectively, and for AWGN PSDs of $N_0[N = 16] = 4N_0[N = 64] = 1 \times 10^{-12}$ W/Hz. Note that the N_0 values are chosen in order to have the same E_b/N_0 ratio at each OBO value for both 16 and 64 subcarriers cases. Again, results show similar behaviors for all estimators and equalizers in both cases. Let us focus on Figure 6.19 which represents the 64 subcarriers case. Results for the one-tap equalizer show that there is a considerable gain in terms of minimum bit error rate depending on the type of channel estimator. The 3 taps channel case presents the best results. In this scenario, the minimum bit error rate obtained using the MMSE estimator is only twice the one for the perfect estimator and approximately eight times better than the one given by the ZF. As the number of taps increase, the performances of both MMSE and perfect estimators also decrease. For a 6 taps channel, the MMSE estimator is shown to have a minimum bit error rate only half of the one given by the ZF. Nevertheless, its performance curve is relatively flat over a wide OBO range, allowing a higher dynamic range of the input signal. For a 10 taps channel, the minimum bit error rate of the MMSE estimator is only slightly better than the one given by the ZF estimator. Yet, the former always outperforms the later.

Results for the ML algorithm with five iterations indicate that it can be used to optimize the equalization process. However, its performance is highly dependent on both number of channel taps and channel estimator. In fact, its performance is maximum if fed with perfect channel estimates. Moreover, its best performance is given when a

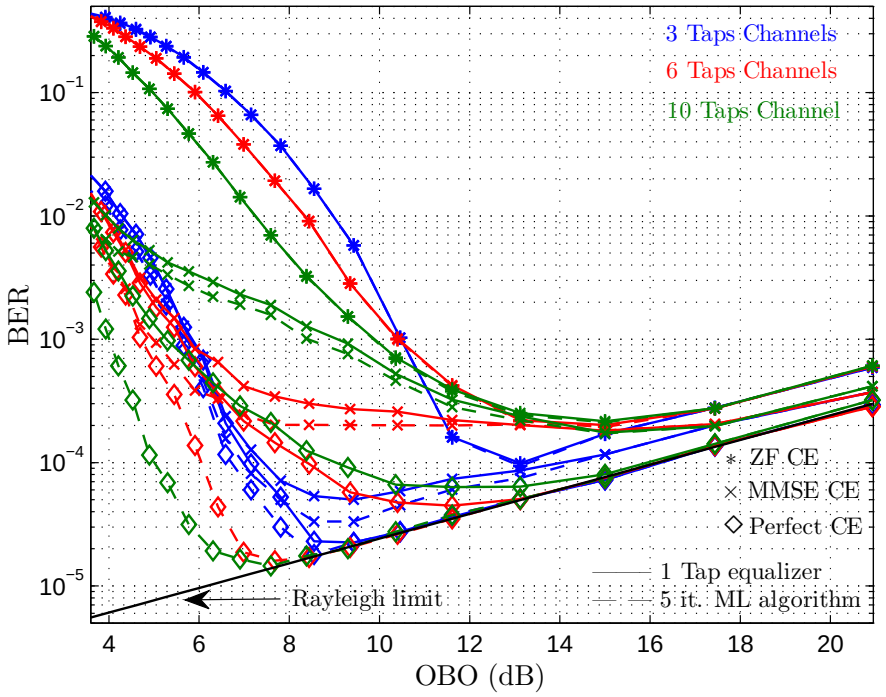

FIGURE 6.18: Bit error rate vs OBO for faded OFDM/BPSK signals with 16 subcarriers and an AWGN PSD of 1×10^{-12} W/Hz considering ZF, MMSE and ideal channel estimations, both one-tap equalizer and it. ML algorithm and various taps channels.

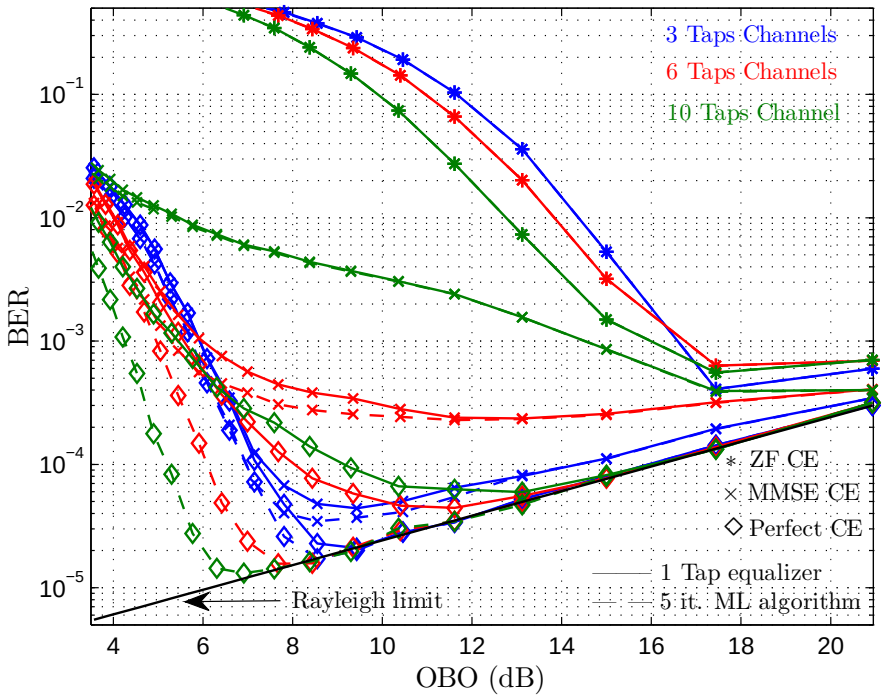

FIGURE 6.19: Bit error rate vs OBO for faded OFDM/BPSK signals with 64 subcarriers and an AWGN PSD of 2.5×10^{-13} W/Hz considering ZF, MMSE and ideal channel estimations, both one-tap equalizer and it. ML algorithm and various taps channels.

high number of channel taps is considered. In this scenario, the minimum BER level has an improvement of seven times. As the number of taps decrease, the performance improvement also decreases. This result comes from the capability of the iterative ML algorithm to use the IMD component to maximize the likelihood function. Regarding the results when considering the MMSE estimator, relatively small improvement of the minimum bit error rate is reported. For the ZF estimator, no improvement is observed when the iterative ML algorithm is used.

Similarly to what was performed in section 5.3.3 an optimum nonlinear operating point in terms of error probability performance for both one-tap and iterative ML algorithm based equalizers is expected to exist for a given bit error rate. So, the total degradation (TD) parameter is evaluated as a function of the output back-off. The total degradation parameter is defined as [100, 101]

$$\mathrm{TD[dB]} = \left[\left(\frac{E_b}{N_0}\right)_{NL} - \left(\frac{E_b}{N_0}\right)_{L}\right] + \mathrm{OBO} \tag{6.41}$$

where $\left(\frac{E_b}{N_0}\right)_{NL}$ is the required SNR per bit in decibels at the input of the threshold detector to obtain a fixed BER for a given OBO value and $\left(\frac{E_b}{N_0}\right)_{L}$ is the required SNR per bit in decibels to obtain the same fixed BER in absence of nonlinearity. Note that the multipath channel is Rayleigh distributed, hence, $\left(\frac{E_b}{N_0}\right)_{L}$ is approximately 23.9 dB for a bit error rate target of 10^{-3}. The optimum operating point is given by the OBO value that minimizes the total degradation given by (6.41).

In Figure 6.20 it is plotted the total degradation parameter as a function of the OBO for OFDM/BPSK with 16 and 64 subcarriers, considering all previously referred estimators and equalizers and Rayleigh distributed 6 taps channels. A bit error rate target of 10^{-3} is considered. From the observation of the Figure, we can see that there are some differences between the 16 and 64 subcarriers cases. The ZF estimator shows to have a lower total degradation for a 16 subcarriers signal rather for 64. While the former case shows a minimum TD of 16.7 dB at an optimum OBO value of 11.6 dB, the later presents a minimum TD of 22 dB for an OBO of 17.4 dB. Results for the MMSE estimator followed by an one-tap equalizer indicate that similar minimum TDs of 15.4 dB are obtained for signals with both 16 and 64 subcarriers. Yet, while for the 16 subcarriers signal the minimum TD is achieved at an OBO value of 11.6 dB,

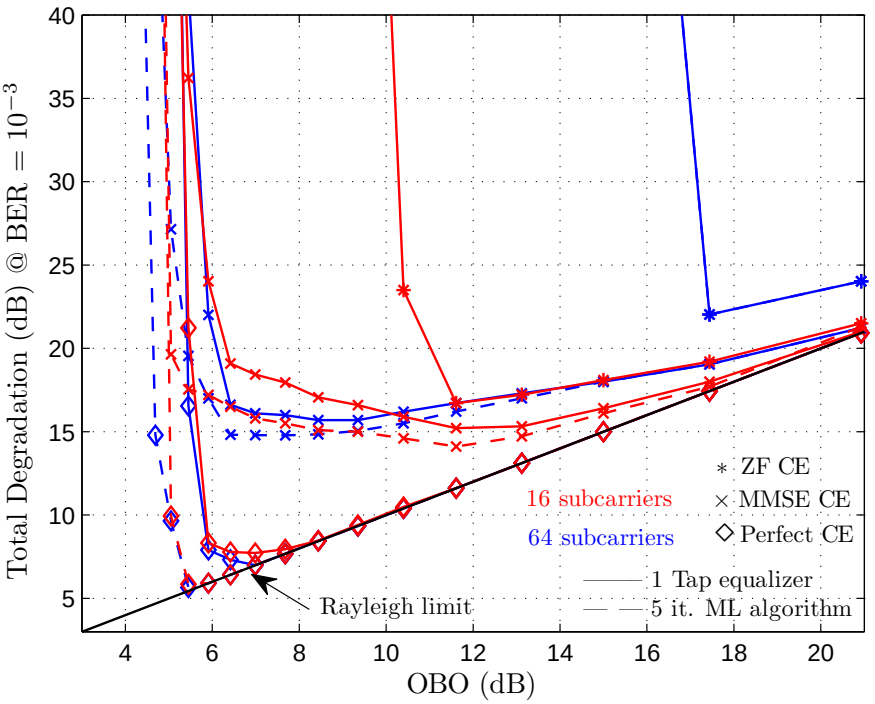

FIGURE 6.20: Total degradation vs OBO for faded OFDM/BPSK signals with 16 and 64 subcarriers considering ZF, MMSE and ideal channel estimations and both one-tap equalizer and iterative ML algorithm for a BER = 10^{-3}. Results for 6 taps channels.

for the 64 subcarriers case the OBO is decreased to approximately 9 dB, which implies an extra gain at the input of the nonlinearity to compensate the 2.6 dB difference at the output. Regarding the iterative ML algorithm, improvements of 1.1 dB on the minimum TD are observed for both 16 and 64 subcarriers transmissions. Furthermore, the minimum TD remains unchanged over a wide OBO range between 6.4 dB and 9 dB for the 64 subcarriers transmission. Finally, results for the perfect estimation followed by an one-tap equalizer indicate minimum TD values of 7.7 dB and 7 dB for the 16 and 64 subcarriers transmissions, respectively, at the same OBO value of 7 dB. When the iterative ML algorithm is considered, an improvement of 2 dB and 1.2 dB for the 16 and 64 subcarriers transmissions, respectively, are observed for an OBO value of 5.4 dB.

In conclusion, the MMSE estimator presents a maximum link gain margin of 7.5 dB to the ZF estimator.

For comparison purposes between OFDM/BPSK and OFDM/QPSK signals, Figure 6.21 depicts the required SNR per bit as a function of the OBO to achieve a bit error rate of 10^{-3}. Again, the channel is considered to be Rayleigh distributed with 6

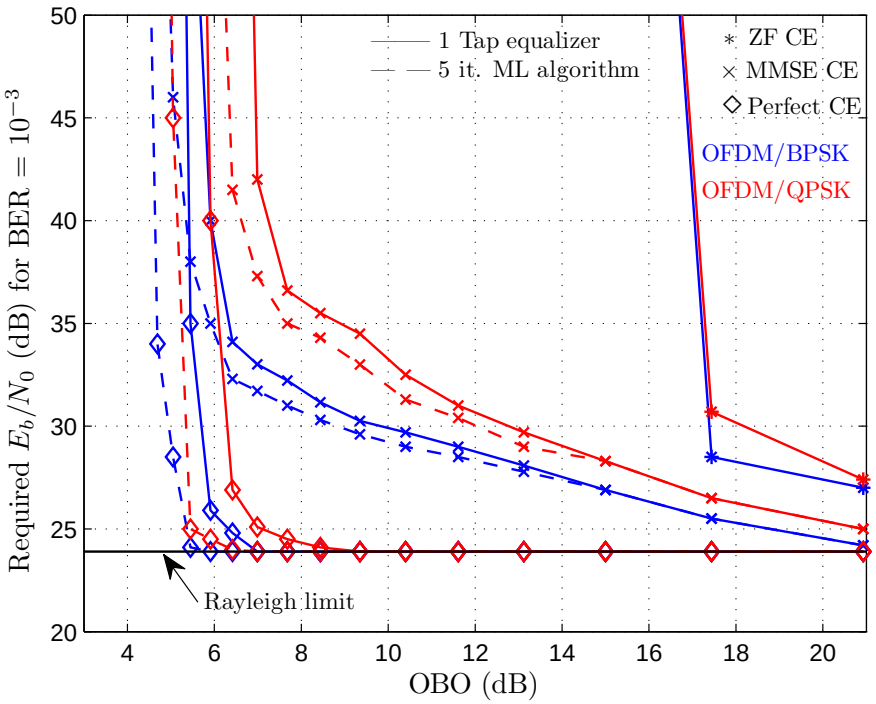

FIGURE 6.21: Comparison of required E_b/N_0 to achieve BER = 10^{-3} as a function of OBO for faded OFDM/B-QPSK signals with 64 subcarriers considering ZF, MMSE and ideal channel estimations and both one-tap equalizer and it. ML algorithm. Results for 6 taps channels.

taps and all channel estimators and equalizers previously referred are considered. An observation of the Figure indicates that the performances of all estimators and equalizers for the OFDM/BPSK signal transmission outperforms the ones of the OFDM/QPSK.

6.5.2 Rician fading channel

We will now study the performance of the MMSE estimator for Rician distributed channels in the presence of a nonlinearity. As previously referred, a Rician distributed channel has a strong dominant component present which can be for instance the LOS. The Rician K-factor defined as the ratio of the signal power in dominant component over the power of the scattered is used to control how strong the dominant path is. For a $K \to -\infty$ dB the distribution tends Rayleigh, while for $K \to +\infty$ dB a non-fading and pure AWGN channel is obtained. For indoor channels with unobstructed LOS path, the K-factor takes values typically between 4 dB and 12 dB.

The bit error rate performance curves of all channel estimators and equalizers previously referred are depitcted in Figure 6.22 as a function of the Rician K-factor for an

OBO value of 3.4 dB and two E_b/N_0 values of 10 dB and 20 dB. Due to the relatively low E_b/N_0 and OBO values considered, for very low Rician K-factors all estimators show high error probability performances. As a dominant path starts to emerge, the error probabilities decrease drastically. Let us first analyze the performance behavior of the one-tap equalizer. For an SNR per bit of 20 dB, the results given by the perfect estimator equal the ones given by the MMSE estimator for $K > 3$ dB. Performance results of the ZF estimator show a bit error rate five times worst than the one for the perfect estimation for $K < 14$ dB, and a degradation by a factor of two for $K > 14$ dB. Regarding the results for an SNR per bit of 10 dB, we can note that all performance curves tend to the same error probability value due to the severe impact of the nonlinear noise from the ICI term. In fact, the one-tap equalizer curves tend to a bit error rate that is 50 times worst than the one for the AWGN channel.

Regarding the results given by the iterative ML algorithm, several conclusions can also be taken. First, it can be seen that the performance curves of the MMSE estimator are very close to the ones for the perfect estimation. Moreover, for an SNR per bit of 20 dB they are identical and, as the the one-tap equalizer starts to converge to a non-optimum BER level, the iterative ML algorithm continues to improve. Additionally, for an SNR per bit of 10 dB, the perfect estimator equals the Rician limit and is followed very close by the MMSE estimator curve. Regarding the ZF estimator, results indicate that the iterative ML algorithm diverges and that it can not be used. The disparity of the results is the consequence of a bad channel estimation due to the relatively low OBO and, consequently, the high attenuation induced by compression and desensitization terms that affect the OFDM training symbol on the estimation process (stage one) of the OFDM signal transmission. Note the one-tap equalizer does not diverges for high Rician K-factors since the frequency response of the channel is almost flat. In this scenario, the equalizer acts almost as a gain/attenuator of the received signal.

In conclusion, results indicate that the MMSE estimator produces error probabilities very close to the ones given by the perfect channel estimation, especially for high Rician K-factors.

In Figure 6.23 it is depicted the required E_b/N_0 to achieve a bit error rate target of 10^{-3} as a function of the Rician K-factor for faded OFDM/BPSK signals with 64

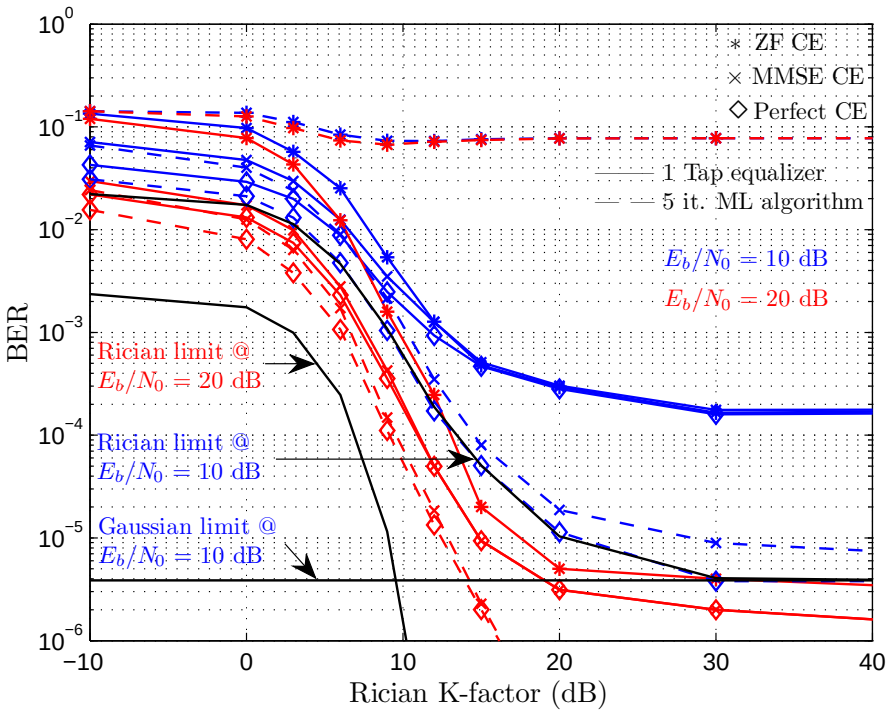

FIGURE 6.22: Bit error rate vs Rician K-factor for faded OFDM/BPSK signals with 64 subcarriers and an OBO of 3.4 dB for two E_b/N_0 levels of 10 dB and 20 dB. Results for 6 taps channels considering ZF, MMSE and ideal channel estimations and both one-tap equalizer and iterative ML algorithm.

subcarriers and two OBO values of 3.4 dB and 7.7 dB. Results given are for Rician distributed 6 taps channels considering all estimators and equalizers previously referred. From the observation of the Figure, we can see that for one-tap equalizers, it is not possible to achieve the target error probability when considering a signal transmission with an OBO value of 3.4 dB and Rician distributed channels with $K < 9$ dB. In fact, results show that for $K = 9$ dB the required SNR per bit are 12.8 dB and 14 dB for the perfect and MMSE estimators, respectively, which correspond to E_b/N_0 degradations of 2.5 dB and 3.7 dB relatively to the Rician limit. If the ML algorithm is considered, the Rician K-factor can decrease to 6 dB. Here, the required E_b/N_0 values are 20 dB and 23 dB for the perfect and MMSE estimators, respectively, which correspond to E_b/N_0 degradations of 5 dB and 8 dB relatively to the Rician limit. For the ZF estimator case, the minimum Rician K-factor is reported to be 12 dB, with a required E_b/N_0 of 10.5 dB.

On the other hand, results for an OBO value of 7.7 dB indicate that the bit error rate target is always archived for -10 dB $< K <$ 25 dB using MMSE and perfect estimators. While the perfect estimator exhibits required E_b/N_0 values identical to the ones for the

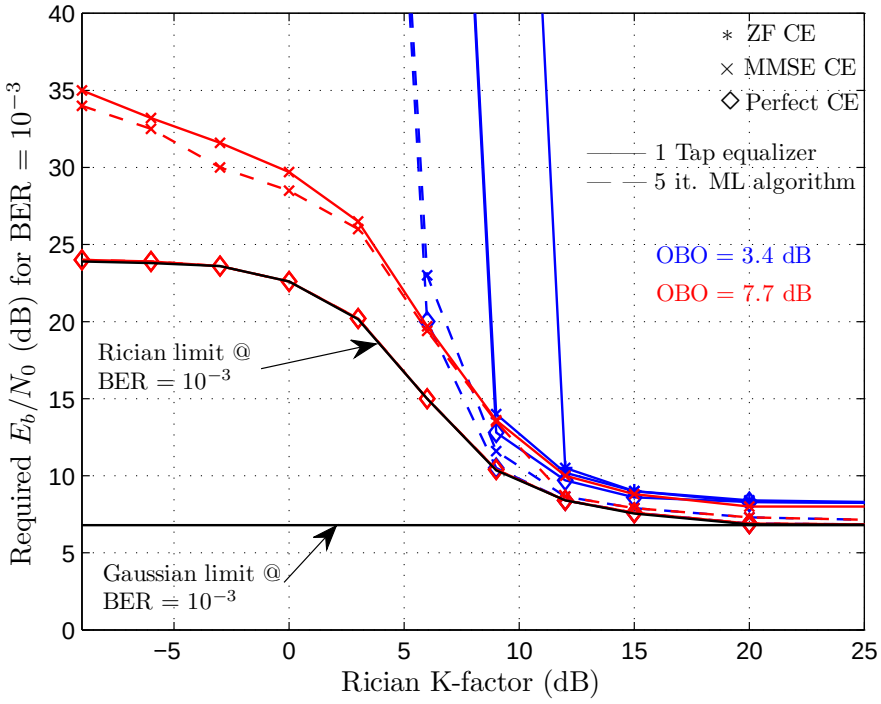

FIGURE 6.23: Comparison of required E_b/N_0 to achieve a bit error probability of 10^{-3} as a function of Rician K-factor for faded OFDM/BPSK signals with 64 subcarriers considering ZF, MMSE and ideal channel estimations and both one-tap equalizer and iterative ML algorithm.

Rician limit, the MMSE estimator followed by the one-tap equalizer exhibits E_b/N_0 degradations relative to the Rician limit that range from 1 dB for $K = 25$ dB and 12 dB for $K = -10$ dB. If the ML algorithm is considered, the required E_b/N_0 decreases approximately 1 dB, comparatively to the one-tap equalizer.

Note that ZF results are only reported for the lowest OBO value. At this operating point, the ZF channel frequency estimate has its phase rotated by 180°, as previously explained. Moreover, it is considered that the estimator compensates this effect. For an OBO value of 7.7 dB, both compression and desensitization terms attenuate tremendously the ZF estimate and, thus, the channel frequency estimation is mainly composed by noise terms.

6.5.3 Joint multipath channel and carrier frequency and phase offsets estimations

In this section we will analyze the performance of the joint MMSE multipath/CFO estimator in the presence of a nonlinearity. Here we consider that the faded OFDM

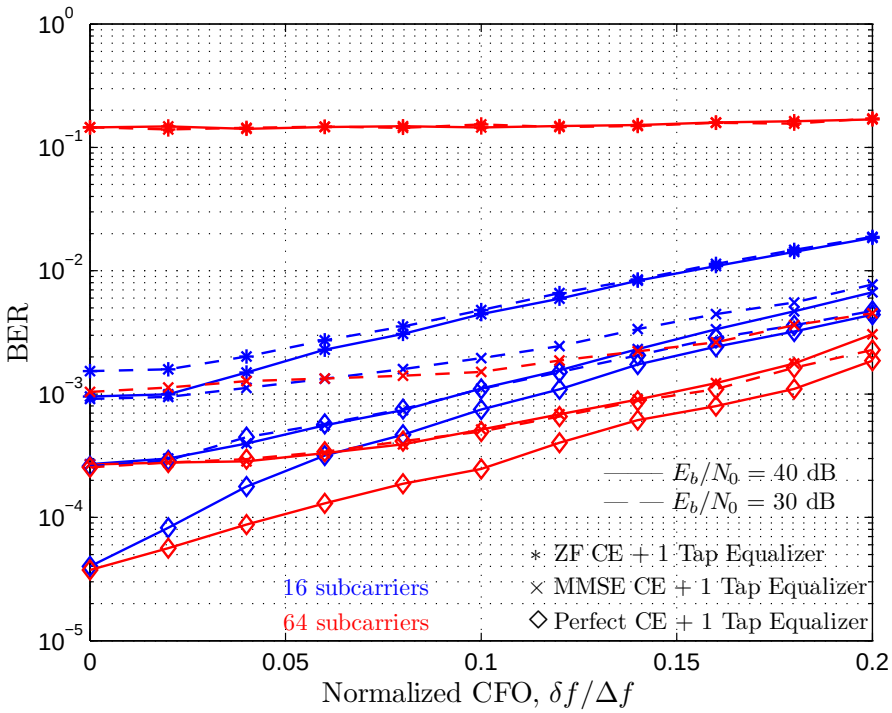

FIGURE 6.24: Bit error rate vs normalized CFO for faded OFDM/BPSK signals with 16 and 64 subcarriers and an OBO of 10.4 dB for two E_b/N_0 levels of 30 dB and 40 dB. Results for Rayleigh distributed channels considering ZF, MMSE and ideal channel estimations followed by a one-tap equalizer.

signal passes through the nonlinearity and a AWGN source corrupts the signal before its detection and demodulation. Moreover, it is considered that there is a difference between the LO of the transmitter and the receiver, inducing a CFO. The constant phase offset is set to zero since it can be easily compensated without loss. Both ZF and perfect channel estimators are also considered, followed by a one-tap equalizer. Here we assume that the perfect channel estimator also knows the averaged phase rotation induced by the CFO.

Results for the bit error rate performance as a function of the normalized CFO are plotted in Figure 6.24. Rayleigh faded OFDM/BPSK signals with 16 and 64 subcarriers and an OBO value of 10.4 dB are considered, as well as two SNR per bit values of 30 dB and 40 dB. As expected, results indicate that the performance deteriorates as the CFO increases due to the increasing variance of the ICI component. Nevertheless, it can be seen that as the CFO increases, the difference between performance curves of the perfect and MMSE estimators diminishes.

Finally, results of the total degradation parameter for a error probability target of

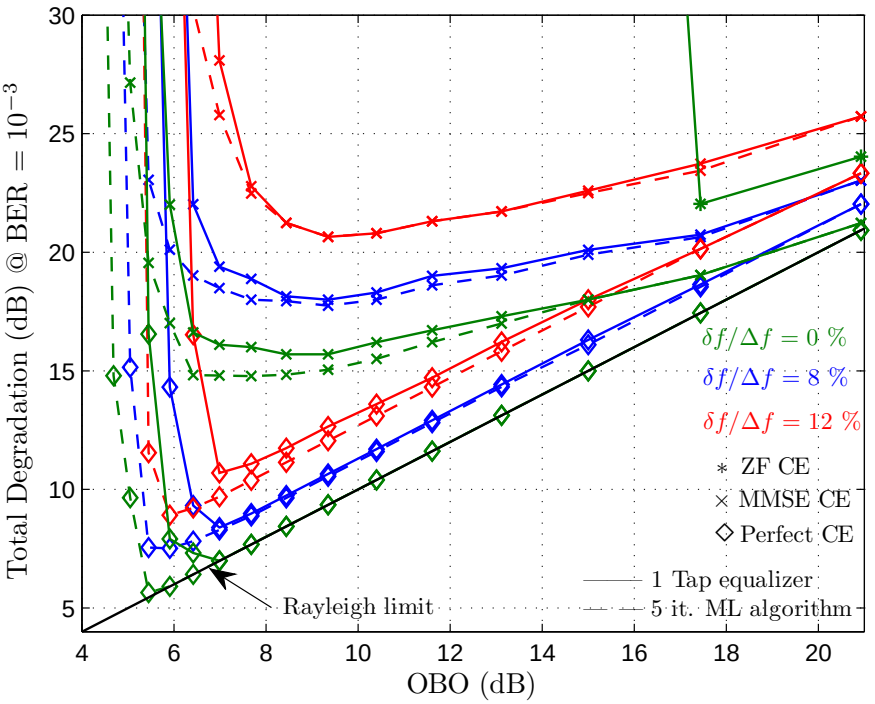

FIGURE 6.25: Total degradation vs OBO for faded OFDM/BPSK signals with 64 subcarriers affected by CFO considering ZF, MMSE and ideal channel estimations and both one-tap equalizer and iterative ML algorithm for a BER = 10^{-3}. Results for 6 taps channels.

10^{-3} as a function of OBO are also depicted in Figure 6.25 for OFDM/BPSK signals with 64 subcarriers and considering three different normalized CFO values of 0%, 8% and 12%. Results for one-tap equalizer as well as iterative ML algorithm are present. The main difference between these TD results and the ones presented in previous sections is that the performance curves do not converge to the linear case for high OBO values. This constant difference, which is clearly seen in the perfect estimator case, is only due to the ICI term induced by the CFO. Therefore, an extra SNR per bit degradation, which corresponds to the variance of the extra noise term, is reported in all curves.

6.6 Considerations on the MMSE channel estimator structure, complexity and performance

The computation of the MMSE estimator can be in fact quite complex. The order of the complexity grows with both the order of the nonlinearity and the number of subcarriers considered. Moreover, it is assumed that both the nonlinear input-output characteristic

of the channel and the statistical properties of the multipath channel are known by the estimator. Nevertheless, if the nonlinear channel is assumed to be static and the statistical properties of the fading process do not change over time, the estimator only needs to perform the linear transformation remains constant and the estimation process reduces to a matrix multiplication.

Another important issue is the set of known symbols or pilots $\mathbf{S}'$. Here we have fixed an arbitrary sequence and all performance results were obtained for that specific set. Moreover, we have considered that all subcarriers are pilots. By doing so, we can estimate the frequency response of the channel at all subcarriers frequencies without the use of interpolation techniques. Yet, due to the IMD induced by the nonlinearity, the choice of the set and their frequency allocation may be crucial and a subject of future studies.

6.7 Summary

In this chapter we started by introducing the multipath channel modeling and analytically describing an OFDM uplink transmission scheme composed by a bandpass fading and bandpass nonlinearity. Here, we have discussed the main impairments induced by both channels and AWGN on an OFDM signal and to both the estimation and equalization procedures. Then, a new MMSE channel estimator for nonlinearly distorted faded OFDM signals corrupted by AWGN was presented and analytically derived. This estimator takes into account the correlation between complex symbols conveyed by different subcarriers due to both fading and nonlinear distortion. The MMSE estimator was shown to be given by a set of N linear filters or, equivalently, a set of correlators matched to every possible frequency components followed by a linear transformation, i.e., it can be implemented by using a conventional OFDM receiver capable to extract a set of sufficient statistics followed by a linear transformation.

Subsequently, we have also demonstrated that a joint multipath and carrier frequency and phase offsets MMSE estimator can be obtained without significant changes to the original structure.

Finally, we have conducted several simulations in order to evaluate the estimator performance under different nonlinear operating points, AWGN noise levels and Rician

K-factors. The performance of the MMSE estimator was compared with both conventional ZF and perfect channel estimators. Additionally, for equalization purposes, we have considered the one-tap equalizer and the previously derived iterative ML algorithm detector fed with channels estimates. We can conclude that a ZF based estimator is severally affected by the nonlinear noise. As a dominant path emerges (e.g. the LOS path), its performance starts to increase and, depending on the nonlinear operating point considered, it even converges to the perfect estimation result.

Results for the MMSE estimator have shown that it is suitable for an uplink scheme configuration in which a faded OFDM signal is nonlinearly distorted and corrupted by AWGN. For Rayleigh fading channel models with a number of taps lower than 6, our estimator exhibit a performance behavior relatively close to the one for perfect estimation. For Rician fading channels, it almost equals the ones given by the perfect estimator.

Regarding the iterative ML algorithm detector, a major impact on the performance of the perfect estimation for both Rayleigh and Rician fading channels was observed. When the MMSE estimator is considered, total degradation results have shown improvements of around 1 dB for Rayleigh fading channels. As the Rician K-factor increases, results have shown that the MMSE virtually equals the ones for perfect estimation. Also, total degradation results for a Rayleigh distributed channel show that the MMSE estimator presents a maximum link gain margin of 7.5 dB to the ZF estimator for a BER target of 10^{-3}. This margin can be used to increase the link transmission range and still obtain the same BER level and degradation as the ZF.

Additionally, it was also observed that the number of taps of the multipath channel model, and consequently the maximum delay spread, affects both the estimation and equalization procedures, especially for transmissions at relatively low OBO values.

In the next chapter a case study on RoF systems is presented. We concentrate on the uplink of intensity modulation/direct detection RoF systems where the OFDM signal suffers from linear distortion (fading), nonlinear distortion and noise.

Chapter 7

Radio-over-fiber system case study

7.1 Introduction

In this chapter we present a case study application for the techniques detailed in previous chapters. Particularly, we consider the use of those techniques in an uplink radio-over-fiber (RoF) transmission.

It is true that the demand for broadband contents and services in both wired and wireless technologies has been growing. We are living in an era where broadband Internet with high bandwidth services and applications such as high definition multimedia, web-TV with multi-casting capabilities, real-time video, fast peer-to-peer and on-line gaming are in continuous evolution and demanding for even higher data rates. The residential home market has also grown tremendously in the past few years leading to an increase in the number of wireless access subscribers demanding for higher bandwidths. Additionally, it is expected that this demand will be for both indoor and outdoor wireless coverages.

An interesting phenomenon that is being observed in the past few years is the uplink data traffic increase. This phenomenon is mainly due to the exponential use of Internet services like social networks and video/photo sharing services combined with the ever increasing mobile systems with full-HD capabilities and high speed connectivity. Therefore, it is clear that wireless standards will have to be able to provide both broadband

downlink and uplink solutions.

To reduce system cost, maintenance and complexity, it is important to simplify antenna units or base stations (BS) and to concentrate signal processing functions at a centralized headend, usually referred as the central station (CS). With the ever increasing throughput at each BS an attractive solution is to use an optical fiber based backbone.

For our RoF case study, we have considered the uplink transmission of OFDM signals based on both IEEE802.11g/n and ultra wide-band ECMA-368 standards in a typical scenario where high data rate services are provided by an operator central headend to a subscriber.

Currently, there is a considerable widespread interest in using RoF techniques to transport and deliver RF signals from BSs to the CS, including wireless OFDM based standards. In our case study we have considered an intensity modulation/direct detection (IM/DD) system employing a Mach-Zehnder modulator (MZM) which is an electro-optic device responsible for the conversion of the electrical signal into the optical domain. It exhibits a frequency independent nonlinear behavior and will be the key element in our case study. We have considered the MZM due to its high popularity and analytic tractability. Nevertheless, other types of modulators such as the electro-absorption could also be a subject of study using the same methodology. In an uplink system, the faded OFDM signal arriving at the BS is nonlinearly distorted by the MZM before traveling through the optical fiber and being detected at the CS.

We start this chapter by briefly introducing in section 7.2 the current state-of-art wireless standards and particularly the ones in the 60 GHz spectrum region. Then, in section 7.3 we introduce the RoF concept where its main characteristics, advantages and impairments are discussed. Subsequently, in section 7.4 we present our case study in RoF where the mathematical model of the system is derived. In section 7.5, several simulation results of the techniques detailed in previous chapters are presented and discussed for the case study considering the transmission of OFDM signals based on IEEE802.11g/n and ECMA-368 standards. Finally, in section 7.6 the main contributions of this chapter are summarized.

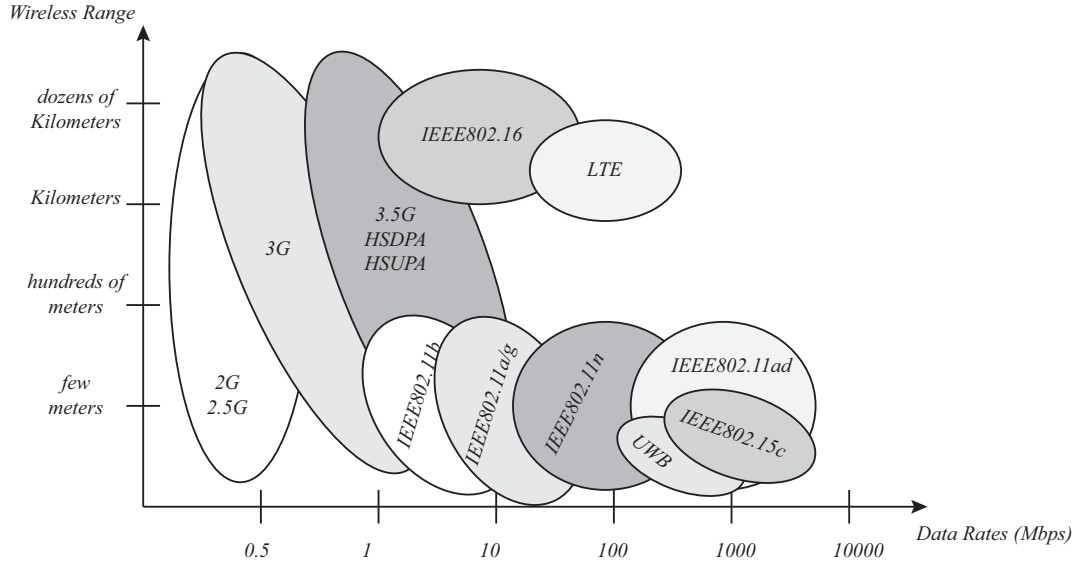

FIGURE 7.1: Data rates and range requirements for wireless standards and applications.

7.2 Broadband wireless standards evolution

Figure 7.1 depicts the wireless standards evolution in terms of data rates and wireless ranges [129].

In a modern broadband wireless local network it is expected that every terminal such as TVs, media-centers, mobile phones, printers, storage servers, laptops and desktops will be jointly connected. In other words, we are continuously moving on to an era of communication "anytime, anywhere, and with anything". Furthermore, broadband wireless technologies are penetrating in all sectors and expanding in all businesses. In fact, standards based on wireless technologies capable of delivering high data rates are continuously being proposed and approved using microwave and millimeter waves (2 – 60 GHz spectrum region), such as IEEE802.16 WiMAX [7], IEEE802.11a/b/g/n WLAN Wi-Fi [4–6], ECMA-368 ultra wide-band (UWB) [1] and, more recently, the 60 GHz frequency region multi-gigabit pre-standards IEEE802.15.3c [130] and IEEE802.11ad [13].

7.2.1 The 60 GHz frequency spectrum region

In order to provide multi-gigabit wireless a high frequency carrier must be used. The millimeter wave region is being appointed as the most promising candidate for future

very-high data rate wireless systems [26, 131, 132]. Several countries have already allocated a bandwidth of about 7 GHz around the 60 GHz region for wireless communications, and the European Union is currently creating similar allocations. Due to the high atmospheric gaseous losses around 60 GHz, wireless transmission at these frequencies are only considered for short- and mid-range indoor applications (less than ten meters). On the other hand, this high propagation loss not only limits undesired propagation over long distances which can be a concern especially to video copyright owners, but also allows the reuse of the carrier frequency without the fear of spectrum collision.

The WirelessHD™and the Wireless Gigabit Alliance (WiGig™) groups are two industry-led consortiums that are defining specifications for the next generation of multi-gigabit wireless communications around 60 GHz for consumer electronics products [133, 134]. In December 2009, WiGig Alliance announced completion of its wireless specification capable of supporting data rates up to 7 Gbps and backward compatibility with IEEE802.11 standards. In January 2010, WirelessHD™group also announced the second generation of their standard and its backward compatibility with products complying with WirelessHD™ 1.0, the world's first 60 GHz wireless, that is in the market since early 2009. The WirelessHD™ 2.0 standard specifications allows unprecedented level of data rates up to 28 Gbps that will support the demands of future high definition displays, 3D and $4K$ resolution formats (the same as many digital theaters), IP connectivity for Internet access, support for lossless video and up to 1 Gbps data connectivity in low-power portable devices like smartphones and netbooks. SiBeam Inc. (now Silicon Image Inc. [135]) was the first company to develop multi-gigabit WirelessHD™chipsets at mass market prices and to deliver true uncompressed and lossless high definition digital video, audio and data, end-to-end, without compression or buffering, specifically to achieve the highest quality wireless video solution.

In order to transport and deliver broadband wire and wireless networks, several mediums capable of delivering them are used, like coaxial cables and copper twisted pairs, but the ideal medium for such a converged network is the optical fiber [16, 20]. Optical fiber based networks have been grown due to their properties such as low loss and huge bandwidth available. We will now introduce the RoF concept that merges the optical fiber and wireless worlds.

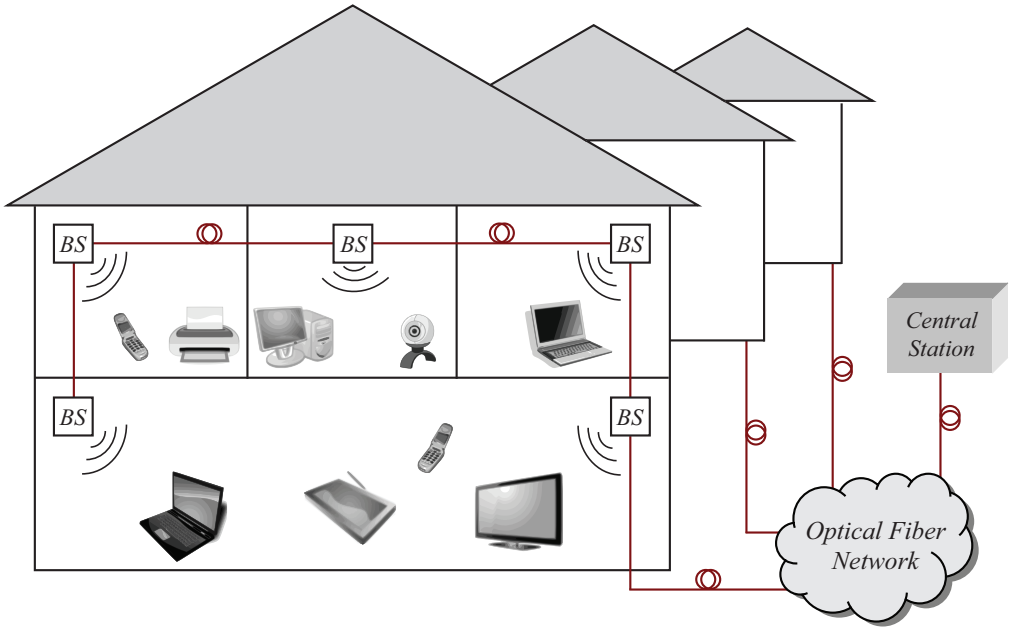

FIGURE 7.2: In-building radio-over-fiber concept.

7.3 The radio-over-fiber concept

Radio-over-fiber technology is a technique of modulating RF signals onto an optical carrier for distribution over an optical fiber based network [28]. In Figure 7.2 it is illustrated a RoF concept in an in-building network. A generic RoF system consists of a CS, where all switching, routing, medium access control and frequency management functions are performed, and several BSs designed only for wireless signal distribution. To connect all BSs to the CS, an optical fiber based network is used. Depending on the application, the optical fiber network can be either active or passive. In a 'last mile' wireless access system all the active devices are located at the CS and BS, enabling also the use of RoF in passive optical fiber networks (PON) [16, 136]. RoF systems can be completely transparent to all signals conveyed in the optical channel. Moreover, when combined with multiplexing schemes, like sub-carrier multiplexing (SCM) and wavelength division multiplexing (WDM), it allows multiple services to be supported on a single fiber and at the same time.

By using the optical fiber as the transport medium, we take all the advantages of the fiber, namely, low loss, high bandwidth and immunity to electromagnetic interference. In its simple architecture RoF conceives no signal processing neither high speed ADC/DAC operations at the antenna location. In fact, in RoF systems BSs are inherently simple

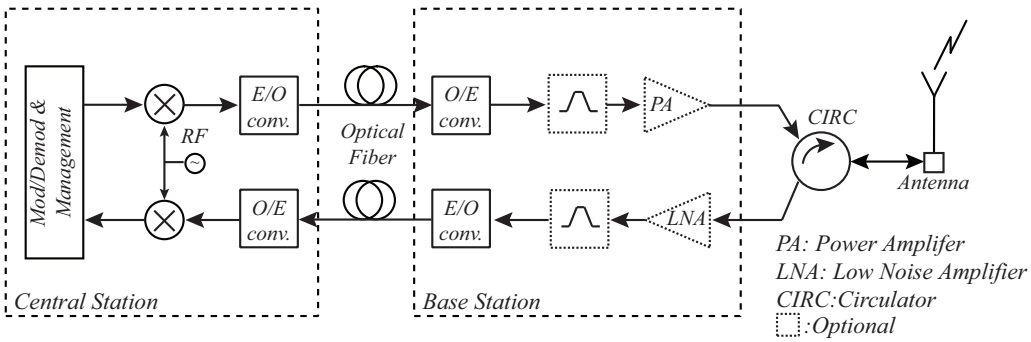

FIGURE 7.3: Generic architecture of an RF-over-fiber system.

since they usually only need to perform optic-electric-optic (O/E/O) conversion and, in some cases, filter and amplification operations. Moreover, their simple structure allows a simple maintenance, a very small size and weight and high reliability. Moreover, all signal processing functions and expensive high frequency equipment can be shared and concentrated at the CS. Additionally, centralization of all RF equipment enables future upgrade tasks easier and system installation and maintenance cost savings, especially in picocell broadband networks where a large number of BSs is used [16, 19].

In order to transport and deliver the modulated signal conveyed in the optical channel, three methods can be used: RF-over-fiber, intermediate frequency (IF)-over-fiber and baseband (BB)-over-fiber and [19, 28]. In a BB-over-fiber network, a baseband signal modulates an optical carrier and is transported over fiber to the BS, while in IF-over-fiber, the baseband signal is first upconverted to an intermediate band at the CS before being sent through the fiber medium. In both schemes the BS must perform up-conversion operations to reestablish the RF signal.

In Figure 7.3 it is depicted a generic architecture for a RF-over-fiber system. In this scheme, the modulated signal is generated at the CS in a RF band and then is transported through the fiber to the BS where it is converted to the electric domain and transmitted to the antenna. This scheme eliminates all the up/down conversion from the BS. Nevertheless, for high RF carrier frequencies, fiber chromatic dispersion can severely affect the performance of the transmission [137, 138]. In order to counteract the effect of chromatic dispersion in a RF-over-fiber transmission link, single-side band (SSB) modulation techniques can be used [139], as well as advanced modulation techniques such as OFDM that are more robust and easier to equalize when transmitted over dispersive channels.

Note that all three transportation methods have their merits and demerits. Nevertheless, RF-over-fiber architectures have been considered for the future delivery of very high data rate wireless signals to customers due to the fact that its scheme enables a centralized control and monitoring of channel allocation. Additionally, BS architecture are relatively simple because no up/down conversion devices nor mixers are required.

Over the past few years, it has been experimentally demonstrated that RoF networks are well suited to simultaneously transport several wireless standards like wideband code division multiple access (WCDMA), IEEE802.11 wireless local area network (WLAN) [140], global system for mobile communications (GSM) [141], WiMAX [20] and ultra wide-band (UWB) [16, 142]. Furthermore, several experimental results of multi-Gigabit wireless signals at 60 GHz over RoF are continuously being published in the literature [21, 26, 131, 132, 143–145].

7.3.1 The optical medium: single-mode fiber versus multi-mode fiber

Although single-mode fiber (SMF) has been routinely considered as the choice for RoF system design due to its high performance characteristics, multi-mode fiber (MMF) can also be used, especially for short-range applications at moderate frequencies [16]. Nowadays, the majority of the building networks are based on MMF. In fact, in-building networks employing MMF topologies for high speed short-range (10 Gbps, up to 300 meters) represent around 90% of all in-building networks [146]. Consequently, the use of MMF in RoF networks has attracted much attention in the last years. Presently, it is predicted that the fastest growing part of the optical communications market will be targeting legacy MMF in currently installed networks [147].

Due to their low cost components, maintenance, easy installation and connectorization, MMF is still being extensively installed in small range high data rate networks like in-building networks. Furthermore, new developments in the MMF design and fabrication process have recently led to fibers with very high nominal 3 dB bandwidth length products around 4.7 GHz·km and even higher [16]. Particularly, polymer optical fibers (POF) are even easier to install, as a result of their large core diameter and its high mechanical flexibility. In fact, even grimp-on connectors that attaches directly to the coating of polymer fibers without the need of expensive tools used in glass fibers are

a reality. With this "revolution", polymer fibers are being appointed as the transport medium for very low cost optical networks and has opened the world of optical networks to the *do it yourself* (DIY) concept. State-of-the-art perfluorinated graded-index POF (PF-GIPOF) with 3 dB bandwidth length products of around 1.4 GHz·km and losses below 10 dB/km, jointly with low-cost vertical cavity surface emitting LASERs (VCSELs) operating in the 850 nm and 1300 nm wavelength band are being considered for in-building short-range networks [148]. In 2010, Oliveira *et al.* [149, 150] have experimentally demonstrate the uplink of a MB-OFDM UWB signal over two different PF-GIPOFs using low-cost optical-to-electrical transceivers based on commercial off-the-shelf (COTS) 850 nm VCSELs and PIN photodiodes. The transmission at 480 Mbps over large core diameter (120 μm) PF-GIPOFs using commercial UWB transceivers and low-cost COTS was experimentally verified.

The frequency response of a MMF link strongly depends on the modal power distribution induced by launching conditions. Under arbitrary operating conditions (e.g., link length, installation bend, connector offsets), it becomes unpredictable. As a result, the performance of RoMMF systems can be severely limited. Nevertheless, several authors demonstrate that it is possible to transmit RF signals with frequencies up to 10 GHz in few hundreds of meters of MMF/POF in conjunction with COTS components which are suitable for modern Wi-Fi, WiMAX, 3G and UWB standards [24, 25, 146, 151–154]. Due to the short-range characteristics of in-building networks, the high attenuation drawback inherent to MMF and POF is not a concern.

Techniques to overcome limitations of both glass and polymer based multimode links are also being a subject of study [155, 156], in particular the optical frequency multiplication (OFM) concept for microwave signals generation proposed by Koonen and Ng'oma [156–159]. Results show that both modal and chromatic dispersions can be quite well tolerated by the OFM technique and that POFs, jointly with the OFM technique, are suitable for carrying microwave signals in radio-over-fiber networks, such as Wi-Fi, UWB and even future 60 GHz standards.

7.3.2 Techniques for RF signal generation and transportation

The transmission of RF signals over fiber using intensity modulation/direct detection (IM/DD) techniques are simple to implement but may require the use of very high frequency transmitters and receivers if multi-GHz signal are considered.

Optical heterodyning using two LASER sources is the most straightforward method to generate multi-GHz signals [18, 160, 161]. Yet, the phase noise correlation and spectral linewidths from the LASERs can affect severely the performance of the system. Complex techniques like optical phase locked loops (OPLL) and optical injection locking (OIL) are often used in order to overcome these limitations [161, 162].

Techniques based on the generation of multiple high-frequency harmonics by exploiting nonlinear processes, like FM-to-IM conversion, are also suitable to optically generate microwave and millimeter-wave signals. The principle of optical frequency up-conversion is to optically generate high-order harmonics using an E/O converter, such as a MZM driven by an RF signal with a given frequency [18, 163, 164]. For instance, due to the nonlinear transfer characteristic given by a cosine law (see Figure 7.4(b)), the electric field at the output of the MZM is composed by several high-order optical harmonics separated by the modulating frequency, f_c, and centered at the optical frequency, f_0. The beat of two high-order optical harmonics or the beat of high-order optical harmonics with the optical carrier component at the photodetector will generate RF signals at higher frequencies. Up conversion methods for doubling [164], quadrupling [163, 165], sextupling [166] and 12-tupling [167] have also been proposed in literature.

Since we focus on IM/DD systems, we will describe it in more detail in the next section. Additionally, the high interest in simplified, source-free and even passive BS structures specially for picocell networks is also a motivation for a further insight of optical transceivers based on reflective electro-absorption modulators (EAM).

7.3.2.1 Basic direct intensity modulation

In order to generate RF intensity modulation of a CW optical carrier two methods can be applied. One is by performing direct RF modulation of a LASER, like distributed feedback LASER (DFB) or VCSEL as depicted in Figure 7.4(a). The second one is by RF modulation of the CW optical carrier via an external modulator, like a MZM

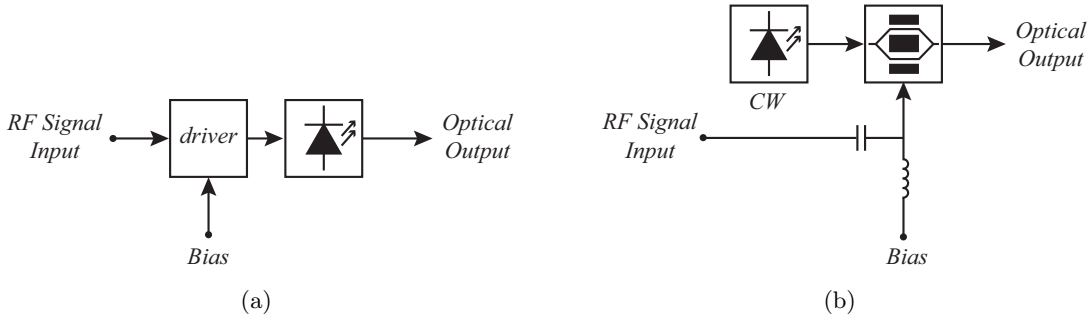

FIGURE 7.4: Generation of optical intensity modulated signal using (a) a LASER and (b) an external modulator.

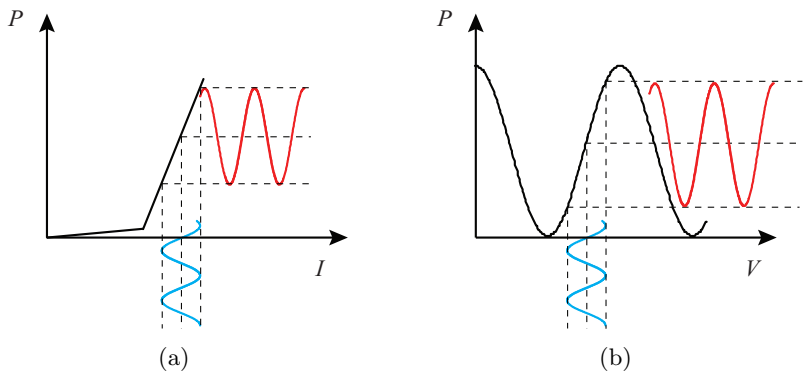

FIGURE 7.5: Schematic of the relationship between output optical power and RF signal amplitude for (a) a LASER and (b) an external Mach-Zehnder modulator (MZM).

or EAM (Figure 7.4(b)). Note that in both cases the modulating signal is the analog RF signal. If the RF signal carries data, then the amplitude of the photocurrent after detection is proportional to the transmitted RF signal and the modulation format is (ideally) preserved.

Direct modulation of the LASER is the most simple and less expensive of both methods. However, the useful bandwidth that can be used is limited to the range from DC to the LASER relaxation frequency, which is around a few tens of Gigahertz for high performance LASERs [168]. Figure 7.5 represents, in a generic form, the (nonlinear) relation between optical output power and drive current or voltage, for the LASER and MZM, respectively, and their response to a sine wave signal. Whether using direct or external modulation, the output of all modulation devices is an intensity modulated optical wave, and thus it is common to say that the optical carrier is intensity modulated (IM). Note that both LASER and external modulators like MZM are nonlinear devices. While the former exhibits a frequency dependent nonlinearity, the later is frequency

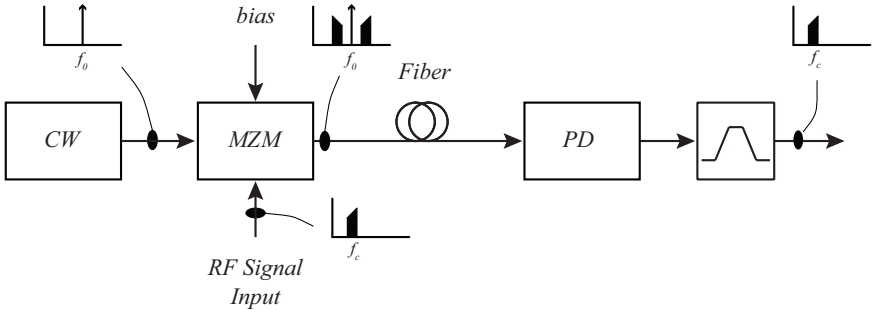

FIGURE 7.6: Representation of an intensity modulation direct detection (IM/DD) RoF link.

independent. In section 7.4 the MZM will be the subject of study and its analytical model and complex envelope nonlinear input-output characteristic are derived.

In order to recover the modulated signal from the optical to the electrical domain a photodiode (PD), like a PIN, is required. The photodiode generates a current that is proportional to the optical power of the incident lightwave and, consequently, proportional to the RF signal [168]. If the RF signal used to modulate the optical carrier is itself modulated with data, then the generated RF signal will be carrying the same data and its modulation format is preserved. This simple but efficient detection method is denoted as direct detection (DD).

A schematic representation of an intensity modulation direct detected (IM/DD) RoF link configuration using an external modulator is represented in Figure 7.6.

The major advantage of direct intensity modulation is its simple implementation. Additionally, if the optical to electrical converter is considered to be linear and the dispersive effect of the fiber is neglected, the system becomes transparent to the RF signal, acting as an attenuator or amplifier [161]. Typically, external modulators have a wider bandwidth, lower noise figure and larger spurious free dynamic range (SFDR). Furthermore, only external modulation of a high-speed MZM or EAM permits modulations with RF signals with frequencies up to 100 GHz. Yet, they usually require high drive voltages, leading to very costly drive amplifiers. Moreover, linearity requirements of system components are more strict in IM/DD due to the fact that analog applications are more sensitive to nonlinearities [168].

7.3.2.2 Electro-absorption transceiver

The simplest BS structure, in terms of component number that can be implemented, is probably the optical transceiver based on electro-absorption modulators (EAM). Moreover, they provide source free BSs which are ideal for colorless RoF networks. These BSs are based on a single electro-absorption waveguide device in which a single component acts as a modulator for the uplink and as photoreceiver for the downlink [169, 170]. Therefore, this transceiver device is a very attractive solution for a full-duplex RoF transmission.

Although a RoF system based on electro-absorption transceiver (EAT) leads to low power consumption as well as low component count, a more desirable solution based on powerless passive EATs have also been already reported [27]. Moreover, a dual lightwave approach can also be performed. By using two different wavelengths it is possible to optimize the insertion loss of the transceiver for both uplink and downlink signal transmission, i.e., segregation of uplink and downlink signals is performed using different wavelengths. Some authors have been appointing optical transceivers as a key component to realize low-cost BS in the long run [27].

The reflective (R-)EAM is an interesting device in which the rear facet is coated with high reflection layer enabling it to operate simultaneously as a modulator and photoreceiver. These R-EAMs lead to a even more simple and cost effective BS structure since no optical nor electrical circulators are required. Recently, Oliveira *et al.* [171–173] have proposed and analyzed in terms of SNR and link gain, a colorless transceiver solution for short wireless range applications based on R-EAMs and considering both Wi-Fi and MB-OFDM UWB signals. Both passive and biased BS solutions are discussed. Results show that no amplification and power supply are needed at the BS when Wi-Fi signals are considered. On the other hand, the transmission of UWB signals requires a biased R-EAM. Nevertheless, the R-EAM can be optimally biased using a small battery, which can last for several months, allowing the BS to operate as a passive device, thus reducing size and complexity. An illustrative representation of an R-EAM based BS is depicted in Figure 7.7.

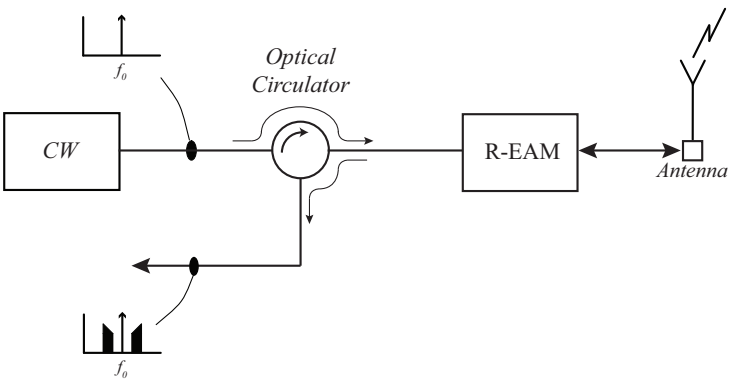

FIGURE 7.7: Representation of a base station based on a single R-EAM.

7.3.3 Chromatic dispersion induced effects

In a typical IM/DD scheme, the optical carrier is modulated by the RF signal applied to the modulator and generates a double-sideband (DSB+Carrier) modulation optical field (see Figure 7.6). At the photodiode, each sideband beats with the optical carrier component and a constructively interference between them originates a single component at the RF signal frequency. However, when the optical signal travels through a single mode fiber, each optical frequency experiences different velocities due to chromatic dispersion. Thus, each sideband will suffer a different phase shift and the interference between beats at the photodiode may not be always constructive. In fact, for certain fiber lengths and frequencies, the interference can be destructive and the intensity of the signals is severely affected, as well as its carrier to noise ratio (CNR) [139].

Figure 7.8 represents the power fading due to chromatic dispersion when a DSB modulated optical signal is transmitted through an SMF. As it can be seen, there is a severe power penalty at certain fiber link distances. In fact, the fiber lengths at which the RF power is null depends on the RF frequency f_{RF}, fiber dispersion parameter D and optical wavelength λ_0, and are given by [139]

$$L_{null} = \frac{ic}{2D\lambda_0^2 f_{RF}^2}, \quad i = 1, 3, 5, \cdots \tag{7.1}$$

where c is the speed of light. Generically, the total RF power degradation is proportional to

$$P_{RF} \propto \cos^2\left(\frac{\pi L D}{c}\lambda_0^2 f_{RF}^2\right) \tag{7.2}$$

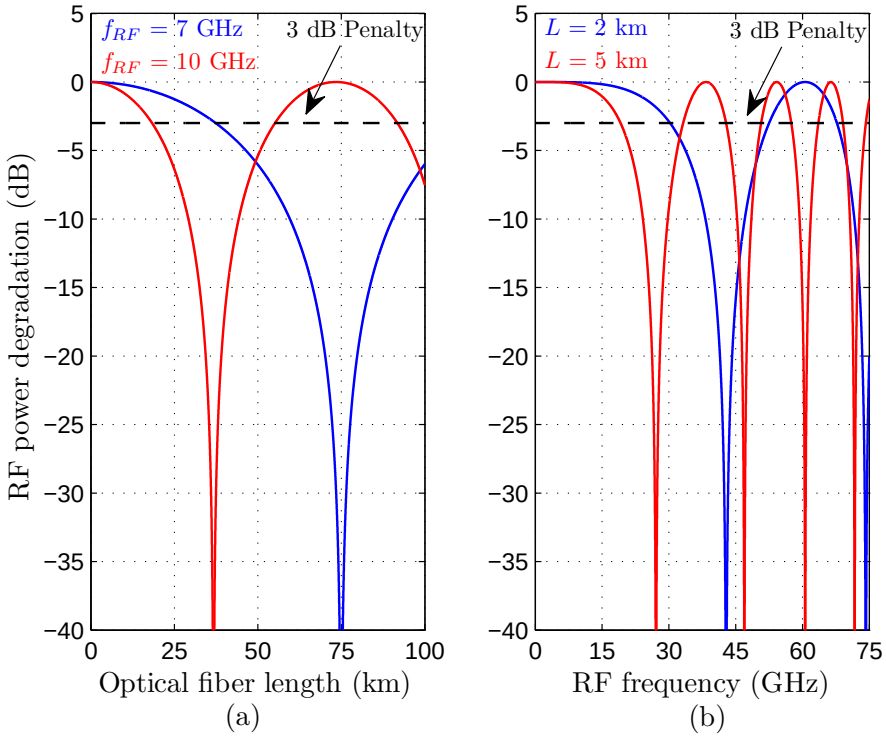

FIGURE 7.8: RF power degradation due to chromatic dispersion as a function of (a) optical fiber length and (b) RF frequency. Results for a fiber dispersion parameter $D = 17\,\text{ps/nm/km}$ and an optical wavelength $\lambda_0 = 1550\,\text{nm}$.

Results from 7.8 show that for a fixed frequency of 10 GHz the first null occurs at a fiber length of approximately 38 km whereas for 7 GHz the optical fiber distance without nulls is doubled. It is interesting to note that a 3 dB power penalty occurs at lengths of 18 km and 37 km for fixed frequencies of 10 GHz and 7 GHz, respectively. It can also be seen that there is a severe power penalty with frequency. In fact, as the frequency increases, the periodicity of nulls increases as well. Also, from (7.1) and (7.2) it can be seen that for 60 GHz the first null and the 3 dB power penalty occur at a fiber lengths of approximately 1000 and 500 meters, respectively.

In order to overcome the chromatic effect limitation in RoF systems, several solutions can be adopted. As it was previously stated, the effect of chromatic dispersion can be reduced by transmitting the signal at moderate frequencies, i.e., using IF-over-fiber or even BB-over-fiber. Also, by introducing a large negative chirp to the modulated signal by means of a dual-arm external modulator, we can shift the fiber length at which null power occurs and the transmission distance can be doubled [139]. Moreover, dispersion effects can be almost eliminated by generating SSB techniques, either using optical filters

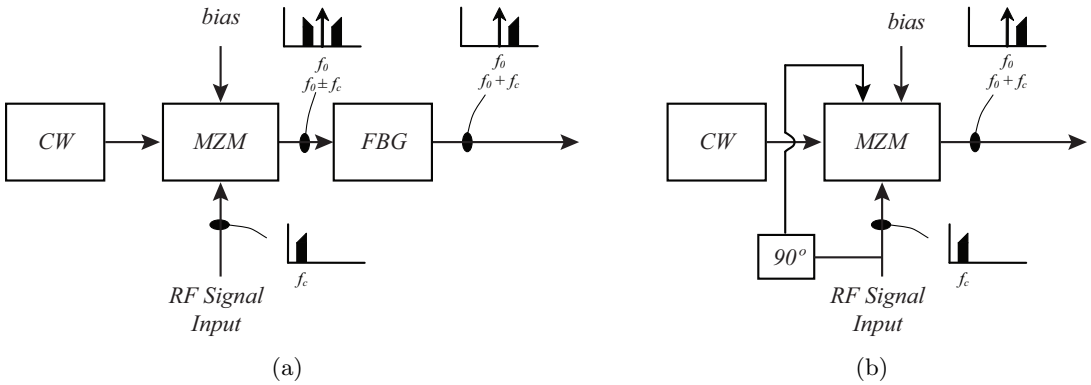

FIGURE 7.9: Optical single sideband (SSB) generation using (a) a fiber Bragg grating (FBG) and (b) a dual-arm MZM with a 90 degree phase shifter.

to eliminate one of the sidebands (see Figure 7.9(a)) or using modulation techniques to generate a SSB signal at the modulator (see Figure 7.9(b)). At the photodiode, the single side band component beats only with the optical carrier which results in single component at the RF signal frequency with minimal effects of fiber dispersion [174]. Note that the SSB generation method based on dual-arm MZM needs a broadband phase shifter to perform a 90 degree phase shift. Additionally, SSB generation can also be achieved by means of Hilbert transform techniques in both electrical and optical domain [175].

7.4 IM/DD externally modulated RoF uplink system

After introducing the radio-over-fiber concept and main characteristics, let us now focus on the specific RoF system configuration that will be used as a case study for the results developed in previous chapters.

The model depicted in Figure 7.10 is a schematic illustration of an uplink RoF transmission and represents the system model that we will consider. The RF modulated signal (considered to be OFDM) generated by a mobile station (MS), passes through a wireless medium and is detected by a base station (BS) antenna. Here, the RF signal is amplified and used to externally modulate a CW LASER by means of a Mach-Zehnder modulator (MZM). The RF modulated optical signal reaches a PIN photodiode through an optical fiber and is converted to the electrical domain. Note that both OFDM transmitter and receiver blocks also perform RF up/down conversions.

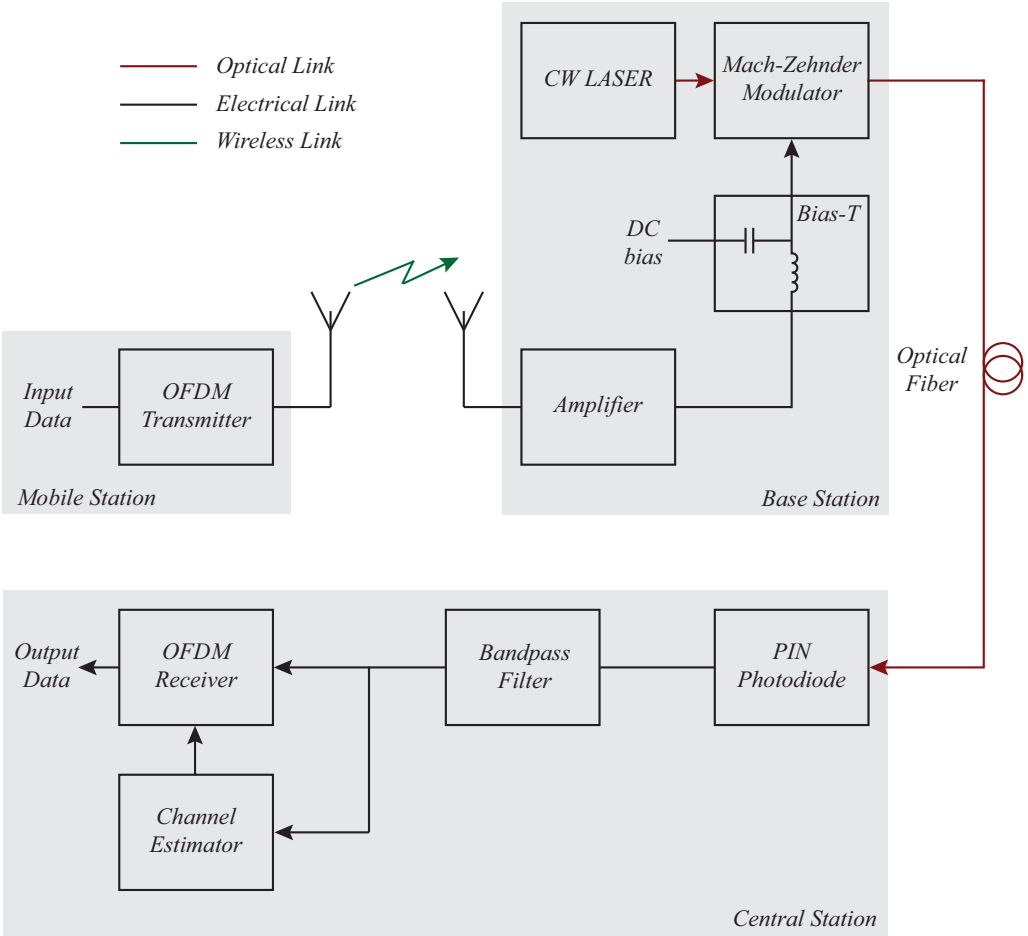

FIGURE 7.10: Schematic representation of the considered case study: uplink radio-over-fiber system based on external modulation of a LASER.

As degradation factors in the system, we consider that the wireless channel is a Rician fading channel with a strong LOS path and that acts also as an attenuator, as happens in in-building networks. The nonlinear element in the model is given by the MZM transfer function which is well modeled by a Taylor series expansion. Additionally, the following noise sources are also considered: the antenna at the BS given by an equivalent antenna temperature; the relative intensity noise (RIN) from the CW LASER; and the both shot and thermal noises at the PIN photodiode. The optical fiber is considered to act only as an attenuation channel. Note that this assumption is realistic for setups with a fiber length up to a few tens of kilometers (see section 7.3.3) for a DSB signal transmission or to be (almost) independent of fiber length for SSB transmission[1].

[1]The SSB transmission induces a phase rotation for each RF frequency component. Since the OFDM signal is composed by several narrowband subchannels, we can assume that each subchannel will experience a constant and deterministic phase shift that can be equalized jointly with CFO.

Additional impairments such as MZM chirp, IQ imbalances and nonlinear effects of the fiber are not considered in our study.

In the following section we will model the transfer function of the optical channel composed by a MZM and a PIN photodiode.

7.4.1 The Mach-Zehnder modulator lowpass equivalent response

The Mach-Zehnder Modulator (MZM) is an external electro-optic modulator based on the principle of the interferometry. A layout representation of an MZM is depicted in Figure 7.11. In its most typical configuration, a dual-drive MZM is composed by two 'Y' junctions, a 3 dB power splitter and combiner, interconnected by dielectric optical waveguides that act as optical phase modulators. Usually, the optical waveguides are made by lithium niobate material and the principle of operation of each phase modulator is based on the variation of the refractive index of the waveguides induced by an electric field.

As seen in Figure 7.11, the optical signal from the CW LASER travels through a waveguide and is (typically) split equally between the two arms. The electric field applied to each arm induces a proportional refractive index change in a effect known as linear electro-optic effect or the Pockels effect. Consequently, the phase of the optical signal changes as well. After traveling through two branches of the same size and suffering different phase shifts, both signals are combined again in a 'Y' junction. The relative phase shift between the waves traveling in both arms results in both destructive and constructive interferences after the combiner junction and an amplitude modulation of the signal is obtained. We will now derive the mathematical equations that rule the modulator.

Each optical signal undergoes a phase shift proportional to the refractive index change, Δn given by [176–178]

$$\Delta\phi = \frac{2\pi}{\lambda_0}\Delta n L \tag{7.3}$$

where λ_0 is the wavelength of the optical signal and L is the length of the dielectric material. The refractive index of the medium is in fact a function of the applied electric field and consequently of the voltage applied and can be expanded in a Taylor's series

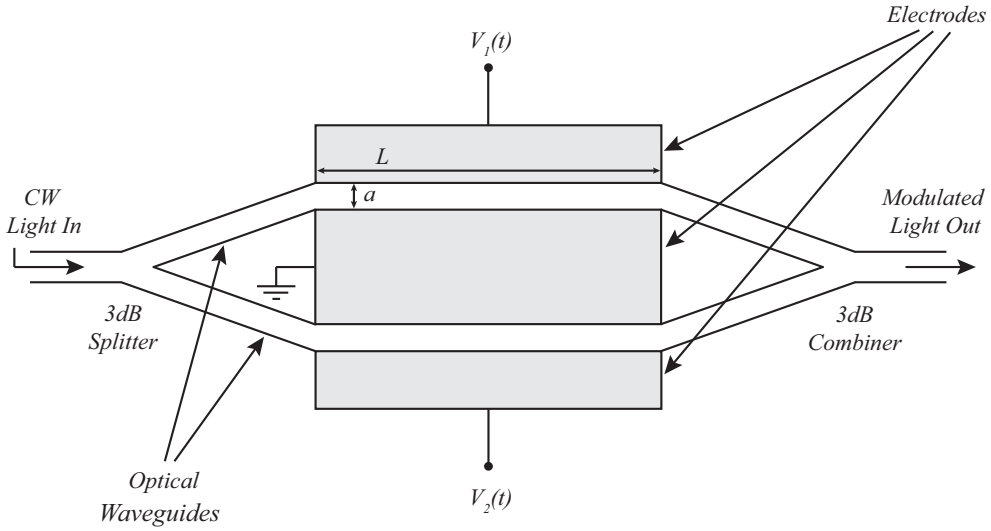

FIGURE 7.11: A Mach-Zehnder Modulator layout representation.

about $E = 0$ [176, 179]. Thus, the refractive index change is given by

$$\begin{aligned} \Delta n(E) &\approx -\frac{1}{2} r n^3 E \\ &= -\frac{1}{2} r n^3 \frac{V}{a} \end{aligned} \tag{7.4}$$

where r is the Pockels coefficient, E is the applied electric field change, V is the applied voltage change and a is the distance between electrodes plates (see Figure 7.11).

From (7.3) and (7.4), the phase shift can be written as

$$\begin{aligned} \Delta\phi &= -\frac{r n^3 L}{\lambda_0 a} \pi V \\ &= -\pi \frac{V}{V_\pi} \end{aligned} \tag{7.5}$$

where $V_\pi = (\lambda_0 a)/(r n^3 L)$ is the voltage required to induce a π phase in the optical signal.

In a dual-drive Mach-Zehnder Modulator, two different drive voltages can be applied to each arm. By denoting $V_1(t)$ and $V_2(t)$ the voltage signals applied in arm one and two, respectively, and their corresponding phase changes $\Delta\phi_1(t)$ and $\Delta\phi_2(t)$, the electric field response of a perfectly balanced MZM is given by

$$\begin{aligned} E_{out}(t) &= \frac{E_{in}(t)}{2} \left[e^{-j\Delta\phi_1(t)} + e^{-j\Delta\phi_2(t)} \right] \\ &= E_{in}(t) \cos\left\{ \frac{\pi}{2V_\pi} \left[V_1(t) - V_2(t) \right] \right\} e^{-j\frac{\pi}{2V_\pi}[V_1(t)+V_2(t)]} \end{aligned} \tag{7.6}$$

From (7.6) we can note that the electric field response of the MZM can present both amplitude and phase modulation. We consider that the voltage signals applied to each arm have opposite phases so the phase modulation term can be eliminated. It is then said that the MZM is operating in *push-pull* mode.

The intensity response of the MZM is then given by

$$\begin{aligned} P_{out}(t) &= P_{CW}\cos^2\left(\frac{\pi}{V_\pi}V(t)\right) \\ &= \frac{P_{CW}}{2}\left[1+\cos\left(\frac{2\pi}{V_\pi}v(t)+\frac{2\pi}{V_\pi}V_b\right)\right] \end{aligned} \tag{7.7}$$

where P_{CW} is the optical power of the CW LASER at the input of the MZM, $V(t) = v(t) + V_b$, $v(t)$ is the AC component of the voltage signal and V_b is the applied DC bias voltage. From (7.7), we can see that the intensity response of the MZM follows a *cosine* law, as it is also depicted in Figure 7.5(b).

To operate the MZM in the most linear region possible a bias voltage of $V_\pi(k-1/2)/2$, $k \in \mathbb{Z}$ must be applied. A good choice is $V_b = -V_\pi/4$ since it ensures a positive slop of the transfer function. Note that the bias voltage is applied in both arms but with opposite signs. Thus, the relative difference of the bias voltage between arms is $-V_\pi/2$.

Finally, we can write the intensity response as the sum of a steady-state, $P_{0,MZM}$, and a time-varying component, $p_{out}(t)$, given by

$$P_{0,MZM} = \frac{P_{CW}}{2} \tag{7.8}$$

$$p_{out}(t) = \frac{P_{CW}}{2}\sin\left[\frac{2\pi}{V_\pi}v(t)\right] \tag{7.9}$$

Let us focus now on the time-varying component of the intensity response. By applying the Taylor series expansion of the *sine* function to (7.9), i.e.,

$$p_{out}(t) = \sum_{\text{odd } n\geq 1} \frac{P_{CW}}{2}\frac{(-1)^{\frac{n-1}{2}}}{n!}\left(\frac{2\pi}{V_\pi}\right)^n v^n(t) \tag{7.10}$$

it can be seen that the intensity response is composed by a summation of odd harmonics of the modulated signal $v(t)$. By writing the applied voltage signal in complex envelope

notation we get

$$\begin{aligned} v(t) &= \Re\left\{\tilde{v}(t)e^{j\omega t}\right\} \\ &= \frac{1}{2}\left(\tilde{v}(t)e^{j\omega t} + \tilde{v}^*(t)e^{-j\omega t}\right) \end{aligned} \tag{7.11}$$

where $\tilde{v}(t)$ is the equivalent lowpass signal and $\omega = 2\pi f_c$, where f_c is the carrier frequency of $v(t)$. By using the binomial theorem, the applied voltage signal raised to the nth order can be written as function of its complex envelope notation as

$$v^n(t) = \sum_{k=0}^{(n-1)/2} \binom{n}{k} \left(\frac{1}{2}\right)^{n-1} \Re\left\{\left[\widetilde{v}(t)\right]^{n-k} \left[\widetilde{v}^*(t)\right]^k e^{j(n-2k)\omega t}\right\} \tag{7.12}$$

Note that several harmonics arise from the intensity response. However, we are only interested in the ones that are in fundamental frequency zone, i.e., in the frequency spectral region centered at ω. All the other high order frequency components are considered to be filtered by a zonal filter. Thus, only components given by $k = (n-1)/2$ in (7.12) are the ones of interest. So, the complex envelope of the intensity response of the MZM at the fundamental frequency zone reduces to a summation of odd order terms given by

$$\begin{aligned} \widetilde{p}_{out,\omega}(t) &= P_{CW} \sum_{\text{odd } n \geq 1} \tilde{c}_n \tilde{v}(t) \left|\tilde{v}(t)\right|^{n-1} \\ &= P_{CW}\left[\tilde{c}_1\tilde{v}(t) + \tilde{c}_3\tilde{v}(t)\left|\tilde{v}(t)\right|^2 + c_5\tilde{v}(t)\left|\tilde{v}(t)\right|^4 + \cdots\right] \end{aligned} \tag{7.13}$$

and the coefficients $\tilde{c}_n$ by

$$\tilde{c}_n = \binom{n}{\frac{n-1}{2}} \frac{(-1)^{(n-1)/2}}{n!} \left(\frac{\pi}{V_\pi}\right)^n \tag{7.14}$$

The nonlinear operating point is now defined by the modulation index of the time-varying component of the voltage signal. Mathematically, it is given by the following ratio

$$m_i = \frac{\sigma_v}{0.25V_\pi} \tag{7.15}$$

where σ_v is the standard deviation of the voltage signal. In our case, $v(t)$ is an OFDM signal and the modulation indexes are obtained by varying the amplitude of the complex modulated symbols.

In the next section we will present a brief overview of the PIN photodiode response to an incident optical light.

7.4.2 The PIN photodiode response

Among all types of semiconductor photodetectors, the PIN photodiode is the most common. The structure of this semiconductor consists of a junction formed by 'p' and 'n' materials separated by a layer of a lightly doped 'n' material, i.e., a nearly intrinsic 'i' region [176, 180, 181].

By applying a sufficiently large reverse bias voltage to the junction, a depletion region (devoid of free charge carriers) and a diffusion region emerge. When such junction is illuminated by incident photons, electron-hole pairs (also known as photocarriers) are created through absorption. Consequently, the electric field causes the electron and hole to be swept across the semiconductor, originating a current flow known as photocurrent, I, that is directly proportional to the incident optical power $P_{in,PD}$, i.e.,

$$\begin{aligned} I(t) &= \mathcal{R} P_{in,PD}(t) \\ &= I_0 + i(t) \end{aligned} \tag{7.16}$$

where $\mathcal{R}$ is the responsivity of the photodiode and I_0 and $i(t)$ are the DC and time-varying components of the photocurrent, respectively. The responsivity specifies the photocurrent that is generated per unit optical power and characterizes the performance of the photodiode.

In conclusion, the complex envelope of the time-varying component of the photocurrent generated by the PIN photodiode and after the fundamental zonal filter for a MZM based IM/DD system is given by the intensity response (7.13) affected by the optical fiber attenuation value, $0 < L_{OF} < 1$, and the responsivity, i.e.,

$$\tilde{i}(t) = \mathcal{R} P_{CW} L_{OF} \left[\tilde{c}_1 \tilde{v}(t) + \tilde{c}_3 \tilde{v}(t) \left|\tilde{v}(t)\right|^2 + c_5 \tilde{v}(t) \left|\tilde{v}(t)\right|^4 + \cdots \right] \tag{7.17}$$

By knowing the coefficients $\tilde{c}_n$, for odd n, that rule the nonlinear input-output characteristic of the detected photocurrent we can now apply all the algorithms and results obtained in previous chapters.

Furthermore, at the output of the photodiode we also have noise terms. Some are often defined as optical intensity dependent, namely relative intensity and shot noises, while the thermal noise is temperature dependent [168]. The shot, relative intensity laser and thermal noises have, referred at the photodiode output, power spectral densities given, respectively, by

$$I_{SN}^2 = 2q\left(\mathcal{R}P_{0,PD}\right) \tag{7.18}$$

$$I_{RIN}^2 = RIN\left(\mathcal{R}P_{0,PD}\right)^2 \tag{7.19}$$

$$I_{TN}^2 = \frac{4k_BT}{R_{load}} \tag{7.20}$$

where RIN is defined as the mean of the square noise power divided by the mean power squared, q is the electron charge, k_B is the Boltzman constant, $T = 290\,\mathrm{K}$ is the room temperature and R_{load} is the photodiode load resistance. Note that $P_{0,PD} = P_{0,MZM}L_{OF} = P_{CW}L_{OF}/2$ is the mean incident optical power at the input of the photodiode. Note also that $I_0 = \mathcal{R}P_{0,PD}$. Typical RIN values for LASERs range from $-170\,\mathrm{dB/Hz}$ to $-130\,\mathrm{dB/Hz}$. Although the PSD of both shot and relative LASER intensity noises do not have a flat distribution, it is common to assume that they have a constant power spectral density at a given bandwidth. Figure 7.12 shows the relation between the receiver noise spectral density and the mean incident optical power for two RIN levels and a load resistance R_{load} of $500\,\Omega$. Additionally, the limits of the three noise terms are also depicted. At low optical power levels the thermal noise is clearly dominant whereas shot noise and RIN increase with increasing power levels.

7.5 Simulation results

In the next sections we will introduce both IEEE802.11g/n and ECMA-368 standards. Then, we present the simulation results for the transmission of OFDM signals based on these standards through the case study system depicted in Figure 7.10[2]. We consider both non-fading and fading channels. Results were obtained using Matlab/C++ as both numeric calculator and simulator. A sampling frequency high enough to accommodate

[2]Note that the algorithms and techniques proposed in the previous chapters can be applied to an OFDM signal centered at an arbitrary frequency f_c such as 60 GHz. Nevertheless, for this case study we have considered OFDM signals based on more well established and mass market standards.

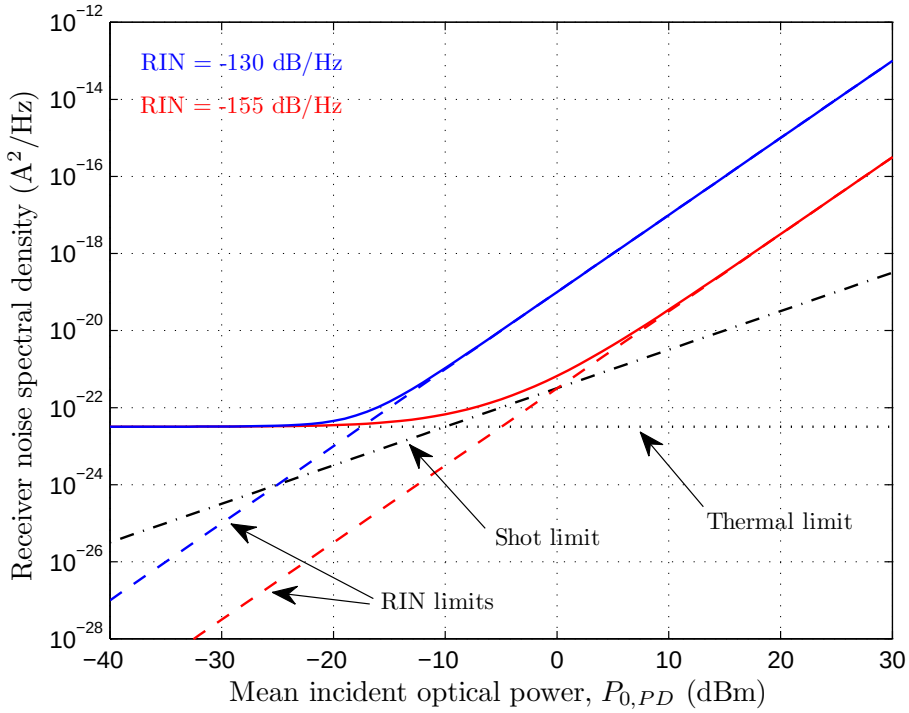

FIGURE 7.12: Receiver noise spectral density as a function of the mean incident optical power. Results for $\mathcal{R} = 1\,\mathrm{A/W}$.

nonlinear intermodulation products generated by the $15th$ order was considered. The iterative ML algorithm was designed to extract the set of sufficient statistics and to evaluate them up to the $15th$ order. Additionally, the linear transformation of the MMSE channel estimator structure was obtained for intermodulation products up to the $7th$ order due to its high computation complexity associated with higher orders[3].

7.5.1 IEEE802.11g/n over fiber

In this section, we present simulation results for the system depicted in Figure 7.10 for OFDM/16-QAM signals based on the IEEE802.11g/n standards [5, 6].

The IEEE802.11n was published in October 2009 and is an amendment to the worldwide used wireless communication standard IEEE802.11. It is based on previous IEEE802.11 standards and dramatically improves the performance of wireless LANs, while keeping backward compatibility with older IEEE802.11 standards. In fact, the new

[3]Simulation results for MMSE channel estimators up to the $5th$ order were also obtained for certain cases and it was found that the difference for the ones up to the $7th$ order was minimal. This indicates that the difference between results for the $7th$ order and the ones for higher orders are even lower and likely to be negligible.

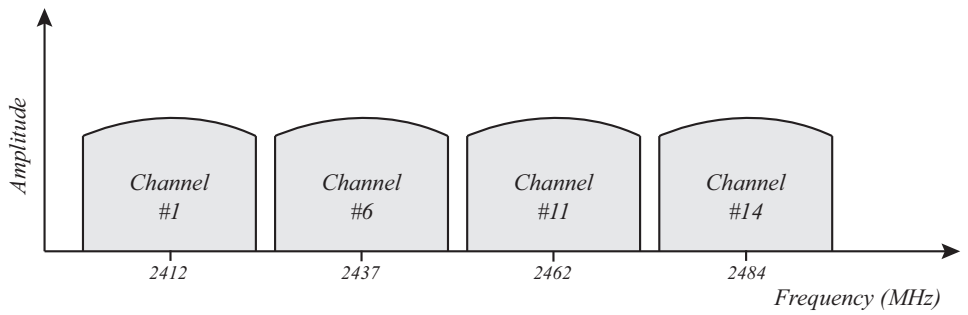

FIGURE 7.13: IEEE802.11g/n 2.4 GHz spectrum division for non-overlapping channels.

amendment support raw data rates up to 600 Mb/s, which is almost twelve times more than the 54 Mb/s limit for the IEEE802.11g. This is mainly due to the increase of the bandwidth of each channel from 20 MHz to 40 MHz and the introduction of multi-input multiple-output (MIMO) technologies through spatial division multiplexing. Moreover, the IEEE802.11n can operate on both 2.4 GHz and 5 GHz spectrum region.

The 2.4 GHz region is divided in 14 channels ranging from 2402 MHz up to 2483 MHz separated by 5 MHz with the exception of the last channel. Thus, most of the channels are in fact overlapped. Since the standard requires a 25 MHz channel separation, only four are non-overlapping, namely channel 1, 6, 11 and 14. Figure 7.13 represents the 2.4 GHz spectrum region considering only the 20 MHz bandwidth non-overlapping channels.

Each OFDM subcarrier may convey symbols from BPSK, QPSK, 16-QAM or 64-QAM constellations, depending on the data rate considered which ranges from 6 Mb/s up to 54 Mb/s or 600 Mb/s for the IEEE802.11g or IEEE802.11n, respectively. For our simulations, we considered the transmission of OFDM/16-QAM signals with the parameters summarized in Table 7.1. Each OFDM symbol is created using a IFFT/FFT algorithm with 64 points[4] and a period of 3.2 μs. The total number of subcarriers used is 52 from which 48 are for data, 4 for pilots and the remaining eight are considered to be null-valued pilots, one located at the center (DC term) and eleven at the edges. A cyclic prefix of 0.8 μs is appended at the beginning of the symbol (1/4 of the FFT period), which makes a total OFDM symbol time of 4.0 μs. From the parameters given by Table 7.1, we obtain a raw data rate, considering only data subcarriers, of 60 Mb/s.

[4]The IEEE802.11n also have channels with 40 MHz of bandwidth for 128 FFT points. Yet, we chose to use the ones for 64 FFT points as we will present results for 128 FFT points on the ECMA-368 transmission case.

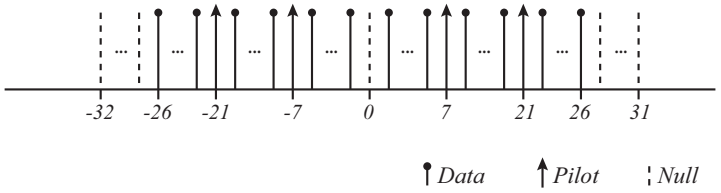

FIGURE 7.14: Mapping of the different types of subcarriers to logical frequencies.

TABLE 7.1: IEEE802.11g/n simulation related parameters

Parameter	Value
Maximum transmitted power density	0 dBm/MHz
Modulation	16-QAM
Carrier frequency (f_c)	2.412 GHz (channel #1)
Channel bandwidth (B)	20 MHz
Total number of subcarriers (N_{FFT})	64
Number of data subcarriers (N_D)	48
Number of defined pilot subcarriers (N_P)	4
Number of total subcarriers used (N_T)	52 ($N_D + N_P$)
Subcarrier frequency spacing (Δf)	312.5 kHz (B/N_{FFT})
IFFT/FFT period (T_{FFT})	3.2 μs ($1/\Delta f$)
Cyclic prefix duration (T_{CP})	0.8 μs ($T_{FFT}/4$)
Total symbol duration (T_{SYM})	4.0 μs ($T_{CP} + T_{FFT}$)

The pilot subcarriers can be used to help synchronization and to allow a coherent robust detection against frequency offsets and phase noise. Null-tones are inserted to provide control over the use of the spectrum. The mapping of the different types of subcarriers within an OFDM symbol is defined in Figure 7.14. Note that the logical frequency '0' corresponds to the carrier frequency.

The standard defines a packet layer convergence protocol (PLCP) to operate the PHY with the MAC service. Each MAC frame is formed by a PLCP packet data unit (PPDU) formed by three parts: a PLCP preamble, a PLCP header and PLCP service data unit (PSDU). The standard PLCP preamble is composed by 10 short OFDM symbols for signal detection and time/frequency synchronization and 2 long OFDM symbols for channel and CFO estimation, while the PSDU has a variable length and contains the data payload. The structure of the standard PPDU frame structure is depicted in

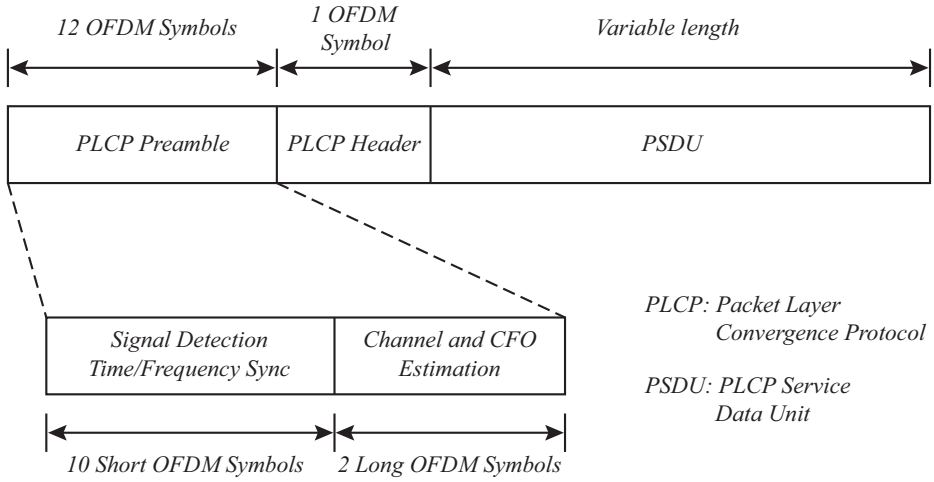

FIGURE 7.15: IEEE802.11g PLCP packet data unit structure.

Figure 7.15. The complete frequency-domain channel estimation sequence defined by the standard is given by Table B.1.

The standard may also define frequency domain spreading (FDS), time domain spreading (TDS), forward error correction (FEC) coding and scramblers to vary the data rates and to improve robustness to link impairments. Yet, these techniques are not considered in our simulations since we focus on the receiver performance of raw data.

7.5.1.1 Non-fading channel

In this section, we will present several simulation results for the uplink radio-over-fiber system depicted in Figure 7.10 corresponding to an OFDM signal based on the IEEE802.11g/n standard. The wireless channel is considered to be non-fading, i.e., it is considered to be a direct link between the antenna transmitter and receiver introducing only an attenuation of L_{WC}. Furthermore, it is also considered that the optical fiber introduces an attenuation of L_{OF}. The responsivity of the photodiode is set to $\mathcal{R} = 1\,\mathrm{A/W}$.

The characteristics used for the OFDM signal are summarized in Table 7.1 and the mapping of the different types of subcarriers are given by Figure 7.14.

The total degradation (TD) for the system considered is plotted in Figure 7.16 for a target bit error rate of 10^{-3}. Moreover, results for a normalized CFO of 5% between transmitter and receiver are also considered. A limit denoted as "linear channel" is also plotted to indicate the degradation value if a linear channel was considered. It

is obtained using the *erfc* function considering only the transmission through a linear channel followed by a AWGN channel. We consider that the total degradation is defined at the output of the MZM and is written as

$$\mathrm{TD[dB]} = \left[\left(\frac{E_b}{N_0}\right)_{NL} - \left(\frac{E_b}{N_0}\right)_{L}\right] + \mathrm{OBO} \tag{7.21}$$

Note that a complex automatic gain control (CAGC) must be computed and applied in order to correctly demodulate amplitude modulations like 16-QAM for each modulation index value.

Results of TD show that for the target BER there is a considerable gain when using the iterative ML algorithm. For the 0% CFO case, the minimum TD values for the conventional receiver and ML algorithm with one and five iterations are 6.4 dB, 5 dB and 3.5 dB, respectively. Thus, a maximum improvement of approximately 3 dB is reported. For the 5% normalized CFO, we consider that the induced constant phase rotation of the received constellation is compensated and that only the ICI term is present. The minimum TD values reported are 8.5 dB, 7 dB and 5.5 dB, for the conventional, one and five iterations ML algorithm, respectively, which represents a maximum improvement of 3 dB. Results indicate that the iterative ML algorithm is still able to process the nonlinear noise even in the presence of a CFO. It is also interesting to note that the five iterations algorithm for a normalized CFO of 5% still outperforms the conventional receiver for the 0% CFO case. As previously referred in section 5.3.3, the total degradation improvement between receiver structures can also be seen as the link gain margin that we have to obtain that same BER level. Thus, we conclude that for a BER level of 10^{-3}, a 3 dB link gain is achieved. This margin can be used to relax the receiver's noise level or to decrease the signal's power by increasing the optical link path in up to 8 km (considering an optical loss of 0.2 dB/km). Nevertheless, if a BER target of 10^{-4} and/or a higher number of iterations of the ML algorithm were considered, then a higher link gain margin would be expected.

To perform a bit error rate analysis, we set the mean incident optical power at the input of the photodiode[5] to −33 dBm and the overall noise PSD at the photodiode

[5]To avoid very low bit error rates that would take too much time to simulate, a relatively low optical power at the input of the photodiode is considered. Nevertheless, results from the previous chapters

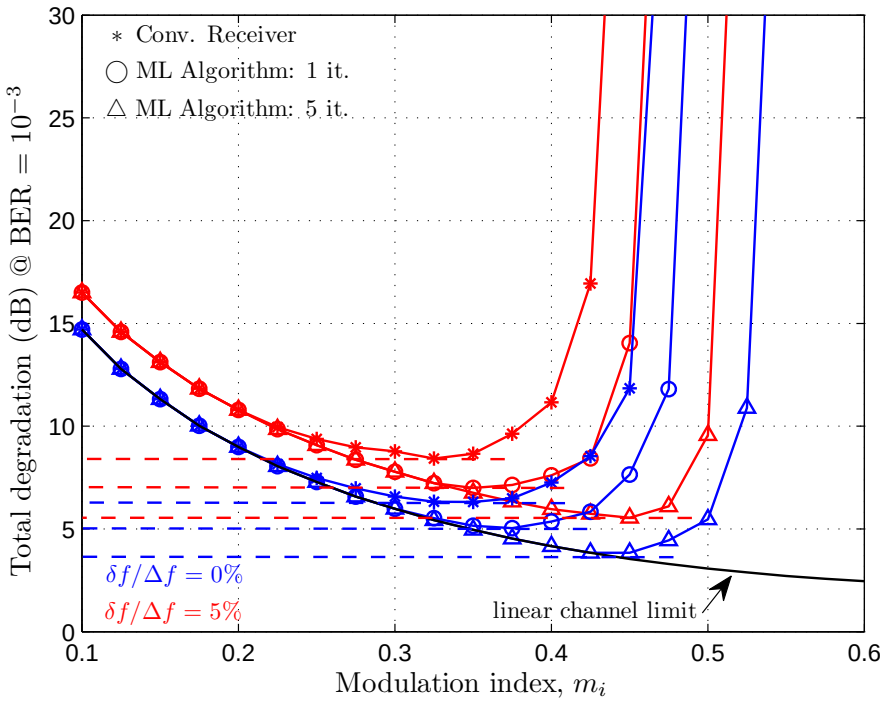

FIGURE 7.16: Total degradation as a function of the modulation index considering both the conventional receiver and ML algorithm with 1 and 5 iterations for a target bit error rate of 10^{-3} and for normalized CFO values of 0% and 5%.

to $3.5 \times 10^{-23}\,\mathrm{A}^2/\mathrm{Hz}$. This noise level accounts for RIN, shot and thermal noises[6] (see Figure 7.12), the later one being dominant. The equivalent antenna noise power is defined by its temperature, T_a, and is given by

$$P_{AN} = k_B T_a B \tag{7.22}$$

We set an equivalent antenna temperature of 290 K, which results in a noise power density of −114 dBm/MHz. Thus, for an acceptable SNR of 20 dB necessary for a reliable transmission [182], the minimum received power density at the BS antenna is −94 dBm/MHz. Moreover, for a maximum transmitted power by the mobile device of 0 dBm/MHz (see Table 7.1) and an antenna gain of 4 dB the total free-space path loss

indicate that if higher optical powers and hence higher E_b/N_0 levels were used, then an increase of the performance of the proposed receivers is also expected.

[6]In our analysis we consider a constant noise level given by the summation of all noise contributions. Moreover, the overall noise PSD is considered to be constant over the band of interest.

(FSPL) equals 98 dB. Using the definition, FSPL is given by (e.g. [69])

$$\text{FSPL[dB]} = 20\log_{10}(Z_{WC}) + 20\log_{10}(f_c) - 147.55 \tag{7.23}$$

where Z_{WC} and f_c are the length of the wireless channel in meters and carrier frequency of the signal in hertz, respectively, the maximum wireless link distance is approximately 700 m. Note that the FSPL depends on the frequency. Yet, we consider a mean value for the FSPL based on the carrier frequency of the signal. Additionally, the FSPL considers a LOS channel without reflections.

Figure 7.17 shows the bit error rate as function of the modulation index for both conventional and ML algorithm for one and five iterations. Results for both ideal non-ideal antennas with SNR values of $\text{SNR}_{\text{AN}} = +\infty$ and $\text{SNR}_{\text{AN}} = 20\,\text{dB}$, respectively, are also presented. The overall noise is now composed by the contributions from the photodiode, antenna and the signal-noise beat from the IMD term. It is important to note that the modulation index is now obtained taking into account the antenna noise PSD level.

Results for the ideal antenna show improvements in terms of minimum error rate of approximately 10 and 30 times for the ML algorithm with one and five iterations, respectively, relatively to the conventional receiver. Regarding the results for the SNR of 20 dB at the BS antenna, the ML algorithm still outperforms the conventional one. In fact, and noticing that the ML algorithm is not optimum anymore, a gain of approximately 20 times is still achieved in terms of minimum bit error rate. In other words, by post compensating the signal, it is possible to decrease the BER level of the raw data, which ultimately allows an increase of the useful data rate. Furthermore, post compensation also allows a much wider dynamic range of the signal for transmissions with BER levels no greater than a given value.

Figure 7.18 plots the bit error rate as a function of the number of iterations for the ML algorithm and considering Hamming distances of one and two. Moreover, results are presented for two modulation indexes values of $m_i = 0.40$ and $m_i = 0.50$. Results show that the performance of the iterative ML algorithm is highly dependent on the number of iterations used. For a Hamming distance of one, the error probability only seems to tend to a given value at iterations eight and nine. Yet, when a Hamming distance of

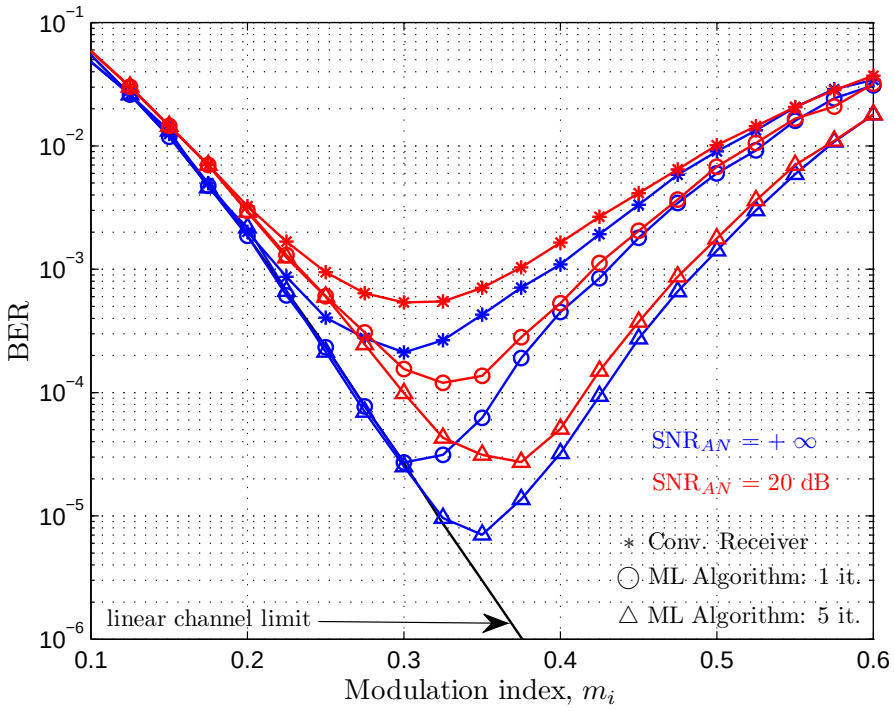

FIGURE 7.17: Bit error rate as a function of the modulation index considering both the conventional receiver and ML algorithm with 1 and 5 iterations. Results for two SNR levels at the BS antenna, $\mathrm{SNR}_{\mathrm{AN}} = +\infty$ and $\mathrm{SNR}_{\mathrm{AN}} = 20\,\mathrm{dB}$.

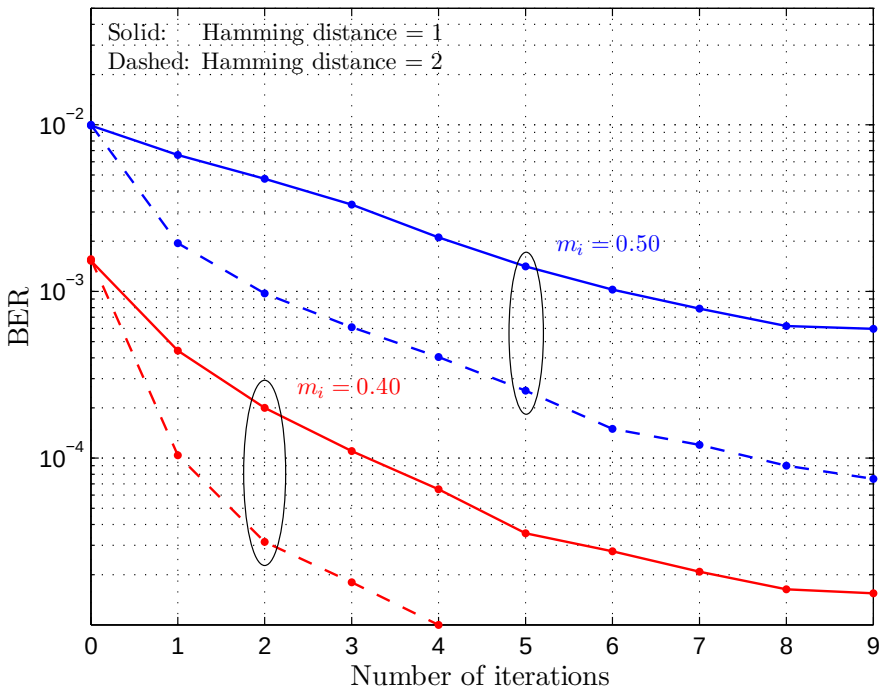

FIGURE 7.18: Bit error rate as a function of the number of iterations of the ML algorithm for two Hamming distances and considering two modulation index values $m_i = 0.40$ and $m_i = 0.50$.

two is considered for the iterative ML algorithm, the bit error rate after one iteration drops ten times relatively to the conventional receiver (iteration 'zero') and continues to decrease beyond nine iterations. This behavior is reported for both modulation index values. Moreover, results from Figure 7.18 suggest that even total degradation values lower than the ones depicted in Figure 7.16 could be achieved if more iterations were considered.

7.5.1.2 Rician fading channel

Here we consider that the OFDM signal based on the IEEE802.11g/n parameters is affected by a Rician fading channel before being nonlinearly distorted (see Figure 7.10). Different channel models and parameters are often considered in the literature. Yet, a commonly adopted channel model is the exponential one, where each channel tap is modeled by an independent complex Gaussian RV affected by a power delay profile (PDP) [183]. The PDP profile is considered to be given by

$$\Omega(\tau) \propto e^{-\tau/\tau_{rms}} \tag{7.24}$$

where τ_{rms} is the RMS delay spread set to 100 ns in order to ensure no ISI. The equivalent TDL model for the PDP is depicted in Figure 7.19 assuming that the PDP is normalized and that the average received power equals to one.

We set the fading channel to be given by a 6 tap TDL channel, Rician distributed with a typical Rician K-factor of 10 dB, i.e., each tap is modeled by a non-zero mean complex Gaussian distributed RV affected by the PDP [45]. Again we consider that a complex automatic gain control (CAGC) is computed and applied in order to correctly demodulate amplitude modulations like 16-QAM for each modulation index value.

Here we will consider the transmission of two known OFDM symbols for channel estimation purposes in a block-type pilot arrangement with complex symbols given by Table B.1. Simulation results were obtained by performing a two stage approach where the first is responsible for frequency-domain channel estimation and the second is the equalization process. Initially, two OFDM symbols composed by pilot subcarriers are generated taking into account the mapping of the types of subcarriers (see Figure 7.15 and 7.14); then, the convolution between the OFDM pilot symbol and a randomly

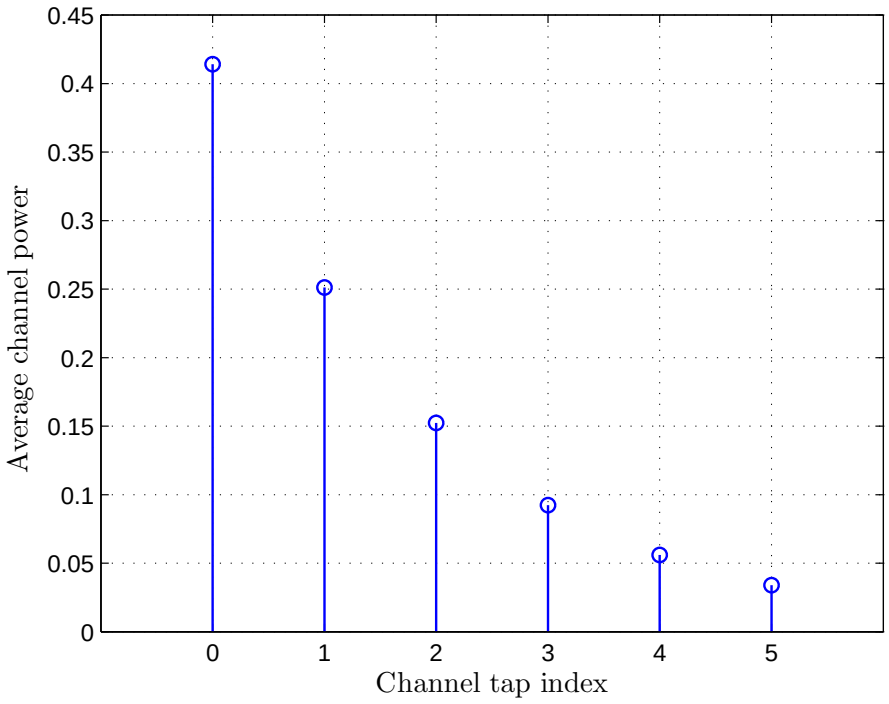

FIGURE 7.19: Power delay profile of a 6 tap channel.

generated multipath channel IR is performed; subsequently, the faded OFDM symbol is corrupted by noise from the BS antenna and then distorted by the nonlinearity; finally, after being corrupted by photodiode noise, it is used to estimate the frequency response of the multipath channel. The overall estimate is then given by the average estimate of the two OFDM symbols.

In the second stage, a randomly OFDM symbol is generated, again taking into account the mapping of the different types of subcarriers; then, a convolution between the OFDM symbol and the multipath channel IR generated in stage one is performed; subsequently, the faded OFDM symbol is corrupted by noise from the BS antenna and then distorted by the nonlinearity and corrupted again by the photodiode noise; finally, by means of an equalizer and using the previous estimates of the multipath channel frequency response, an estimation of the transmitted complex symbols is obtained. In conclusion, stage one is responsible for the multipath channel estimation whereas stage two is responsible for the equalization and recover of useful data. Here it is considered that the multipath channel is constant over both stages.

Similarly to the previous section, we present the results for the total degradation

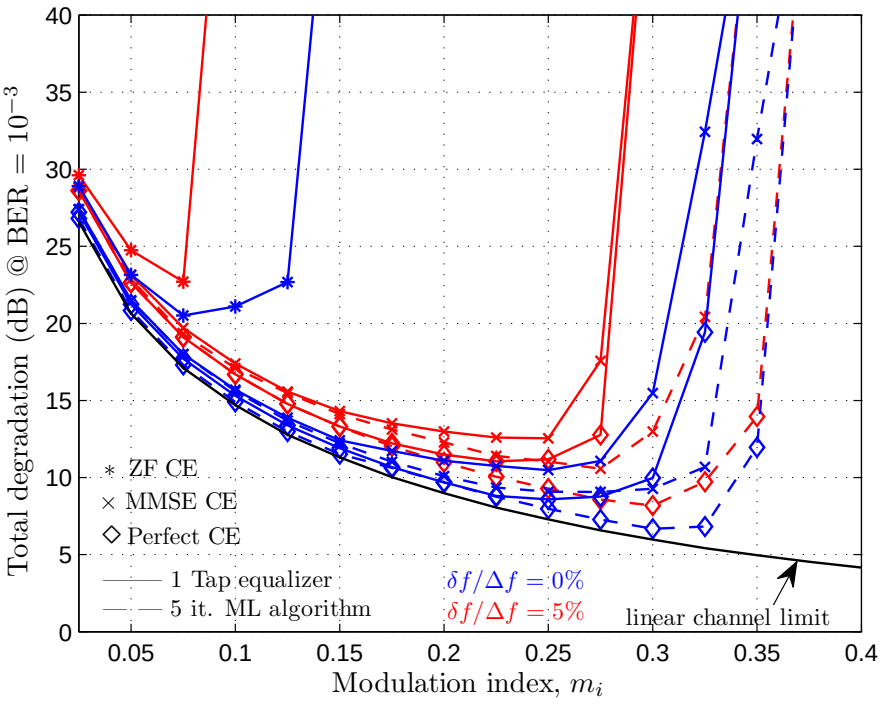

FIGURE 7.20: Total degradation as a function of the modulation index considering the ZF, MMSE and perfect channel estimations and both the one-tap equalizer and the 5 iterations ML algorithm for a target bit error rate of 10^{-3}. Results are plotted for normalized CFO values of 0% and 5%.

(TD) for the considered system in Figure 7.20 for a target bit error rate of 10^{-3}. Results for a normalized CFO of 5% between transciever and receiver are also considered. Moreover, we present results for ZF, MMSE and perfect channel estimators, as well as both one-tap and a five iterations ML algorithm equalizers. The "linear channel limit" plotted represents the theoretical BER limit considering a Rician distributed channel.

Results of TD show that for the target BER there is a considerable gain when using the MMSE estimator instead of a simple ZF. Yet, they do not match the perfect estimation curves. Let us first consider the 0% CFO case. Results show minimum TD values of 10.5 dB and 8.6 dB for the MMSE and perfect estimation followed by one-tap equalizer, respectively, and 9 dB and 6.7 dB when followed by the 5 iterations ML algorithm equalizer. In other words, the MMSE algorithm show degradation values relative to the perfect estimator of 1.9 dB and 2.3 dB for one-tap and iterative ML equalizers, respectively. The ZF estimator presents a minimum TD 11.5 dB higher than the MMSE estimator. With respect to the 5% normalized CFO case, the MMSE algorithm shows a degradation relative to the perfect estimation of 1.5 dB and 2.3 dB for one-tap and 5

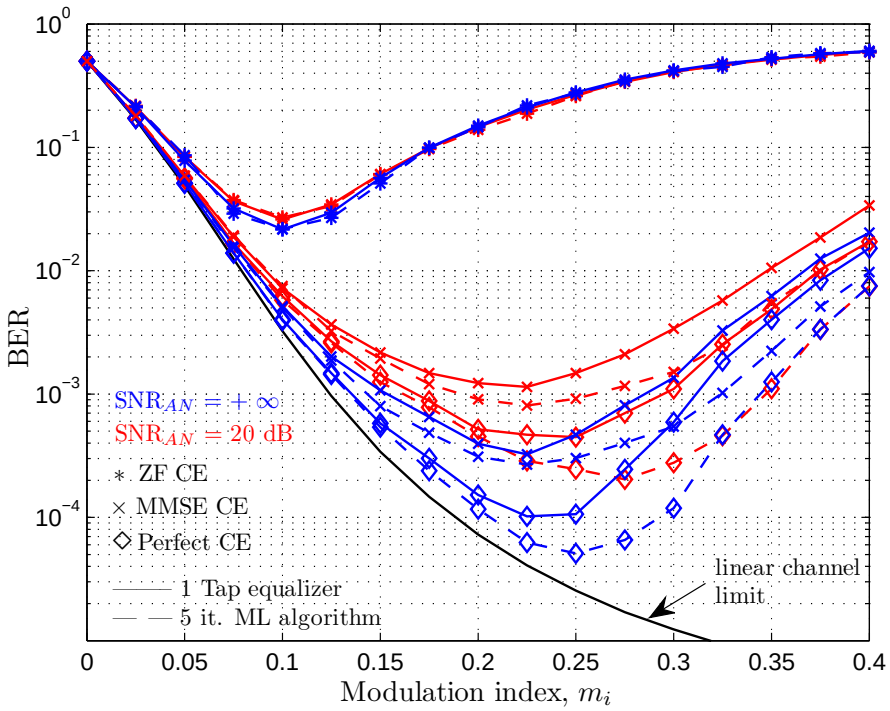

FIGURE 7.21: Bit error rate as a function of the modulation index considering the ZF, MMSE and perfect channel estimations and both the one-tap equalizer and the 5 iterations ML algorithm. Results for two SNR levels at the BS antenna, $\mathrm{SNR_{AN}} = +\infty$ and $\mathrm{SNR_{AN}} = 20\,\mathrm{dB}$.

iterations ML algorithm equalizers. These results sugggest a small relative improvement in terms of total degradation when using the MMSE channel estimator/one-tap equalizer in a CFO scenario. Moreover, the ZF estimator presents a minimum TD 12.2 dB higher than the MMSE estimator. This huge link gain margin obtained by using post compensation techniques allows us to increase the attenuation of the optical link up to 12 dB, which is equivalent to 30 km of optical fiber, and still obtain a TD value equal to the one when using a conventional receiver structure.

To perform a bit error rate analysis, we set the overall noise level at the photodiode to $3.5 \times 10^{-23}\,\mathrm{A^2/Hz}$ and the incident optical power at the input of the photodiode to $-19\,\mathrm{dBm}$. Figure 7.21 shows the bit error rate as function of the modulation index for both one-tap equalizer and a five iterations ML algorithm acting as equalizer as well for two $\mathrm{SNR_{AN}}$ levels at the BS antenna, $\mathrm{SNR_{AN}} = +\infty$ and $\mathrm{SNR_{AN}} = 20\,\mathrm{dB}$. Moreover, results for the ZF, MMSE and perfect channel estimators are also depicted. From the observation of the Figure 7.21, it can be seen that a significant improvement is reported when using the MMSE channel estimator for both antenna noise levels. Furthermore,

a performance improvement is also obtained if a 5 iterations ML algorithm is used as equalizer, instead of the conventional one-tap. Regarding the non-ideal antenna case, the MMSE channel estimator is no longer optimum in the MSE sense. Nevertheless, it is still capable to process the distorted signal.

7.5.2 MB-OFDM ECMA-368 over fiber

In this section, we present simulation results for the system depicted in Figure 7.10 for OFDM/QPSK signals based on the ECMA-368 standard [1].

According to Federal Communications Commission (FCC), an UWB signal is defined as an RF modulated signal that occupies a fractional bandwidth larger than 500 MHz or greater than 20% of the center frequency. Despite UWB being commonly referred as a new and trendy wireless technology, its origins can be traced back to the 1960s [184]. As many other innovating technologies, it has its roots in labs, but rapidly its potential was recognized and applied in military applications such as radar, localization and military communication. In the year of 2002, FCC released a report and authorized the use of UWB signals transmission in the range of 3.1 GHz to 10.6 GHz for unlicensed use [185]. This UWB spectrum allocation led to a revived interest research activities and the opportunity for companies to explore and develop broadband indoor and outdoor market applications. UWB signals are characterized by their huge bandwidth occupancy, high data rates, and very weak power density (-41.3 dBm/MHz), which gives them a noise-like signal characteristic, facilitating both interference mitigation and very low device power consumption. On the other hand, its very low intensity and high data rates limit the coverage to a few meters distance. However, by using radio-over-fiber networks as a transparent signal transportation technique, it is possible to perform a range extension of the wireless transmission and to deliver UWB signals over optical based networks such as in-building.

The MB-OFDM UWB ECMA-368 standard is based on the initial proposal by Batra *et al.* [61, 62] and defines both the physical (PHY) and MAC interface. Here we will concentrate only on the PHY layer of the standard. The standard specifies data rates that range from 53.3 Mb/s up to 480 Mb/s. The spectrum is divided in 14 bands each

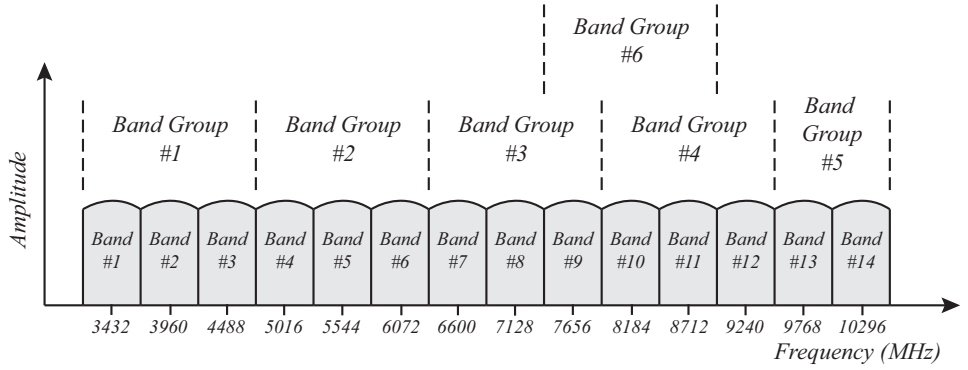

FIGURE 7.22: ECMA-368 spectrum division.

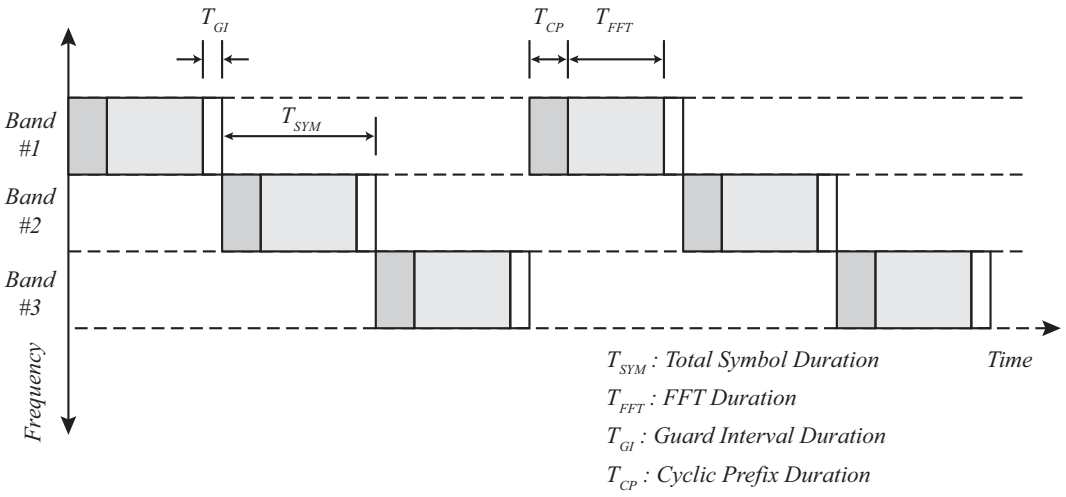

FIGURE 7.23: Example of a TF coding using the first three bands.

with 528 MHz of bandwidth, grouped in 5 band groups as it is shown in Figure 7.22. A sixth band group is also considered due to spectrum regulations in some countries.

As depicted in 7.22, the UWB spectrum is divided em several bands. The ECMA-368 standard defines up to ten different logical channels for each band group. Each logical channel is ruled by a unique time-frequency code (TFC). In Figure 7.23 an example of a TFC for the band group #1 is illustrated. Additionally, Table 7.2 summarizes all ten TFCs for band group #1.

Each OFDM subcarrier may convey symbols from a QPSK constellation or using a dual carrier modulation (DCM) scheme, depending on the data rate considered. The parameters of the MB-OFDM UWB signal considered for simulations are summarized in Table 7.3. The signal is considered to be in band #1, with a carrier frequency of 3.432 GHz (TFC 5). Each OFDM symbol conveys QPSK symbols and is created using a IFFT/FFT algorithm with 128 points and a period of 242.42 ns. The total number of

Table 7.2: MB-OFDM UWB TFCs for Band Group #1

TFC Number	Band Number					
1	1	2	3	1	2	3
2	1	3	2	1	3	1
3	1	1	2	2	3	3
4	1	1	3	3	2	2
5	1	1	1	1	1	1
6	2	2	2	2	2	2
7	3	3	3	3	3	3
8	1	2	1	2	1	2
9	1	3	1	3	1	3
10	2	3	2	3	2	3

subcarriers used is 122 from which 100 are for data, 12 for pilots and 10 act as guard subcarriers. The remaining six are null-valued pilots, one located at the center (DC term) and five at the edges. A cyclic prefix of 60.61 ns is appended at the beginning of the symbol (1/4 of the FFT period) and a zero-valued guard interval of 9.47 ns, at the end, reaching a total OFDM symbol time of 312.5 ns. From the parameters given by Table 7.3, we obtain a raw data rate, considering only data subcarriers, of 825 Mb/s. The pilot subcarriers are used to allow coherent detection, to help synchronization and to provide robustness against CFO and phase noise, while guard subcarriers are inserted for ISI mitigation. Null-tones are inserted to provide control over the use of the spectrum. The mapping of the subcarriers within an OFDM symbol is defined in Figure 7.24.

In a similar away to the IEEE802.11 standard, the ECMA-368 also defines a PLCP composed by the same three parts to operate the PHY with the MAC service. A diagram of the structure of the standard PPDU frame structure is depicted in Figure 7.25. Here, the standard PLCP preamble is composed by 24 OFDM symbols for packet/frame synchronization and 6 OFDM symbols for channel estimation, while the PSDU has a variable length and contains the data payload. The complete frequency-domain channel estimation sequence defined by the standard is given by Table B.2.

The standard may also define frequency domain spreading (FDS), time domain spreading (TDS), forward error correction (FEC) coding and scramblers to vary the

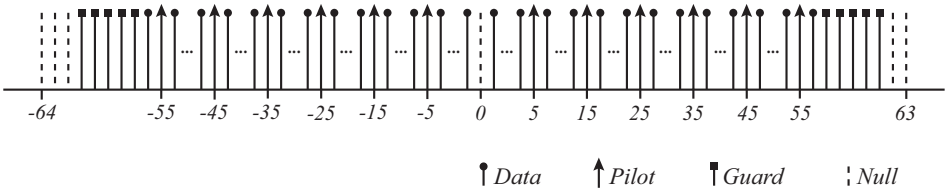

FIGURE 7.24: Mapping of the different types of subcarriers to logical frequencies.

TABLE 7.3: ECMA-368 simulation related parameters

Parameter	Value
Maximum transmitted power density	$-41.3\,\mathrm{dBm/MHz}$
Modulation	QPSK
Carrier frequency (f_c)	3.432 GHz (band #1)
Channel bandwidth (B)	528 MHz
Total number of subcarriers (N_{FFT})	128
Number of data subcarriers (N_D)	100
Number of defined pilot subcarriers (N_P)	12
Number of guard subcarriers (N_G)	10
Number of total subcarriers used (N_T)	122 ($N_D + N_P + N_G$)
Subcarrier frequency spacing (Δf)	4.125 MHz (B/N_{FFT})
IFFT/FFT period (T_{FFT})	242.42 ns ($1/\Delta f$)
Cyclic prefix duration (T_{CP})	60.61 ns ($T_{FFT}/4$)
Guard interval duration (T_{GI})	9.47 ns ($5/B$)
Total symbol duration (T_{SYM})	312.5 ns ($T_{CP} + T_{FFT} + T_{GI}$)

data rates and to improve robustness to link impairments. Yet, these techniques are not considered in our simulations since we focus on the receiver performance of raw data.

7.5.2.1 Non-fading channel

In this section, we will now present several simulation results for uplink radio-over-fiber system depicted in Figure 7.10 for an OFDM signal based on the ECMA-368 standard. Again, we consider first a non-fading channel introducing only an attenuation of L_{WC} and a non-dispersive optical fiber with attenuation L_{OF}. The responsivity of the photodiode is set to $\mathcal{R} = 1\,\mathrm{A/W}$.

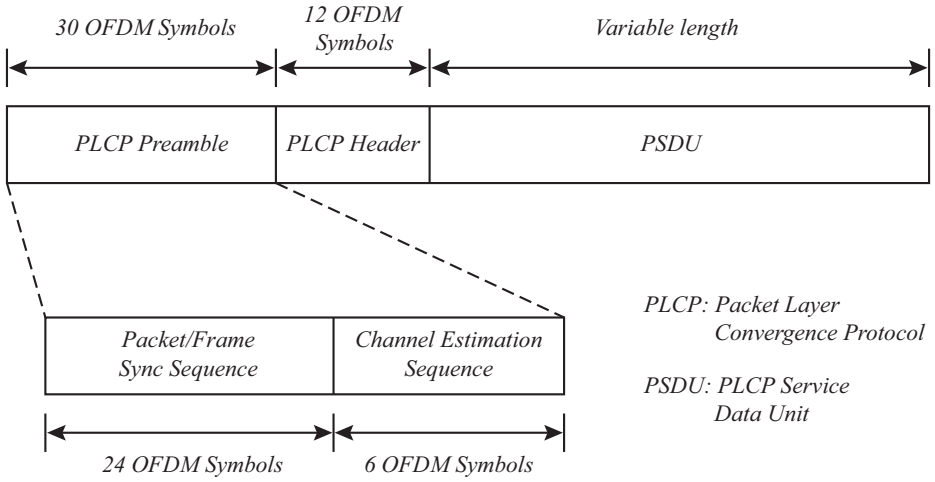

FIGURE 7.25: ECMA-368 PLCP packet data unit structure.

The characteristics used for the OFDM signal are summarized in Table 7.3 and the mapping of the different types of subcarriers are given in Figure 7.24.

Figure 7.26 plots the total degradation as a function of the modulation index for a target bit error rate of 10^{-3}. Additionally, results for a normalized CFO of 10% are also presented. The performance difference between curves for both CFO cases is approximately 1.5 dB. From the observation of the results, it can be seen that for 0% CFO, the total degradation minimum ranges from 4.6 dB to 2.6 dB for the conventional and five iterations of the ML algorithm, respectively, which corresponds to a decrease of 2 dB. This link gain margin obtained by using post compensation techniques allows us to increase the attenuation of the optical link up to 2 dB, which is equivalent to 5 km of optical fiber, and obtain a TD value equal to the one when using a conventional receiver. For the 10% normalized CFO the minimum TD ranges from 6.6 dB to 4 dB which represents a decrease of 2.6 dB. Thus, a degradation difference of 0.6 dB is reported between both CFO cases.

To perform a bit error rate analysis, the mean incident optical power at the input of the photodiode[7] is now set to -22 dBm and the overall noise PSD at the photodiode to $3.5 \times 10^{-23}\,\mathrm{A}^2/\mathrm{Hz}$.

Figure 7.27 shows the bit error rate behavior as a function of the modulation index for two SNR levels at the BS antenna. Note again that the overall noise is composed by

[7]Again, to avoid very low bit error rates that would take too much time to simulate, a relatively low incident optical power at the input of the photodiode is considered. A different approach would be to consider higher optical powers and additional noise terms or higher RIN levels.

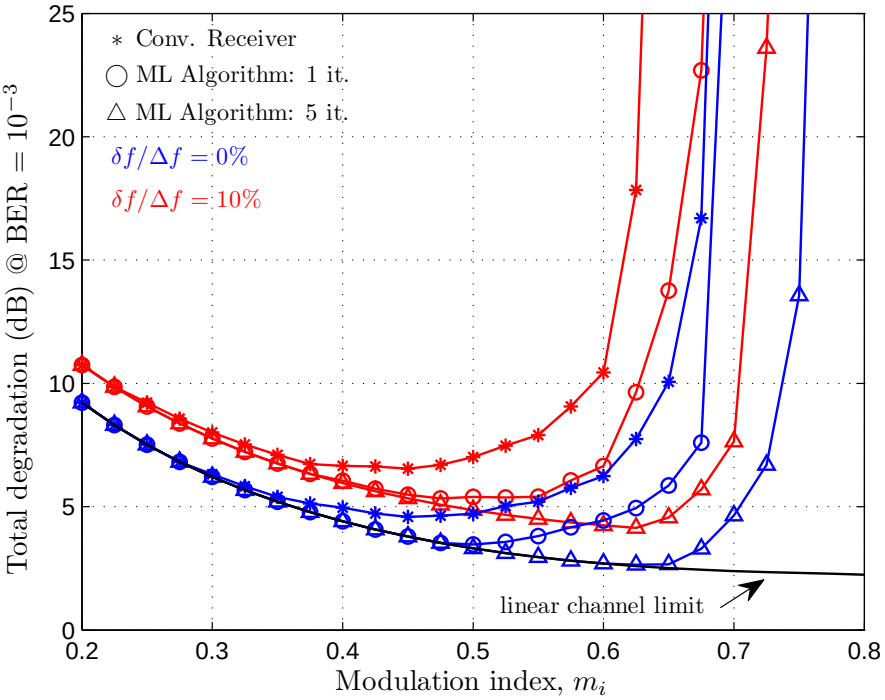

FIGURE 7.26: Total degradation as a function of the modulation index considering both the conventional receiver and ML algorithm with 1 and 5 iterations for a target bit error rate of 10^{-3}. Results are plotted for normalized CFO values of 0% and 10%.

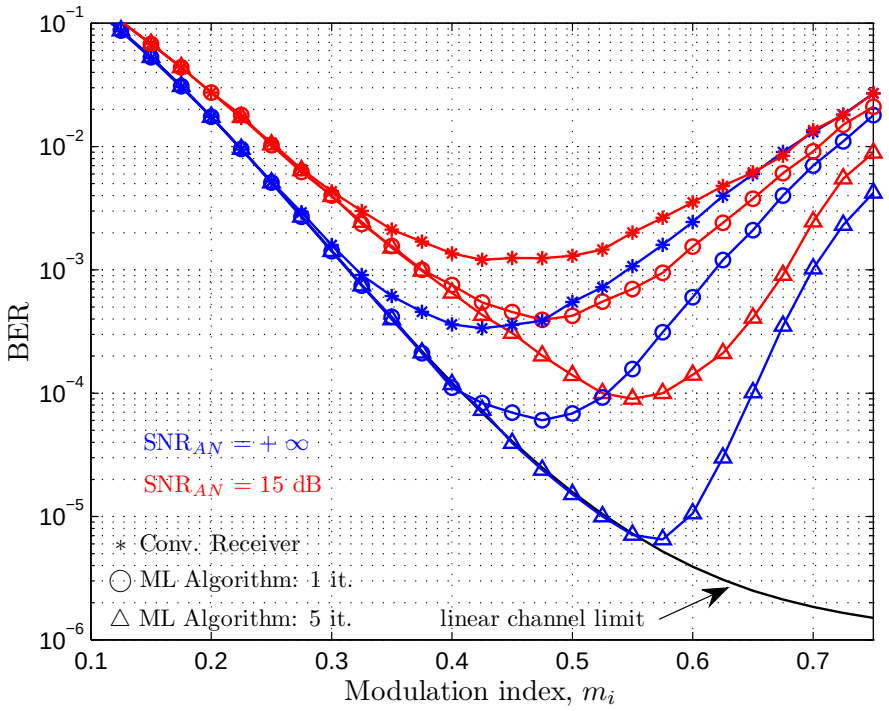

FIGURE 7.27: Bit error rate as a function of the modulation index considering both the conventional receiver and ML algorithm with 1 and 5 iterations. Results for two SNR levels at the BS antenna, $\mathrm{SNR}_{\mathrm{AN}} = +\infty$ and $\mathrm{SNR}_{\mathrm{AN}} = 15\,\mathrm{dB}$.

both photodiode, antenna and the signal-noise beat from the IMD term and that the modulation index is obtained taking into account the antenna noise. Here we have also considered two thermal noise levels at the BS antenna, the ideal and the realistic with a noise power density of $-114\,\mathrm{dBm/MHz}$. Considering an acceptable $\mathrm{SNR_{AN}}$ of $15\,\mathrm{dB}$ at the antenna, a maximum transmission power of $-41.3\,\mathrm{dBm/MHz}$ (see Table 7.3) and an antenna gain $4\,\mathrm{dB}$, the FSPL in a non-fading channel equals $61.7\,\mathrm{dB}$. From (7.23), the maximum wireless link distance for an $\mathrm{SNR_{AN}} = 15\,\mathrm{dB}$ is approximately 9 meters.

Results for the ideal antenna case show a clear improvement in terms of bit error rate when the iterative ML algorithm is considered. In fact, gains in terms of minimum BER of 5.5 and 55 times are reported for the one and five iterations ML algorithms for the given noise power density. Furthermore, a maximum gain of 12 times is reported for an $\mathrm{SNR_{AN}} = 15\,\mathrm{dB}$ when the five iterations ML algorithm is considered. It is interesting to note that the iterative ML algorithm is still able to process the received signal corrupted by both nonlinear noise and signal-antenna noise beat terms and to produce a lower minimum BER result than the one given by the conventional receiver for the ideal antenna case.

Furthermore, we present in Figure 7.28 the bit error rate as a function of the number of iterations for the ML algorithm. Only a Hamming distance of one was considered due to very high time consuming simulations. Results for modulation index values of $m_i = 0.50$ and $m_i = 0.60$ are reported. From the observation of the Figure we can see that both AWGN limits are achieved after 5 and 9 iterations for the $m_i = 0.50$ and $m_i = 0.60$, respectively. These results also suggest that even lower total degradation values could be achieved if more iterations were considered.

7.5.2.2 Rician fading channel

In this section we consider transmission of OFDM signals based on the ECMA-368 parameters affected by a Rician fading channel before being nonlinearly distorted (see Figure 7.10). The UWB signals are in fact a different class of wireless signals. Their huge bandwidth can even be used to perform object measurements due to the fact that each object produces distinguishable signal reflections. In fact, it has been verified by indoor channel measurements that the received multipath delayed versions of the signal arrive

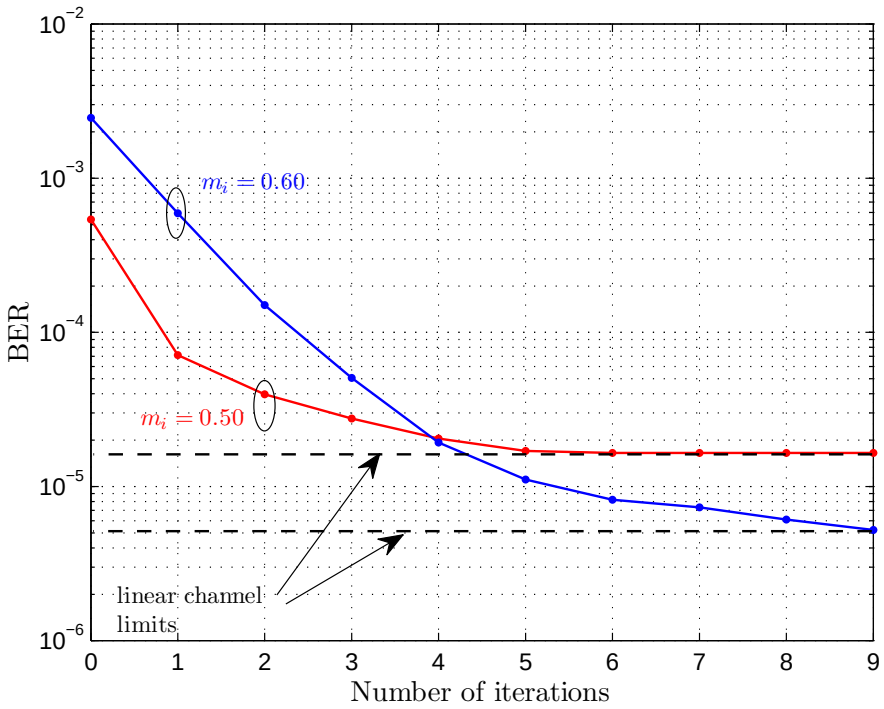

FIGURE 7.28: Bit error rate as a function of the number of iterations of the ML algorithm for a Hamming distance of one and considering two modulation index values $m_i = 0.50$ and $m_i = 0.60$.

in clusters, each with several rays as described by the Saleh-Valenzuela model [183]. Moreover, it has been found out that amplitudes of multipath fading follow Nakagami distribution rather than Rayleigh. Nevertheless, in our approach we do not consider that specific model. Instead, we consider that the room is sufficient large so the exponential model described previously is still valid. Here we consider that the channel is also given by a 6 tap TDL filter with the PDP profile given by Figure 7.19 and a RMS delay spread of 0.76 ns.

Simulation results were obtained for the system under consideration by implementing the same procedure as described in section 7.5.1.2. Here, the stage one responsible for the channel estimation is considered to be composed by six OFDM symbols (see Figure 7.25) and the mapping of the different types of subcarriers is given by Figure 7.24.

In Figure 7.29 it is depicted the total degradation for the considered system for a target bit error rate of 10^{-3}. Results for a normalized CFO of 10% between transmitter and receiver are also plotted. Moreover, we present results for ZF, MMSE and perfect channel estimators, as well as for both one-tap and a five iterations ML algorithm

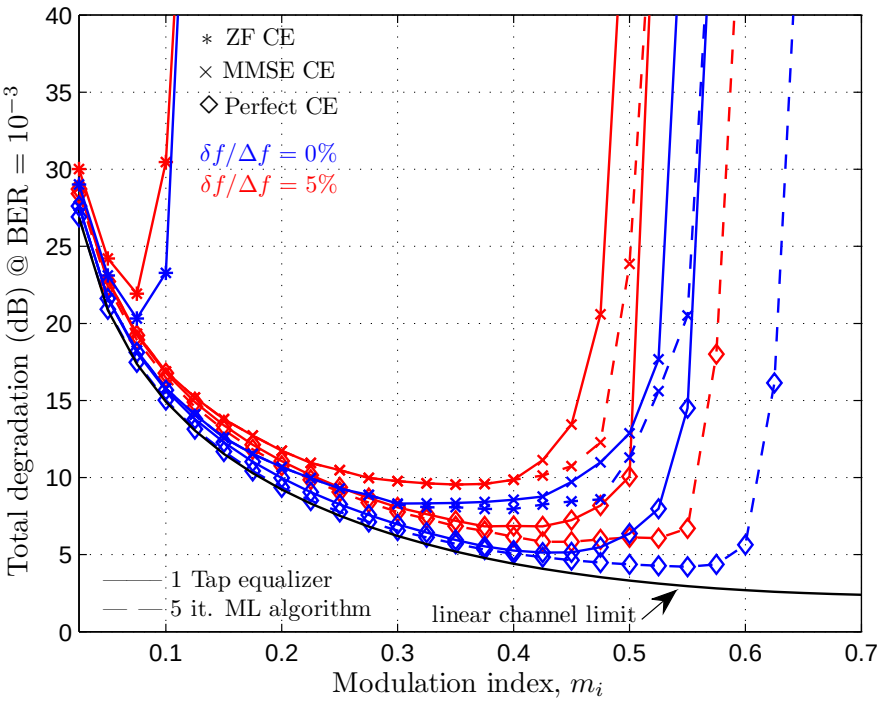

FIGURE 7.29: Total degradation as a function of the modulation index considering the ZF, MMSE and perfect channel estimations and both the one-tap equalizer and the 5 iterations ML algorithm for a target bit error rate of 10^{-3}. Results for normalized CFO values of 0% and 10%.

equalizers.

Similarly to what was observed in section 7.5.1.2 for the IEEE802.11g/n based OFDM signals, results of TD show that for the target BER there is a considerable gain when using the MMSE algorithm instead of a simple ZF. Let us first consider the 0% CFO case. Results show minimum TD values of 8.3 dB and 5.2 dB for the MMSE and perfect estimation followed by one-tap equalizer, respectively, and 7.9 dB and 4.2 dB when followed by the 5 iterations ML algorithm equalizer. In other words, the MMSE algorithm shows degradation values relative to the perfect estimator of approximately 2.9 dB and 3.7 dB for one-tap and ML equalizers, respectively. The ZF estimator presents a minimum TD of 12.4 dB higher than the MMSE estimator. This link gain margin obtained by using the MMSE channel estimator allows us to increase the attenuation of the optical link up to 12.4 dB, which is equivalent to 31 km of optical fiber, and obtain a TD value equal to the one when using the ZF estimator.

With respect to the 10% normalized CFO case, the MMSE algorithm shows degradation values relative to the perfect estimation of approximately 2.7 dB and 3.7 dB for

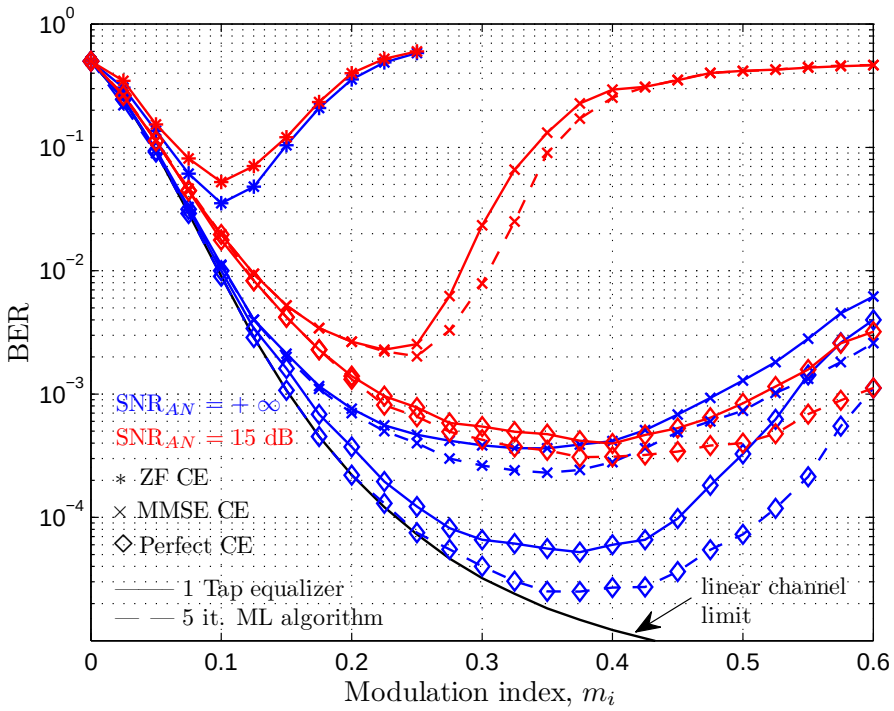

FIGURE 7.30: Bit error rate as a function of the modulation index considering the ZF, MMSE and perfect channel estimations and both the one-tap equalizer and the 5 iterations ML algorithm. Results for two SNR levels at the BS antenna, $\mathrm{SNR_{AN}} = +\infty$ and $\mathrm{SNR_{AN}} = 15\,\mathrm{dB}$.

one-tap and 5 iterations ML algorithm equalizers. The ZF estimator presents a minimum TD of 12.4 dB higher than the MMSE estimator.

To perform a bit error rate analysis, we set the overall noise level at the photodiode to $3.5 \times 10^{-23}\,\mathrm{A^2/Hz}$ and the incident optical power at the input of the photodiode to $-5\,\mathrm{dBm}$. Figure 7.30 shows the bit error rate as function of the modulation index for both one-tap equalizer and a five iterations ML algorithm acting as equalizer for two levels of $\mathrm{SNR_{AN}}$ at the BS antenna, $\mathrm{SNR_{AN}} = +\infty$ and $\mathrm{SNR_{AN}} = 15\,\mathrm{dB}$. Moreover, results for the ZF, MMSE and perfect channel estimators are also depicted. It can be seen that the MMSE channel estimator outperforms the ZF. Furthermore, results also show an improvement when using the five iterations ML algorithm for both MMSE and perfect estimators. Regarding the results for $\mathrm{SNR_{AN}} = 15\,\mathrm{dB}$, the MMSE estimator behavior presents a visible degradation for high modulation index values. Nevertheless, it is still able to process the distorted signal.

7.6 Summary

In this chapter we have considered the application of the techniques proposed and developed in the previous chapters in a specific scenario: IM/DD externally modulated uplink radio-over-fiber system. We have considered a MZM as the electro-optic converter device since it exhibits a frequency independent nonlinear behavior and it is widely used in RoF systems.

First, we have introduced the state-of-art wireless standards, giving an overview of current and future trends of wireless signals in consumers. In particular, the unlicensed band at the 60 GHz frequency region is being considered as the only possible frequency band capable to accommodate multi-Gigabit signals such as uncompressed full HD signals. Then, the radio-over-fiber concept was addressed along with an overview on technologies, architectures and known issues. Subsequently, the IM/DD case study was presented and mathematically derived. Here we have derived the equivalent low pass representation for an IM/DD based on a dual-electrode MZM. Moreover, the main noise contributions in these systems were identified. Finally, we have presented simulation results for specific transmissions of OFDM signals based on both IEEE802.11g/n and UWB ECMA-368 standards.

From an overall point of view, results suggest that both the optimum OFDM receiver and the MMSE channel estimator structures can be used to relax the linearity requirements of optical components in the uplink of RoF based wireless networks. Furthermore, they can also be combined simultaneously with added benefit. Note that the uplink scenario is of particular importance due to the effects of the radio environment on the OFDM signal, namely frequency selective fading.

Results from both signals over non-fading channels show that the ML algorithm provides significant improvement when an uplink antenna noise is considered. In this case, the noise levels considered in both cases were close to the maximum allowed by standards in order to have an acceptable SNR for reliable transmissions. We have also analyzed its robustness to CFO and concluded that it does not significantly affects its performance. Moreover, results have shown that the minimum total degradation can be reduced by up to 3 dB for a BER target of 10^{-3}, which corresponds to the attenuation of 8 km of optical fiber. Nevertheless, if a BER target of 10^{-4} and/or a higher number

of iterations of the ML algorithm were considered, then a higher link gain margin would be expected.

Regarding the Rician fading channel results, we can conclude that the proposed MMSE estimator can be used to estimate, in terms of linear MSE, the frequency response of the multipath channel. Results for non-zero antenna noise level also suggest that the estimator is still capable to process the distorted signal and to take advantage of the correlation between subcarriers. Additionally, the joint channel and CFO MMSE estimator have also shown slight improvements for both OFDM signals transmissions. Furthermore, the iterative ML algorithm has shown to improve the performance of both MMSE and perfect estimators. However, the improvement is more clear when it is followed by a perfect estimation of the channel. Results of minimum total degradation levels at a BER of 10^{-3} indicate that with the proposed algorithms it is possible to add up to 31 km of optical fiber and still obtain the same TD as the conventional structures.

In conclusion, this case study shows that it is possible to process the distorted OFDM received signal in order to improve performance without using pre-distortion techniques which can reduce the complexity of the wireless devices. Additionally, results show that by using the proposed post compensation techniques, it is possible to relax the noise requirements of the receiver or, similarly, they allow a higher attenuation of the optical link equivalent to several kilometers in order to obtain the same degradation as the conventional structures. On the other hand, for a given receiver's noise level and by post compensate the signal, a decrease of the raw data BER in several orders of magnitude was reported. This allows both an increase of the useful data rate and a higher dynamic range of the signal. The proposed channel estimators and receivers are therefore suitable for improving the performance of the uplink of fiber supported wireless systems.

Chapter 8

Concluding remarks

The main goal of this work is the study and development of receiver structures suitable for radio-over-fiber uplink systems transporting OFDM signals. In particular, the development of post-compensation techniques capable to process nonlinearly distorted and faded OFDM signals and the study of the impact of those impairments in the received constellation. Both the estimation of the frequency response of the multipath channel and the estimation of the transmitted complex symbols are topics addressed in this work.

An overview of the OFDM and its main system blocks were reviewed in chapter 2. Moreover, an introduction to both nonlinear distortion and time/frequency synchronization errors that so severely affect OFDM signals were also addressed.

The structure of the optimum receiver in terms of error probability for nonlinearly distorted OFDM signals corrupted by AWGN was presented in chapter 3. This receiver is obtained by maximizing the ML function of received OFDM symbols. The structure is composed by two parts: a sufficient statistics extractor followed by a maximum likelihood sequence estimator (MLSE). The first part is given by a set of correlators matched to every possible frequency components of the received signal. For an OFDM signal with N subcarriers and a nonlinearity of maximum order L, the received OFDM signal is spread over $1 + L(N - 1)$ frequency components. The second part is responsible for the computation of the M^N euclidean distances between the sufficient statistics and all possible combinations of transmitted vectors. To alleviate the complexity associated with the true ML detection, an iterative algorithm is also discussed. The iteration 'zero' is considered to be given by a conventional received composed by N matched correlators,

while the subsequent optimum estimations of the transmitted vector are obtained by searching for the one whose sufficient statistics are responsible for the maximization of the likelihood function. The size of the search region is user defined and can range from a Hamming distance of one up to M^N, which corresponds to the true ML. Moreover, it is not guaranteed that the iterative ML algorithm converges to the optimum solution and a sub-optimum result is more likely.

An optimum structure in terms of MSE for nonlinearly distorted OFDM signals in the presence of AWGN was proposed in chapter 4. The estimates of the transmitted complex symbols in subcarrier n are considered to be given by the sampled output of the linear filter $u_n(t)$. The impulse responses of the set of N filters were analytically derived and was found that the MMSE receiver can also be given by a conventional receiver capable to extract a set of sufficient statistics followed by a linear transformation of size $[1 + L(N-1)] \times [N]$. The expressions that give the optimum linear transformation were also analytically derived and computed for M-PSK and 16-QAM modulation schemes. Yet, they can also be extended to generic M-QAM schemes. An iterative algorithm based on LMS was also proposed to adjust the coefficient values and to be able to track channel fluctuations. The MMSE receiver takes advantage of the IMD term of the received OFDM signal and explores the correlation between symbols conveyed in different subcarriers. Moreover, it can be said that after the computation of the expected values, its usage and implementation are simple since it only adds a matrix product operation to a sufficient statistics extractor. Results presented in chapter 4 show that a minimization of the MSE is obtained, specially when a relatively low number of subcarriers is considered and also for low AWGN PSD levels.

We have started chapter 5 by evaluating both analytical and by means of simulation the impact of third order nonlinearities exhibiting both AM/AM and AM/PM on the received constellation, considering M-PSK and 16-QAM constellation schemes. Here we have considered that the OFDM signal is non-faded, i.e., it is considered that the multipath channel is given by a very strong LOS path. The impact of the compression gain, desensitization and IMD terms are evaluated in terms of mean and variance for every subchannel and conditioned to every possible constellation points of the considered schemes.

A comparative study of the performances of both iterative ML algorithm and MMSE receivers as well as the conventional receiver is also performed in chapter 5. Different iterative ML algorithm implementations considering various numbers of iterations and search region sizes were used. Results showed that its performance is highly dependent on the search region size and on the number of iterations. Several results for various OBO values and AWGN PSD level are presented for M-PSK and 16-QAM modulation schemes. Moreover, optimum operating points in terms of minimum total degradation for a target BER of 10^{-3} were obtained and a considerable gain in terms of minimum degradation was reported for the iterative ML algorithm.

The performance dependency of the iterative ML algorithm with the number of subcarriers used was also a subject of study. Results for the conventional receiver showed that for high E_b/N_0 values, a worst number of subcarriers between 12 and 24 does exist. This effect can be explained by the result of two effects: the increase of the variance of the IMD term and simultaneous decrease of the heaviness of the tails of its distribution, both with the increase of the number of subcarriers. Similar results for the iterative ML algorithm were also obtained, suggesting that its performance is highly dependent on iteration 'zero', which is given by the conventional receiver.

We have also studied the impact of both an additional AWGN source before the nonlinear channel and a CFO on the performance of both conventional and iterative ML algorithm. A statistical analysis of the additional noise term given by the beat between the OFDM and noise signals was conducted. From the analysis of both CDF and kurtosis/skewness coefficients we have concluded that this new term approaches well a Gaussian process for OBO values greater than 2.5 dB and also for OFDM signals with a large number of subcarriers. Results for bit error rate indicate that the iterative ML algorithm is still able to process the nonlinear noise. Also, results concerning the CFO show that, as expected, the performance of both conventional and iterative ML algorithm start to degrade with the CFO. In spite of that, the results for minimum total degradation considering the iterative ML algorithm in the presence of CFO indicate a performance improvement comparatively to the results given by the conventional receiver.

Finally, in chapter 5 we have also analyzed the performance of the proposed MMSE

receiver. Results showed that in fact it only produces acceptable BER improvements for OFDM/BPSK signals with a relatively low number of subcarriers. However, in these conditions, it largely outperforms the iterative ML algorithm with up to five iterations, suggesting that it can be used in specific applications with the cost of a simple linear transformation. Furthermore, results for the proposed MMSE/iterative ML algorithm showed that it outperforms the stand alone iterative algorithm. Interestingly, by using the MMSE structure for iteration 'zero', BER performance results showed that it combines the very good performance for low number of subcarriers of the MMSE receiver with the also good performance of the iterative ML algorithm for high number of subcarriers, i.e., its performance is given by a mixture of the best individual algorithm performances.

A channel estimation structure that minimizes the linear MSE for a system intended to describe an uplink radio transmission is proposed in chapter 6. The OFDM signal is considered to be faded and then nonlinearly distorted and finally corrupted by an AWGN source. We have analytically derived expressions for the optimum linear transformation for both Rayleigh and Rician distributed fading channels. Additionally, an extension of the structure to include compensation of carrier frequency and phase offsets was also developed. The performance of the MMSE estimator was compared with both conventional ZF and perfect channel estimators followed by both the one-tap equalizer and the iterative ML algorithm fed with the channel estimate. While the ZF estimator is severely affected by the nonlinear noise, specially for Rayleigh fading channels, the MMSE estimator showed to be robust and to present good performance. In fact, for Rician fading channels it almost equals the perfect estimation performance. Regarding the iterative ML algorithm, it was shown that it outperforms the one-tap equalizer and that in a perfect estimation scenario it was the best receiver configuration. Note that the true ML fed with perfect channel estimates would be the ultimate optimum receiver. Additionally, we have also proposed an extension to the estimator to accommodate carrier frequency and phase offsets without significant changes to the original structure. Despite the interesting results for the MMSE estimator, there is still a gap for the perfect estimator curves, indicating that channel estimation in uplink scenarios is undoubtedly a subject for further research.

A case study on RoF systems is presented in chapter 7. We have considered an uplink IM/DD RoF uplink system where the OFDM signal suffers from fading and attenuation from the multipath channel, nonlinear distortion from the MZM, Gaussian noise at both the uplink BS antenna and at the photodiode and CFO between transmitter and receiver. The techniques developed were applied to assess and improve the performance of RoF uplink systems. Results for specific OFDM transmissions based on both IEEE802.11g/n and UWB ECMA-368 standards were presented. It was shown that both the iterative ML algorithm and the MMSE channel estimator are suitable for both faded and non-faded OFDM transmissions and also to be quite robust to uplink antenna noise and CFO. Additionally, results show that their usage reduces significantly the minimum BER levels allowing standards to operate at higher useful data rates or to add several kilometers of optical fiber to the link and still maintain the same performance as the conventional structures.

In conclusion, this work has provided a further insight in the study of receiver design for nonlinearly distorted OFDM signals. In particular for uplink scenarios where both multipath and antenna noise are present and likely to degrade significantly the OFDM signal prior to the nonlinear channel. We have demonstrated that a simple linear transformation and an iterative ML algorithm can be used to relax the linearity requirements of the system without incurring significant complexity penalties for applications with OFDM signals. Furthermore, both the optimum ML, iterative OFDM receiver and the MMSE channel estimator structures were proven to be suitable to uplink systems and in particular to RoF systems based on MZMs without using pre-distortion techniques. This is important because it can reduce the complexity of the wireless devices and BS, leaving all the complex operations to the CS.

8.1 Recommendation for future work

Based on the presented work, several research directions for future work may be suggested. Amongst these, we highlight the following:

- Extension of the MMSE channel estimator to accommodate fast fading channel models and comb-type pilot arrangements. The MMSE channel estimator derived

is based on a block-type pilot arrangement and it was considered that the multipath channel is quasi-static, i.e., it remains unchanged over a block of OFDM symbols. However, in certain environments and/or applications this may not be guaranteed. Therefore, the introduction of fast fading channel models that also consider Doppler shifts and the spectral broadening caused by the movement and to derive an equivalent MMSE estimator that takes into account the time correlation between OFDM symbols are clearly subjects for further work in the context of chapter 6. Also, due to the IMD induced by the nonlinearity, the choice of the set of pilots and their frequency allocation may be crucial for the estimator performance and should be further investigated. Additionally, comb-type pilot arrangements and optimized interpolation techniques for channel estimation in nonlinearly distorted OFDM transmissions are also of great interest.

- Nonlinear MMSE (NL-MMSE) receiver and channel estimator structures for faded and nonlinearly distorted OFDM signals. Although the proposed linear MMSE channel estimator exhibits a good performance, there was still a performance gap for the results given by the perfect channel estimator. Thus, the development of a more robust and, in principle, efficient estimator based on NL-MMSE is also a topic for further study. Yet, a more complex structure is likely to be expected. Additionally, it would be also interesting to derive the NL-MMSE receiver structure for (non-faded) nonlinearly distorted OFDM signals.

- Investigation of synchronization techniques suitable for nonlinearly distorted and faded OFDM signals. The nonlinear distortion interacts with the faded OFDM in such way that both frequency and time synchronization techniques may be severely affected, specifically time synchronization data-aided techniques that use correlation operations to search for the start of the OFDM symbol. Thus, it is also an important topic to be considered in future work.

- Evaluation of the developed techniques in IM/DD radio-over-fiber systems based on electro-absorption modulators (EAM). The increase interest in colorless and/or passive BSs based on EAM transceivers indicate that it is an application of great interest. Moreover, since its transfer function can also be modeled as frequency

independent, all the techniques developed throughout this thesis can be applied with minor changes.

- Development of equivalent techniques for frequency dependent nonlinearities. Several nonlinear elements, including directly modulated LASERs, exhibit frequency dependent nonlinear behavior. Therefore, the development of optimum receivers and channel estimators considering those systems are also of extreme importance.

- Real-time and/or off-line implementation of the developed techniques and performance evaluation in an experimental radio-over-fiber uplink system testbed by integrating the software written during this work in C++ in a field-programmable gate array (FPGA) or equivalent dedicated hardware.

Appendix A

Signal statistical properties & representation

In this appendix we introduce some signal statistical properties of signals that are used through the thesis. Also, the heavily used complex envelope notation of signals is also addressed.

A.1 Stationary stochastic processes

Contrary to what happens in deterministic processes, in a random or stochastic process it is not possible to exactly know how the process might evolve in the future. In a random experiment where each outcome is associated with a sample point, the totality of samples points is called the sample space. The ensemble of all sample points defines a stochastic process. At any given time instant, the value of the outcome is a random variable. Thus, a stochastic process can also be viewed as a collection of random variables indexed by the parameter t. When the joint PDF of a stochastic process is invariant with time, it is said to be stationary [69, 71, 84].

Let us consider now a stochastic process $X(t)$ initiated at $t = -\infty$ and n random variables obtained from $X(t)$ at observation time instants $t_1, t_2, \cdots, t_n$ denoted by $\{X_{t_1}, X_{t_2}, \cdots, X_{t_n}\} = \{X(t_1), X(t_2), \cdots, X(t_n)\}$, respectively. The joint PDF that statistically characterizes this set is $p(x_{t_1}, x_{t_2}, \cdots, x_{t_n})$. Suppose now another set of n random variables $X_{t_1+\tau}, X_{t_2+\tau}, \cdots, X_{t_n+\tau}$ and their joint PDF $p(x_{t_1+\tau}, x_{t_2+\tau}, \cdots, x_{t_n+\tau})$.

The stochastic process $X(t)$ is said to be strictly stationary when the joint PDFs of both random variables X_{t_i} and $X_{t_i+\tau}$, $i = 1, 2, \cdots, n$ are identical, i.e., when

$$p(x_{t_1}, x_{t_2}, \cdots, x_{t_n}) = p(x_{t_1+\tau}, x_{t_2+\tau}, \cdots, x_{t_n+\tau}) \tag{A.1}$$

for all time shifts τ, all n and all observation time instants t_k. Stated in other way, the probabilistic properties of a stationary stochastic process do not change with time translations, thus processes $X(t)$ and $X(t+\tau)$ are identically distributed. On the other hand, if (A.1) is not satisfied, the stochastic process is said to be nonstationary.

By definition, the mean and autocorrelation function of a process $X(t)$ are the expectation of a random variable obtained at observation instant t_1 and the expectation of two random variables obtained at instants t_1 and t_2, respectively. Mathematically,

$$m_x(t_1) \triangleq \mathrm{E}[X_{t_1}] = \int_{-\infty}^{\infty} x_{t_1} p(x_{t_1}) dx_{t_1} \tag{A.2}$$

$$R_{xx}(t_1, t_2) \triangleq \mathrm{E}[X_{t_1} X_{t_2}] = \int_{-\infty}^{\infty} \int_{-\infty}^{\infty} x_{t_1} x_{t_2} p(x_{t_1}, x_{t_2}) dx_{t_1} dx_{t_2} \tag{A.3}$$

As it was previously stated, when a process is strictly stationary, the PDF is independent of time and, consequently, the mean of a strictly stationary process is constant, i.e.,

$$m_x(t) = m_x, \quad \forall t \tag{A.4}$$

In a similar way, from (A.1), the joint PDF of X_{t_1} and X_{t_2} is independent of time observations instants, thus the autocorrelation function only depends only on the difference $t_1 - t_2 = \tau$. Consequently, we can write

$$R_{xx}(t_1, t_2) = R_{xx}(t_1 - t_2) = R_{xx}(\tau) \tag{A.5}$$

The autocorrelation function has several important properties that can be easily proven from (A.2). We can highlight the following:

- The autocorrelation function of a stochastic process $X(t)$ is an even function, that is, $R_{xx}(\tau) = R_{xx}(-\tau)$.

- The average power of the stochastic process $X(t)$, i.e., the mean-square value of $X(t)$ is given by $R_{xx}(0) = \mathrm{E}[X_t^2]$.

- The Wiener-Khinchin theorem states that the power spectral density (PSD), which describes how the power of a signal is distributed with frequency, and the autocorrelation of the stochastic process $X(t)$ are related via the Fourier transform, i.e.,

$$R_{xx}(\tau) = \int_{-\infty}^{\infty} S_x(f) e^{j2\pi f\tau} df \tag{A.6}$$

$$S_x(f) = \int_{-\infty}^{\infty} R_{xx}(\tau) e^{-j2\pi f\tau} d\tau \tag{A.7}$$

Similarly, the covariance function of a strictly stationary stochastic process $X(t)$ is defined and given by

$$\begin{aligned} C_x(t_1, t_2) &\triangleq \mathrm{E}\{[X_{t_1} - m_x(t_1)][X_{t_2} - m_x(t_2)]\} \\ &= R_x(\tau) - m_x^2 \end{aligned} \tag{A.8}$$

Note that conditions (A.4) and (A.5) are not sufficient to define a process as strictly stationary. However, if a nonstationary process satisfies (A.4) and (A.5) it is said to be a wide-sense (WS) or weakly stationary process. From now on, when referring to a stationary stochastic process, the wide-sense condition is always implied.

A.2 Representation of signals and systems

In communications it is common to transmit digital information in a signal centered at a certain carrier f_c. A bandpass signal can be defined as one whose spectrum is confined to an interval of frequencies around the carrier frequency. In other words, the signal spectrum is contained in $f_c - B/2 < f < f_c + B/2$. In order to transmit bandpass signals, frequency translation operations both at the transmitter and receiver side must be performed to recover the signal. Since in signal processing it is necessary to sample and process these signals, it is of great interest to introduce a mathematical technique to analyze bandpass signals (and systems) as if they were lowpass. Moreover, the equivalent lowpass representation of bandpass signals and systems is independent

of carrier frequencies, providing an extra flexibility when studying the performance of these systems [71, 83].

In the following sections, the complex envelope notation will be presented.

A.2.1 Equivalent lowpass representation of bandpass signals

Consider now a real-valued bandpass signal $g(t)$ and its Fourier transform pair denoted by $G(f)$. Due to the Hermitian property of $G(f)$, it is sufficient to specify the Fourier transform of a real-valued signal only for non-negative frequency components and still be able to reconstruct $g(t)$. From a mathematical point of view, the positive frequency components of $G(f)$ can be represented by [69, 84]

$$G_+(f) = 2G(f)u(f) \tag{A.9}$$

where $u(f)$ is the Heaviside step function and a factor of 2 is considered in order to have the same energy.

By taking the inverse Fourier transform of $G_+(f)$, the equivalent time-domain expression can be given by

$$\begin{aligned} g_+(t) &= \mathcal{F}^{-1}[2u(f)] * \mathcal{F}^{-1}[G(f)] \\ &= \left[\delta(t) + \frac{j}{\pi t}\right] * g(t) \\ &= g(t) + j\hat{g}(t) \end{aligned} \tag{A.10}$$

where $\hat{g}(t)$ is the convolution of the signal $g(t)$ with the time function $h(t) = 1/(\pi t)$ and the operator $\mathcal{F}^{-1}$ represents the inverse Fourier transformation. On the other hand, the signal $\hat{g}(t)$ can also be seen as the *Hilbert transform* of signal $g(t)$ defined as

$$\hat{g}(t) = h(t) * g(t) \triangleq \frac{1}{\pi}\int_{-\infty}^{\infty} \frac{g(\tau)}{t-\tau} d\tau \tag{A.11}$$

The complex signal $g_+(t)$ is called the *analytic signal* of signal $g(t)$. Note that $g(t)$ can be obtained by taking the real part of $g_+(t)$.

The frequency response of the Hilbert transformer can be easily obtained by taking the Fourier transform of $h(t)$, hence,

$$\begin{aligned} H(f) &\triangleq \int_{-\infty}^{\infty} h(t)e^{-j2\pi ft} \\ &= \begin{cases} j, & f < 0 \\ 0, & f = 0 \\ -j, & f > 0 \end{cases} \end{aligned} \tag{A.12}$$

From (A.12) we observe that the Hilbert transformer has an unitary magnitude and a phase response that shifts negative frequency components of a signal by $\pi/2$ and positive frequency components by $-\pi/2$. As a consequence, we can emphasize the following properties:

- If $\hat{g}(t)$ is the Hilbert transform of $g(t)$, then the Hilbert transform of $\hat{g}(t)$ is $-g(t)$.
- The transform pair $g(t)$ and $\hat{g}(t)$ is orthogonal and has the same amplitude spectrum, i.e.,

$$\langle g(t), \hat{g}(t) \rangle = 0 \tag{A.13}$$

$$|G(f)| = |\hat{G}(f)| \tag{A.14}$$

  where $\langle \cdot, \cdot \rangle$ represents the inner product.

- A given signal $g(t)$ and its Hilbert transform have the same autocorrelation function and symmetric cross-correlation functions, i.e., respectively,

$$R_{gg}(t_1, t_2) = R_{\hat{g}\hat{g}}(t_1, t_2) \tag{A.15}$$

$$R_{g\hat{g}}(t_1, t_2) = -R_{\hat{g}g}(t_1, t_2) \tag{A.16}$$

Let us now consider a real and bandpass signal $g(t)$ centered at frequency f_c, with zero amplitude spectrum for $f < f_c - B/2$ and $f > f_c + B/2$ (as it is represented in Figure A.1(a)) and its associated analytic signal $g_+(t)$. An equivalent lowpass representation of $g(t)$ can be obtained by carrying out a frequency translation of f_c in respect to the

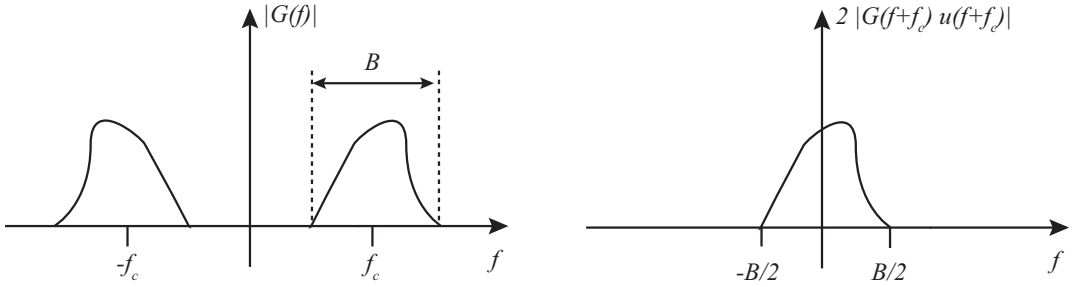

(a) Bandpass signal. (b) Lowpass equivalent signal.

FIGURE A.1: Amplitude spectrum representation of a real bandpass signal and its equivalent lowpass.

analytic signal, i.e., [69, 84]

$$\tilde{G}(f) = G_+(f + f_c) \tag{A.17}$$

$$\begin{aligned} \tilde{g}(t) &= g_+(t)e^{-j2\pi f_c t} \\ &= g_I(t) + jg_Q(t) \end{aligned} \tag{A.18}$$

where $\tilde{G}(f)$ and $\tilde{g}(t)$ are the frequency and time-domain representations, respectively, of the equivalent lowpass of $g(t)$. The signal $\tilde{g}(t)$ is usually called the *complex envelope* of the real bandpass signal $g(t)$ and can also be represented by its real and imaginary components, $g_I(t)$ and $g_Q(t)$. Using the relation between the analytic signal $g_+(t)$ and the bandpass signal $g(t)$ given by (A.10), we can write the real and imaginary parts of the complex envelope $\tilde{g}(t)$ as a function of the bandpass signal $g(t)$ as follows

$$g_I(t) = g(t)\cos(2\pi f_c t) + \hat{g}(t)\sin(2\pi f_c t) \tag{A.19}$$

$$g_Q(t) = -g(t)\sin(2\pi f_c t) + \hat{g}(t)\cos(2\pi f_c t) \tag{A.20}$$

In Figure A.1(b) it is depicted a representation of the spectrum of the complex envelope signal. As it can be seen, $\tilde{g}(t)$ is now centered at the origin and is band-limited to $f < B/2$ and $f > B/2$. Nonetheless, both signals $\tilde{g}(t)$ and $g(t)$ carry the same information.

Equation (A.10) shows that the bandpass signal $g(t)$ is given by taking the real part of the analytic signal $g_+(t)$. By considering the definition of complex envelope given by (A.18), the bandpass signal $g(t)$ can be rewritten in terms of its complex envelope as

the follows

$$\begin{aligned} g(t) &= \Re\left\{g_+(t)\right\} \\ &= \Re\left\{\tilde{g}(t)e^{j2\pi f_c t}\right\} \end{aligned} \tag{A.21}$$

We may therefore use (A.18) and (A.21) to obtain the often designated canonical form of $g(t)$ given by

$$\begin{aligned} g(t) &= \Re\left\{[g_I(t) + jg_Q(t)]e^{j2\pi f_c t}\right\} \\ &= g_I(t)\cos(2\pi f_c t) - g_Q(t)\sin(2\pi f_c t) \end{aligned} \tag{A.22}$$

which corresponds to the representation of $g(t)$ by means of two lowpass signals, namely the in-phase and quadrature components, $g_I(t)$ and $g_Q(t)$, respectively, which correspond to the real and imaginary parts of the complex envelope. Additionally, a vector representation of the bandpass signal $g(t)$ can also be derived by expressing $\tilde{g}(t)$ in a polar form as

$$\tilde{g}(t) = A_g(t)e^{j\theta_g(t)} \tag{A.23}$$

where $A_g(t)$ and $\theta_g(t)$ are both real-valued lowpass functions representing the envelope and phase of $g(t)$, respectively, and given by

$$A_g(t) = \sqrt{g_I^2(t) + g_Q^2(t)} \tag{A.24}$$

$$\theta_g(t) = \arctan\left[\frac{g_Q(t)}{g_I(t)}\right] \tag{A.25}$$

Thus, based on the polar form of the complex envelope of $g(t)$ given by (A.23) and the definition in (A.21), the bandpass signal $g(t)$ can also be defined by

$$g(t) = A_g(t)\cos\left(2\pi f_c t + \theta_g(t)\right) \tag{A.26}$$

Note that the envelope $A_g(t)$ is a real-valued lowpass signal that equals the magnitude of the complex envelope $\tilde{g}(t)$ and also the magnitude of the analytic signal $g_+(t)$. It is also important to note that both lowpass envelope signals $A_g(t)$ and $\tilde{g}(t)$ do not depend on the carrier frequency f_c, which gives them an analytic advantage over the bandpass signal $g(t)$.

Therefore, we can represent a real bandpass signal using two equivalent ways: a canonical form in terms of a in-phase and quadrature components, as it is defined in (A.22), or by its envelope and phase components, as in (A.26). From the analysis above we can also conclude that the complex envelope of a bandpass signal preserves all the information of a bandpass signal.

Let us now mathematically obtain the relationship between the spectrum and energy of $g(t)$ and $\tilde{g}(t)$. Using the following identity

$$\Re\{\xi\} = \frac{1}{2}\left(\xi + \xi^*\right) \tag{A.27}$$

we can rewrite (A.21) as

$$g(t) = \frac{1}{2}\left[\tilde{g}(t)e^{j2\pi f_c t} + \tilde{g}^*(t)e^{-j2\pi f_c t}\right] \tag{A.28}$$

Therefore, by applying the Fourier transform to (A.28) we get

$$G(f) = \frac{1}{2}\left[\tilde{G}(f - f_c) + \tilde{G}^*(-f - f_c)\right] \tag{A.29}$$

where $G(f)$ and $\tilde{G}(f)$ are the Fourier transforms of $g(t)$ and $\tilde{g}(t)$, respectively. From (A.29) we can see that the spectrum of the equivalent lowpass signal can be obtained by taking the positive frequencies part of the bandpass signal, shift it to the origin and scaling it by a factor of two [71].

The energy of a continuous time signal $g(t)$ is defined as the inner product with itself and is given by

$$\mathcal{E}_g \triangleq \langle g(t), g(t)\rangle = \int_{-\infty}^{\infty} |g(t)|^2 dt \tag{A.30}$$

Note that from the definition of energy, it can be seen that the energy of the sum of N orthogonal signals equals the sum of their energies [84]. Using a similar procedure as used to obtain the spectrum relationship between $g(t)$ and $\tilde{g}(t)$, we may use (A.27) and (A.21) and rewrite (A.30) as

$$\begin{aligned}\mathcal{E}_g &= \int_{\infty}^{\infty} \left|\frac{1}{2}\left[\tilde{g}(t)e^{j2\pi f_c t} + \tilde{g}^*(t)e^{-j2\pi f_c t}\right]\right|^2 dt \\ &= \frac{1}{2}\int_{\infty}^{\infty} |A_g(t)|^2\, dt + \frac{1}{2}\int_{-\infty}^{\infty} A_g(t)^2 \cos(2\pi(2f_c)t + 2\theta_g(t))dt\end{aligned} \tag{A.31}$$

Assuming that the signal bandwidth is much larger than the carrier frequency, the envelope $A_g(t)$ should change much slowly than the rapid variations of the cosine function, thus the second term of (A.31) will be much smaller than the first. Therefore,

$$\mathcal{E}_g = \frac{1}{2}\int_{\infty}^{\infty} |A_g(t)|^2 \, dt \tag{A.32}$$

A.2.2 Equivalent lowpass stationary stochastic processes representation

In Section A.2.1 we have presented a notation to represent a bandpass signal in terms of equivalent lowpass signals. We now consider a specific case where we have a real narrowband wide-sense stationary (WSS) stochastic (or random) process. Let $n(t)$ be a sample function of a WSS stochastic process with zero mean, band-limited and centered at a given frequency f_c. From (A.10) and (A.18), its associated analytic signal and complex envelope are given by, respectively,

$$n_+(t) = n(t) + j\hat{n}(t) \tag{A.33}$$

$$\tilde{n}(t) = n_+(t)e^{-j2\pi f_c t} \tag{A.34}$$

where $\hat{n}(t)$ is the Hilbert transform of $n(t)$. As it was previously described in Section A.2.1, we can represent $n(t)$ by the following equivalent forms

$$n(t) = \Re\left\{\tilde{n}(t)e^{j2\pi f_c t}\right\} \tag{A.35}$$

$$n(t) = n_I(t)\cos(2\pi f_c t) - n_Q(t)\sin(2\pi f_c t) \tag{A.36}$$

$$n(t) = A_n(t)\cos\left(2\pi f_c t + \theta_n(t)\right) \tag{A.37}$$

where $n_I(t)$ and $n_Q(t)$ are the in-phase and quadrature components of $n(t)$, respectively and $A_n(t)$ and $\theta_n(t)$ are the envelope and phase components of $n(t)$, respectively. Both in-phase and quadrature components are lowpass signals and are representative of the sample function $n(t)$.

We will now derive two important functions, namely the autocorrelation function and the power spectral density, of the equivalent lowpass signal relative to the bandpass signal.

From (A.5) and (A.35), the autocorrelation of the WSS random process $n(t)$ is given by

$$R_{nn}(\tau) = \mathrm{E}\left[n(t)n(t+\tau)\right] \tag{A.38}$$

$$= \frac{1}{2}\Re\left\{R_{\tilde{n}\tilde{n}}e^{j2\pi f_c\tau}\right\} \tag{A.39}$$

The PSD of the stochastic process $n(t)$ is given by the Fourier transform of the autocorrelation function, thus

$$S_n(f) = \frac{1}{4}\left[S_{\tilde{n}}(f-f_c) + S_{\tilde{n}}(-f-f_c)\right] \tag{A.40}$$

where $S_{\tilde{n}}(f)$ is the psd of the complex envelope $\tilde{n}(t)$. Thus, the last equality yields

$$S_{\tilde{n}}(f) = 4S_n(f+f_c)u(f+f_c) \tag{A.41}$$

where $u(f)$ is the Heaviside step function. Note that (A.41) can also be directly obtained from the definitions of the analytic signal and complex envelope spectra given by (A.9) and (A.17), respectively. In other words, the PSD of the complex envelope $\tilde{n}(t)$ can be evaluated as the PSD of the bandpass signal $n(t)$ times the squared magnitude of the transfer function $[2u(f)]$ and shifted by f_c.

A.2.2.1 Narrowband white noise representation

The special case of additive white noise is usually assumed to be a WSS Gaussian process with a PSD that is constant over the entire frequency range. Since such infinite-power signal has no physical meaning, and knowing that every signal contaminated by additive noise is bandpass filtered at the receiving terminal, we can assume that the noise has a finite bandwidth that is wider than the filter's bandwidth. Thus, a narrowband white noise can be defined as a real-valued Gaussian stationary process with zero-mean that passes through an ideal bandpass filter with a bandwidth B centered at f_c.

Appendix B

PLCP preamble channel estimation sequences

In this appendix, we list the PLCP preamble frequency-domain channel estimation sequences defined in the IEEE802.11g/n (Table B.1) and ECMA-368 (Table B.2) standards.

Table B.1: IEEE802.11g/n PCLP preamble frequency-domain channel estimation sequence

Logic Freq.	Value	Logic Freq.	Value	Logic Freq.	Value	Logic Freq.	Value
-32	0	-16	1	0	0	16	1
-31	0	-15	1	1	1	17	-1
-30	0	-14	1	2	-1	18	-1
-29	0	-13	1	3	-1	19	1
-28	0	-12	1	4	1	20	-1
-27	0	-11	-1	5	1	21	1
-26	1	-10	-1	6	-1	22	-1
-25	1	-9	1	7	1	23	1
-24	-1	-8	1	8	-1	24	1
-23	-1	-7	-1	9	1	25	1
-22	1	-6	1	10	-1	26	1
-21	1	-5	-1	11	-1	27	0
-20	-1	-4	1	12	-1	28	0
-19	1	-3	1	13	-1	29	0
-18	-1	-2	1	14	-1	30	0
-17	1	-1	1	15	1	31	0

Table B.2: ECMA-368 PLCP preamble frequency-domain channel estimation sequence

Logic Freq.	Value	Logic Freq.	Value	Logic Freq.	Value	Logic Freq.	Value
-61	$(-1+j)/\sqrt{2}$	-30	$(1-j)/\sqrt{2}$	1	$(1+j)/\sqrt{2}$	32	$(1+j)/\sqrt{2}$
-60	$(-1+j)/\sqrt{2}$	-29	$(-1+j)/\sqrt{2}$	2	$(1+j)/\sqrt{2}$	33	$(1+j)/\sqrt{2}$
-59	$(-1+j)/\sqrt{2}$	-28	$(-1+j)/\sqrt{2}$	3	$(-1-j)/\sqrt{2}$	34	$(-1-j)/\sqrt{2}$
-58	$(-1+j)/\sqrt{2}$	-27	$(1-j)/\sqrt{2}$	4	$(1+j)/\sqrt{2}$	35	$(-1-j)/\sqrt{2}$
-57	$(-1+j)/\sqrt{2}$	-26	$(1-j)/\sqrt{2}$	5	$(-1-j)/\sqrt{2}$	36	$(1+j)/\sqrt{2}$
-56	$(1-j)/\sqrt{2}$	-25	$(1-j)/\sqrt{2}$	6	$(-1-j)/\sqrt{2}$	37	$(-1-j)/\sqrt{2}$
-55	$(1-j)/\sqrt{2}$	-24	$(-1+j)/\sqrt{2}$	7	$(1+j)/\sqrt{2}$	38	$(1+j)/\sqrt{2}$
-54	$(-1+j)/\sqrt{2}$	-23	$(1-j)/\sqrt{2}$	8	$(-1-j)/\sqrt{2}$	39	$(1+j)/\sqrt{2}$
-53	$(1-j)/\sqrt{2}$	-22	$(1-j)/\sqrt{2}$	9	$(1+j)/\sqrt{2}$	40	$(1+j)/\sqrt{2}$
-52	$(1-j)/\sqrt{2}$	-21	$(1-j)/\sqrt{2}$	10	$(-1-j)/\sqrt{2}$	41	$(-1-j)/\sqrt{2}$
-51	$(1-j)/\sqrt{2}$	-20	$(-1+j)/\sqrt{2}$	11	$(1+j)/\sqrt{2}$	42	$(-1-j)/\sqrt{2}$
-50	$(1-j)/\sqrt{2}$	-19	$(1-j)/\sqrt{2}$	12	$(1+j)/\sqrt{2}$	43	$(1+j)/\sqrt{2}$
-49	$(1-j)/\sqrt{2}$	-18	$(-1+j)/\sqrt{2}$	13	$(-1-j)/\sqrt{2}$	44	$(1+j)/\sqrt{2}$
-48	$(-1+j)/\sqrt{2}$	-17	$(1-j)/\sqrt{2}$	14	$(-1-j)/\sqrt{2}$	45	$(-1-j)/\sqrt{2}$
-47	$(1-j)/\sqrt{2}$	-16	$(1-j)/\sqrt{2}$	15	$(-1-j)/\sqrt{2}$	46	$(-1-j)/\sqrt{2}$
-46	$(-1+j)/\sqrt{2}$	-15	$(-1+j)/\sqrt{2}$	16	$(1+j)/\sqrt{2}$	47	$(1+j)/\sqrt{2}$
-45	$(-1+j)/\sqrt{2}$	-14	$(-1+j)/\sqrt{2}$	17	$(1+j)/\sqrt{2}$	48	$(-1-j)/\sqrt{2}$
-44	$(1-j)/\sqrt{2}$	-13	$(-1+j)/\sqrt{2}$	18	$(-1-j)/\sqrt{2}$	49	$(1+j)/\sqrt{2}$
-43	$(1-j)/\sqrt{2}$	-12	$(1-j)/\sqrt{2}$	19	$(1+j)/\sqrt{2}$	50	$(1+j)/\sqrt{2}$
-42	$(-1+j)/\sqrt{2}$	-11	$(1-j)/\sqrt{2}$	20	$(-1-j)/\sqrt{2}$	51	$(1+j)/\sqrt{2}$
-41	$(-1+j)/\sqrt{2}$	-10	$(-1+j)/\sqrt{2}$	21	$(1+j)/\sqrt{2}$	52	$(1+j)/\sqrt{2}$
-40	$(1-j)/\sqrt{2}$	-9	$(1-j)/\sqrt{2}$	22	$(1+j)/\sqrt{2}$	53	$(1+j)/\sqrt{2}$
-39	$(1-j)/\sqrt{2}$	-8	$(-1+j)/\sqrt{2}$	23	$(1+j)/\sqrt{2}$	54	$(-1-j)/\sqrt{2}$
-38	$(1-j)/\sqrt{2}$	-7	$(1-j)/\sqrt{2}$	24	$(-1-j)/\sqrt{2}$	55	$(1+j)/\sqrt{2}$
-37	$(-1+j)/\sqrt{2}$	-6	$(-1+j)/\sqrt{2}$	25	$(1+j)/\sqrt{2}$	56	$(1+j)/\sqrt{2}$
-36	$(1-j)/\sqrt{2}$	-5	$(-1+j)/\sqrt{2}$	26	$(1+j)/\sqrt{2}$	57	$(-1-j)/\sqrt{2}$
-35	$(-1+j)/\sqrt{2}$	-4	$(1-j)/\sqrt{2}$	27	$(1+j)/\sqrt{2}$	58	$(-1-j)/\sqrt{2}$
-34	$(-1+j)/\sqrt{2}$	-3	$(-1+j)/\sqrt{2}$	28	$(-1-j)/\sqrt{2}$	59	$(-1-j)/\sqrt{2}$
-33	$(1-j)/\sqrt{2}$	-2	$(1-j)/\sqrt{2}$	29	$(-1-j)/\sqrt{2}$	60	$(-1-j)/\sqrt{2}$
-32	$(1-j)/\sqrt{2}$	-1	$(1-j)/\sqrt{2}$	30	$(1+j)/\sqrt{2}$	61	$(-1-j)/\sqrt{2}$
-31	$(1-j)/\sqrt{2}$	0	0	31	$(1+j)/\sqrt{2}$	62	0

Bibliography

[1] ECMA-368 Standard, "High rate ultra wideband PHY and MAC standard (3rd ed.)," December 2008.

[2] ETSI EN 300 744 Standard, "Digital video broadcasting (DVB): Framing structure, channel coding and modulation for digital terrestrial television (DVB-T)," Mar. 1997.

[3] ETSI EN 300 401 Standard, "Digital audio broadcasting (DAB): Digital audio broadcasting to mobile, portable and fixed receivers," Feb. 1995.

[4] IEEE 802.11a-1999 Standard, "Local and metropolitan area networks – Specific requirements – Part 11: Wireless LAN medium access control (MAC) and physical layer (PHY) specification – High-speed physical layer in the 5 GHz band," September 1999.

[5] IEEE 802.11g-2003 Standard, "Local and metropolitan area networks – Specific requirements – Part 11: Wireless LAN medium access control (MAC) and physical layer (PHY) specification – Amendment 4: Further high data rate extension in the 2.4 GHz band," June 2003.

[6] IEEE 802.11n-2009 Standard, "Local and metropolitan area networks – Specific requirements – Part 11: Wireless LAN medium access control (MAC) and physical layer (PHY) specification: Enhancements for higher throughput," October 2009.

[7] IEEE 802.16-2004 Standard, "Local and metropolitan area networks – Part 16: Air interface for fixed broadband wireless access systems," October 2004.

[8] IEEE 802.16e-2005 Standard, "Local and metropolitan area networks – Part 16: Air interface for fixed and mobile broadband wireless access systems – Amendment 2: Physical and medium access control layers for combined fixed and mobile operation in licensed bands and corrigendum 1," February 2006.

[9] IEEE 802.20-2008 Standard, "Local and metropolitan area networks – Part 20: Air interface for mobile broadband wireless access systems supporting vehicular mobility – Physical and media access control layer specification," August 2008.

[10] A. Langowski, "Time and Frequency Synchronisation in 4G OFDM Systems," *EURASIP Journal on Wireless Communications and Networking*, 2009.

[11] D. Astély, E. Dahlman, A. Furuskar, Y. Jading, M. Lindstrom, and S. Parkvall, "LTE: The evolution of mobile broadband," *IEEE Communications Magazine*, vol. 47, no. 4, pp. 44–51, 2009.

[12] E. Dahlman, *3G evolution: HSPA and LTE for mobile broadband.* Academic Press, 2007.

[13] G. Hiertz, D. Denteneer, L. Stibor, Y. Zang, X. Costa, and B. Walke, "The IEEE 802.11 universe," *Communications Magazine, IEEE*, vol. 48, no. 1, pp. 62–70, 2010.

[14] Z. Jia, J. Yu, and G. Chang, "A full-duplex radio-over-fiber system based on optical carrier suppression and reuse," *Photonics Technology Letters, IEEE*, vol. 18, no. 16, pp. 1726–1728, 2006.

[15] L. Chen, H. Wen, and S. Wen, "A radio-over-fiber system with a novel scheme for millimeter-wave generation and wavelength reuse for up-link connection," *Photonics Technology Letters, IEEE*, vol. 18, no. 19, pp. 2056–2058, 2006.

[16] M. Sauer, A. Kobyakov, and J. George, "Radio over fiber for picocellular network architectures," *IEEE Journal of Lightwave Technology*, vol. 25, no. 11, pp. 3301–3320, 2007.

[17] N. Pleros, K. Vyrsokinos, K. Tsagkaris, and N. Tselikas, "A 60 GHz radio-over-fiber network architecture for seamless communication with high mobility," *Journal of Lightwave Technology*, vol. 27, no. 12, pp. 1957–1967, 2009.

[18] J. Yao, "Microwave photonics," *IEEE Journal of Lightwave Technology*, vol. 27, no. 3, pp. 314–335, 2009.

[19] C. Lim, A. Nirmalathas, M. Bakaul, P. Gamage, K. Lee, Y. Yang, D. Novak, and R. Waterhouse, "Fiber-wireless networks and subsystem technologies," *Lightwave Technology, Journal of*, vol. 28, no. 4, pp. 390–405, 2010.

[20] N. Gomes, M. Morant, A. Alphones, B. Cabon, J. Mitchell, C. Lethien, M. Csörnyei, A. Stöhr, and S. Iezekiel, "Radio-over-fiber transport for the support of wireless broadband services [Invited]," *Journal of Optical Networking*, vol. 8, no. 2, pp. 156–178, 2009.

[21] A. Kim, Y. Joo, and Y. Kim, "60 GHz wireless communication systems with radio-over-fiber links for indoor wireless LANs," *IEEE Transactions on Consumer Electronics*, vol. 50, no. 2, pp. 517–520, 2004.

[22] A. Koonen, H. Yang, H.-D. Jung, M. Larrode, and E. Tangdiongga, "Radio-over-fiber techniques for advanced in-building networks," in *IEEE/LEOS Summer Topical Meeting*, pp. 39–40, July 2009.

[23] A. M. J. Koonen, M. G. Larrode, A. Ng'oma, K. Wang, H. Yang, Y. Zheng, and E. Tangdiongga, "Perspectives of radio over fiber technologies," *Proceedings of Conference on Optical Fiber communication/National Fiber Optic Engineers Conference*, pp. 1–3, Feb. 2008.

[24] Y. Le Guennec, A. Pizzinat, S. Meyer, B. Charbonnier, P. Lombard, M. Lourdiane, B. Cabon, C. Algani, A. Billabert, M. Terré, *et al.*, "Low-cost transparent radio-over-fiber system for in-building distribution of UWB signals," *IEEE Journal of Lightwave Technology*, vol. 27, pp. 2649–2657, 2009.

[25] C. Lethien, C. Loyez, and J. Vilcot, "Potentials of radio over multimode fiber systems for the in-buildings coverage of mobile and wireless LAN applications," *IEEE Photonics Technology Letters*, vol. 17, no. 12, pp. 2793–2795, 2005.

[26] A. Stöhr, A. Akrout, R. Buß, B. Charbonnier, F. van Dijk, A. Enard, S. Fedderwitz, D. Jäger, M. Huchard, F. Lecoche, *et al.*, "60 GHz radio-over-fiber technologies for broadband wireless services [Invited]," *Journal of Optical Networking*, vol. 8, no. 5, pp. 471–487, 2009.

[27] K. Kitayama, "Architectural considerations of fiber-radio millimeter-wave wireless access systems," *Fiber and Integrated Optics*, vol. 19, no. 2, pp. 167–186, 2000.

[28] A. Nirmalathas, C. Lim, D. Novak, and R. Waterhouse, "Progress in millimeter-wave fiber-radio access networks," *Annals of Telecommunications*, vol. 56, no. 1, pp. 27–38, 2001.

[29] P. Banelli and S. Cacopardi, "Theoretical analysis and performance of OFDM signals in nonlinear AWGN channels," *IEEE Transactions on Communications*, vol. 48, no. 3, pp. 430–441, 2000.

[30] P. Banelli, "Theoretical analysis and performance of OFDM signals in nonlinear fading channels," *IEEE Transactions on Wireless Communications*, vol. 2, no. 2, pp. 284–293, 2003.

[31] L. Rugini and P. Banelli, "BER of OFDM systems impaired by carrier frequency offset in multipath fading channels," *IEEE Transactions on Wireless Communications*, vol. 4, no. 5, pp. 2279–2288, 2005.

[32] D. Dardari, V. Tralli, and A. Vaccari, "A theoretical characterization of nonlinear distortion effects in OFDM systems," *IEEE Transactions on Communications*, vol. 48, no. 10, pp. 1755–1764, 2000.

[33] G. Santella and F. Mazzenga, "A model for performance evaluation in M-QAM-OFDM schemes in prescence of nonlinear distortions," in *IEEE 45th Vehicular Technology Conference*, vol. 2, pp. 830–834, IEEE, 1995.

[34] E. Costa and S. Pupolin, "M-QAM-OFDM system performance in the presence of a nonlinear amplifier and phase noise," *IEEE Transactions on Communications*, vol. 50, no. 3, pp. 462–472, 2002.

[35] S. Han and J. Lee, "An overview of peak-to-average power ratio reduction techniques for multicarrier transmission," *IEEE Wireless Communications*, vol. 12, no. 2, pp. 56–65, 2005.

[36] R. Baxley and G. Zhou, "Comparing selected mapping and partial transmit sequence for PAR reduction," *Broadcasting, IEEE Transactions on*, vol. 53, no. 4, pp. 797–803, 2007.

[37] J. Armstrong, "Peak-to-average power reduction for OFDM by repeated clipping and frequency domain filtering," *IEEE Electronics letters*, vol. 38, no. 5, pp. 246–247, 2002.

[38] X. Li and L. Cimini Jr, "Effects of clipping and filtering on the performance of OFDM," in *IEEE 47th Vehicular Technology Conference*, vol. 3, pp. 1634–1638, IEEE, 2002.

[39] S. Yoo, S. Yoon, S. Kim, and I. Song, "A novel PAPR reduction scheme for OFDM systems: selective mapping of partial tones (SMOPT)," *IEEE Transactions on Consumer Electronics*, vol. 52, no. 1, pp. 40–43, 2006.

[40] S. Heo, H. Noh, J. No, and D. Shin, "A modified SLM scheme with low complexity for PAPR reduction of OFDM systems," in *IEEE 18th International Symposium on Personal, Indoor and Mobile Radio Communications*, pp. 1–5, IEEE, 2007.

[41] M. Chandwani, A. Singhal, N. VishnuKanth, and V. Chakka, "A low complexity SLM technique for PAPR reduction in OFDM using Riemann sequence and thresholding of power amplifier," in *IEEE Annual India Conference*, pp. 1–4, IEEE, 2010.

[42] K. Yang and S. Chang, "Peak-to-average power control in OFDM using standard arrays of linear block codes," *IEEE Communications Letters*, vol. 7, no. 4, pp. 174–176, 2003.

[43] H. Chen and A. Haimovich, "Iterative estimation and cancellation of clipping noise for OFDM signals," *Communications Letters, IEEE*, vol. 7, no. 7, pp. 305–307, 2003.

[44] T. Jiang and Y. Wu, "An overview: Peak-to-average power ratio reduction techniques for OFDM signals," *IEEE Transactions on Broadcasting*, vol. 54, no. 2, pp. 257–268, 2008.

[45] R. Prasad, *OFDM for wireless communications systems.* Artech House Publishers, 2004.

[46] M. L. Doelz, E. T. Heald, and D. L. Martin, "Binary data transmission techniques for linear systems," *Proceedings of the IRE*, vol. 45, pp. 656–661, May 1957.

[47] R. Chang, "Synthesis of band-limited orthogonal signals for multichannel data transmission," *Bell System Technical Journal*, vol. 45, no. 10, pp. 1775–1796, 1966.

[48] B. Saltzberg, "Performance of an efficient parallel data transmission system," *IEEE Transactions on Communication Technology*, vol. 15, pp. 805–811, Dec. 1967.

[49] S. Weinstein and P. Ebert, "Data transmission by frequency-division multiplexing using the discrete Fourier transform," *IEEE Transactions on Communication Technology*, vol. 19, pp. 628–634, Oct. 1971.

[50] J. Cooley and W. Cochran, "What is the fast Fourier transform," *IEEE Transactions on Audio and Electroacoustics*, vol. 15, pp. 45–55, 1967.

[51] K. Sistanizadeh, P. Chow, and J. Cioffi, "Multi-tone transmission for asymmetric digital subscriber lines (ADSL)," *IEEE International Conference on Communications*, vol. 2, 1993.

[52] ITU-T G.992.1 Standard, "Series G: Transmission systems and media, digital systems and networks – Digital sections and digital line system – Access networks: Asymmetric digital subscriber line (ADSL) transceivers," July 1999.

[53] ITU-T G.992.3 Standard, "Series G: Transmission systems and media, digital systems and networks – Digital sections and digital line system – Access networks: Asymmetric digital subscriber line transceivers 2 (ADSL2)," 2005.

[54] ITU-T G.992.5 Standard, "Series G: Transmission systems and media, digital systems and networks – Digital sections and digital line system – Access networks:

Asymmetric digital subscriber line (ADSL) transceivers – Extended bandwidth ADSL2 (ADSL2plus)," 2005.

[55] J. Lechleider and M. Bellcore, "High bit rate digital subscriber lines: A review of HDSL progress," *IEEE Journal on Selected Areas in Communications*, vol. 9, no. 6, pp. 769–784, 1991.

[56] J. Werner, "The HDSL environment," *IEEE Journal on Selected Areas in Communications*, vol. 9, no. 6, pp. 785–800, 1991.

[57] J. Chow, J. Tu, and J. Cioffi, "A discrete multitone transceiver system for HDSL applications," *IEEE Journal on Selected Areas in Communications*, vol. 9, no. 6, pp. 895–908, 1991.

[58] P. Chow, J. Tu, and J. Cioffi, "Performance evaluation of a multichannel transceiver system for ADSL and VHDSL services," *IEEE Journal on Selected Areas in Communications*, vol. 9, no. 6, pp. 909–919, 1991.

[59] ITU-T G.993.1 Standard, "Series G: Transmission systems and media, digital systems and networks – Digital sections and digital line system – Access networks: Very high speed digital subscriber line transceivers," June 2004.

[60] ITU-T G.993.2 Standard, "Series G: Transmission systems and media, digital systems and networks – Digital sections and digital line system – Access networks: Very high speed digital subscriber line transceivers 2 (VDSL2)," February 2006.

[61] A. Batra, J. Balakrishnan, A. Dabak, *et al.*, "Multi-band OFDM physical layer proposal for IEEE 802.15 task group 3a," 2003.

[62] A. Batra, J. Balakrishnan, A. Dabak, *et al.*, "TI physical layer proposal for IEEE 802.15 task group 3a," 2003.

[63] J. Armstrong, "OFDM for optical communications," *IEEE Journal of Lightwave Technology*, vol. 27, no. 3, pp. 189–204, 2009.

[64] A. Lowery, L. Du, and J. Armstrong, "Performance of optical OFDM in ultralong-haul WDM lightwave systems," *IEEE Journal of Lightwave Technology*, vol. 25, no. 1, pp. 131–138, 2007.

[65] W. Shieh and I. Djordjevic, *OFDM for optical communications.* Academic Press, 2009.

[66] T. Kobayashi, A. Sano, E. Yamada, Y. Miyamoto, H. Takara, and A. Takada, "Electro-optically multiplexed 110 Gbit/s optical OFDM signal transmission over 80 km SMF without dispersion compensation," *IEEE Electronics Letters*, vol. 44, no. 3, pp. 225–226, 2008.

[67] S. Jansen, I. Morita, T. Schenk, and H. Tanaka, "121.9-Gb/s PDM-OFDM transmission with 2-b/s/Hz spectral efficiency over 1000 km of SSMF," *IEEE Journal of Lightwave Technology*, vol. 27, no. 3, pp. 177–188, 2009.

[68] H. Schulze and C. Luders, *Theory and applications of OFDM and CDMA: Wideband wireless communications.* Wiley, 2005.

[69] J. Proakis, *Digital communications.* McGraw-Hill New York, fourth edition ed., 2001.

[70] A. Peled and A. Ruiz, "Frequency domain data transmission using reduced computational complexity algorithms," vol. 5, 1980.

[71] S. Haykin, *Communication systems.* Wiley Publishing, 2009.

[72] J. Bussgang, L. Ehrman, and J. Graham, "Analysis of nonlinear systems with multiple inputs," *Proceedings of the IEEE*, vol. 62, no. 8, pp. 1088–1119, 1974.

[73] P. Moose, "A technique for orthogonal frequency division multiplexing frequency offset correction," *IEEE Transactions on Communications*, vol. 42, no. 10, pp. 2908–2914, 1994.

[74] T. Schmidl and D. Cox, "Robust frequency and timing synchronization for OFDM," *IEEE Transactions on Communications*, vol. 45, no. 12, pp. 1613–1621, 1997.

[75] J. van de Beek, M. Sandell, and P. Borjesson, "ML estimation of time and frequency offset in OFDM systems," *IEEE Transactions on Signal Processing*, vol. 45, no. 7, pp. 1800–1805, 1997.

[76] J. van de Beek, P. Borjesson, M. Boucheret, D. Landstrom, J. Arenas, P. Odling, C. Ostberg, M. Wahlqvist, and S. Wilson, "A time and frequency synchronization scheme for multiuser OFDM," *IEEE Journal on Selected Areas in Communications*, vol. 17, no. 11, pp. 1900–1914, 1999.

[77] Y. Yao and G. Giannakis, "Blind carrier frequency offset estimation in SISO, MIMO, and multiuser OFDM systems," *IEEE Transactions on Communications*, vol. 53, no. 1, pp. 173–183, 2005.

[78] H. Minn, V. Bhargava, and K. Letaief, "A robust timing and frequency synchronization for OFDM systems," *IEEE Transactions on Wireless Communications*, vol. 2, pp. 822–839, 2003.

[79] M. Sandell, J. van de Beek, and P. Börjesson, "Timing and frequency synchronization in OFDM systems using the cyclic prefix," *Proceedings of the IEEE International Symposium on Synchronization*, pp. 16–19, December 1995.

[80] P. Dharmawansa, N. Rajatheva, and H. Minn, "An exact error probability analysis of OFDM systems with frequency offset," *Communications, IEEE Transactions on*, vol. 57, no. 1, pp. 26–31, 2009.

[81] J. van de Beek, *Synchronization and channel estimation in OFDM systems.* PhD thesis, Luleå tekniska universitet, 1998.

[82] A. Bahai, B. Saltzberg, and M. Ergen, *Multi-carrier digital communications: theory and applications of OFDM.* Springer Verlag, 2004.

[83] M. Jeruchim, P. Balaban, and K. Shanmugan, *Simulation of communication systems: modeling, methodology, and techniques.* Springer Us, 2000.

[84] S. Benedetto and E. Biglieri, *Principles of digital transmission: with wireless applications.* Plenum Pub Corp, 1999.

[85] V. Meghdadi, J. Cances, F. Chevallier, B. Rojat, and J. Dumas, "Modeling of solid state power amplifiers (SSPA) and validation by means of a system simulator," *Annals of Telecommunications*, vol. 53, no. 1, pp. 4–14, 1998.

[86] G. Zhou, H. Qian, L. Ding, and R. Raich, "On the baseband representation of a bandpass nonlinearity," *IEEE Transactions on Signal Processing*, vol. 53, no. 8, pp. 2953–2957, 2005.

[87] R. Raich and G. Zhou, "On the modeling of memory nonlinear effects of power amplifiers for communication applications," in *Proceedings of 10th IEEE Digital Signal Processing Workshop and the 2nd Signal Processing Education Workshop*, pp. 7–10, IEEE, 2003.

[88] R. Raich, *Nonlinear system identification and analysis with applications to power amplifier modeling and power amplifier predistortion.* PhD thesis, Georgia Institute of Technology, 2004.

[89] K. Gard, L. Larson, and M. Steer, "Autocorrelation analysis of distortion generated from bandpass nonlinear circuits," in *IEEE Conference on Custom Integrated Circuits*, pp. 345–348, IEEE, 2002.

[90] W. Van Etten and F. Van Vugt, "Maximum likelihood receivers for data sequences transmitted over nonlinear channels," *Archiv Elektronik und Uebertragungstechnik*, vol. 34, pp. 216–223, 1980.

[91] J. Wozencraft and I. Jacobs, *Principles of communication engineering.* Wiley New York, 1965.

[92] A. Papoulis, S. Pillai, and S. Unnikrishna, *Probability, random variables, and stochastic processes.* McGraw-Hill New York, 2002.

[93] H. Nishijima, M. Okada, and S. Komaki, "A sub-optimum non-linear distortion compensation scheme fororthogonal multi-carrier modulation systems," *7th IEEE International Symposium on Personal, Indoor and Mobile Radio Communications*, vol. 1, 1996.

[94] M. Okada, H. Nishijima, and S. Komaki, "A new nonlinear distortion compensator for OFDM signals in a multipath fading channel," *IEEE International Symposium on Personal Indoor and Mobile Radio Communications*, pp. 1100–1104, 1997.

[95] M. Rodrigues and I. Wassell, "Optimum receivers for non-linearly distorted OFDM signals," *IEEE 59th Vehicular Technology Conference*, pp. 1223–1227, 2004.

[96] R. Weinstock, *Calculus of variations: with applications to physics and engineering.* Dover Pubns, 1974.

[97] M. Rodrigues, *Modelling and performance assessment of OFDM communication systems in the presence of non-linearities.* PhD thesis, London (United Kingdom): University of London, 2002.

[98] W. Liu, J. Principe, and S. Haykin, *Kernel adaptive filtering: A comprehensive introduction.* Wiley Publishing, 2010.

[99] M. Solomou, D. Rees, and N. Chiras, "Frequency domain analysis of nonlinear systems driven by multiharmonic signals," *IEEE Transactions on Instrumentation and Measurement*, vol. 53, no. 2, pp. 243–250, 2004.

[100] G. Santella and F. Mazzenga, "A hybrid analytical-simulation procedure for performance evaluation in M-QAM-OFDM schemes in presence of nonlinear distortions," *IEEE Transactions on Vehicular Technology*, vol. 47, no. 1, pp. 142–151, 1998.

[101] H. Zareian and V. Vakili, "Analytical EVM, BER, and TD performances of the OFDM systems in the presence of jointly nonlinear distortion and IQ imbalance," *Annals of Telecommunications*, vol. 64, no. 11, pp. 753–762, 2009.

[102] M. Rodrigues, J. Mitchell, and I. Darwazeh, "On the error probability performance of non-linearly distorted OFDM signals," in *IEEE 57th Vehicular Technology Conference*, vol. 2, pp. 1278–1282, IEEE, 2003.

[103] M. Core, R. Campbell, P. Quan, and J. Wada, "Semianalytic BER for PSK," *IEEE Transactions on Wireless Communications*, vol. 8, no. 4, pp. 1644–1648, 2009.

[104] M. Abramowitz and I. Stegun, *Handbook of mathematical functions with formulas, graphs, and mathematical tables.* Dover publications, 1964.

[105] N. Balakrishnan and C. Lai, *Continuous bivariate distributions.* Springer, 2009.

[106] M. Rodrigues, I. Darwazeh, and J. O'Reilly, "Error probability behaviour of nonlinearly distorted OFDM signals," *IEEE Electronics Letters*, vol. 39, no. 22, pp. 1620–1622, 2003.

[107] W. Feller, *An introduction to probability theory and its applications Vol. 1.* Wiley, New York, 1968.

[108] M. Hsieh and C. Wei, "A low-complexity frame synchronization and frequency offset compensation scheme for OFDM systems over fading channels," *IEEE Transactions on Vehicular Technology*, vol. 48, no. 5, pp. 1596–1609, 2002.

[109] D. Tse and P. Viswanath, *Fundamentals of wireless communication.* Cambridge Univ Pr, 2005.

[110] M. Simon and M. Alouini, *Digital communication over fading channels*, vol. 86. Wiley-IEEE Press, 2005.

[111] G. Turin, F. Clapp, T. Johnston, S. Fine, and D. Lavry, "A statistical model of urban multipath propagation," *Vehicular Technology, IEEE Transactions on*, vol. 21, no. 1, pp. 1–9, 1972.

[112] H. Hashemi, "Impulse response modeling of indoor radio propagation channels," *Selected Areas in Communications, IEEE Journal on*, vol. 11, no. 7, pp. 967–978, 1993.

[113] P. Bello, "Characterization of randomly time-variant linear channels," *Communications Systems, IEEE Transactions on*, vol. 11, no. 4, pp. 360–393, 1963.

[114] S. Wu and Y. Bar-Ness, "OFDM channel estimation in the presence of frequency offset and phase noise," in *Communications, 2003. ICC'03. IEEE International Conference on*, vol. 5, pp. 3366–3370, IEEE, 2003.

[115] O. Edfors, M. Sandell, J. van de Beek, S. Wilson, and P. Borjesson, "OFDM channel estimation by singular value decomposition," *IEEE Transactions on Communications*, vol. 46, no. 7, pp. 931–939, 1998.

[116] S. Coleri, M. Ergen, A. Puri, and A. Bahai, "Channel estimation techniques based on pilot arrangement in OFDM systems," *Broadcasting, IEEE Transactions on*, vol. 48, no. 3, pp. 223–229, 2002.

[117] T. Hwang, C. Yang, G. Wu, S. Li, and G. Ye Li, "OFDM and its wireless applications: a survey," *Vehicular Technology, IEEE Transactions on*, vol. 58, no. 4, pp. 1673–1694, 2009.

[118] D. Lowe and X. Huang, "Adaptive low-complexity MMSE channel estimation for OFDM," in *Communications and Information Technologies, 2006. ISCIT'06. International Symposium on*, pp. 638–643, IEEE, 2006.

[119] M. Morelli and U. Mengali, "A comparison of pilot-aided channel estimation methods for ofdm systems," *Signal Processing, IEEE Transactions on*, vol. 49, no. 12, pp. 3065–3073, 2001.

[120] J. Van de Beek, O. Edfors, M. Sandell, S. Wilson, and P. Borjesson, "On channel estimation in OFDM systems," in *Vehicular Technology Conference, 1995 IEEE 45th*, vol. 2, pp. 815–819, IEEE, 1995.

[121] M. Ozdemir and H. Arslan, "Channel estimation for wireless OFDM systems," *Communications Surveys & Tutorials, IEEE*, vol. 9, no. 2, pp. 18–48, 2007.

[122] M. Hsieh and C. Wei, "Channel estimation for OFDM systems based on comb-type pilot arrangement in frequency selective fading channels," *Consumer Electronics, IEEE Transactions on*, vol. 44, no. 1, pp. 217–225, 1998.

[123] M. Ozdemir, H. Arslan, and E. Arvas, "Toward real-time adaptive low-rank LMMSE channel estimation of MIMO-OFDM systems," *Wireless Communications, IEEE Transactions on*, vol. 5, no. 10, pp. 2675–2678, 2006.

[124] Y. Gong and K. Letaief, "Low complexity channel estimation for space-time coded wideband OFDM systems," *Wireless Communications, IEEE Transactions on*, vol. 2, no. 5, pp. 876–882, 2003.

[125] A. Duel-Hallen, "Fading channel prediction for mobile radio adaptive transmission systems," *Proceedings of the IEEE*, vol. 95, no. 12, pp. 2299–2313, 2007.

[126] M. Souryal and R. Pickholtz, "Adaptive modulation with imperfect channel information in OFDM," in *Communications, 2001. ICC 2001. IEEE International Conference on*, vol. 6, pp. 1861–1865, IEEE, 2001.

[127] I. Wong and B. Evans, "Joint channel estimation and prediction for OFDM systems," in *Global Telecommunications Conference, 2005. GLOBECOM'05. IEEE*, vol. 4, pp. 5–pp, IEEE, 2005.

[128] L. Isserlis, "On a formula for the product-moment coefficient of any order of a normal frequency distribution in any number of variables," *Biometrika*, vol. 12, no. 1/2, pp. 134–139, 1918.

[129] S. Yong and C. Chong, "An overview of multigigabit wireless through millimeter wave technology: potentials and technical challenges," *EURASIP Journal on Wireless Communications and Networking*, no. 1, 2007.

[130] H. Singh, S. Yong, J. Oh, and C. Ngo, "Principles of IEEE 802.15. 3c: Multigigabit millimeter-wave wireless PAN," in *Computer Communications and Networks, 2009. ICCCN 2009. Proceedings of 18th Internatonal Conference on*, pp. 1–6, IEEE, 2009.

[131] M. Weiß, M. Huchard, A. Stohr, B. Charbonnier, S. Fedderwitz, and D. Jager, "60-GHz Photonic millimeter-wave link for short-to medium-range wireless transmission up to 12.5 Gb/s," *IEEE Journal of Lightwave Technology*, vol. 26, no. 15, pp. 2424–2429, 2008.

[132] Z. Genc, B. Dang, J. Wang, and I. Niemegeers, "Home networking at 60 GHz: challenges and research issues," *Annals of Telecommunications*, vol. 63, no. 9, pp. 501–509, 2008.

[133] W. G. W. Alliance. `http://wirelessgigabitalliance.org`.

[134] W. Consortium. `http://www.wirelesshd.org/`.

[135] S. I. Inc. `http://www.siliconimage.com/`.

[136] H. Chettat, L. Simohamed, Y. Bouslimani, and H. Hamam, "RoF Networks : A comprehensive study," in *3rd International Symposium on Wireless Pervasive Computing*, pp. 495–498, May 2008.

[137] U. Gliese, S. Norskov, and T. Nielsen, "Chromatic dispersion in fiber-optic microwave and millimeter-wave links," *IEEE Transactions on Microwave Theory and Techniques*, vol. 44, pp. 1716–1724, Oct 1996.

[138] H. Schmuck, "Comparison of optical millimetre-wave system concepts with regardto chromatic dispersion," *IEEE Electronics Letters*, vol. 31, no. 21, pp. 1848–1849, 1995.

[139] G. Smith, D. Novak, and Z. Ahmed, "Overcoming chromatic-dispersion effects in fiber-wireless systems incorporating external modulators," *IEEE Transactions on Microwave Theory and Techniques*, vol. 45, no. 8, pp. 1410–1415, 1997.

[140] J. Mitchell, "Performance of OFDM at 5.8 GHz using radio over fibre link," *IEEE Electronics Letters*, vol. 40, no. 21, pp. 1353–1354, 2004.

[141] P. Tang, L. Ong, A. Alphones, B. Luo, and M. Fujise, "PER and EVM measurements of a radio-over-fiber network for cellular and WLAN system applications," *IEEE Journal of Lightwave Technology*, vol. 22, no. 11, pp. 2370–2376, 2004.

[142] M. Jazayerifar, B. Cabon, and J. Salehi, "Transmission of multi-band OFDM and impulse radio ultra-wideband signals over single mode fiber," *IEEE Journal of Lightwave Technology*, vol. 26, no. 15, pp. 2594–2603, 2008.

[143] A. Pizzinat, F. Payoux, B. Charbonnier, and S. Meyer, "Ultra wideband over fibre transparent architecture for high-bit-rate home networks," *Annals of Telecommunications*, vol. 63, no. 9, pp. 455–462, 2008.

[144] M. Huchard, M. Weiss, A. Pizzinat, S. Meyer, P. Guignard, and B. Charbonnier, "Ultra-broadband wireless home network based on 60-GHz WPAN cells interconnected via RoF," *IEEE Journal of Lightwave Technology*, vol. 26, no. 15, pp. 2364–2372, 2008.

[145] A. Chowdhury, H. Chien, Y. Hsueh, and G. Chang, "Advanced system technologies and field demonstration for in-building optical-wireless network with integrated broadband services," *IEEE Journal of Lightwave Technology*, vol. 27, pp. 1920–1927, 2009.

[146] C. Lethien, C. Loyez, J. Vilcot, L. Clavier, M. Bocquet, and P. Rolland, "Indoor coverage improvement of MB-OFDM UWB signals with radio over POF system," *Optics Communications*, 2009.

[147] N. Gomes, A. Das, A. Nkansah, M. Mjeku, and D. Wake, "Multimode fiber-fed indoor wireless networks," in *Proceedings of IEEE Topical Meeting on Microwave Photonics*, 2006.

[148] C. Lethien, C. Loyez, J. Vilcot, N. Rolland, and P. Rolland, "Potential of the polymer optical fibers deployed in a 10Gbps small office/home office network," *Optics Express*, vol. 16, no. 15, pp. 11266–11274, 2008.

[149] J. Oliveira, S. Silva, L. Pessoa, D. Coelho, H. Salgado, and J. Castro, "UWB radio over perfluorinated GI-POF for low-cost in-building networks," in *IEEE Topical Meeting on Microwave Photonics*, pp. 317–320, IEEE, 2010.

[150] J. Oliveira, S. Silva, L. Pessoa, H. Salgado, and J. Castro, "Performance evaluation of MB-OFDM UWB over GI-POF," in *15th European Conference on Networks and Optical Communications*, pp. 8–10, 2010.

[151] A. Das, A. Nkansah, N. Gomes, I. Garcia, J. Batchelor, and D. Wake, "Design of low-cost multimode fiber-fed indoor wireless networks," *IEEE Transactions on Microwave Theory and Techniques*, vol. 54, no. 8, pp. 3426–3432, 2006.

[152] P. Hartmann, X. Qian, A. Wonfor, R. Penty, and I. White, "1-20 GHz directly modulated radio over MMF link," in *IEEE Topical Meeting on Microwave Photonics*, pp. 95–98, 2005.

[153] M. Chia, B. Luo, M. Yee, and E. Hao, "Radio over multimode fibre transmission for wireless LAN using VCSELs," *IEEE Electronics Letters*, vol. 39, p. 1143, 2003.

[154] R. Alemany, J. Perez, R. Llorente, V. Polo, and J. Marti, "Coexistence of WiMAX 802.16d and MB-OFDM UWB in radio over multi-mode fiber indoor systems," in *IEEE Topical Meetings on Microwave Photonics, 2008. Jointly held with the 2008 Asia-Pacific Microwave Photonics Conference*, pp. 74–77, 2008.

[155] M. Larrodé and A. Koonen, "Theoretical and experimental demonstration of OFM robustness against modal dispersion impairments in radio over multimode fiber links," *IEEE Journal of Lightwave Technology*, vol. 26, no. 12, pp. 1722–1728, 2008.

[156] T. Koonen, A. Ng'oma, P. Smulders, H. van den Boom, I. Monroy, and G. Khoe, "In-house networks using multimode polymer optical fiber for broadband wireless services," *Photonic Network Communications*, vol. 5, no. 2, pp. 177–187, 2003.

[157] T. Koonen, H. van den Boom, A. Ngoma, I. Monroy, and G. Khoe, "Integrated-services in-building POF networks using novel signal multiplexing methods," in *Proceedings of the 12th International Conference on Plastic Optical Fibers*, pp. 44–47, 2003.

[158] A. Ng'oma, T. Koonen, I. Monroy, H. van den Boom, P. Smulders, and G. Khoe, "Distributing microwave signals via polymer optical fiber (POF) systems," in *Proceedings of the 6th IEEE/LEOS Benelux Chapter Symposium*, (Brussels, Belgium), pp. 157–160, 2001.

[159] T. Koonen, A. Ngoma, H. Van Den Boom, I. Monroy, P. Smulders, and G. Khoe, "Carrying microwave signals in a GIPOF-based wireless LAN," in *Proceedings of the 10th International Conference on Plastic Optical Fibers*, pp. 27–30, Citeseer, 2001.

[160] A. Koonen and M. Larrodé, "Radio-over-MMF techniques - Part II: Microwave to millimeter-wave systems," *IEEE Journal of Lightwave Technology*, vol. 26, no. 15, pp. 2396–2408, 2008.

[161] U. Gliese, T. Nielsen, S. Norskov, and K. Stubkjaer, "Multifunctional fiber-optic microwave links based on remote heterodyne detection," *IEEE Transactions on Microwave Theory and Techniques*, vol. 46, no. 5 Part 1, pp. 458–468, 1998.

[162] A. Seeds, "Microwave photonics," *IEEE Transactions on Microwave Theory and Techniques*, vol. 50, no. 3, pp. 877–887, 2002.

[163] H. Chi and J. Yao, "Frequency quadrupling and upconversion in a radio over fiber link," *IEEE Journal of Lightwave Technology*, vol. 26, no. 15, pp. 2706–2711, 2008.

[164] J. O'reilly and P. Lane, "Remote delivery of video services using mm-waves and optics," *IEEE Journal of Lightwave Technology*, vol. 12, no. 2, pp. 369–375, 1994.

[165] C. Lin, P. Shih, J. Chen, W. Jiang Jr, S. Dai, P. Peng, Y. Ho, and S. Chi, "Optical millimeter-wave up-conversion employing frequency quadrupling without optical filtering," *IEEE Transactions on Microwave Theory and Techniques*, vol. 57, no. 8, 2009.

[166] M. Mohamed, X. Zhang, B. Hraimel, and K. Wu, "Frequency sixupler for millimeter-wave over fiber systems," *Optics Express*, vol. 16, no. 14, pp. 10141–10151, 2008.

[167] P. Shih, J. Chen, C. Lin, W. Jiang Jr, H. Huang, P. Peng, and S. Chi, "Optical millimeter-wave signal generation via frequency 12-tupling," *IEEE Journal of Lightwave Technology*, vol. 28, pp. 71–78, 2010.

[168] W. Chang, *RF photonic technology in optical fiber links.* Cambridge Univ Pr, 2002.

[169] D. Wake, D. Johansson, and D. Moodie, "Passive picocell: A new concept in wireless network infrastructure," *IEEE Electronics Letters*, vol. 33, no. 5, pp. 404–406, 1997.

[170] A. Stohr, K. Kitayama, and D. Jager, "Full-duplex fiber-optic rf subcarrier transmission using a dual-function modulator/photodetector," *IEEE Transactions on Microwave Theory and Techniques*, vol. 47, no. 7, pp. 1338–1341, 1999.

[171] L. Pessoa, D. Coelho, J. Oliveira, J. Castro, and H. Salgado, "Experimental evaluation of R-EAM performance in RoF networks," in *Proceedings of the International Symposium on Green Radio over Fibre & All optical Technologies for Wireless Access Networks*, 2011.

[172] L. Pessoa, D. Coelho, J. Oliveira, J. Castro, and H. Salgado, "Assessment of noise impact on UWB signans in R-EAM based optical links," in *IEEE Avionics, Fiber-Optics and Photonics Technology Conference*, IEEE, 2011.

[173] L. Pessoa, J. Oliveira, D. Coelho, J. Castro, and H. Salgado, "Experimental evaluation of a R-EAM and noise impact analysis for UWB and Wi-Fi transmission in RoF networks," *Submitted to Annals of Telecommunications*, 2011.

[174] G. Smith, D. Novak, and Z. Ahmed, "Technique for optical SSB generation to overcome dispersion penalties in fibre-radio systems," *IEEE Electronics Letters*, vol. 33, no. 1, pp. 74–75, 1997.

[175] Z. Li, H. Chi, X. Zhang, and J. Yao, "Optical single-sideband modulation using a fiber-Bragg-grating-based optical Hilbert transformer," *IEEE Photonics Technology Letters*, no. 99, 2011.

[176] G. Agrawal, *Fiber-Optic communication systems.* Wiley-Interscience, 2002.

[177] C. Cox III, *Analog optical links: theory and practice.* Cambridge University Press, 2004.

[178] C. Lee, *Microwave photonics.* CRC, 2006.

[179] B. Saleh and M. Teich, *Fundamentals of photonics.* John Wiley & Sons, 2007.

[180] G. Keiser, *Optical fiber communications.* McGraw-Hill Science Engineering, 2000.

[181] J. Senior, *Optical fiber communications.* Prentice/Hall International, 1985.

[182] W. N. Corporation, "Product specifications of DNMA-92, an IEEE80211n a/b/g/n Mini-PCI module, version 1.6," April 2009.

[183] Y. Cho, J. Kim, W. Yang, and C. Kang, *MIMO-OFDM wireless communications with MATLAB.* Wiley, 2010.

[184] R. Aiello and A. Batra, *Ultra wideband systems: technologies and applications.* Newnes, 2006.

[185] FCC, "First report and order, revision of part 15 of the commission's rules regarding ultra-wideband transmission systems," 2002.